

Technische Universität München

Max-Planck-Institut für Physik  
(Werner-Heisenberg-Institut)

# Evaluation of multi-loop multi-scale integrals and phenomenological two-loop applications

**Sophia Carola Borowka**

Vollständiger Abdruck der von der Fakultät für Physik  
der Technischen Universität München zur Erlangung des akademischen Grades  
eines

**Doktors der Naturwissenschaften (Dr. rer. nat.)**  
genehmigten Dissertation.

Vorsitzender: Univ.-Prof. Dr. L. Oberauer  
Prüfer der Dissertation: 1. Hon.-Prof. Dr. W. F. L. Hollik  
2. Univ.-Prof. Dr. A. Ibarra

Die Dissertation wurde am 04.06.2014  
bei der Technischen Universität München eingereicht und  
durch die Fakultät für Physik am 03.07.2014 angenommen.



---

This thesis is based on the author’s work conducted at the Max Planck Institute for Physics (Werner-Heisenberg-Institut) in Munich. Parts of this work have already been published in Refs. [1–7].

## Articles

- [1] Borowka, Sophia and Carter, Jonathon and Heinrich, Gudrun  
“Numerical Evaluation of Multi-Loop Integrals for Arbitrary Kinematics with SecDec 2.0”, *Comput.Phys.Commun.* **184** (2013) 396-408, [arXiv:1204.4152](#) [[hep-ph](#)]
- [2] Borowka, Sophia and Heinrich, Gudrun  
“Massive non-planar two-loop four-point integrals with SecDec 2.1”, *Comput.Phys.Commun.* **184** (2013) 2552-2561, [arXiv:1303.1157](#) [[hep-ph](#)]
- [3] Borowka, S. and Hahn, T. and Heinemeyer, S. and Heinrich, G. and Hollik, W.  
“Momentum-dependent two-loop QCD corrections to the neutral Higgs-boson masses in the MSSM”, [arXiv:1404.7074](#) [[hep-ph](#)]

## Proceedings

- [4] Borowka, Sophia and Carter, Jonathon and Heinrich, Gudrun  
“SecDec: A tool for numerical multi-loop calculations”, *J.Phys.Conf.Ser.* **368** (2012), [arXiv:1206.4908](#) [[hep-ph](#)]
- [5] Borowka, Sophia and Heinrich, Gudrun  
“Numerical evaluation of massive multi-loop integrals with SecDec”, *PoS* **LL2012** (2012) 038, [arXiv:1209.6345](#) [[hep-ph](#)]
- [6] Borowka, Sophia and Heinrich, Gudrun  
“Numerical multi-loop calculations with SecDec”, *C13-05-16*, [arXiv:1309.3492](#) [[hep-ph](#)]
- [7] Borowka, Sophia and Heinrich, Gudrun  
“Two-loop applications of the program SecDec”, *PoS* **RADCOR2013** (2014) 009, [arXiv:1311.6476](#) [[hep-ph](#)]



## Abstract

In this thesis, major new developments in the program SECDEC are presented. SecDec is a publicly available program for the numerical evaluation of multi-loop multi-scale integrals and in this thesis it has been extended from Euclidean to physical kinematics.

The program SECDEC is based on sector decomposition to extract dimensionally regulated singularities. To deal with integrable singularities due to mass thresholds, the integrand is analytically continued to the complex plane. Further improvements are shown, proving invaluable in the two applications within this thesis.

In the first application, numerical results for several massive two-loop four-point functions are presented. In particular, results for two of the most complicated massive non-planar two-loop box integrals entering the heavy-quark pair production at next-to-next-to leading order in QCD are shown. A mixed analytical and numerical approach proves beneficial in the evaluation of the most complicated diagram. It is shown that the program can deal not only with scalar integrals, but also with tensor integrals of in principle arbitrary rank.

In its second application within this thesis, the neutral MSSM Higgs-boson spectrum is discussed. In particular, the calculation of the leading momentum-dependent order  $\mathcal{O}(\alpha_s\alpha_t)$  corrections using a mixed on-shell/ $\overline{DR}$  renormalization scheme is presented. Integrals which are available in analytic form have been implemented in a way allowing for a stable numerical evaluation. Analytically inaccessible integrals are evaluated numerically using the program SECDEC. The combination of the new momentum-dependent two-loop contribution with the existing one- and two-loop corrections in the on-shell/ $\overline{DR}$  scheme leads to an improved prediction of the light MSSM Higgs-boson mass and a correspondingly reduced theoretical uncertainty. The effect of the newly included momentum-dependent terms on the neutral  $\mathcal{CP}$ -even Higgs-boson masses is discussed. The corresponding shifts in the lightest Higgs-boson mass  $M_h$  are below 1 GeV in all scenarios considered, but can extend up to the level of the current experimental accuracy. The results are included in the code FEYNHIGGS, a publicly available program to calculate parameters related to the Higgs-boson sector in the framework of the MSSM.



# Contents

<b>1</b>	<b>Introduction</b>	<b>1</b>
<b>2</b>	<b>Higgs-bosons in the MSSM</b>	<b>5</b>
2.1	The Higgs-boson sector of the MSSM at tree-level . . . . .	5
2.2	The scalar quark sector and SQCD at tree-level . . . . .	10
2.3	Higher-order Higgs-boson mass corrections within the real MSSM . . . . .	14
<b>3</b>	<b>Multi-scale integrals beyond one loop</b>	<b>19</b>
3.1	The two loop frontier . . . . .	19
3.2	Two and more loop integrals with multiple scales . . . . .	21
3.3	Introduction of Feynman parametrization . . . . .	23
3.4	The virtues of a Mellin-Barnes representation . . . . .	26
3.5	The method of differential equations . . . . .	27
3.6	Further analytic developments . . . . .	29
3.7	Motivation for adopting a numerical approach . . . . .	30
<b>4</b>	<b>The method of sector decomposition</b>	<b>33</b>
4.1	Conceptual idea . . . . .	33
4.1.1	Generation of primary sectors . . . . .	34
4.1.2	Iterated sector decomposition . . . . .	36
4.1.3	Extraction of the poles . . . . .	37
4.1.4	Calculation of the pole coefficients . . . . .	38
4.2	The choice of algorithm . . . . .	38
4.2.1	Goals . . . . .	38
4.2.2	A heuristic algorithm for slim results . . . . .	39
4.2.3	Algorithms guaranteed to stop . . . . .	40
<b>5</b>	<b>Singularity structure of Feynman integrals</b>	<b>43</b>
5.1	Euclidean vs. physical kinematics . . . . .	43
5.2	Landau equations . . . . .	44
5.3	Deformation of the integration contour . . . . .	45
5.3.1	Cauchy theorem . . . . .	45
5.3.2	Deformation . . . . .	46

<b>6</b>	<b>Extension of the program SECDEC to physical kinematics</b>	<b>53</b>
6.1	Functionality . . . . .	53
6.2	Characteristic features . . . . .	55
6.2.1	Loop integrals . . . . .	55
6.2.2	Parametric integrals . . . . .	56
6.2.3	Implementation of Contour deformation . . . . .	57
6.3	Additional capabilities . . . . .	58
6.3.1	Evaluation of user-defined functions with arbitrary kinematics . . . . .	58
6.3.2	Topology-based construction of the integrand . . . . .	59
6.3.3	Looping over ranges of parameters . . . . .	59
6.3.4	Integration-by-parts relations . . . . .	59
6.3.5	Leaving functions implicit during the algebraic part . . . . .	60
6.3.6	Assessing the reliability of the numerical result . . . . .	60
6.3.7	Automated remapping to one endpoint . . . . .	61
6.3.8	A word on the numerical integration . . . . .	61
6.4	Operational sequence . . . . .	63
6.5	Selection of checks and examples . . . . .	64
6.5.1	A two-loop three-point function . . . . .	64
6.5.2	Massive tensor two-loop two-point functions . . . . .	66
6.6	Future developments . . . . .	67
<b>7</b>	<b>Non-planar two-loop four-point integrals with external or internal masses</b>	<b>73</b>
7.1	Analytical preparation of the non-planar seven propagator integral $ggtt_2$ . . . . .	75
7.1.1	Integration in a sub-loop . . . . .	76
7.1.2	Backwards transformation . . . . .	78
7.2	Expected thresholds from the Landau equations . . . . .	82
7.3	Numerical evaluation . . . . .	83
7.3.1	The $ggtt_2$ diagram . . . . .	83
7.3.2	The $ggtt_1$ diagram . . . . .	86
7.3.3	Planar seven-propagator all massive graph $M_7^P$ . . . . .	89
7.3.4	Non-planar seven-propagator all massive graph $M_7^{NP}$ . . . . .	89
7.3.5	Non-planar six-propagator diagram . . . . .	90
7.4	Summary . . . . .	93
<b>8</b>	<b>Neutral MSSM Higgs-boson spectrum at the two-loop level</b>	<b>95</b>
8.1	Dominant momentum-dependent two-loop QCD corrections . . . . .	96
8.2	Self-energy diagrams . . . . .	96
8.3	Renormalization . . . . .	98
8.3.1	Two-loop counter terms for the renormalization at $\mathcal{O}(\alpha_s\alpha_t)$ . . . . .	100
8.3.2	Renormalization at the sub-loop level . . . . .	104
8.4	Treatment of the integrals . . . . .	109
8.4.1	Analytically known integrals . . . . .	110
8.4.2	Analytically unknown integrals . . . . .	113



8.5	Evaluation of the additional shifts to the Higgs-boson masses . . . . .	115
8.5.1	Phenomenological motivation for two different scenarios . . . . .	116
8.5.2	Renormalized $\mathcal{O}(\alpha_s\alpha_t)$ self-energies . . . . .	118
8.5.3	Neutral $\mathcal{CP}$ -even Higgs-boson mass corrections . . . . .	124
8.6	Summary and Perspectives . . . . .	130
<b>9</b>	<b>Conclusions</b>	<b>133</b>
<b>A</b>	<b>Appendix</b>	<b>137</b>
A.1	Analytical formulae . . . . .	137
A.1.1	One-loop representations . . . . .	138
A.1.2	Two-loop representations . . . . .	140
A.2	SECDEC User Manual . . . . .	141
A.2.1	Installation . . . . .	141
A.2.2	Operation . . . . .	142
A.2.3	Program input parameters . . . . .	143
A.2.4	Input for the definition of the integrand . . . . .	149
A.2.5	Topology based construction of an integrand . . . . .	150
A.2.6	Utilization of the user-defined setup . . . . .	151
A.2.7	Looping over ranges of parameters . . . . .	152
A.2.8	Leaving functions implicit during the algebraic part . . . . .	154



# 1 | Introduction

Hadron colliders have set the stage to a whole new era of discovery. With the increasing wealth of high energy collision data, physics up to the TeV scale is being explored. Within the theoretical framework of the Standard Model of particle physics (SM) [8–14] most of the observations made by past and present collider experiments can successfully be described. Its predictive power has lead to the discovery of almost all of its constituents. These are three families of quarks and leptons, four gauge bosons mediating the electroweak and strong interaction, and the simplest manifestation of the Brout-Englert-Higgs mechanism [15–18] - the Higgs-boson. Although the discovery of the latter is still not fully confirmed, a particle behaving like the Standard Model Higgs-boson has recently been observed [19, 20] in the ATLAS and CMS experiments at the Large Hadron Collider (LHC). The characteristics of this new boson with a mass around 125 GeV have been determined already rather accurately [21–24]. If deviations with respect to the SM characteristics are found with the collation of more data, this particle must be interpreted within a different model. There are already several other reasons to search for an embedding of the Standard Model as an effective theory into a more general theoretical framework. Apart from the fact that gravity is not incorporated, the indirect observation of dark matter [25–27] does not find a description in the Standard Model either. Furthermore, the predicted violation of the  $\mathcal{CP}$  symmetry is not large enough as to explain the observed excess of matter over antimatter in the universe. More peculiarities are related to the newly found boson. If it indeed is the SM Higgs-boson, it is discussed [28–31] that the electroweak vacuum of the Standard Model may not be absolutely stable and its low mass can only be accommodated for by assuming an unnatural amount of fine-tuning [32]. Ideas for models beyond the Standard Model in which the newly found boson is realized range from interpreting it as a dilaton [33, 34] or in the framework of a composite Higgs model [35, 36]. A different proposal for a new framework is formulated as a supersymmetric extension to the Standard Model, in particular the Minimal Supersymmetric Standard Model (MSSM) [37–39]. It has been broadly discussed over the last few decades.

The motivation for supersymmetry (SUSY) [40–46] is twofold. On the one hand, it can provide for a solution to the fine-tuning and the hierarchy problem, achieve a gauge coupling unification and moreover accommodate for a dark matter candidate. On the other hand, it allows for the embedding of present observations into a more generalized mathematical framework. Supersymmetry arises as the only possible extension to the

Poincaré algebra [47], evading the no-go-theorem found by Coleman and Mandula [48]. In supersymmetric theories, all known fermionic particles of the Standard Model are assigned a scalar superpartner and all bosonic SM particles a fermionic one. The Standard Model contains one scalar doublet. In renormalizable supersymmetric models, the necessity for an even number of scalar doublets arises. At least two Higgs doublets are required, to give mass to respectively both, up-type and down-type particles and scalar particles (sparticles) [49–55]. The MSSM contains two scalar doublets which conserve hypercharge gauge invariance. Due to this invariance, all up-type particles and sparticles couple exclusively to one scalar doublet, while all down-type (s)particles couple to the other doublet. This evades constraints from flavor-changing neutral currents (FCNCs), as was pointed out by Glashow and Weinberg [56]. The two scalar doublets of the MSSM give rise to five physical Higgs-bosons. In lowest order, these are the light and heavy  $\mathcal{CP}$ -even, the  $\mathcal{CP}$ -odd, and the charged Higgs-bosons. While the mass of the Higgs-boson remains a free input parameter in the Standard Model, it is predicted within the MSSM. Associating the newly observed boson with the lightest  $\mathcal{CP}$ -even Higgs-boson  $h^0$ , the upper bound on its predicted mass  $m_{h^0}$  at leading order (LO) is given by the  $Z$  gauge boson mass. This would already have led to the exclusion of the MSSM at past collider experiments. Yet, higher-order quantum corrections to the MSSM Higgs-boson masses lead to a shift in the upper limit towards  $m_{h^0} \lesssim 135$  GeV.

Higher-order corrections are not only decisive in the precise prediction of physics beyond the Standard Model, but are of proven importance in the understanding of SM processes at colliders. The state of the art of higher-order corrections to Standard Model processes and a future wish list is summarized in the proceedings of the 2013 Les Houches workshop [57]. The more accurate predictions are desired, the more involved the calculations become. Leading order theoretical predictions can most commonly not meet the current experimental precision. The calculation of perturbative corrections at next-to-leading order (NLO) in the strong or electroweak coupling constant has reached an impressive level of automation meanwhile. Corrections beyond NLO accuracy still require quite some effort, both on the conceptual and on the technical side before they can be performed in a largely automated way. There are a few processes measured at the LHC where the need for next-to-next-to leading order (NNLO) QCD predictions arises. One of them is top-quark pair production. Top-quark pair production is vital for the precise measurements of the top-quark properties but also enters into other measurements, e.g., of parton distributions. At the LHC top quarks are produced so numerously that they also constitute a significant background to new physics signals. It is therefore crucial to understand this background properly to be able to discriminate the signal. A full NNLO prediction for the total cross section of top-quark pair production is known in a semi-numerical form [58] along with many partial results in semi-numerical and analytical form [59–71]. Soft gluon and Coulomb effects also have been taken into account beyond the next-to-leading logarithmic accuracy and have been combined with fixed order results to come up with predictions as precise as possible [72–79]. Among the key ingredients of the full NNLO calculation are complicated two-loop integrals entering the virtual corrections. Analytical expressions for these are known for diagrams dependent on relatively few mass scales [60–62, 69, 80, 81]. As soon as several mass scales

---

are involved, numerical methods to calculate multi-loop integrals become increasingly important.

The brief outline of this thesis is as follows: In Chapters 2-5, the basic concepts of the author's work presented in this thesis are established. In Chapter 6, the developed version 2 of the program SECDEC is described, laying the foundation for two applications presented in Chapters 7 and 8.

More comprehensively, Chapter 2 covers an introduction of the tree-level Higgs-boson sector of the MSSM. The scalar quark (squark) sector is discussed as well, focussing on strong and Yukawa-type interactions. Afterwards, a motivation for higher-order corrections to the Higgs-boson masses is discussed, along with an introduction to their computation. The latter involves the evaluation of two-loop integrals with multiple scales, leading to mass thresholds. Different methods to approach multi-loop multi-scale integrals are reviewed in Chapter 3, before motivating the pursuit of a universal numerical approach using Feynman parameterization. The method of sector decomposition is used for the disentanglement of overlapping ultraviolet (UV), collinear and infrared (IR) singularities, as discussed in Chapter 4. Various algorithms performing differently with respect to this task are also reviewed.

In Chapter 5, the appearance of thresholds is discussed. To compute integrable thresholds, the integrand needs to be analytically continued to the complex plane. Towards this aim, a deformation of the integration contour, applicable in numerical calculations, is explained. Finally, studies by the author are presented which tune the analytical continuation further towards a stable evaluation of integrals containing thresholds.

In Chapter 6, the features incorporated in an upgrade of the open-source program SECDEC are presented. Based on the concepts introduced in Chapters 3-5, SECDEC allows the automated numerical computation of multi-loop multi-scale integrals, in addition to an evaluation of more general parametric integrals. Restricted to non-physical kinematics in version 1, the extension to physical kinematics including thresholds is achieved in version 2 of the program. The upgraded features are presented along with diverse other improvements.

In Chapter 7, the full power of the program SECDEC is shown in an application to massive non-planar two-loop four-point functions, among them various ones where analytical results are unknown. Several of the topologies shown are computed in a fully automated way. For one topology which is of particular interest in the top-quark pair production at NNLO, analytical transformations beforehand are shown, improving on the numerical stability. In particular, the integration of one Feynman parameter of a sub-loop is found to be beneficial. Furthermore, a transformation first introduced by the author and collaborators, proves to allow for a simplification of the singularity structure, leading to a reduction in the number of sub-functions to be integrated. The transformation is presented in detail.

In Chapter 8, the calculation of the dominant neutral  $\mathcal{CP}$ -even MSSM Higgs-boson mass corrections at the two-loop order including momentum dependence is presented. This requires the calculation of two-loop self-energies with a proper renormalization at the two-loop level, using an overall mixed on-shell and  $\overline{DR}$  scheme for the renormal-

ization. The program SECDEC is used in the evaluation of analytically inaccessible integrals. The mass shifts resulting from the additional momentum-dependent contributions are presented.

The conclusions are given in Chapter 9.

## 2 | Higgs-bosons in the MSSM

In the following, the Higgs-boson, quark and scalar quark (squark) sector of the MSSM are introduced. The tree-level mass matrices are derived from the MSSM Lagrangian. All interactions appearing in the two-loop corrections to the MSSM Higgs-boson masses discussed in Chap. 8 are shown as well. This includes supersymmetric QCD (SQCD) interactions. The following two sections, Sec. 2.1 and 2.2, are based on Refs. [38, 82–86]. Afterwards, the current status of higher-order Higgs-boson mass corrections in the MSSM is reviewed in Sec. 2.3.

### 2.1 The Higgs-boson sector of the MSSM at tree-level

The Higgs-boson sector of the MSSM with real parameters (rMSSM) is part of the full MSSM Lagrangian and consists of the following four components

$$\mathcal{L}_{\text{MSSM}} \supset \mathcal{L}_{\text{H}_{\text{free}}} + \mathcal{L}_{\text{H}_V} + \mathcal{L}_{\text{H}_{\text{int}}} + \mathcal{L}_{\text{H}_{\text{fix}}} + \mathcal{L}_{\text{H}_{\text{ghost}}} , \quad (2.1)$$

where  $\mathcal{L}_{\text{H}_{\text{free}}}$  contains the free-field kinetic terms,  $\mathcal{L}_{\text{H}_V}$  is derived from the Higgs-boson potential, and  $\mathcal{L}_{\text{H}_{\text{fix}}}$  is the gauge-fixing term. With the introduction of a gauge-fixing term, unphysical degrees of freedom arise which are compensated by Faddeev-Popov ghost terms [87] in  $\mathcal{L}_{\text{H}_{\text{ghost}}}$ . The interaction part of the Higgs-boson sector Lagrangian can be summarized as

$$\begin{aligned} \mathcal{L}_{\text{H}_{\text{int}}} = & \mathcal{L}_{\text{HHH}} + \mathcal{L}_{\text{HHHH}} \\ & + \mathcal{L}_{\text{HHV}} + \mathcal{L}_{\text{HVV}} + \mathcal{L}_{\text{HHVV}} \\ & + \mathcal{L}_{\text{H}\psi\bar{\psi}} + \mathcal{L}_{\text{H}\tilde{s}\tilde{s}} + \mathcal{L}_{\text{HH}\tilde{s}\tilde{s}} \\ & + \mathcal{L}_{\text{H}\tilde{\chi}\tilde{\chi}} . \end{aligned} \quad (2.2)$$

All physical neutral and charged Higgs-boson fields are referred to with the index H, the index V is short for vector boson fields,  $\psi$  and  $\bar{\psi}$  denote the Standard Model quarks and leptons,  $\tilde{s}$  denotes all squarks and scalar leptons (sleptons) and  $\tilde{\chi}$  symbolizes the neutralinos and charginos. Adopting the Feynman-'t Hooft gauge, all ghost contributions vanish.

The MSSM requires two doublets  $\mathcal{H}_1$  and  $\mathcal{H}_2$  of complex scalar fields, which are

conventionally written in terms of their components as follows,

$$\mathcal{H}_1 = \begin{pmatrix} \mathcal{H}_1^0 \\ \mathcal{H}_1^- \end{pmatrix} = \begin{pmatrix} v_1 + \frac{1}{\sqrt{2}}(\phi_1^0 - i\chi_1^0) \\ -\phi_1^- \end{pmatrix}, \quad (2.3)$$

$$\mathcal{H}_2 = \begin{pmatrix} \mathcal{H}_2^+ \\ \mathcal{H}_2^0 \end{pmatrix} = \begin{pmatrix} \phi_2^+ \\ v_2 + \frac{1}{\sqrt{2}}(\phi_2^0 + i\chi_2^0) \end{pmatrix}, \quad (2.4)$$

with an associated hypercharge  $Y_1 = -1$  and  $Y_2 = +1$ , respectively. Their vacuum expectation values are given by  $v_1$  and  $v_2$ , respectively. The fields  $\phi_i$  and  $\chi_i$  are still unphysical, but are brought into the physical basis

$$\begin{pmatrix} H^0 \\ h^0 \end{pmatrix} = A(\alpha) \begin{pmatrix} \phi_1^0 \\ \phi_2^0 \end{pmatrix}, \quad \begin{pmatrix} G^0 \\ A^0 \end{pmatrix} = A(\beta) \begin{pmatrix} \chi_1^0 \\ \chi_2^0 \end{pmatrix}, \quad \begin{pmatrix} G^\pm \\ H^\pm \end{pmatrix} = A(\beta) \begin{pmatrix} \phi_1^\pm \\ \phi_2^\pm \end{pmatrix} \quad (2.5)$$

via orthogonal transformations of the type

$$A(x) = \begin{pmatrix} \cos(x) & \sin(x) \\ -\sin(x) & \cos(x) \end{pmatrix}, \quad (2.6)$$

giving rise to the particle spectrum of physical Higgs- and unphysical Goldstone-bosons, compare Tab. 2.1.

2 neutral $\mathcal{CP}$ -even Higgs-bosons	$h^0, H^0$
1 neutral $\mathcal{CP}$ -odd Higgs-boson	$A^0$
1 neutral $\mathcal{CP}$ -odd Goldstone boson	$G^0$
2 charged Higgs-bosons	$H^+, H^-$
2 charged Goldstone bosons	$G^+, G^-$

Table 2.1: Higgs- and Goldstone boson particle spectrum.

The kinetic part of the MSSM Higgs-boson sector Lagrangian reads

$$\mathcal{L}_{\phi_{\text{free}}} = \sum_{a=1}^2 \partial_\mu \mathcal{H}_a^\dagger \partial^\mu \mathcal{H}_a. \quad (2.7)$$

Note the index  $\phi$  instead of  $H$  in Eq. (2.7). It is introduced to distinguish between the  $\phi_1^0$ - $\phi_2^0$  and the  $h^0$ - $H^0$  basis.

The potential part of the rMSSM Higgs-boson sector Lagrangian  $\mathcal{V}_\phi$  can be written in terms of the supersymmetric F- and D-term contributions

$$\mathcal{V}_{\phi_{\text{F}}} = |\mu|^2 (\mathcal{H}_1^{i\dagger} \mathcal{H}_1^i + \mathcal{H}_2^{i\dagger} \mathcal{H}_2^i), \quad (2.8)$$

and

$$\mathcal{V}_{\phi_{\text{D}}} = \frac{1}{8} (g^2 + g'^2) (\mathcal{H}_1^{i\dagger} \mathcal{H}_1^i - \mathcal{H}_2^{i\dagger} \mathcal{H}_2^i)^2 + \frac{1}{2} g^2 |H_1^{i\dagger} \mathcal{H}_2^i|^2, \quad (2.9)$$



where  $i = 1, 2$  from now on. In contrast to the Standard Model, the Higgs-boson self-couplings in the MSSM, resulting from Eq. (2.9), are determined through the gauge coupling constants. The dagger in Eqs. (2.8) and (2.9) indicates Hermitian adjoints,  $\mu$  is the higgsino (fermionic superpartner of the Higgs-boson) mass parameter,  $g$  is the  $SU(2)_L$  and  $g'$  the  $U(1)_Y$  coupling constant. The coupling constants  $g$  and  $g'$  are related to the electric charge  $e$  and the electro-weak mixing angle  $\theta_W$  of the Standard Model by

$$g = \frac{e}{\sin \theta_W}, \quad g' = \frac{e}{\cos \theta_W}. \quad (2.10)$$

Due to the non-observation of supersymmetric partners to the Standard Model particles, supersymmetry must be broken. Various supersymmetry breaking mechanisms can be considered [49–55, 88]. In the MSSM, explicit breaking terms [51, 88] parameterize the effect of SUSY breaking. In order to accommodate for a solution to the hierarchy problem, these terms may not introduce additional quadratic divergences. They must have mass dimension less than four. These so called soft supersymmetry breaking terms are added to the MSSM Higgs-boson potential

$$\mathcal{V}_{\phi_{\text{soft}}} = m_1^2(\mathcal{H}_1^{i\dagger}\mathcal{H}_1^i) + m_2^2(\mathcal{H}_2^{i\dagger}\mathcal{H}_2^i) - m_{12}^2(\varepsilon_{ij}\mathcal{H}_1^i\mathcal{H}_2^j + h.c.), \quad (2.11)$$

where  $j = 1, 2$  from now on, and with  $\varepsilon_{ij}$ <sup>1</sup> being totally antisymmetric, resulting in an overall MSSM Higgs-boson potential of

$$\mathcal{V}_\phi = \mathcal{V}_{\phi_F} + \mathcal{V}_{\phi_D} + \mathcal{V}_{\phi_{\text{soft}}}. \quad (2.12)$$

Relating the MSSM Higgs-boson potential to the MSSM Lagrangian by

$$\mathcal{L}_{\phi_V} = - \left( \int d^2\theta \mathcal{V}_{\phi_F} + \iint d^2\theta d^2\bar{\theta} \mathcal{V}_{\phi_D} + \mathcal{V}_{\phi_{\text{soft}}} \right), \quad (2.13)$$

where the F-term part of the potential is integrated over the auxiliary superspace component  $\theta$ , while the D-term part of the potential is integrated over both superspace components  $\theta$  and  $\bar{\theta}$ . In the following, the notation

$$\int d^2\theta \mathcal{V} = [\mathcal{V}]_F \quad \text{and} \quad \iint d^2\theta d^2\bar{\theta} \mathcal{V} = [\mathcal{V}]_D \quad (2.14)$$

is adopted.

Until now, the MSSM Higgs-boson potential, Eq. (2.12), contains four free parameters:  $m_1$ ,  $m_2$ ,  $m_{12}$  and  $\mu$ . Exploiting the fact that the two vacuum expectation values  $v_1$  and  $v_2$  need to minimize the potential and be nonzero at the same time, the following necessary minimization conditions

$$\frac{\partial}{\partial \mathcal{H}_a^i} \mathcal{V}_\phi \Big|_{\text{lin}} = 0, \quad a = 1, 2 \quad (2.15)$$

<sup>1</sup>Note the convention:  $\varepsilon_{ij} = -\varepsilon^{ij}$ , with  $\varepsilon_{12} = -1$  and  $\varepsilon_{21} = 1$ .

are required to hold. The minimization conditions originate from the equations of motion, compare Eq. (2.56). In Eq. (2.15), the linear part of the rMSSM potential reads

$$\begin{aligned} \mathcal{V}_\phi \Big|^\text{lin} = & \sqrt{2}\tilde{m}_1^2 v_1 \phi_1^0 + \sqrt{2}\tilde{m}_2^2 v_2 \phi_2^0 + \sqrt{2}m_{12}^2 (v_2 \phi_1^0 + v_1 \phi_2^0) \\ & + \frac{1}{2\sqrt{2}}(g^2 + g'^2)(v_1^2 - v_2^2)(v_1 \phi_1^0 - v_2 \phi_2^0), \end{aligned} \quad (2.16)$$

where  $\tilde{m}_i^2 \equiv m_i + |\mu|^2$ . It should be noted that there are no contributions from the fields  $\chi_a^0$  and  $\phi_a^\pm$  to the linear part of the potential. This is due to the fact that the MSSM potential is  $\mathcal{CP}$ -conserving, meaning that it is invariant under the consecutive application of a charge conjugation  $\mathcal{C}$  and a parity transformation  $\mathcal{P}$ . Without imposing the minimization condition just yet, and writing the coefficients to the fields  $\phi_1^0, \phi_2^0$  in Eq. (2.16) as tadpole parameters  $T_a$  instead, the parameters  $\tilde{m}_1$  and  $\tilde{m}_2$  can be expressed in terms of experimentally accessible quantities  $(g, g', v_1, v_2)$  and the parameter  $m_{12}$

$$\tilde{m}_1^2 = \frac{1}{\sqrt{2}v_1}T_1 - \frac{v_2}{v_1}m_{12}^2 - \frac{1}{4}(g^2 + g'^2)(v_1^2 - v_2^2), \quad (2.17)$$

$$\tilde{m}_2^2 = \frac{1}{\sqrt{2}v_2}T_2 - \frac{v_1}{v_2}m_{12}^2 + \frac{1}{4}(g^2 + g'^2)(v_1^2 - v_2^2). \quad (2.18)$$

Consequently, after making use of Eq. (2.15), the tadpole parameters  $T_a$  vanish

$$T_a = 0. \quad (2.19)$$

Turning to the part of the MSSM Higgs-boson potential which is bilinear in the fields, the mass matrices  $M_{\phi^0}^2$ ,  $M_{\chi^0}^2$  and  $M_{\phi^\pm}^2$  of the scalar fields of the neutral  $\mathcal{CP}$ -even, the neutral  $\mathcal{CP}$ -odd and, respectively, the charged Higgs- and Goldstone-bosons can be identified

$$\mathcal{V}_\phi \supset \frac{1}{2} \begin{pmatrix} \phi_1^0 & \phi_2^0 \end{pmatrix} M_{\phi^0}^2 \begin{pmatrix} \phi_1^0 \\ \phi_2^0 \end{pmatrix} + \frac{1}{2} \begin{pmatrix} \chi_1^0 & \chi_2^0 \end{pmatrix} M_{\chi^0}^2 \begin{pmatrix} \chi_1^0 \\ \chi_2^0 \end{pmatrix} + \begin{pmatrix} \phi_1^+ & \phi_2^+ \end{pmatrix} M_{\phi^\pm}^2 \begin{pmatrix} \phi_1^- \\ \phi_2^- \end{pmatrix}, \quad (2.20)$$

where  $\phi_2^- = (\phi_2^+)^*$  and  $\phi_1^+ = (\phi_1^-)^*$ . The tree-level mass matrix of the neutral  $\mathcal{CP}$ -odd bosons reads

$$M_{\chi^0}^2 = \begin{pmatrix} \tilde{m}_1^2 + \frac{1}{4}(g^2 + g'^2)(v_1^2 - v_2^2) & m_{12}^2 \\ m_{12}^2 & \tilde{m}_2^2 + \frac{1}{4}(g^2 + g'^2)(v_2^2 - v_1^2) \end{pmatrix} \quad (2.21a)$$

$$= m_{12}^2 \begin{pmatrix} -\frac{v_2}{v_1} & 1 \\ 1 & -\frac{v_1}{v_2} \end{pmatrix}, \quad (2.21b)$$

where in the last step, the relations of Eqs. (2.17-2.19) were used. Afterwards, the mass matrix can be made diagonal

$$\text{diag}(m_{G^0}^2, m_{A^0}^2) = A(\beta)^T M_{\chi^0}^2 A(\beta) \quad (2.22a)$$

$$= \begin{pmatrix} 0 & 0 \\ 0 & -m_{12}^2(\tan \beta + \cot \beta) \end{pmatrix}, \quad (2.22b)$$

resulting with the tree-level relation for the physical neutral  $\mathcal{CP}$ -odd Higgs-boson mass  $m_{A^0}^2$ . Note that the tree-level  $A^0$ -boson mass  $m_{A^0}^2$  does not attain any dependence on the Standard Model vector-boson masses  $m_W$  or  $m_Z$ . Defining the vacuum expectation values  $v_1$  and  $v_2$  as

$$v_1 \equiv \frac{\sqrt{2}m_W \cos \beta}{g}, \quad v_2 \equiv \frac{\sqrt{2}m_W \sin \beta}{g}, \quad (2.23)$$

the following relation results

$$\tan \beta = \frac{v_2}{v_1}, \quad 0 \leq \beta \leq \frac{\pi}{2}. \quad (2.24)$$

The lower and upper bound on the angle  $\beta$  result from the assumption that  $v_1$  and  $v_2$  are real and positive, compare Ref. [82].

Hereby, all free mass parameters are expressed in terms of physical observables and the MSSM Higgs-boson potential is fixed by the parameters  $v_1$ ,  $v_2$ ,  $m_A$ ,  $g'$  and  $g$ . With this knowledge in mind, the masses of the neutral  $\mathcal{CP}$ -even Higgs-bosons can be derived from the mass matrix

$$M_{\phi^0}^2 = \begin{pmatrix} M_{\phi_1^0 \phi_1^0}^2 & M_{\phi_1^0 \phi_2^0}^2 \\ M_{\phi_2^0 \phi_1^0}^2 & M_{\phi_2^0 \phi_2^0}^2 \end{pmatrix} \quad (2.25a)$$

$$= \begin{pmatrix} m_{A^0}^2 \sin^2 \beta + m_Z^2 \cos^2 \beta & -(m_{A^0}^2 + m_Z^2) \sin \beta \cos \beta \\ -(m_{A^0}^2 + m_Z^2) \sin \beta \cos \beta & m_{A^0}^2 \cos^2 \beta + m_Z^2 \sin^2 \beta \end{pmatrix}, \quad (2.25b)$$

being written in terms of the three parameters  $m_{A^0}$ ,  $m_Z$  and the angle  $\beta$ . After bringing the mass matrix into diagonal form, the physical  $\mathcal{CP}$ -even Higgs-boson masses read

$$m_{H^0, h^0}^2 = \frac{1}{2} \left( m_{A^0}^2 + m_Z^2 \pm \sqrt{(m_{A^0}^2 + m_Z^2)^2 - 4m_{A^0}^2 m_Z^2 \cos^2(2\beta)} \right). \quad (2.26)$$

The mass of the light  $\mathcal{CP}$ -even Higgs-boson is therefore bound from above through the relation  $m_{h^0} \leq \min(m_Z, m_{A^0}) |\cos(2\beta)|$ .

For completeness, the masses of the charged Higgs-bosons can be derived via the mass matrix of the charged-boson components

$$M_{\phi^\pm}^2 = \begin{pmatrix} \tilde{m}_1^2 + \frac{1}{4}(g^2 + g'^2)(v_1^2 - v_2^2) + \frac{1}{2}g^2 v_2^2 & m_{12}^2 - \frac{1}{2}g^2 v_1 v_2 \\ m_{12}^2 - \frac{1}{2}g^2 v_1 v_2 & \tilde{m}_2^2 + \frac{1}{4}(g^2 + g'^2)(v_2^2 - v_1^2) + \frac{1}{2}g^2 v_1^2 \end{pmatrix} \quad (2.27)$$

as

$$\text{diag}(m_{G^\pm}^2, m_{H^\pm}^2) = A(\beta)^T M_{\phi^\pm}^2 A(\beta) \quad (2.28a)$$

$$= \begin{pmatrix} 0 & 0 \\ 0 & -m_{12}^2(\tan \beta + \cot \beta) + m_W^2 \end{pmatrix}, \quad (2.28b)$$

where relations Eqs. (2.17-2.18) are again useful. Similar to the SM relations, the gauge-boson masses are given by

$$m_W^2 = \frac{1}{2}g^2(v_1^2 + v_2^2), \quad m_Z^2 = \frac{1}{2}(g^2 + g'^2)(v_1^2 + v_2^2), \quad m_\gamma^2 = 0. \quad (2.29)$$

The rich phenomenological implications of the real MSSM can be explored further, when studying the dependence on the angles  $\alpha$  and  $\beta$ . The angle  $\beta$  is linked to the vacuum expectation values through Eq. (2.24). In turn, the angle  $\alpha$  can be determined from the rotation of Eq. (2.25b) into the physical basis. The following basic relation among the two angles holds [83]

$$\tan(2\alpha) = \tan(2\beta) \frac{m_{A^0}^2 + m_Z^2}{m_{A^0}^2 - m_Z^2}, \quad -\frac{\pi}{2} < \alpha < 0. \quad (2.30)$$

Many more relations among the angles can be found, compare Ref. [82, 83]. When expressing the couplings in terms of these, they can be formulated as angle suppression factors with respect to Standard Model Higgs-boson couplings to, e.g., vector bosons

$$\frac{g_{h^0VV}}{g_{hVV}} \propto \sin(\beta - \alpha), \quad (2.31)$$

$$\frac{g_{H^0VV}}{g_{hVV}} \propto \cos(\beta - \alpha), \quad (2.32)$$

where  $h$  denotes the Standard Model Higgs-boson and  $h^0, H^0$  the MSSM Higgs-bosons.

Besides, in order not to be a toy model, the features of the Standard Model must be reproduced in the MSSM, at least in certain parametric limits. This is fulfilled in the decoupling limit, taking the limit  $m_{A^0} \rightarrow \infty$ . Then, the physical Higgs-bosons  $A^0, H^0$  and  $H^\pm$  decouple from the theory and the Standard Model Higgs-boson sector consisting of a single physical  $\mathcal{CP}$ -even scalar  $h^0$  results. Additionally, a SUSY mass scale much larger than the electro-weak scale can be assumed. Then,  $h^0$  becomes indistinguishable from the Higgs-boson  $h$  of the Standard Model, since all Standard Model tree-level and loop-induced couplings to Standard Model gauge bosons and fermions are reproduced. A decoupling may also occur independent of the  $A^0$  boson mass in other regions of the MSSM parameter space. For a discussion, see Refs. [85, 89].

## 2.2 The scalar quark sector and SQCD at tree-level

In light of the calculation to be discussed in detail in Chap. 8, an introduction of the tree-level quark and squark interactions is necessary, including those of supersymmetric Quantum Chromodynamics (SQCD). Interactions with the Higgs-boson sector are also discussed.

The relevant parts of the MSSM Lagrangian regarding SQCD, the fermion  $\psi$  and the scalar fermion (sfermion)  $\tilde{s}$  sector, reads

$$\mathcal{L}_{\text{MSSM}} \supset \mathcal{L}_{\tilde{s}\text{free}} + \mathcal{L}_{\psi\text{free}} + \mathcal{L}_{\tilde{s}\text{int}} + \mathcal{L}_{\psi\text{int}} + \mathcal{L}_G + \mathcal{L}_{\tilde{g}}, \quad (2.33)$$

superfield	particle content	spin	sparticle content	spin	Y
$\hat{Q}$	$Q = \begin{pmatrix} u_L \\ d_L \end{pmatrix}$	$\frac{1}{2}$	$\tilde{Q} = \begin{pmatrix} \tilde{u}_L \\ \tilde{d}_L \end{pmatrix}$	0	1/3
$\hat{U}$	$U = u_R^\dagger$	$\frac{1}{2}$	$\tilde{U} = \tilde{u}_R^*$	0	-4/3
$\hat{D}$	$D = d_R^\dagger$	$\frac{1}{2}$	$\tilde{D} = \tilde{d}_R^*$	0	2/3
$\hat{L}$	$\begin{pmatrix} \nu_L \\ e_L \end{pmatrix}$	$\frac{1}{2}$	$\begin{pmatrix} \tilde{\nu}_L \\ \tilde{e}_L \end{pmatrix}$	0	-1
$\hat{E}$	$e_R^\dagger$	$\frac{1}{2}$	$\tilde{e}_R^*$	0	2
$G^a$	$G_\mu^a$	1	$\tilde{g}^a$	$\frac{1}{2}$	0
$W$	$W_\mu^i$	1	$\tilde{W}^i$	$\frac{1}{2}$	2
$B$	$B_\mu$	1	$\tilde{B}$	$\frac{1}{2}$	2
$H_1$	$H_1$	0	$\tilde{H}_1$	$\frac{1}{2}$	-1
$H_2$	$H_2$	0	$\tilde{H}_2$	$\frac{1}{2}$	+1

Table 2.2: The superfield content of the MSSM, the respective spin of the particles and sparticles and the corresponding weak hypercharge  $Y$ . The index  $a$  labels the different components. Neutralinos and charginos are formed from linear combinations of the gauginos,  $\tilde{B}$  and  $\tilde{W}^i$ , and the higgsinos  $\tilde{H}_{1,2}$ .

where the first two terms on the righthand side of Eq. (2.33) are the free field equations for the squarks and sleptons and the quarks and leptons, respectively. The last two terms are the QCD and SQCD gauge field contributions. They can be combined as follows

$$\mathcal{L}_G + \mathcal{L}_{\tilde{g}} = \left[ \frac{1}{16g_s^2} W_s^{a\alpha} W_{s\alpha}^a + h.c. \right]_F + \mathcal{L}_{\tilde{g}_{\text{soft}}} , \quad (2.34)$$

where  $W_s^a$  in the first term on the righthand side is the supersymmetric SU(3) Yang-Mills field-strength tensor defined as

$$W_{s\alpha}^a = -\frac{1}{4} \bar{D}_\alpha \bar{D}^\alpha (e^{-2g_s t_s^a G^a} D_\alpha e^{2g_s t_s^a G^a}) , \quad (2.35)$$

compare Ref. [90]. Here, the  $t_s^a$  denote the generators of SU(3) $_c$ ,  $g_s$  is the strong coupling constant and the  $G^a$  represent the gluon and gluino fields, compare Tab. 2.2. The  $D_\alpha$  and  $\bar{D}_\alpha$  are the covariant derivatives with respect to the superspace coordinates and are defined as

$$D_\alpha = \partial_\alpha - i\sigma_{\alpha\beta}^\mu \bar{\theta}^\beta \partial_\mu, \quad \bar{D}^\alpha = \bar{\partial}^\alpha - i\bar{\sigma}^{\mu\alpha\beta} \theta_\beta \partial_\mu . \quad (2.36)$$

While the gluon is massless, the gluino acquires a mass term from explicit but soft supersymmetry breaking

$$\mathcal{L}_{\tilde{g}_{\text{soft}}} = -\left(\frac{1}{2} m_{\tilde{g}} \tilde{g}^\dagger \tilde{g} + h.c.\right) . \quad (2.37)$$

This type of mass term can rather generically be introduced for all fermions of a supergauge multiplet, compare Refs. [51, 88].

Following Ref. [82], the third and fourth term in Eq. (2.33) can be split into F-terms, D-terms and soft breaking terms. Additionally, interactions between the gluino  $\tilde{g}$ , a quark and a squark must be taken into account. Hence, the full potential reads

$$\mathcal{L}_{\tilde{s}_{\text{int}}} + \mathcal{L}_{\psi_{\text{int}}} = -[\mathcal{V}_{\tilde{s}_{\text{F}}}]_F - [\mathcal{V}_{\tilde{s}_{\text{D}}}]_D - \mathcal{V}_{\tilde{s}_{\text{soft}}} + \mathcal{L}_{\psi} + \mathcal{L}_{qqG} + \mathcal{L}_{\tilde{q}\tilde{q}\tilde{q}\tilde{q}}^s + \mathcal{L}_{\tilde{q}\tilde{q}G} + \mathcal{L}_{q\tilde{q}\tilde{g}}. \quad (2.38)$$

The F-term contributions are

$$\begin{aligned} \mathcal{V}_{\tilde{s}_{\text{F}}} = & |-\mu^\dagger \mathcal{H}_1^{i\dagger} + y_u \tilde{Q}^{i\dagger} \tilde{U}|^2 + |\mu^\dagger \mathcal{H}_2^{i\dagger} + y_d \tilde{Q}^{i\dagger} \tilde{D}|^2 \\ & + y_u^2 |\varepsilon_{ij} \mathcal{H}_2^i \tilde{Q}^j|^2 + y_d^2 |\varepsilon_{ij} \mathcal{H}_1^i \tilde{Q}^j|^2 \\ & + (y_u \mathcal{H}_2^{i\dagger} \tilde{U}^\dagger - y_d \mathcal{H}_1^{i\dagger} \tilde{D}^\dagger)(y_u \mathcal{H}_2^i \tilde{U} - y_d \mathcal{H}_1^i \tilde{D}) \end{aligned} \quad (2.39)$$

where Yukawa interactions of the type  $H\tilde{s}\tilde{s}$ ,  $HH\tilde{s}\tilde{s}$  and  $\tilde{s}\tilde{s}\tilde{s}\tilde{s}$  can be read off. While the  $\tilde{Q}$ ,  $\tilde{U}$  and  $\tilde{D}$  denote the scalar superfields, see Tab. 2.2, the Yukawa couplings read

$$y_u = \frac{g m_u}{\sqrt{2} m_W \sin \beta}, \quad y_d = \frac{g m_d}{\sqrt{2} m_W \cos \beta}. \quad (2.40)$$

The D-terms contributing to the scalar potential Eq. (2.38) read

$$\begin{aligned} \mathcal{V}_{\tilde{s}_{\text{D}}} = & \frac{1}{8} g^2 \left( 4|\mathcal{H}_1^{i\dagger} \tilde{Q}^i|^2 + 4|\mathcal{H}_2^{i\dagger} \tilde{Q}^i|^2 - 2(\tilde{Q}^{i\dagger} \tilde{Q}^i)(\mathcal{H}_1^{i\dagger} \mathcal{H}_1^i + \mathcal{H}_2^{i\dagger} \mathcal{H}_2^i) + (\tilde{Q}^{i\dagger} \tilde{Q}^i)^2 \right) \\ & + \frac{1}{4} g'^2 (\mathcal{H}_2^{i\dagger} \mathcal{H}_2^i - \mathcal{H}_1^{i\dagger} \mathcal{H}_1^i) (Y_q \tilde{Q}^{i\dagger} \tilde{Q}^i + Y_u \tilde{U}^\dagger \tilde{U} + Y_d \tilde{D}^\dagger \tilde{D}) \\ & + \frac{1}{8} g'^2 \left( Y_q \tilde{Q}^{i\dagger} \tilde{Q}^i + Y_u \tilde{U}^\dagger \tilde{U} + Y_d \tilde{D}^\dagger \tilde{D} \right)^2, \end{aligned} \quad (2.41)$$

where  $Y_q = \frac{1}{3}$ ,  $Y_u = -\frac{4}{3}$  and  $Y_d = \frac{2}{3}$  are the hypercharges of the respective superfield. The squarks couple not only weakly to each other, but also strongly via

$$\mathcal{L}_{\tilde{q}\tilde{q}\tilde{q}\tilde{q}}^s = -\frac{1}{2} g_s^2 \sum_a (\tilde{q}_L^\dagger t_s^a \tilde{q}_L - \tilde{q}_R^\dagger t_s^{*a} \tilde{q}_R)^2, \quad (2.42)$$

compare e.g. Ref. [91]. The soft-breaking part of the potential reads

$$\begin{aligned} \mathcal{V}_{\tilde{s}_{\text{soft}}} = & M_{\tilde{Q}}^2 \tilde{Q}^{i\dagger} \tilde{Q}^i + M_{\tilde{u}}^2 \tilde{U}^\dagger \tilde{U} + M_{\tilde{d}}^2 \tilde{D}^\dagger \tilde{D} \\ & + m_6 (-\varepsilon^{ij} y_u A_u H_2^i \tilde{Q}^j \tilde{U}^\dagger + \varepsilon^{ij} y_d A_d H_1^i \tilde{Q}^j \tilde{D}^\dagger + h.c.), \end{aligned} \quad (2.43)$$

where the products  $m_6 A_{u,d}$  denote the trilinear couplings of the Higgs-bosons to the squarks. In the following,  $m_6 = 1$  is chosen by convention.  $M_{\tilde{Q}}$  is the mass parameter of the left-hand sparticles,  $M_{\tilde{u}}$  and  $M_{\tilde{d}}$  are the mass parameters of the righthand up-type and down-type sparticles, respectively. The soft breaking terms lead at most to a logarithmically divergent behavior and gauge invariance is ensured, see Refs. [51, 88].

The slepton fields  $\tilde{L}$ ,  $\tilde{E}$  are omitted here but can be included as well with an appropriate choice of hypercharges. The Yukawa interaction of the quarks and leptons reads

$$\mathcal{L}_\psi = -\varepsilon_{ij}(y_d \mathcal{H}_1^i Q^j D - y_u \mathcal{H}_2^i Q^j U + y_e \mathcal{H}_1^i L^j E) + h.c. , \quad (2.44)$$

where  $y_e$  is the Yukawa coupling to the leptons. The quark and lepton masses purely arise from the Yukawa interactions, therefore the quark and lepton mass matrices can be directly deduced from the Yukawa terms. The interaction of two quarks with a gluon reads

$$\mathcal{L}_{q\bar{q}G} = -g_s G_\mu^a \sum_{i=u,d} \bar{q}_j \gamma^\mu (t_s^a)_{jk} q_k , \quad (2.45)$$

where  $j$  and  $k$  are color indices. Now, the squark-squark gluon interaction is

$$\mathcal{L}_{\tilde{q}\tilde{q}G} = -ig_s G_\mu^a \sum_{i=u,d} \tilde{q}_i^{j\dagger} (t_s^a)_{jk} \partial^\mu \tilde{q}_i^k , \quad (2.46)$$

where the sums run over both left- and righthanded components, compare Ref. [38]. Finally, the squark-quark-gluino interaction reads

$$\mathcal{L}_{q\tilde{q}\tilde{g}} = -\sqrt{2}g_s (t_s^a)_{jk} \sum_{i=u,d} (\tilde{g}_a^\dagger P_L q_i^k \tilde{q}_{iL}^{j\dagger} + q_i^{j\dagger} P_R \tilde{g}_a \tilde{q}_{iL}^k - \tilde{g}_a^\dagger P_R q_i^k \tilde{q}_{iR}^{j\dagger} - q_i^{j\dagger} P_L \tilde{g}_a \tilde{q}_{iR}^k) , \quad (2.47)$$

where the relative minus sign comes in with the negative sign of the color generator  $t_s^{a*}$  of the color antitriplets. Likewise, there are electroweak quark-squark-gaugino interactions. They are not listed here because they are not needed in the calculation of Chap. 8.

The squark masses are composed of the soft breaking terms, but also the F- and D-terms of the squark potential, when the Higgs-bosons acquire vacuum expectation values. Altogether, the massive part of the squark sector in the MSSM reads

$$\mathcal{L}_{\tilde{q},\text{mass}} = -\begin{pmatrix} \tilde{u}_L^\dagger & \tilde{u}_R^\dagger \end{pmatrix} M_{\tilde{u}LR}^2 \begin{pmatrix} \tilde{u}_L \\ \tilde{u}_R \end{pmatrix} - \begin{pmatrix} \tilde{d}_L^\dagger & \tilde{d}_R^\dagger \end{pmatrix} M_{\tilde{d}LR}^2 \begin{pmatrix} \tilde{d}_L \\ \tilde{d}_R \end{pmatrix} , \quad (2.48)$$

where the up-type squark mass matrix is given by

$$M_{\tilde{u}LR}^2 = \begin{pmatrix} M_{\tilde{Q}}^2 + y_u^2 v_2^2 + \frac{1}{4}(g^2 - Y_q g'^2)(v_1^2 - v_2^2) & y_u v_2 (A_u^\dagger - \mu \cot \beta) \\ y_u v_2 (A_u - \mu^\dagger \cot \beta) & M_{\tilde{u}}^2 + y_u^2 v_2^2 + \frac{1}{4}g'^2 Y_u (v_2^2 - v_1^2) \end{pmatrix} , \quad (2.49)$$

with  $y_u v_2 = m_u$  from previous definitions in Eq. (2.23) and Eq. (2.40). The parameter  $\mu$  is taken to be real in the rMSSM. A similar mass matrix can be set up for the down-type squarks from the previously described parts of the Lagrangian. Using further the definitions of Eq. (2.10) and of the hypercharges below Eq. (2.41), the up-type squark mass matrix can be written as

$$M_{\tilde{u}LR}^2 = \begin{pmatrix} M_{\tilde{Q}}^2 + m_u^2 + m_Z^2 \cos 2\beta (I_u^3 - Q_u \sin^2 \theta_W) & m_u X_{\tilde{u}} \\ m_u X_{\tilde{u}} & M_{\tilde{u}}^2 + m_u^2 + m_Z^2 \cos 2\beta Q_u \sin^2 \theta_W \end{pmatrix} , \quad (2.50)$$

with  $X_{\bar{u}} = A_u - \mu \cot \beta$  and where  $Q_u$  denotes their charge and  $I_u^3$  the third component of the isospin of the up-type squark, respectively. For completeness, the down-type squark mass matrix is also given,

$$M_{\bar{d}LR}^2 = \begin{pmatrix} M_{\bar{Q}}^2 + m_d^2 + m_Z^2 \cos 2\beta (I_d^3 - Q_d \sin^2 \theta_W) & m_d X_{\bar{d}} \\ m_d X_{\bar{d}} & M_{\bar{d}}^2 + m_d^2 + m_Z^2 \cos 2\beta Q_d \sin^2 \theta_W \end{pmatrix}, \quad (2.51)$$

with  $X_{\bar{d}} = A_d - \mu \tan \beta$ . The squark mass matrices can be rotated into the physical basis

$$\mathcal{L}_{\tilde{q},\text{mass}} = - \begin{pmatrix} \tilde{q}_1^\dagger & \tilde{q}_2^\dagger \end{pmatrix} M_{\tilde{q}12}^2 \begin{pmatrix} \tilde{q}_1 \\ \tilde{q}_2 \end{pmatrix}, \quad (2.52)$$

with the physical squark mass eigenstates  $m_{\tilde{q}_1}^2$  and  $m_{\tilde{q}_2}^2$ . The new mass eigenstates are related to the unphysical masses via an orthogonal transformation

$$M_{\tilde{q}LR}^2 = U_{\tilde{q}}^T M_{\tilde{q}12}^2 U_{\tilde{q}} \quad (2.53a)$$

$$= \begin{pmatrix} \cos^2 \theta_{\tilde{q}} m_{\tilde{q}_1}^2 + \sin^2 \theta_{\tilde{q}} m_{\tilde{q}_2}^2 & \sin \theta_{\tilde{q}} \cos \theta_{\tilde{q}} (m_{\tilde{q}_1}^2 - m_{\tilde{q}_2}^2) \\ \sin \theta_{\tilde{q}} \cos \theta_{\tilde{q}} (m_{\tilde{q}_1}^2 - m_{\tilde{q}_2}^2) & \sin^2 \theta_{\tilde{q}} m_{\tilde{q}_1}^2 + \cos^2 \theta_{\tilde{q}} m_{\tilde{q}_2}^2 \end{pmatrix}, \quad (2.53b)$$

where the unitarity matrix

$$U_{\tilde{q}} = \begin{pmatrix} \cos \theta_{\tilde{q}} & \sin \theta_{\tilde{q}} \\ -\sin \theta_{\tilde{q}} & \cos \theta_{\tilde{q}} \end{pmatrix} \quad (2.54)$$

is parametrized by the mixing angle  $\theta_{\tilde{q}}$ .

Matching the two mass matrices in Eq. (2.50) and Eq. (2.53b), an expression for the parameter  $X_{\tilde{q}}$  can be formulated as follows

$$X_{\tilde{q}} = \frac{\sin \theta_{\tilde{q}} \cos \theta_{\tilde{q}} (m_{\tilde{q}_1}^2 - m_{\tilde{q}_2}^2)}{m_q}. \quad (2.55)$$

## 2.3 Higher-order Higgs-boson mass corrections within the real MSSM

With the light neutral  $\mathcal{CP}$ -even Higgs-boson tree-level mass  $m_{h^0}$  being limited to  $m_Z$  at most, compare Eq. (2.26), the MSSM could already have been excluded at LEP due to the lack of its observation. Yet, higher-order self-energy corrections shifted the upper bound on the light Higgs-boson mass considerably. There are mainly three different methods to approach higher-order mass corrections. They can be combined as well. An exact calculation, invariant under different gauge-fixing terms, is achieved using the Feynman-diagrammatic (FD) approach, where the self-energy diagrams are evaluated explicitly. The second method uses an effective potential approximation further developed for higher loop calculations, compare Ref. [92]. In this approach, the scalar



Higgs-boson fields are expanded around their vacuum expectation values. This allows for the computation of the higher-loop effective potential, involving vacuum diagrams of the given loop order. The results are compact, but also of limited accuracy. As this approach expands around a constant value of the fields, the momentum dependence of the two-loop self-energies cannot be taken into account. A third approach uses effective Lagrangians capturing the dynamics and symmetries of a system in generic terms, while the phenomenology is contained in their coefficients. Effective Lagrangians are often used in model-independent analyses.

In the calculation presented in Chap. 8 of this thesis, the Feynman-diagrammatic approach is adopted. In this approach, higher order mass corrections are computed by allowing for perturbations to the propagators of the fields  $\phi_a^0$ ,  $\chi_a^0$ ,  $\phi_a^\pm$  which result from the solutions to the equations of motion. For completeness

$$\partial_\mu \left( \frac{\partial \mathcal{L}}{\partial(\partial_\mu x_a)} \right) - \frac{\partial \mathcal{L}}{\partial x_a} = 0, \quad (2.56)$$

where  $x = \phi^0$ ,  $\chi^0$ ,  $\phi^\pm$  and where  $a = 1, 2$ . Firstly, the equations of motion require that the terms of the MSSM potential part of the Lagrangian linear in the  $\mathcal{CP}$ -even Higgs-boson fields  $\phi_a^0$ , see Eq. (2.16), must vanish. For this condition to be met, all higher-order corrections up to  $l^{\text{th}}$  order need to be seen as canceling. At tree level, the terms linear in the fields are tadpole coefficients. Higher orders include additional propagators to tadpole lines in terms of loops, where the coefficients are termed  $T_a^{(l)}$ . In conclusion, the statement reads

$$\sum_{a=1}^2 (T_a + T_a^{(1)} + T_a^{(2)} + \dots) = 0. \quad (2.57)$$

Secondly, the bilinear free field and potential parts of the Lagrangian, Eq. (2.7) and Eqs. (2.8)-(2.11), lead to the following contributions to the equations of motion

$$(\partial_\mu \partial^\mu + M_{x_a x_a}^2) x_a + \varepsilon_{ab} M_{x_a x_b}^2 x_b = 0 \quad \text{with } a, b = 1, 2; \quad a \neq b. \quad (2.58)$$

Hence, those terms bilinear in the same field get solutions to the equations of motion in terms of causal Green functions including a momentum and a massive part, while the solutions to terms bilinear in two different fields contain only a massive part. Computing higher orders in perturbation theory corresponds to adding one-particle irreducible terms  $\Sigma(p^2)$  to the propagators [93]

$$\frac{i}{p^2 - M_{x_a x_a}^2} \quad (2.59)$$

$$= \frac{i}{p^2 - M_{x_a x_a}^2} + \frac{i}{p^2 - M_{x_a x_a}^2} (-i\Sigma_{x_a x_a}(p^2)) \frac{i}{p^2 - M_{x_a x_a}^2} + \frac{i}{p^2 - M_{x_a x_a}^2} (-i\Sigma_{x_a x_a}(p^2)) \frac{i}{p^2 - M_{x_a x_a}^2} (-i\Sigma_{x_a x_a}(p^2)) \frac{i}{p^2 - M_{x_a x_a}^2} + \dots \quad (2.60)$$

$$= \frac{i}{p^2 - M_{x_a x_a}^2 - \Sigma_{x_a x_a}(p^2)}, \quad (2.61)$$

where the bold-faced propagator is the one corrected to all orders in perturbation theory and where each one-particle irreducible term can be split into its different orders,

$$\Sigma_{x_a x_b} = \Sigma_{x_a x_b}^{(1)} + \Sigma_{x_a x_b}^{(2)} + \dots \quad (2.62)$$

A geometric series relation is used in the last step from Eq. (2.60) to Eq. (2.61). The cases where different fields enter the time ordered two-point correlation functions can be treated similarly. Assuming that the self-energy corrections in Eq. (2.62) can be renormalized, the renormalized self-energies  $\hat{\Sigma}_{x_a x_b}(p^2)$  enter as corrections to the inverse propagator matrix of the field  $x$ ,

$$(\Delta_x)^{-1} = -i \begin{pmatrix} p^2 - m_{x_1}^2 + \hat{\Sigma}_{x_1 x_1}(p^2) & -m_{x_1 x_2}^2 + \hat{\Sigma}_{x_1 x_2}(p^2) \\ -m_{x_1 x_2}^2 + \hat{\Sigma}_{x_1 x_2}(p^2) & p^2 - m_{x_2}^2 + \hat{\Sigma}_{x_2 x_2}(p^2) \end{pmatrix}. \quad (2.63)$$

The loop-corrected masses  $M_{x_1}$  and  $M_{x_2}$  are determined by the real parts of the propagator matrix of the field  $x$ . This is equivalent to solving the equation

$$\left[ p^2 - m_{x_1}^2 + \hat{\Sigma}_{x_1 x_1}(p^2) \right] \left[ p^2 - m_{x_2}^2 + \hat{\Sigma}_{x_2 x_2}(p^2) \right] - \left[ -m_{x_1 x_2}^2 + \hat{\Sigma}_{x_1 x_2}(p^2) \right]^2 = 0. \quad (2.64)$$

The status of the available self-energy corrections to the real MSSM can be summarized as follows.

At the one-loop level, the full corrections to the MSSM Higgs-boson masses are known, including gauge bosons contributions and momentum dependence, see Refs. [94–101].

At two loops, a full result using an effective potential approach is known [102,103]. Preceding works used a two-loop renormalization group equation (RGE) improved one-loop effective potential approach [104–108], or a two-loop effective potential approach [109–116]. Furthermore, explicit computations have been performed in the Feynman-diagrammatic approach, neglecting gauge contributions and assuming vanishing external momentum [117–120]. The latter cover the dominant corrections of the order  $\mathcal{O}(\alpha_s \alpha_t)$  and  $\mathcal{O}(\alpha_t^2)$  and the sub-dominant two-loop contributions of the order  $\mathcal{O}(\alpha_s \alpha_b)$ ,  $\mathcal{O}(\alpha_t \alpha_b)$  and  $\mathcal{O}(\alpha_b^2)$ . The orders are given in terms of the coupling factors entering the vertices of the loop diagrams. These are the strong coupling constant  $\alpha_s = \frac{g_s^2}{4\pi}$  and the Yukawa couplings  $\alpha_t = \frac{y_t^2}{4\pi}$  and  $\alpha_b = \frac{y_b^2}{4\pi}$  of the top and the bottom quark, respectively. The relative size of a correction can be estimated a priori by assessing the relative size of its couplings. Due to supersymmetry, the Yukawa couplings for the quarks and squarks are equivalent  $\alpha_{\tilde{t},\tilde{b}} = \alpha_{t,b}$ . The soft supersymmetry **breaking** terms contributing in the coupling of the Higgs-bosons to the squarks are proportional to the Standard Model Yukawa couplings as well, compare Eq. (2.43). Therefore, no distinction between  $\alpha_{\tilde{q}}$  and  $\alpha_q$  is needed.

Complementary to the Feynman-diagrammatic approach, higher-order corrections to the Higgs-boson masses have been found using the effective Lagrangian approach [121–126]. Other studies aim towards a combination of the existing two-loop results obtained in different approaches, see Refs. [110–112, 127, 128].

Regarding the third order, the dominant corrections of the order  $\mathcal{O}(\alpha_s^2 \alpha_t)$  are available [129–131], where gauge contributions and a non-vanishing external momentum still

need to be incorporated in future calculations. Also, third and higher order resummation effects have recently been taken into account [132, 133].

Remarkably, all these higher-order corrections lead to an approximate upper bound of  $m_{h,0} \lesssim 135$  GeV, where the maximal value for the light Higgs-boson mass depends sensitively on the precise value of the top-quark mass, compare Refs. [119, 128].

While the one-loop corrections relocate the upper bound towards higher masses, the two-loop corrections enter with competing signs and the three-loop corrections further stabilize the mass, entering with both signs. The overall dominant corrections come from those self-energies involving the top quark and the scalar top (stop) quarks.

The remaining contributions of higher orders can be estimated based on the already available results. To reach a theoretical precision matching or even surpassing the experimental one, corrections beyond the above mentioned ones must be taken into account. At two loops, the remaining uncertainties originate from neglecting gauge contributions and momentum dependence [134]. Therefore, the calculation of the momentum dependent two-loop corrections to the MSSM Higgs-boson self-energies is of interest. The momentum dependence at the one-loop level is known to generally amount to less than 2 GeV, compare Ref. [135]. The dominant corrections at the two-loop level have been calculated adopting a full  $\overline{DR}$  renormalization scheme, see Refs. [136–138]. Higher-order corrections to the tree-level MSSM Higgs-boson masses can only be applied consistently if they are computed within the same renormalization scheme. It is therefore interesting to analyze the momentum-dependent contribution again, but using an on-shell renormalization for all masses entering the calculation. Although the calculation becomes more involved with this renormalization scheme choice, the benefit of being able to incorporate those corrections into the public program FEYNHIGGS [139–142] and thereby making the corrections readily available, is outweighing.



# 3 | Multi-scale integrals beyond one loop

This chapter explores diverse techniques regarding the computation of multi-scale integrals beyond one loop. In particular, a focus is laid on two-loop calculations, where fully differential phenomenological predictions start to emerge for a variety of processes. The chapter culminates in a motivation for the usage of Feynman parameterization in a tool to compute multi-loop multi-scale integrals in an automated way.

## 3.1 The two loop frontier

Due to the high energies at present hadron colliders, processes at very small distances can be resolved. At the Tevatron and the LHC, these dominantly involve quarks and gluons (partons). While the Tevatron is a proton-antiproton collider, the dominant production channel has  $q\bar{q}$  pairs in the initial state, at the LHC the  $gg$  channel is the dominant initial state. Compared to  $e^+e^-$  annihilation processes at past colliders this is one additional external leg when higher orders are computed. This greatly increases the complexity of such a computation.

At next-to-leading order <sup>1</sup> in perturbative QCD, the frontier is looking at final states with many particles and matching them with a parton shower. The motivation to go to NNLO accuracy is at least twofold. First, the dependence on the renormalization scale is expected to be reduced. Second, a process has more partons in the final state. This initiates the reconstruction of the parton shower, thus approaching an experimental jet reconstruction.

The forefront at NNLO is the computation of four-point processes, where various complications can arise, one being a complicated singularity structure of individual diagrams, and the other the involvement of internal and external masses leading to multi-scale problems. This can render the evaluation of sometimes just single diagrams a highly non-trivial task. While multiple legs and scales can already be very complicated at NLO, at NNLO completely new challenges arise in addition when generalizing the techniques employed at NLO to NNLO and diverse conceptual differences must be acknowledged.

---

<sup>1</sup>It should be noted that the leading order usually encompasses tree-level diagrams, but there are LO processes (e.g. Higgs production in gluon fusion) which start with loop diagrams.

Beyond NLO, the renormalization procedure for the cancellation of ultraviolet (UV) singularities involves not only counter-terms of the loop order to be considered but also counter-terms of lower loop order with insertions. Finding the full but minimal set of diagrams is non trivial but was solved and further developed by Bogoliubov, Parasiuk, Hepp and Zimmermann, summarized in the (BPHZ) theorem, see Refs. [143–145].

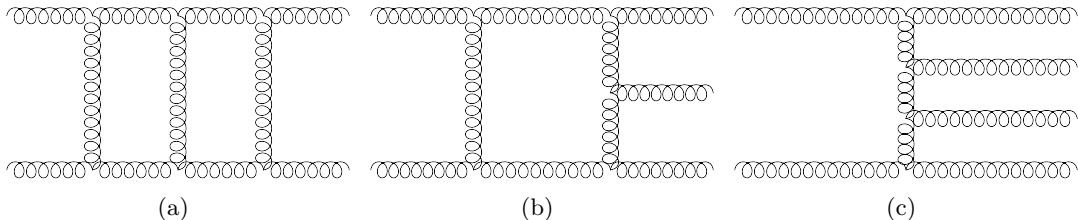


Figure 3.1: Example diagrams for double virtual (a), real virtual (b) and double real radiation (c) contributions entering an NNLO calculation are shown.

Furthermore, a mixture of real radiation and virtual corrections enter a cross section at NNLO, in addition to double real and double virtual contributions. The typical ingredients of an NNLO calculation are depicted in Fig. 3.1. Given the fact that now three pieces enter the calculation which are all part of different phase space dimensions, the need for more discriminating and refined subtraction schemes emerges.

At NLO, subtraction schemes are already well established, see Refs. [146–148]. At NNLO there are various subtraction schemes available, all with different aims and capabilities. After the introduction of  $q_T$  subtraction by Catani and Grazzini [149, 150], the idea of using the sector decomposition algorithm [151, 152] for a complete NNLO calculation was originally proposed by Heinrich [153]. It was taken up and further developed into a full subtraction scheme in Refs. [154–156], and first applied to a full process in Ref. [157]. The idea proposed by Czakon to combine sector decomposition applied to real emission integrals with phase-space partitioning from FKS subtractions, lead to the sector improved residue subtraction [158], successfully applied, e.g., in Refs. [65, 159]. Further, the antenna factorization introduced in Refs. [160–162] was explicitly worked out and applied to full NNLO processes [163–166]. Lastly, a direct generalization of dipole subtraction to NNLO processes was presented by Somogyi, Trocsanyi et al. [167, 168].

While for the real radiation the computation of more and more legs is of interest, for the virtual contributions higher-order loop integrals need to be solved. In light of the fact that the number of diagrams contributing to higher-order processes increases tremendously from one order to the next, and the diagrams themselves become more and more complicated, it is desirable to find highly automatable procedures to tackle these. At NLO, tools towards this aim are already highly developed and sophisticated. The procedure of generating the real radiation and loop amplitudes contributing to a full process is automated to a large extent by programs like AMC@NLO [169], BLACKHAT [170], FEYNARTS, FORMCALC & LOOPTOOLS [171], GoSAM [172], HELAC-

NLO [173], HERWIG++ [174], MATCHBOX [175], MCFM [176], NJET [177] OPEN LOOPS [178], POWHEG [179], RECOLA [180], SHERPA [181], VBFNLO [182]. There are diverse tools allowing for an automated generation of the pure Feynman amplitudes. The programs with loop capabilities are FEYNARTS [183,184] or QGRAF [185].

The full basis of irreducible master integrals is known at one-loop order. It comprises scalar pentagon, box, triangle, bubble and tadpole diagrams which are known analytically or can be computed numerically [186–189]. Beyond one loop, the set of irreducible integrals, so called master integrals, is not known which makes the decomposition more difficult. Master integrals beyond one loop can have irreducible numerators which need to be evaluated in addition. In the reduction of multi-loop amplitudes to a set of resulting master integrals, integration by parts relations [190–192] and identities resulting from Lorentz invariance [193] are indispensable. The former are based on the fact that the integral over the total derivative with respect to any loop momentum  $k_l$  vanishes in dimensional regularization

$$0 = \int d^D k_l \frac{\partial}{\partial k_l^\mu} f(k_l, \dots), \quad (3.1)$$

where the integrand  $f$  may contain any combination of propagators, scalar products and loop momentum vectors. Together with the exploitation of Lorentz invariance by

$$\left( p_1^\nu \frac{\partial}{\partial p_{1\mu}} - p_1^\mu \frac{\partial}{\partial p_{1\nu}} + \dots + p_n^\nu \frac{\partial}{\partial p_{1\mu}} - p_n^\mu \frac{\partial}{\partial p_{1\nu}} \right) G(\{p\}, \{m\}) = 0, \quad (3.2)$$

where  $n$  is the number of external momenta  $p_i$  and  $m$  the internal masses, the reduction to master integrals can be achieved. The full reduction into less complicated integrals can be done if the number of constraints matches or exceeds the number of unknown integrals.

In the following, the general structure of the resulting master integrals is shown and different methods to solve them are described.

## 3.2 Two and more loop integrals with multiple scales

The difficulty of such multi-loop integrals has led to their extensive study and the development of various specialized integration techniques. In the following, a general multi-loop integral is introduced before presenting a variety of techniques to tackle these.

A general Feynman loop integral  $G$  at  $L$  loops with  $N$  propagators, where the propagators  $P_j$  can have in principle arbitrary powers  $\nu_j$  and mass  $m_j$ , has the following representation in momentum space

$$G_{l_1 \dots l_R}^{\mu_1 \dots \mu_R}(\{p\}, \{m\}) = \prod_{l=1}^L \int d^D \kappa_l \frac{k_{l_1}^{\mu_1} \dots k_{l_R}^{\mu_R}}{\prod_{j=1}^N P_j^{\nu_j}(\{k\}, \{p\}, m_j^2)} \quad (3.3)$$

$$d^D \kappa_l = \frac{\mu_r^{4-D}}{i\pi^{\frac{D}{2}}} d^D k_l, \quad P_j(\{k\}, \{p\}, m_j^2) = q_j^2 - m_j^2 + i\delta, \quad (3.4)$$

where the  $q_j$  are linear combinations of external momenta  $p_i$  and loop momenta  $k_l$ . While the rank  $R$  of the integral is indicated by the number of loop momenta appearing in the numerator, the indices  $l_i$  denote which of the  $L$  loop momenta belongs to which Lorentz index  $\mu_i$ . The factor of  $i\pi^{\frac{D}{2}}$  in  $\kappa$  is chosen by convention to remove any dependence on  $\pi$  after the integration over the loop momenta within Feynman parameterization. The renormalization scale is denoted by  $\mu_r$ . The  $+i\delta$  in Eq. (3.4) results from the solutions of the field equations in terms of causal Green functions.

The integral is regulated dimensionally meaning that the integer dimension number  $d$  is shifted by an infinitesimal quantity  $\varepsilon$  to the new dimension variable  $D = d - 2\varepsilon$ . Infrared or ultraviolet poles then appear as poles in the regulator  $\varepsilon$ . Careful distinction has to be made between ultraviolet ( $\varepsilon > 0$ ) and infrared regulators ( $\varepsilon < 0$ ). Formally, the theory is first renormalized dimensionally by going a little below the integer number  $d$  of space-time dimensions and afterwards analytically continued to a little value above  $d$  to regulate the mass singularities, see Ref. [194] for a comprehensive discussion. A modified version of the dimensional regularization is the dimensional reduction (DR). It is of particular interest in SUSY calculations, since it preserves global gauge invariance and supersymmetry, also at the two loop level [195]. Adopting this regularization scheme first introduced and applied in Refs. [196, 197], all external particles and all gamma matrices  $\{\gamma^\mu, \gamma^5\}$  appearing in the couplings are treated as quasi four-dimensional, while the loop integrals are computed in  $D = 4 - 2\varepsilon$  dimensions. For comparison, the introduction of a cutoff  $\Lambda$  to the propagators to regulate UV divergences corresponds to the Pauli-Villars regularization.

The complexity of the evaluation of loop integrals generally increases with the number of loops and the number of legs. Massive internal lines further increase the level of complexity by raising the number of involved scales. All masses and invariants formed from external momenta are summarized in the term “kinematic invariants”. The sum of independent kinematic variables corresponds to the number of scales involved in a diagram. Already at one-loop many-scale integrals are hard to compute. Multi-loop integrals involving multiple scales are particularly demanding. Further complexity arises with the non-planarity of graphs. Such diagrams only appear beyond one loop. These additional complications make the evaluation of multi-loop integrals an extremely non-trivial task and shrewd and refined techniques need to be employed to tackle these. Analytical techniques are very advanced, but when it comes to automation they very often still reach their limit. Numerical methods are in general easier to automate but issues here are the speed and the accuracy.

In the following, the main technical approaches towards the evaluation of multi-loop and multi-scale integrals are reviewed. The main recent developments are sketched before concluding with a motivation for the method chosen to be investigated in this thesis.



### 3.3 Introduction of Feynman parametrization

A first method to deal with Feynman loop integrals is to introduce Feynman parameters to every propagator. To prove that this technique indeed works, it is descriptive to have a look at a two-propagator example [93]

$$\frac{1}{AB} = \int_0^\infty dx_1 dx_2 \delta(1 - x_1 - x_2) \frac{1}{(x_1 A + x_2 B)^2}, \quad (3.5)$$

with the propagators  $A$  and  $B$  and the Feynman parameters  $x$  and  $y$ . Generalizing this idea to multiple propagators is straightforward [152]

$$\frac{1}{\prod_{j=1}^N P_j^{\nu_j}} = \frac{\Gamma(N_\nu)}{\prod_{j=1}^N \Gamma(\nu_j)} \prod_{j=1}^N \int_0^\infty dx_j x_j^{\nu_j-1} \delta\left(1 - \sum_{i=1}^N x_i\right) \left[ \sum_{j=1}^N x_j P_j \right]^{-N_\nu}, \quad (3.6)$$

where  $N_\nu = \sum_{j=1}^N \nu_j$ . An equivalent representation was derived by Schwinger. Parameters are usually referred to as Schwinger variables when they are assumed to have values between zero and infinity, while values between zero and one are associated with Feynman parameterization. The general form of a multi-loop integral reads

$$G_{l_1 \dots l_R}^{\mu_1 \dots \mu_R} = \frac{\Gamma(N_\nu)}{\prod_{j=1}^N \Gamma(\nu_j)} \int_0^\infty \prod_{j=1}^N dx_j x_j^{\nu_j-1} \delta\left(1 - \sum_{i=1}^N x_i\right) \int d^D \kappa_1 \dots d^D \kappa_L \\ \times k_{l_1}^{\mu_1} \dots k_{l_R}^{\mu_R} \left[ \sum_{i,j=1}^L k_i^T M_{ij} k_j - 2 \sum_{j=1}^L k_j^T \cdot Q_j + J + i \delta \right]^{-N_\nu}, \quad (3.7)$$

where the propagators are written in terms bilinear in the loop momenta with coefficients contained in the matrix  $M$ , terms linear in the loop momenta with coefficients  $Q_j$  and remaining terms included in  $J$  depending on the masses, external momenta and the Feynman parameters only. To be able to integrate out the loop momenta, the terms bilinear and linear in the loop momenta need to be brought into a quadratic form by a shift

$$k_l = \tilde{k}_l + v_l, \quad v_l = \sum_{i=1}^L M_{li}^{-1} Q_i. \quad (3.8)$$

The integration of the quadratic form is then straightforward. After also integrating out the radial coordinates the general loop integral reads

$$G_{l_1 \dots l_R}^{\mu_1 \dots \mu_R} = \frac{(-1)^{N_\nu}}{\prod_{j=1}^N \Gamma(\nu_j)} \prod_{j=1}^N \int_0^\infty dx_j x_j^{\nu_j-1} \delta\left(1 - \sum_{l=1}^N x_l\right) \\ \times \sum_{m=0}^{\lfloor R/2 \rfloor} \left(-\frac{1}{2}\right)^m \Gamma(N_\nu - m - LD/2) \left[ (\tilde{M}^{-1} \otimes g)^{(m)} \tilde{l}^{(R-2m)} \right]^{\Gamma_1, \dots, \Gamma_R} \\ \times \frac{\mathcal{U}^{N_\nu - (L+1)D/2 - R}}{\mathcal{F}^{N_\nu - LD/2 - m}}, \quad (3.9)$$

where

$$\mathcal{F}(\vec{x}) = \det(M) \left[ \sum_{j,l=1}^L Q_j M_{jl}^{-1} Q_l - J - i\delta \right] \quad (3.10)$$

$$\mathcal{U}(\vec{x}) = \det(M), \quad \tilde{M}^{-1} = \mathcal{U} M^{-1}, \quad \tilde{l} = \mathcal{U} v. \quad (3.11)$$

Note the sign of the infinitesimal imaginary part in Eq. (3.10). It results from factoring an overall minus sign into the prefactor during Wick rotation. Each loop momentum  $k_{l_i}$  in the numerator is associated with a fixed Lorentz index  $\mu_i$ . The  $\Gamma_i$  refer to the combination of both indices  $\Gamma_i = (l_i, \mu_i)$ . For rank  $R = 0$ , the second line of Eq. (3.9) reduces to the factor  $\Gamma(N_\nu - LD/2)$ , containing overall UV divergences if present. In the case of  $R = 1$ , the product  $(\tilde{M}^{-1} \otimes g)^{(0)}$  does not contribute and  $\tilde{l}^{(1)} = \tilde{l}_{l_1}^{\mu_1}$ . For loop integrals of higher rank  $R > 1$ , products of the matrix element  $\tilde{M}_{ij}^{-1}$  with the metric tensor  $g^{\mu\nu}$  contribute as a sum of all possible combinations with the vectors  $\tilde{l}$  in the double indices  $\Gamma_i$ . As an example of how to read the notation involving the metric tensors, for rank  $R = 2$  and correspondingly  $m = 1$  it is

$$(\tilde{M}^{-1} \otimes g)^{(1)} = (\tilde{M}^{-1} \otimes g)_{l_1 l_2}^{\mu_1 \mu_2} = \tilde{M}_{l_1 l_2}^{-1} g^{\mu_1 \mu_2}, \quad l_1, l_2 \in \{1, 2\}. \quad (3.12)$$

The functions  $\mathcal{U}$  and  $\mathcal{F}$  in Eq. (3.9) are the first and second Symanzik polynomial, respectively, and are homogeneous (in the Feynman parameters).  $\mathcal{U}$  is positive semi-definite and  $\mathcal{F}$  is negative semi-definite when all propagators are massless. The two

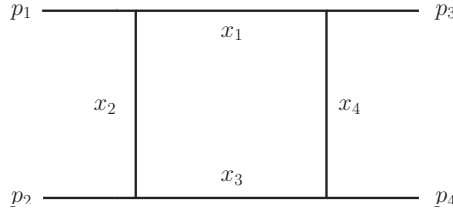
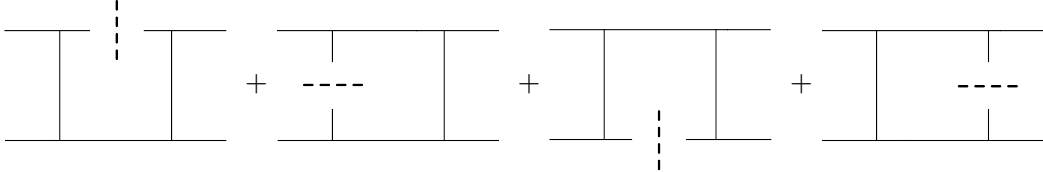


Figure 3.2: The one-loop box diagram with massless propagators.

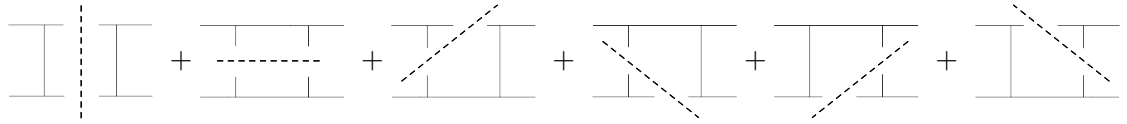
functions can also be obtained using a graph-theoretical method, where the polynomials are constructed from topological cuts of the corresponding Feynman graph. For the construction of the function  $\mathcal{U}$ ,  $L$  lines of the graph are cut, whereas  $L+1$  lines are cut to arrive at the function  $\mathcal{F}$ , see Refs. [152, 198, 199]. To illustrate this for a simple example,

assume a massless one-loop box with all external legs being light-like, compare Fig. 3.2. Then, the first Symanzik polynomial  $\mathcal{U}$  is constructed from adding up all possible  $L$  line cuts of propagators which lead to a tree-level diagram. Each cut propagator contributes with its Feynman parameter, if more than one propagator needs to be cut (which happens for  $L > 1$ ), products of Feynman parameters, all of the same degree, enter the function  $\mathcal{U}$ . In the case of the one-loop box with massless propagators, this reads



$$\mathcal{U} = x_1 + x_2 + x_3 + x_4$$

The second Symanzik polynomial  $\mathcal{F}$  is constructed from adding up all possible  $L + 1$  line cuts of propagators. All  $L + 1$  cut propagators contribute with their Feynman parameter and the squared momentum flowing into the resulting tree. In the case of the one-loop box with massless propagators, the function  $\mathcal{F}$  then reads



$$\mathcal{F} = -s_{12} x_1 x_3 - s_{23} x_2 x_4 - p_1^2 x_1 x_2 - p_2^2 x_2 x_3 - p_3^2 x_3 x_4 - p_4^2 x_4 x_1 .$$

While the prefactor  $\Gamma(N_\nu - m - LD/2)$  in Eq. (3.9) contains overall ultraviolet divergences if present, the vanishing of the function  $\mathcal{U}$  is related to ultraviolet sub-divergences of the graph. The second Symanzik polynomial contains the occurring infrared singularities. The occurrence of these depends not only on the topology as in the UV case, but on the kinematics as well. If some of the kinematic invariants are zero, e.g. when some external momenta are light-like, the vanishing of  $\mathcal{F}$  may induce an infrared (IR) divergence. Therefore general theorems about the IR singularity structure of multi-loop integrals are sparse. For practical purposes sector decomposition can provide information about the singularity structure and numerical results, because it offers a constructive algorithm to extract the poles in  $1/\varepsilon$ . When generalizing the kinematic invariants to physical space, the second Symanzik polynomial can also vanish when linear combinations of Feynman parameters and kinematic invariants vanish. A clever deformation of the integration contour to the complex plane helps dealing with these physical poles and the integration over thresholds.

For a diagram with only massless propagators, the function  $\mathcal{F}$  does not contain any squares in the Feynman parameters. If massive internal lines are present, terms of the

type

$$\mathcal{F}(\vec{x}) \propto \mathcal{U}(\vec{x}) \sum_{j=1}^N x_j m_j^2 \quad (3.13)$$

appear. These are the source of complexity when it comes to the analytical evaluation of multi-scale integrals, as many methods used for the simplification of an integrand can no longer be applied.

This opens the field for a numerical treatment of multi-scale integrals, where squared Feynman parameters are not a bottleneck to the calculation. Additionally, the introduction of Feynman parameters is highly automatable paving the way towards a very general solution to a large class of multi-scale integrals with arbitrary kinematics.

The problems occurring with this method and their solution will be explained in the next two chapters. Beforehand, several other approaches towards solving multi-loop integrals will be reviewed.

### 3.4 The virtues of a Mellin-Barnes representation

In analogy to Eq. (3.5), the main transformation to arrive at a Mellin-Barnes representation can be summarized in one line

$$\frac{1}{(A+B)^\lambda} = \frac{1}{\Gamma(\lambda)} \frac{1}{2\pi i} \int_{-i\infty}^{+i\infty} dz \Gamma(\lambda+z) \Gamma(-z) \frac{B^z}{A^{\lambda+z}}, \quad (3.14)$$

with the difference, that now a sum in the denominator is transformed into a product. The sum on the left-hand side can either be a massive propagator or a sum of two propagators after Feynman parametrization. In the first case, massive propagators are expressible as a continuous superposition of massless propagators. Considering that the massive propagators introduce squares in the Feynman parameters, see Sec. 3.3, this transformation can be very beneficial.

In general, a factorization of the type Eq. (3.14) can be used to achieve a representation of loop integrals in terms of gamma functions, which are in general easier to evaluate. This benefit comes at the cost of extra Mellin integrations. Within their integration domain, poles in the variable  $z$  can occur. Taking these into account, the integration contour must always be chosen such that the poles with a  $\Gamma(\dots + z)$  dependence are placed left of the contour and the poles with a  $\Gamma(\dots - z)$  dependence are situated on the right-hand side with respect to the contour. Closing the contour to the right and taking a series of residues, the integral can be evaluated. Yet, finding the appropriate contour is non-trivial.

With the computation of the planar [200] and non-planar [201] massless two-loop four-point diagram, Smirnov and Tausk pioneered the utilization of a Mellin-Barnes representation finding an appropriate choice of contours for physical kinematics including thresholds. Several software packages became available automating the analytical procedure where possible, see Refs. [202–204]. The more scales are involved, the less

easy it is to arrive at a fully analytical result. Numerical approaches have also been considered [205–207], putting much effort in the automation of a proper analytical continuation of the integrand. Very recently an idea by Pilipp [208] was implemented with in combination with Feynman parametrization to treat such contours in an automated way, see Ref. [207]. It works as follows: The second Symanzik polynomial  $\mathcal{F}$  is decomposed as

$$\mathcal{F}(x_1, \dots, x_n) = \rho F_1(x_i) + F_2(x_i) , \quad (3.15)$$

where a small coefficient to terms in  $\mathcal{F}$  is extracted into the parameter  $\rho$  and where all terms contained in  $F_1$  and  $F_2$  are sufficiently large as not to contribute to a singularity. The Mellin-Barnes representation is then introduced for the product

$$\frac{\Gamma(N_\nu - LD/2)}{(\rho F_1 + F_2)^{N_\nu - LD/2}} = \frac{1}{2\pi i} \int_{-i\infty}^{i\infty} dz \rho^z \frac{\Gamma(N_\nu - LD/2 + z)\Gamma(-z)}{F_1^{-z} F_2^{N_\nu - LD/2 + z}} , \quad (3.16)$$

After the application of sector decomposition which will be described in detail in Chap. 4, the functions  $F_i$  and  $\mathcal{U}$  are constant in the Feynman parameters  $x_i$ , so that the singularity structure is revealed in the exponents of the factorized  $x_i$

$$x_i^{n_i - 1 + b_i \varepsilon + c_i z} , \quad (3.17)$$

where the  $-1$  enters with the Feynman parametrization, and where  $n_i$ ,  $b_i$  and  $c_i$  are some coefficients resulting from the division into sectors. Allowing only those integrals where  $c_i < 0$ , the integration contour of the integral over the variable  $z$  can be closed to the right, allowing for the application of Cauchy's integral theorem. The residues arising from terms of the type  $\Gamma(n_i + b_i \varepsilon + c_i z)$  after  $x_i$  integration need to be taken into account. Afterwards, an expansion in the parameter  $\rho$  can be performed.

The usage of a Mellin-Barnes representation can be very beneficial in diverse contexts and can even be applied in an automated way to the physical region with the computation of asymptotic expansions in the Feynman integrals. Yet, a fully automated approach in all regions of phase space is difficult.

### 3.5 The method of differential equations

As it turns out, a representation for the master integrals resulting from the reduction can also be found by setting up differential equations in all kinematic invariants and solving them with the appropriate boundary conditions. The method was first introduced by Kotikov who related massive loop integrals to massless ones, see Ref. [209] and then generalized to differential equations in all kinematic invariants, see Refs. [210, 211].

Taking the derivative of an integral with respect to one of its invariants yields linear combinations of integrals with at most one additional propagator in the denominator and one additional scalar product in the numerator. The derivatives of the invariants  $s_{ij} = (p_i + p_j)^2$  can be expressed in terms of derivatives in the external momenta, e.g.

for box diagrams

$$s_{ij} \frac{\partial}{\partial s_{ij}} = \frac{1}{2} \left( p_i^\mu \frac{\partial}{\partial p_i^\mu} + p_j^\mu \frac{\partial}{\partial p_j^\mu} - p_k^\mu \frac{\partial}{\partial p_k^\mu} \right), \quad i \neq j \neq k, \quad i, j, k = 1, 2, 3. \quad (3.18)$$

This generates similar expressions as those resulting from IBP relations mentioned in Sec. 3.1 and Lorenz invariance identities (LI) introduced by Gehrmann and Remiddi, see Ref. [193]. Using the IBP and LI relations, the integrals which received an additional propagator or scalar product can be reduced again to such an extent as to result in a system of differential equations. In the example of box diagrams, one of the equations reads

$$s_{ij} \frac{\partial}{\partial s_{ij}} I_{t,t,0}(s_{ij}, s_{jk}, s_{ki}, D) = A(s_{ij}, s_{jk}, s_{ki}, D) I_{t,t,0}(s_{ij}, s_{jk}, s_{ki}, D) + F(s_{ij}, s_{jk}, s_{ki}, D, I_{t-1, N_\nu, R}(s_{ij}, s_{jk}, s_{ki}, D)) \quad (3.19)$$

where  $I_{t, N_\nu, R}$  is an integral of a diagram with four external legs of  $t$  different propagators and  $R$  scalar products and where the function  $A$  is rational. The function  $F$  plays the role of an inhomogeneous term and the integral contained in it,  $I_{t-1, N_\nu, R}$ , is one differing propagator short compared to the  $I_{t, N_\nu, R}$  integral. The boundary conditions can be derived from kinematical limits, e.g. a vanishing invariant  $s_{ij}$ ,

$$I_{t,t,0}(0, s_{jk}, s_{ki}, D) = -A(0, s_{jk}, s_{ki}, D)^{-1} \times F(0, s_{jk}, s_{ki}, D, I_{t-1, N_\nu, R}(0, s_{jk}, s_{ki}, D)), \quad (3.20)$$

where  $A(0, s_{jk}, s_{ki}, D) \neq 0$ . Afterwards, the differential equations can be solved by introducing an integrating factor  $M$  of the type

$$M(s_{ij}) = e^{\int ds_{ij} A(s_{ij}, s_{jk}, s_{ki}, D)}, \quad (3.21)$$

yielding solutions to the inhomogeneous equation

$$I_{t,t,0}(s_{ij}, s_{jk}, s_{ki}, D) = \frac{1}{M(s_{ij})} \times \left( \int ds_{ij} F(s_{ij}, s_{jk}, s_{ki}, D, I_{t-1, N_\nu, R}(s_{ij}, s_{jk}, s_{ki}, D)) M(s_{ij}) + C \right), \quad (3.22)$$

where the integral over the function  $F$  and  $M$  is either known or relatively easy to integrate and where the constant  $C$  is chosen such that it matches the boundary conditions. The nice feature of this technique is that it can be applied to arbitrary multi-loop integrals with arbitrary scales. However, the current bottleneck is related to the appearance of elliptic integrals. These already appear in the rather simple but all-massive two-loop bubble with different masses, see Fig. 3.3. After the developments summarized in this thesis, such an integral is easily treated numerically for in principle arbitrary kinematics and in a fully automated way.

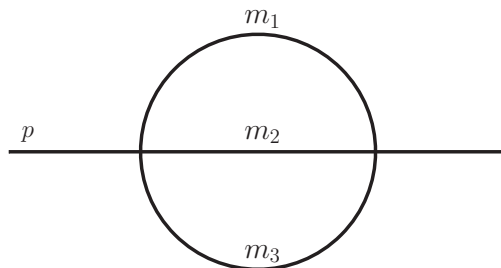


Figure 3.3: Two-loop two-point massive bubble diagram, also termed the "sunrise" topology.

### 3.6 Further analytic developments

Apart from the multi-purpose techniques already mentioned in the previous sections, there are many more specialized tricks to attack a special class of multi-loop integrals on the one hand, and other ideas based on long-known mathematical concepts to simplify the result on the other hand. Furthermore, intensive exploration of diverse mathematical concepts uncovered new criteria and underlying structures to easier access scattering amplitudes.

A presentation of analytic results in terms of generalized hypergeometric functions has been found to yield very compact results. The evaluation of special cases of hypergeometric functions, namely generalized Lauricella functions involving elliptic integrals are not accessible by present analytical techniques. In contrast, for all results expressible in terms of generalized harmonic polylogarithms (GHPLs) a fast, accurate and stable numerical evaluation of the analytical expressions can be found. GHPLs are generalizations of harmonic polylogarithms [212], introduced in Refs. [213, 214] and applied in innumerable phenomenological applications. They are not all independent and relations among them can become very complicated. A systematic approach to govern the complexity of such relations is therefore highly desirable in the study of multi-loop integrals. One such approach is the formulation of results in terms of symbols. The concept, introduced by Zagier and Gonachrov in Refs. [215–217], allows for particularly simple and elegant expressions. After the symbol calculus was applied in the context of  $\mathcal{N} = 4$  supersymmetric Yang-Mills (SYM) theory, see Refs. [218–228], it was found to be also applicable to diverse phenomenological problems, see Refs. [80, 81, 229–236]. The coproduct, as a generalization of the symbol, allowed for the conservation of information on constants with an associated weight, as was pointed out in Refs. [231, 237, 238].

As already mentioned in Sec. 3.1, beyond one-loop the basis of master integrals is not fixed. Finding criteria for an optimal basis was therefore a major breakthrough in the computation of multi-loop amplitudes. These were introduced by Henn, see Ref. [239], and further explored and applied in Refs. [240–245]. They lead to a straightforward iterative solution of the differential equations in the dimensional regulator  $\varepsilon$ .

While the formulation of results in terms of much simpler representations is of vital importance in pushing the frontier towards the computation of higher loop integrals, the introduction of completely different approaches to the computation of the master integrals forms the second pillar in multi-loop computations. Conceptually, every mathematical object constituting a loop integral can be reformulated using a different approach which is more suitable in a specific calculation. Master integrals entering at higher order in perturbation theory can be approached from a graph theoretical point of view, an algebraic or a geometric point of view, to just name a few of the many areas of interplay between physics and mathematics that lead to attractive solutions to yet unsolved integral representations. The liberation from calculations in strictly 4 dimensions, for example, lead to plural ingenious approaches. The old concept of an infinitesimal  $\varepsilon$  shift used in dimensional regularization is predominantly used in the computation of loop integrals. It is also an old concept to shift the dimension by positive or negative integer numbers, see Refs. [198, 246–250], but one may also benefit from an integral representation adopting a negative dimension. The latter was developed in Refs. [251–254] and successfully applied in the computation of a massless two-loop five-propagator diagram, where the expression of a sub-loop is derived using negative dimensions, see Ref. [255]. An abstraction to scalar one-loop vertex functions including internal masses, off-shell legs and arbitrary propagator powers was achieved for general dimensions, see Ref. [256]. Another concept centers around the analysis of discontinuities across the branch cuts of Feynman integrals. In the traditional approach, the integral might be reconstructed directly from one of its discontinuities using a dispersion relation, see Refs. [257–260]. This technique can be generalized to the application of sequential unitarity cuts in different channels, reconstructing one- and multi-loop integrals, see Ref. [235]. Furthermore, the criterion of linear reducibility of a graph has been studied over the past few years and recently used in the computation of diverse examples, compare Refs. [261–268]. The examples, all being linearly reducible in the Feynman parameters, can be integrated sequentially and analytical results can be given in terms of multiple polylogarithms.

### 3.7 Motivation for adopting a numerical approach

One may realize that the quality of an employed technique to tackle multi-leg, -loop and -scale integrals on the one hand lies in its applicability to very generic cases of loop integrals, and on the other hand in the achieved accuracy within a given time span in addition to control over the parametric dependences. A fully automated elegant analytical approach to compute all possibly existing loop integrals would therefore be the perfect solution. Yet, analytical methods are still struggling with the appearance of elliptic integrals, entering already in rather simple two-loop diagrams, while numerical approaches need a better ratio of speed to accuracy to compete with the elegance of analytical results. The two main pillars therefore mutually enrich each other and methods including analytical and numerical approaches push the boundaries of what is computable with present techniques.



While the achievements using analytical methods were analyzed in the previous sections, there are diverse groups who contributed highly non-trivial results to significant phenomenological applications taking up a numerical approach, compare e.g. Refs. [58, 159, 269–278].

In the work summarized in this thesis, a highly automated numerical approach is adopted, filling the gap of the missing automated evaluation of multi-loop multi-scale integrals including thresholds. To this end, a representation of the integrals of interest in terms of plain Feynman parameters is used. Due to its generality, the Feynman parametrization can serve as the most universal approach to a numerical treatment of integrals with arbitrary kinematics. Divergences are regulated dimensionally and are factorized using the method of sector decomposition. The program SECDEC version 1 already implemented the automated formulation of integrals in terms of Feynman parameterization, integration of loop momenta and a series expansion in the dimensional regulator  $\varepsilon$ , where the coefficients to each order in  $\varepsilon$  are integrated numerically. The upgrade of this program to be able to deal with mass thresholds within the integration region is one of the main achievements of the work presented in this thesis. The advancement is accomplished by an automated analytical continuation of the Feynman parametrized integrand, building on work presented in Refs. [274, 275, 279–281]. With the resulting version 2 of SECDEC, valuable predictions and checks can be done, regardless of the number of scales involved. Contrary to analytical methods, it can even be beneficial to include more scales. While purely finite integrals with multiple scales are hard to access with analytical methods, it is comparatively easy using the numerical approach. Finally, it turns out that not only is the developed tool useful for checks against analytical results, but it has also proven powerful in computing analytically inaccessible integrals for phenomenological applications.



# 4 | The method of sector decomposition

As described in the introduction, a theory can be ultra-violet and infrared divergent, The idea of renormalization is to subtract the divergent parts and thereby make the theory finite. Finding the right subtraction terms for the UV divergent parts was a long standing problem whose solution resulted in the BPHZ theorem. To this end Hepp used a decomposition of higher order loop diagrams into sectors to disentangle overlapping UV divergences [144]. Thirty years later, the idea was taken up by Denner and Roth for a disentanglement of UV divergences [282].

The application to infrared singularities and a systematic treatment of these to arbitrary loop order using sector decomposition was pointed out by Binoth and Heinrich [151]. It serves as a local subtraction procedure to separate infrared divergences from individual diagrams.

## 4.1 Conceptual idea

The algorithm to find the subtraction terms of individual graphs works in three main steps. In the first step, the singular components of an integral are disentangled by iteratively decomposing the integral into sectors. In a second step, the pole coefficients to each order in the poles of the dimensional regulator  $\varepsilon$  are extracted. In the last step, the coefficients containing kinematic invariants and Feynman parameters are integrated analytically or numerically if an analytical treatment is not accessible.

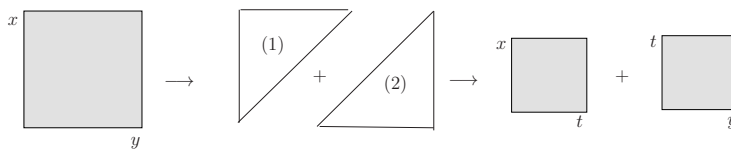


Figure 4.1: The basic idea of sector decomposition.

The idea of sector decomposition is essential for the first step of the algorithm. It is based on splitting the integration region to achieve a disentanglement of the singularities.

As a simple example, consider the following integral

$$\int_0^1 dx_1 \int_0^1 dx_2 \frac{1}{(x_1 + x_2)^{2+\varepsilon}} \quad (4.1a)$$

$$= \int_0^1 dx_1 \int_0^1 dx_2 \frac{1}{(x_1 + x_2)^{2+\varepsilon}} (\Theta(x_1 - x_2) + \Theta(x_2 - x_1)) \quad (4.1b)$$

$$= \int_0^1 dx_1 \int_0^{x_1} dx_2 \frac{1}{(x_1 + x_2)^{2+\varepsilon}} + \int_0^1 dx_2 \int_0^{x_2} dx_1 \frac{1}{(x_1 + x_2)^{2+\varepsilon}} \quad (4.1c)$$

$$= \int_0^1 dx_1 \int_0^1 d\tilde{x}_2 \frac{x_1}{(x_1 + x_1\tilde{x}_2)^{2+\varepsilon}} + \int_0^1 dx_2 \int_0^1 d\tilde{x}_1 \frac{x_2}{(x_2\tilde{x}_1 + x_2)^{2+\varepsilon}}, \quad (4.1d)$$

$$= \int_0^1 dx_1 \int_0^1 d\tilde{x}_2 \frac{1}{x_1^{1+\varepsilon}(1 + \tilde{x}_2)^{2+\varepsilon}} + \int_0^1 dx_2 \int_0^1 d\tilde{x}_1 \frac{1}{x_2^{1+\varepsilon}(\tilde{x}_1 + 1)^{2+\varepsilon}}, \quad (4.1e)$$

where overlapping divergences appear in the limit of a vanishing of both Feynman parameters  $x_1, x_2 \rightarrow 0$  in the first line. In the second line, see Eq. (4.1b), the integration region is split into one part where  $x_1$  is always bigger than  $x_2$  and a second part where the hierarchy is reversed. The splitting can be translated into a change of the integration boundaries, compare Eq. (4.1c). Using the transformation

$$x_1 \rightarrow x_1 \quad (4.2a)$$

$$x_2 \rightarrow x_1\tilde{x}_2 \quad (4.2b)$$

in the first integral on the righthand side of Eq. (4.1c) and the transformation

$$x_1 \rightarrow x_2\tilde{x}_1 \quad (4.3a)$$

$$x_2 \rightarrow x_2 \quad (4.3b)$$

in the second integral on the righthand side of Eq. (4.1c), both integrals are remapped onto the unit hypercube, compare Eq. (4.1d). The transformations in Eqs. (4.2) and (4.3) are known in the mathematical literature as blowing-up an affine  $N$ -dimensional space, compare e.g. Ref. [283]. The number of variables participating in this blowing-up is two, therefore  $N = 2$  in this example. The blowing-up leads to two integrals with disentangled (non-overlapping) singularities, compare Eq. (4.1e).

In the following, all three steps of the algorithm are discussed in more detail. When treating Feynman loop integrals, a decomposition into primary sectors is beneficial and performed before the iterated decomposition into sub-sectors. The description of the algorithm is restricted to scalar multi-loop integrals for better readability, but the extension to multi-loop tensor integrals is straightforward. The discussion of the algorithm is based on Refs. [151, 152].

### 4.1.1 Generation of primary sectors

A general loop integral in Feynman parametrization, compare Eq. (3.3), contains a  $\delta$ -distribution, which can be formulated in various ways. To arrive at the simplest

representation for a subsequent iterated sector decomposition, the representation of the  $\delta$ -distribution is chosen such that a definite hierarchy is introduced after integration, where one Feynman parameter  $x_l$  out of  $N$  is always larger than the rest. To this end, the  $N$  dimensional unit hypercube is split into  $N$  sectors. In each of these so called primary sectors, one Feynman parameter  $x_l$  is chosen to be larger than all others

$$\prod_{j=1}^N \int_0^\infty dx_j = \prod_{j=1}^N \int_0^\infty dx_j \sum_{l=1}^N \Theta(x_l \geq x_j \geq 0) , \quad (4.4)$$

where  $\Theta$  is the Heaviside step function with values

$$\Theta(x - y) = \begin{cases} 1, & x > y , \\ 0, & x \leq y . \end{cases} \quad (4.5)$$

In the distribution sense, it is a generalized function defined as

$$\Theta(x - y) = \int_y^\infty dx \varphi(x) , \quad (4.6)$$

where the derivative of  $\varphi(x)$  with respect to  $x$  gives the Dirac  $\delta$ -distribution. After the decomposition into primary sectors, the integral  $G$  is split into  $N$  integrals  $G_l$  with  $x_l$  the upper integration boundary of all integrals over  $x_i$  ( $\forall i \neq l$ ), compare Eq. (4.1c). In the next step, all integrals are remapped to the unit hypercube by using a blowing up transformation on the Feynman parameters

$$x_j = \begin{cases} x_l t_j, & j \neq l , \\ x_l, & j = l . \end{cases} \quad (4.7)$$

The homogeneity of the functions  $\mathcal{U}$  and  $\mathcal{F}$  lead to a scaling behavior of  $\mathcal{U} \propto x_l^L$  and  $\mathcal{F} \propto x_l^{L+1}$ , where  $L$  is the number of loops of the diagram, see Sec. 3.3. Taking into consideration all powers in  $x_l$  appearing in one sector

$$G_l \propto \int_0^\infty \prod_{\substack{j=1 \\ j \neq l}}^N (x_l^{N-1} dt_j) dx_l (x_l t_j)^{\nu_j-1} x_l^{\nu_l-1} x_l^{L(N_\nu - (L+1)D/2) - (L+1)(N_\nu - LD/2)} \quad (4.8)$$

$$\propto \int_0^\infty \prod_{\substack{j=1 \\ j \neq l}}^N (t_j^{\nu_j-1} dt_j) dx_l x_l^{(\sum_{k=1}^N (\nu_k-1) + N-1)} x_l^{-N_\nu} \quad (4.9)$$

$$\propto \int_0^\infty \prod_{\substack{j=1 \\ j \neq l}}^N (t_j^{\nu_j-1} dt_j) dx_l x_l^{-1} , \quad (4.10)$$

an overall factor of  $x_l^{-1}$  remains. The integration of the  $\delta$ -distribution

$$\int_0^\infty \frac{dx_l}{x_l} \delta(1 - x_l (1 + \sum_{k=1}^{N-1} t_k)) = 1 \quad (4.11)$$

then yields primary sectors of the type

$$G_l = \prod_{\substack{j=1 \\ j \neq l}}^N \int_0^1 dt_j t_j^{\nu_j-1} \frac{\mathcal{U}_l^{N_\nu-(L+1)D/2}(\vec{t})}{\mathcal{F}_l^{N_\nu-LD/2}(\vec{t})}, \quad (4.12)$$

where the  $G_l$  are connected with the full integral  $G$  by

$$G = \frac{(-1)^{N_\nu}}{\prod_{j=1}^N \Gamma(\nu_j)} \Gamma(N_\nu - LD/2) \sum_{l=1}^N G_l. \quad (4.13)$$

### 4.1.2 Iterated sector decomposition

In the one-loop case, the first Symanzik sub-sector polynomials  $\mathcal{U}_l$  are already brought into the form  $\mathcal{U}_l = 1 + \sum_{j=1, j \neq l}^N t_j$  after the decomposition into primary sectors. This is different at higher loop order  $L > 1$  and also for the second Symanzik sub-sector polynomials  $\mathcal{F}_l$ . An iterative procedure allows for the successive disentanglement of all singularities. It follows three steps which are performed until completion.

At first, a minimal set of parameters  $\mathcal{S} = \{t_{\alpha_1}, \dots, t_{\alpha_r}\}$  is assigned which leads to a vanishing of the primary sector functions  $\mathcal{U}_l$  and  $\mathcal{F}_l$  in the limit of vanishing elements of  $\mathcal{S}$ . The success of the decomposition is dependent on the choice of  $\mathcal{S}$  which is by no means unique.

Then, the defined  $r$ -dimensional cube is split into sub-sectors

$$\prod_{j=1}^r \Theta(1 \geq t_{\alpha_j} \geq 0) = \sum_{k=1}^r \prod_{\substack{j=1 \\ j \neq k}}^r \Theta(t_{\alpha_k} \geq t_{\alpha_j} \geq 0). \quad (4.14)$$

Next, the integration boundaries are transformed back to the unit cube by applying a blowing up once more, leading to the following transformation rules for the Feynman parameters

$$t_{\alpha_j} = \begin{cases} t_{\alpha_k} t_{\alpha_j}, & j \neq k, \\ t_{\alpha_k}, & j = k. \end{cases} \quad (4.15)$$

At least one of the functions  $\mathcal{U}_l$  and  $\mathcal{F}_l$  factorize in the parameter  $t_{\alpha_k}$  with the exponent of  $\mathcal{U}_l$  or  $\mathcal{F}_l$ , respectively. Taking the additional Jacobian factor of  $t_{\alpha_k}^{r-1}$  into account, exponents of the type  $A_k - B_k \varepsilon$  result for each integration parameter  $t_{\alpha_k}$ .  $A_k$  and  $B_k$  are numbers independent of the regulator  $\varepsilon$ . The resulting sub-sector integrals are of the form

$$G_{lk} = \prod_{\substack{j=1 \\ j \neq k}}^N \int_0^1 dt_{\alpha_j} \left( t_{\alpha_k}^{A_k - B_k \varepsilon} \right) \frac{\mathcal{U}_{lk}^{N_\nu-(L+1)D/2}(\vec{t}_{\alpha_j})}{\mathcal{F}_{lk}^{N_\nu-LD/2}(\vec{t}_{\alpha_j})}, \quad k = 1, \dots, r. \quad (4.16)$$

The three steps are repeated creating further sub-sectors  $\mathcal{U}_{lk_1k_2\dots k_c}$  and  $\mathcal{F}_{lk_1k_2\dots k_c}$ , until no further set  $\mathcal{S}$  can be found after  $c$  iterations which leads to a vanishing of the sub-sector functions. This is the case when they contain a constant term in form of a 1 in the case of the first, and in form of a kinematic invariant in the case of the second Symanzik polynomial

$$U_{lk_1k_2\dots} = 1 + u(\vec{t}_{\alpha_j}) , \quad (4.17)$$

$$F_{lk_1k_2\dots} = s_1 + \sum_{\beta} (s_{\beta}) f_{\beta}(\vec{t}_{\alpha_j}) , \quad (4.18)$$

where  $u(\vec{t}_{\alpha_j})$  and  $f_{\beta}(\vec{t}_{\alpha_j})$  are polynomials in the Feynman parameters and where kinematic invariants including masses are termed  $s_1$  and  $s_{\beta}$ .

The singular behavior is now contained in the exponent  $A_k$  and all overlapping divergences are disentangled.

### 4.1.3 Extraction of the poles

It is now possible to find subtraction terms to extract poles in a Laurent series in the regulator  $\varepsilon$ . Each obtained sub-sector integrand and all variables  $t_{\alpha_j}$  with exponents  $A_j - B_j \varepsilon$  can be written in the general form

$$I_j = \int_0^1 dt_{\alpha_j} t_{\alpha_j}^{A_j - B_j \varepsilon} \mathcal{I}(t_{\alpha_j}, \{t_{\alpha_i \neq \alpha_j}\}, \varepsilon) , \quad (4.19)$$

where  $\mathcal{I}$  is a function of the decomposed sub-sector functions  $\mathcal{U}_{lk_1k_2\dots k_c}$  and  $\mathcal{F}_{lk_1k_2\dots k_c}$ . If the Feynman parameter is of positive or vanishing exponent,  $A_j \geq 0$ , the integration is finite in the regulator  $\varepsilon$  and no subtraction is needed. In all other cases, the integration will lead to a logarithmic pole for  $A_j = -1$  or a higher pole if  $A_j < -1$  and in the limit of a vanishing Feynman parameter  $t_{\alpha_j}$ . To expand around the pole, an expansion into a Taylor series around  $t_{\alpha_j} = 0$  can be performed

$$\mathcal{I}(t_{\alpha_j}, \{t_{\alpha_i \neq \alpha_j}\}, \varepsilon) = \sum_{p=0}^{|A_j|-1} \mathcal{I}_j^{(p)}(0, \{t_{\alpha_i \neq \alpha_j}\}, \varepsilon) \frac{t_{\alpha_j}^p}{p!} + R(\vec{t}, \varepsilon) , \quad (4.20)$$

where  $R(\vec{t}, \varepsilon)$  denotes the remainder term which does not contain any poles in the parameter  $t_{\alpha_j}$  by construction and where

$$\mathcal{I}^{(p)}(0, \{t_{i \neq j}\}, \varepsilon) = \left. \frac{\partial^p}{\partial t_j^p} \mathcal{I}_j(t_j, \{t_{i \neq j}\}, \varepsilon) \right|_{t_j=0} . \quad (4.21)$$

Reinserting Eq. (4.20) into Eq. (4.19) the only terms depending on the variable  $t_{\alpha_j}$  are powers of it and the remainder polynomial  $R$ . Expanding the whole integrand into plus-distributions using the identity

$$x^{-1+\kappa\varepsilon} = \frac{1}{\kappa\varepsilon} \delta(x) + \sum_{n=0}^{\infty} \frac{(\kappa\varepsilon)^n}{n!} \left[ \frac{\ln^n(x)}{x} \right]_+ , \quad (4.22)$$

where

$$\int_0^1 dx f(x) \left[ \frac{g(x)}{x} \right]_+ = \int_0^1 dx g(x) \left[ \frac{f(x) - f(0)}{x} \right], \quad (4.23)$$

the integration over  $t_{\alpha_j}$  can be performed straightforwardly for the first term on the righthand side of Eq. (4.20), resulting with only the integration left in the finite remainder term

$$I_j = \sum_{p=0}^{|A_j|-1} \frac{1}{A_j - B_j \varepsilon + p + 1} \frac{\mathcal{I}_j^{(p)}(0, \{t_{i \neq j}\}, \varepsilon)}{p!} + \int_0^1 dt_j t_j^{A_j - B_j \varepsilon} R(\vec{t}, \varepsilon). \quad (4.24)$$

In the case of a logarithmic divergence, the sub-sector integrand with poles subtracted in the variable  $t_{\alpha_j}$  would read

$$\begin{aligned} I_j &= \int_0^1 dt_{\alpha_j} t_{\alpha_j}^{-1 - B_j \varepsilon} \mathcal{I}(t_{\alpha_j}, \{t_{\alpha_i \neq \alpha_j}\}, \varepsilon) \\ &= - \frac{\mathcal{I}(0, \{t_{\alpha_i \neq \alpha_j}\}, \varepsilon)}{B_j \varepsilon} \\ &\quad + \int_0^1 dt_{\alpha_j} t_{\alpha_j}^{-1 - B_j \varepsilon} (\mathcal{I}(t_{\alpha_j}, \{t_{\alpha_i \neq \alpha_j}\}, \varepsilon) - \mathcal{I}(0, \{t_{\alpha_i \neq \alpha_j}\}, \varepsilon)). \end{aligned} \quad (4.25)$$

#### 4.1.4 Calculation of the pole coefficients

After repetition of these subtraction steps for all variables  $t_{\alpha_j} \forall j$  and all obtained sub-sectors, nested sums result where each summand can be dependent on the regulator  $\varepsilon$ . The whole expression can be expanded in  $\varepsilon$  yielding a Laurent series with coefficients  $C_{lk_1 k_2 \dots k_c, m}$  for each of the  $c(l)$  sub-sector integrals of the  $l$ -th primary sector

$$G_{lk_1 k_2 \dots k_c} = \sum_{m=-2L}^n C_{lk_1 k_2 \dots k_c, m} \varepsilon^m + \mathcal{O}(\varepsilon^{n+1}) \quad (4.26)$$

which again enter the full result for a (scalar) loop diagram as

$$G = (-1)^N \Gamma(N_\nu - LD/2) \sum_{l=1}^N \sum_{k=1}^{c(l)} G_{lk_1 k_2 \dots k_c}. \quad (4.27)$$

## 4.2 The choice of algorithm

### 4.2.1 Goals

The best suited sector decomposition algorithm may differ in view of the two aspects, applicability and simplicity of the result. One algorithm may be applicable to every multi-loop diagram, but result in very complicated expressions. Another one may lead to relatively simple expressions, but is not guaranteed to stop.



A sector decomposition algorithm does not stop, as soon as it runs into an infinite recursion. The appearance of such can be exemplified assuming the following function

$$f(x_1, x_2, x_3) = x_1^2 + x_2^2 x_3 . \quad (4.28)$$

When decomposing it first in the variables  $x_1$  and  $x_3$ , two sub-sectors with opposite hierarchy

$$f_1(t_1, x_2, x_3) = x_3 (x_3 t_1^2 + x_2^2) \quad (4.29)$$

$$f_2(x_1, x_2, t_3) = x_1 (x_1 + x_2^2 t_3^2) \quad (4.30)$$

are created by rescaling the Feynman parameter  $x_1 = x_3 t_1$  in the first sub-sector of function  $f$ , and  $x_3 = x_1 t_3$  in the second sub-sector. Choosing the sub-sector  $f_1$  and the set  $S = \{2, 3\}$  of Feynman parameters, the initial functional results

$$f_{11}(t_1, t_2, x_3) = x_3^2 (t_1^2 + x_3 t_2^2) \quad (4.31)$$

$$f_{12}(t_1, x_2, t_3) = x_2^2 t_3 (t_3 t_1^2 + x_2) , \quad (4.32)$$

augmented by an additional factor of Feynman parameters. The set  $S = \{1, 2\}$  would instead lead to a termination of the algorithm. If chosen in an inconvenient way, decomposition sequences can complicate integrand functions or even lead to an infinite recursion. The occurrence of the latter limits the applicability. Manifestations of the former have a direct influence on the numerical convergence.

The fewer decomposition steps are needed in an iterative algorithm, the fewer sub-sectors are produced and the smaller the powers of factorized integration parameters are.

### 4.2.2 A heuristic algorithm for slim results

A first algorithm, which is also the one employed in the program SECDEC, is completely heuristic. First, the primary sector decomposition is performed as described in Sec. 4.1.1. Then, each individual primary sector is iteratively decomposed into sub-sectors until both Symanzik polynomials are finite for vanishing Feynman parameters. The procedure works as follows:

- 1) Determine which of the two polynomials  $\mathcal{U}_l$  and  $\mathcal{F}_l$  of the primary sector  $l$  turns zero in the limit of vanishing Feynman parameters. Find the best decomposition set  $\mathcal{S}$  for this function. If both polynomials nullify, find the best decomposition set for  $\mathcal{U}_l$ .
- 2) Compute all possible subsets of Feynman parameters contained in one primary sector.
- 3) Find the smallest set  $\mathcal{S}_{\min}$  that nullifies the function detected in 1). If two or more such sets have equal but minimal length, proceed with step 4), otherwise continue with step 5). The smallest set must contain more than one Feynman parameter, otherwise it would factorize from the polynomials  $\mathcal{U}_l$  and/or  $\mathcal{F}_l$ .

- 4) Discover which of the minimal sets maximizes the number of vanishing sub-sector polynomials. If there are several minimal sets leading to the same maximal number of vanishing polynomials, analyze the powers in the Feynman parameters of each nullifying set for the function detected in 1). Choose the set with lowest powers in the vanishing Feynman parameters.
- 5) Divide both,  $\mathcal{U}_l$  and  $\mathcal{F}_l$  into sub-sectors using the encountered best minimal set.

The procedure is iterated and more sub-sectors are produced as long as there is a set that nullifies  $\mathcal{U}_{k_1 \dots k_c}$  or/and  $\mathcal{F}_{l_{k_1 \dots k_c}}$ .

This heuristic strategy is found to produce the least sectors compared to strategies described separately by Bogner, Weinzierl and Smirnov, Tentyukov, compare Ref. [284] and Ref. [285], respectively. Yet, the algorithm is not guaranteed to stop. The probability for running into an infinite recursion as described in the previous section can be reduced by introducing an additional heuristic strategy to the algorithm. In the latter, a pre-decomposition is carried out for all those Feynman parameters appearing quadratically or in higher powers in the primary sectors. No selection of a subset of Feynman parameters is performed. This treatment has proven to be very beneficial in many cases, especially in the computation of two-loop integrals with massive internal lines, but can lead to an increase in the number of produced sectors if it is always carried out. Applied to inconveniently chosen sectors of complicated integrals, this additional strategy can even introduce higher spurious negative powers in the factorized Feynman parameters.

### 4.2.3 Algorithms guaranteed to stop

There are examples of three-loop diagrams which cannot be treated with the heuristic algorithms described in the previous chapter due to the occurrence of infinite recursion. To this end, it is interesting to find algorithms which are guaranteed to stop, regardless of the numbers of sectors produced.

The possibly simplest algorithm to that matter is the one introduced by Hepp [144], where  $n!$  sectors are produced due to the fact that each sector is split in all Feynman variables  $x_n$ , thereby always choosing the maximal decomposition set. Although this strategy will eventually terminate, the amount of sectors produced is by far too large. The problem can be solved differently by formulating it in terms of the polyhedra game introduced by Hironaka where the player A is supposed to win over player B after a finite number of moves and independent of the reaction of player B, see Ref. [286]. The relation to sector decomposition was found by Bogner and Weinzierl who also analyzed three strategies leading to the termination of the sector decomposition algorithm, see Ref. [284]. The first strategy analyzed there is based on work by Zeilinger [287], the second on a strategy by the mathematician Spivakovsky [288], and the third strategy is inspired by a proof of Encinas and Hauser, see Ref. [289]. The strategies are all based on enforcing a sequence of decreasing decomposition sets of Feynman parameters used for each step in the iterated decomposition into sub-sectors. It was found, that the heuristic strategy always wins over the terminating algorithms in terms of the numbers of sectors produced, see Ref. [284, 290].

---

This situation does not change with the introduction of another strategy  $S$  found by Smirnov and Tentyukov, although it results with less sectors than the previously mentioned terminating strategies, see Ref. [285]. The strategy involves the computation of normal vectors to facets of the convex hull of all weights, where the weights are found by the exponents in the Feynman parameters of each monomial in the sub-sector polynomial. If there is no facet which would lead to a, with respect to the lexicographical ordering, smaller set of Feynman parameters to be decomposed in the next step, the decomposition is finished using strategy which is guaranteed to stop, e.g. the one based on work by Zeilinger. It was also found that strategy  $S$  produces the same number of sectors as the strategy based on Speer sectors [291], which can process more information about the graph to be computed. The introduction of Speer sectors leads to a higher efficiency in the sector decomposition, regarding the speed and the memory intensity, see Refs. [292,293].

Having introduced all these strategies, it would be nice to have a strategy which produces comparatively few sectors with regard to the heuristic strategy and is guaranteed to terminate in a finite number of steps. Such a strategy was introduced by Kaneko and Ueda [294,295]. They take a deterministic approach and reformulate the primary sectors using convex and combinatorial geometry. By the construction of intersections of dual cones to convex polyhedral cones a unique decomposition of the integration region can be found for each polynomial. Some of the cones may still be too complicated for integration, therefore they can be cut into simplices using triangulation. The total number of sectors produced depends on the triangulation algorithm. For the latter, there are many implementations available in the literature, see e.g. Refs. [296,297]. Using the first of the two, the resulting number of sectors is found to be even smaller compared to the heuristic strategy and the algorithm is, by construction, always guaranteed to stop, see Ref. [295]. The drawback is that the resulting functions are more complicated compared to the integrands resulting from the heuristic strategy. This is due to the fact that it is not an iterative algorithm. While currently only the heuristic strategy, augmented by the option of applying a pre-decomposition, is implemented in the program SECDEC, the algorithm of Kaneko and Ueda will be included in the next improved version of the program, see Sec. 6.6.



# 5 | Singularity structure of Feynman integrals

## 5.1 Euclidean vs. physical kinematics

In Sec. 3.3 it was already pointed out that both Symanzik polynomials are of definite sign when computing integrals in the Euclidean region. This implies that the energy component of the external momenta lies on the imaginary axis, leading to negative values in the kinematic invariants  $s_{ij} < 0$  and  $p_i^2 < 0$  and an overall positive contribution in the second Symanzik polynomial  $\mathcal{F}$ . To verify this, compare e.g. with the one-loop box example in Sec. 3.3. Then, together with masses entering with a positive sign,  $\mathcal{F}$  is positive semi-definite. After the application of sector decomposition, all possible singularities appearing in  $\mathcal{F}$  are factorized leading to only positive definite integrands.

Switching to physical kinematics, the invariants formed from external momenta can be real and four-momentum conservation

$$\sum_{\substack{i,j \\ i \neq j}}^{n-1} s_{ij} - \sum_i^n p_i^2 = 0 \quad (5.1)$$

must hold, where  $n$  is the number of external legs of which  $n-1$  are linearly independent. Due to this fact,  $\mathcal{F}$  is no longer definite and further singularities, though integrable, can occur within the integration region.

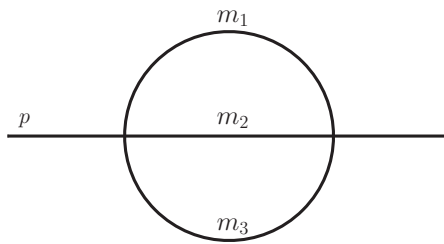


Figure 5.1: Two-loop two-point "sunrise" graph with three internal masses.

An intuitive example are production thresholds which appear as internal particles go on-shell. This means that the overall incoming external momentum reaches any sum

of masses of internal propagators potentially leading to physical final states. A simple example to demonstrate this is a two-loop two-point function with three internal masses, see Fig. 5.1. The three-particle-cut discontinuity occurs for

$$p^2 = (m_1 + m_2 + m_3)^2 . \quad (5.2)$$

The analytical determination of the threshold locations gets more and more complicated, the more external legs and propagators are involved. Writing an integral in Feynman parametrization, thresholds may be parametrized at the integrand level, as a combination of kinematic invariants and Feynman parameters. The full set of thresholds can be determined solving the Landau equations of an integrand.

## 5.2 Landau equations

The Landau equations

$$x_j (q_j^2(\{k\}, \{p\}) - m_j^2) = 0 \quad \forall j \in \{1, \dots, N\} \quad (5.3a)$$

$$\frac{\partial}{\partial k_i^\mu} \sum_{j=1}^N x_j (q_j^2(\{k\}, \{p\}) - m_j^2) = 0 \quad \forall i \in \{1, \dots, L\} , \quad (5.3b)$$

give the necessary (but not sufficient) conditions for a divergence, see Refs. [257,298,299]. In accordance with the notation of Sec. 3.2, the  $q_j$  are linear combinations of external momenta  $p_i$  and loop momenta  $k_i$ ,  $N$  is the number of propagators and  $L$  the number of loops. Paraphrasing Eqs. (5.3a), either the propagator  $q_j^2 - m_j^2$  or their respective Feynman parameter  $x_j$  must vanish to potentially contribute to a singularity. Only if Eqs. (5.3b), involving a derivative by the loop momenta, vanish simultaneously, the conditions for a Landau singularity are fulfilled.

A solution to the system with  $x_j \neq 0 \forall j$  gives the leading Landau singularity, which is not integrable for  $N > 2$  when  $D = 4 - 2\varepsilon$ , and real values of masses and momenta. Those singularities where the vanishing of one Feynman parameter leads to a singular behavior are termed sub-leading Landau singularities. These correspond to the thresholds of a subgraph as a vanishing Feynman parameter can be associated with the removal of one propagator and the junction of two vertices. These singularities are integrable and of logarithmic or square-root type.

The Landau equations can be solved by contracting the momenta of Eq. (5.3b) with those loop and external momenta the equation depends on, to get a system of equations which can be solved by using the constraints arising from Eq. (5.3a). A nice example analysis can be found in Ref. [271]. Another example is shown in Sec. 7.2.

The Landau equations can also be formulated as

$$\mathcal{F}(\vec{x}, \{p, m^2\}) = 0 , \quad (5.4a)$$

$$\frac{\partial}{\partial x_j} \mathcal{F}(\vec{x}, \{p, m^2\}) = 0 \quad \forall j \in \{1, \dots, N\} , \quad (5.4b)$$

after having integrated out the loop momenta, see Ref. [300]. The leading Landau singularity is again given by the solution to the system of equations assuming an empty set of vanishing Feynman parameters.

How we deal with these singularities will be described in the following section.

## 5.3 Deformation of the integration contour

### 5.3.1 Cauchy theorem

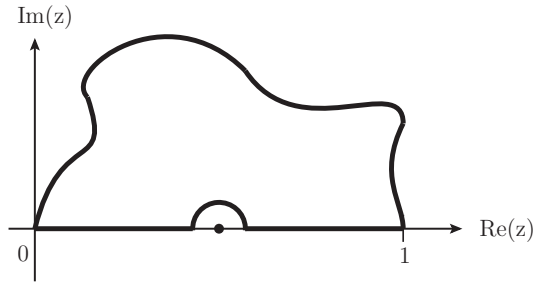


Figure 5.2: Schematic picture of the closed contour avoiding poles on the real axis.

Unless the function  $\mathcal{F}$  is of definite sign for all possible values of invariants and Feynman parameters, the denominator of a multi-loop integral will vanish within the integration region on a hypersurface given by the solutions of the Landau equations. To avoid the non-physical poles on the real axis, the Cauchy theorem

$$\oint_c \prod_{j=1}^N dz_j \mathcal{I}(\vec{z}) = \int_0^1 \prod_{j=1}^N dx_j \mathcal{I}(\vec{x}) + \int_1^0 \prod_{j=1}^N dz_j \mathcal{I}(\vec{z}) = 0 \quad (5.5)$$

can be exploited, where  $\text{Re}(\vec{z}) = \vec{x}$ . To be able to use the theorem, the original integrand, depending only on the real coordinates  $x_j$ , is analytically continued to the complex plane. The coordinate transformation reads

$$\int_0^1 \prod_{j=1}^N dx_j \mathcal{I}(\vec{x}) = \int_0^1 \prod_{j=1}^N dx_j \left| \left( \frac{\partial z_k(\vec{x})}{\partial x_l} \right) \right| \mathcal{I}(\vec{z}(\vec{x})), \quad (5.6)$$

where the new complex coordinates  $\vec{z}$  describe a path parametrized by the variables  $\vec{x}$ . With a given description of the coordinates  $\vec{z}$ , the Cauchy theorem in Eq. (5.5) can be formulated. It is valid in this form as long as the deformation is in accordance with the causal  $i\delta$  prescription of the Feynman propagators, as the region enclosed by the integration contour then does not contain any singular points, compare Fig. 5.2. It is important to keep in mind, that no poles should be crossed while changing the integration path, otherwise Eq. (5.5) is no longer valid.

Finding the right analytical continuation to the coordinates  $\vec{z}$  is equivalent to finding the proper deformation to the integration contour. It is the crucial step for the success of this method and will be treated in the following.

### 5.3.2 Deformation

The aim is to find a clever deformation which is well suited for an automated application in numerical calculations. For its realization, a good parametrization of the complex variables  $z_i$  in Eq. (5.6) must be found which on the one hand preserves the causal  $i\delta$  prescription, and on the other ensures all physical thresholds to appear as such in the result. As the latter are contained in the Landau equations, an inclusion of these in the deformation is desirable. It is therefore required that all Landau equations, Eqs. (5.4), are realized when the deformed function  $\mathcal{F}(\vec{z}(\vec{x}))$  vanishes. Furthermore, the  $i\delta$  prescription for the Feynman propagators requires that the contour deformation to the complex plane is chosen such that the infinitesimal imaginary part is conserved. The negative sign of the imaginary part of the second Symanzik polynomial  $\mathcal{F}$  was discussed in Sec. 3.3. For real masses and Mandelstam invariants  $s_{ij}$ , the following Ansatz [279–281] is therefore convenient

$$\begin{aligned}\vec{z}(\vec{x}) &= \vec{x} - i \vec{\tau}(\vec{x}) \\ \tau_k(\vec{x}) &= \lambda x_k (1 - x_k) \frac{\partial \mathcal{F}(\vec{x})}{\partial x_k},\end{aligned}\tag{5.7}$$

where  $\lambda$  is an arbitrary real and positive parameter. A closed integration contour is guaranteed by the factors  $x_k$  and  $(1 - x_k)$ , keeping the endpoints fixed. From Eq. (5.7), the negative sign of the imaginary part is only guaranteed if the derivative by  $\mathcal{F}(\vec{x})$  is not negative. Assuming the overall deformation to be small, the analytic continuation of the integrand can be expanded into a series

$$\mathcal{F}(\vec{x}) \rightarrow \mathcal{F}(\vec{z}(\vec{x})) = \mathcal{F}(\vec{x}) - i \sum_k \tau_k(\vec{x}) \left( \frac{\partial \mathcal{F}}{\partial x_k} \right)^2 + \mathcal{O}(\tau_k(\vec{x})^2),\tag{5.8}$$

where the expansion is done individually in each component  $k$ . The physically motivated requirement that all Landau equations, Eqs. (5.4), be fulfilled is met in Eq. (5.8), when the deformed integrand  $\mathcal{F}(\vec{z}(\vec{x}))$  vanishes. Furthermore, the imaginary part of  $\mathcal{F}(\vec{z}(\vec{x}))$  is always negative due to an ever positive  $(\frac{\partial \mathcal{F}}{\partial x_k})^2$  term. While the absolute size of the derivative parts are determined by the diagrams to be computed,  $\lambda$  is chosen to be a free parameter determining the scale of the deformation. Following the analysis of Ref. [279], the Ansatz for the analytical continuation must guarantee a full cancellation of singularities in subtraction terms present in the remainder term of Eq. (4.24), see also Eq. (4.25). If the analytic continuation is done only after computing the subtraction terms, one Feynman parameter is deformed, while the one of the subtraction term is not. Assume the deformation of a function  $I$  depending on one Feynman parameter

$$I = \int_0^1 dt_\alpha t_\alpha^{-1+\varepsilon} (\mathcal{I}(t_\alpha, \varepsilon) - \mathcal{I}(0, \varepsilon)).\tag{5.9}$$



Analytic continuation of the parameter  $t_\alpha \rightarrow z_\alpha = t_\alpha + i\tau(t_\alpha)$  yields

$$I = \int_0^1 dt_\alpha \left( 1 + i \frac{\partial \tau(t_\alpha)}{\partial t_\alpha} \right) \frac{\mathcal{I}(t_\alpha + i\tau(t_\alpha), \varepsilon) - \mathcal{I}(0, \varepsilon)}{(t_\alpha + i\tau(t_\alpha))^{1-\varepsilon}}. \quad (5.10)$$

The subtraction term  $\mathcal{I}(0, \varepsilon)$  was set up to cancel the soft singularity in the real part. This parameterization can introduce spurious poles in the imaginary part, which are not taken care of in the limit of  $t_\alpha \rightarrow 0$ , unless  $\tau(t_\alpha)$  vanishes faster than linear in the Feynman parameter  $t_\alpha$ . If the deformation vanishes faster than linear in the Feynman parameter  $t_\alpha$ , the imaginary part vanishes faster than the real part, resulting in the original subtraction term. This condition is no longer necessary, when the analytic continuation is done prior to the construction of the subtraction terms. It is due to this analysis that the analytic continuation of each Feynman parameter is done right after the iterated sector decomposition procedure.

In summary, unless a kinematic point fulfills all Landau equations, where both  $\mathcal{F}$  and its derivatives with respect to  $x_i$  vanish, the deformation of the integration contour leads to a well behaved integral at the points where only the function  $\mathcal{F}$  vanishes.

An implementation and further analysis of this deformation for numerical calculations has already been worked out in Refs. [274, 275]. To assure a high numerical stability of the evaluation of multi-loop integrals, necessary to make the implementation publicly available, supplementary studies of the deformation are necessary which are presented in the following.

### Deformation studies

The aim of these deformation studies is to find an optimal procedure for an optimal choice for the parameter  $\lambda$  which guarantees a good behavior of the integrand. To this end, the terms of order  $\mathcal{O}(\tau_k(\vec{x}))$ ,  $\mathcal{O}(\tau_k(\vec{x}))^2$  and  $\mathcal{O}(\tau_k(\vec{x}))^3$  are analyzed, assuming a decreasing effect in higher orders, as is expected from a convergent Taylor series expansion.

The analytic continuation of  $\mathcal{F}(\vec{z}(\vec{x}))$  to the third power in the deformation reads

$$\begin{aligned} \mathcal{F}(\vec{z}(\vec{x})) = & \mathcal{F}(x) - i\lambda \sum_k x_k(1-x_k) \left( \frac{\partial \mathcal{F}}{\partial x_k} \right)^2 \\ & - \frac{1}{2} \lambda^2 \sum_k x_k^2(1-x_k)^2 \left( \frac{\partial \mathcal{F}}{\partial x_k} \right)^2 \left( \frac{\partial^2 \mathcal{F}}{\partial x_k^2} \right) \end{aligned} \quad (5.11)$$

$$+ \frac{i}{6} \lambda^3 \sum_k x_k^3(1-x_k)^3 \left( \frac{\partial \mathcal{F}}{\partial x_k} \right)^3 \left( \frac{\partial^3 \mathcal{F}}{\partial x_k^3} \right) \quad (5.12)$$

which uncovers two non-trivial aspects of the deformation. One leads to the fact that the term proportional to  $\lambda^2$  contributes to the **real** part of  $\mathcal{F}(\vec{z}(\vec{x}))$  and the other to an ambiguity in the sign of the imaginary part.

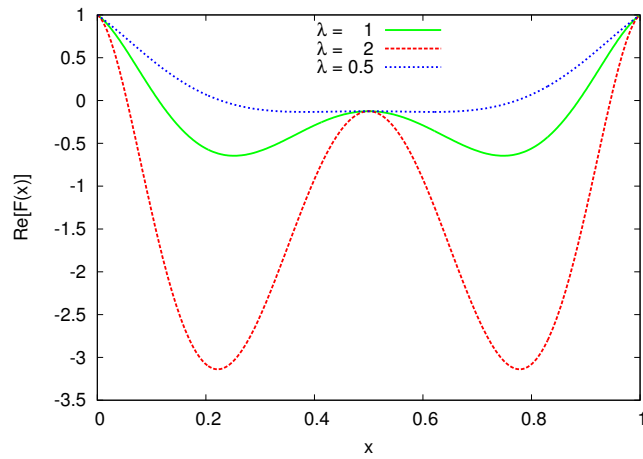


Figure 5.3: Influence of the deformation on the real part for the one-loop bubble and  $m = 1$ ,  $s = 4.5$ .

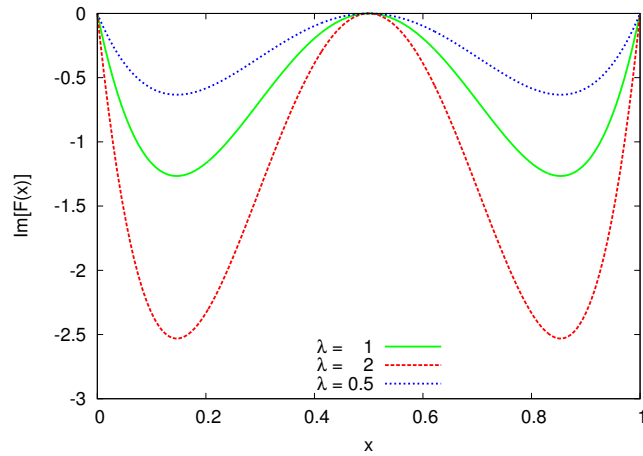


Figure 5.4: Influence of the deformation on the imaginary part for the one-loop bubble and  $m = 1$ ,  $s = 4.5$ .

To show the effect on the real part, it is descriptive to look at the specific but simple example of the massive one-loop bubble, where the leading Landau singularity is well known to be situated at  $s = 4m^2$  when  $x = \frac{1}{2}$ . The function  $\mathcal{F}(x)$  of the one-loop bubble reads

$$\mathcal{F}_{1\text{L-bubble}}(x) = -s x (1 - x) + m^2 - i\delta. \quad (5.13)$$

The real part of  $\mathcal{F}$  after the analytical continuation is shown in Fig. 5.3, where a point above threshold was chosen, with a mass  $m = 1$  and  $s = 4.5$  and assuming arbitrary units.

From its basic geometric properties, it is known that the derivative of  $\mathcal{F}$  in Eq. (5.7) is smallest in the extrema and largest where the slope is maximal. Around  $x = 0.5$ , the function  $\mathcal{F}$  is almost, but not exactly, vanishing. The size of the deformation coming from the derivative of  $\mathcal{F}$  is shown for  $\lambda = 1$ . One can notice that choosing a rather small  $\lambda = 0.5$  the function  $\mathcal{F}$  never vanishes except at the endpoints of the integration region  $x = 0, 1$ , while for the cases of  $\lambda = 1, 2$  the function additionally vanishes in four points. In principle, this should not be a problem, as the imaginary part is not vanishing in any point beyond the end-points, see Fig. 5.4. But the larger the value for  $\lambda$  is chosen, the closer the points where the real part is zero, get to the endpoints, where also the imaginary part is small. This can easily lead to numerical instabilities, so the parameter  $\lambda$  should not be chosen too large.

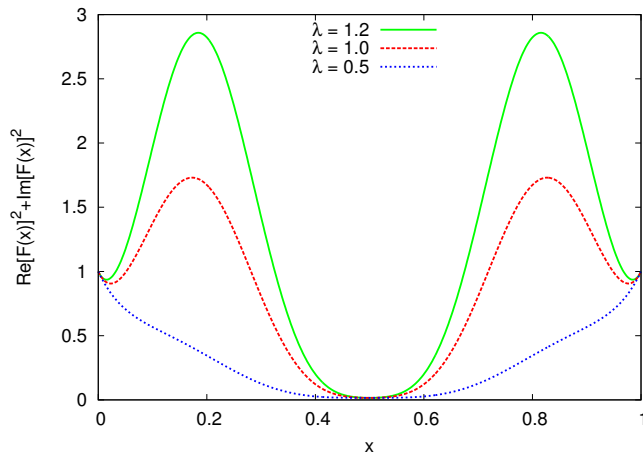


Figure 5.5: Implications for the best choice of  $\lambda$  from the modulus of  $\mathcal{F}(z(x))$  for the one-loop bubble and  $m = 1$ ,  $s = 4.5$ .

It should be noted that a value for  $\lambda > 1$  is still viable, as long as the overall deformation is small. Otherwise, the series in the deformation Eq. (5.8) is no longer converging, leading to a wrong sign of the imaginary part.

After having settled that the deformation parameter should not be chosen too large, it must be found that it should neither be chosen too small, see Fig. 5.5. Though never striking zero, the modulus is extremely small for  $\lambda = 0.5$ , in particular in the vicinity of  $x = 0.5$ , which is bad for the numerical convergence. A maximization of the modulus of the function  $\mathcal{F}(\vec{z}(\vec{x}))$  close to the critical points where it becomes minimal stabilizes the numerical evaluation.

In the case of the one-loop bubble, the term of order  $\lambda^3$  in Eq. (5.12) is zero. This is not the case for more complicated integrals. In order for this term not to grow dominant and by that spoil the overall minus sign of the imaginary part, either lambda must be chosen below one or the terms proportional to the derivative must be  $|\frac{\partial \mathcal{F}(\vec{x})}{\partial x_k}| < 1$ .

This task can be accomplished by performing a small sampling of the derivative terms for each Feynman parameter in various values and divide the parameter  $\lambda$  by the maximally achieved value for the derivative

$$\lambda \rightarrow \tilde{\lambda} = \frac{\lambda}{\max(|\partial\mathcal{F}(\vec{x})/\partial x_1|, \dots, |\partial\mathcal{F}(\vec{x})/\partial x_N|)}. \quad (5.14)$$

Then, the derivative parts are roughly normalized to one and the scale of the deformation is again dominated by the value for the parameter  $\lambda$ .

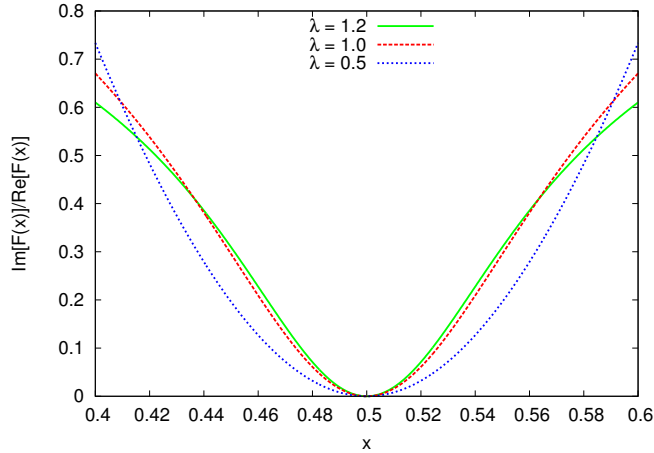


Figure 5.6: Implications for the best choice of  $\lambda$  from the minimization of the complex argument of  $\mathcal{F}(z(x))$  for the one-loop bubble and  $m = 1$ ,  $s = 4.5$ .

In order to further prevent the deformation to become too large, valuable information on the right choice of  $\lambda$  can be extracted from the analysis of the complex argument

$$\varphi_{\mathcal{F}(\vec{z}(\vec{x}))} = \left| \frac{-\sum_k \tau_k(\vec{x}) \left(\frac{\partial\mathcal{F}}{\partial x_k}\right)^2}{\mathcal{F}(\vec{x})} \right|, \quad (5.15)$$

where the numerator contains the coefficient of the imaginary part of order  $\mathcal{O}(\lambda)$ , see Fig. 5.6. Minimizing the complex argument  $\varphi_{\mathcal{F}(\vec{z}(\vec{x}))}$  improves the numerical convergence in the whole integration region when kinematically far from a critical point. When the imaginary part is relatively small compared to the real part, the terms of order  $\lambda^2$  contributing to the real part cannot become too large and those terms going with  $\lambda^3$  cannot spoil the overall sign of the imaginary part. This can be advantageous for speeding up a calculation and is especially interesting in the case of highly fluctuating integrands. Close to a threshold, this additional check is however not advisable because it clashes with the maximization of the modulus of  $\mathcal{F}(\vec{z}(\vec{x}))$ .

For more technical details about the implementation of the deformation, see Sec. 6.2.3.

**Pinch singularities**

If a singularity falls together with an endpoint of the integration region, it is trapped and no proper deformation of the integration contour is possible. The same applies to the case where two singularities fall together, where one singular point could only be bypassed deforming the contour into the direction of the other singularity. The result is a pinch in the integration contour. Both, pinch singularities and singularities at the endpoint of the integration region, are described by the Landau equations, compare Eqs. (5.4).

With the introduction of the analytical continuation to the complex plane and the deformation of the integration contour, integrable singularities do not appear as divergences in the coefficients of the Laurent series in  $\varepsilon$ . Nevertheless, the method leads to numerical instabilities in the vicinity of either a pinch singularity or a singularity at the endpoint of the integration region. This is due to the fact that the deformation of the integration contour becomes negligible. Returning to the one-loop bubble of Eq. (5.13), this behavior can be observed in Fig. 5.5, where the modulus of the function  $\mathcal{F}$  can become very small. The evaluation time and accuracy of an integral close to such a singular point heavily depends on the chosen value for  $\lambda$  and the numerical integrator.



# 6 | Extension of the program SECDEC to physical kinematics

In the following, the public program SECDEC version 2 [1,2,4–7] is presented. SECDEC is a program for the numerical evaluation of multi-scale multi-loop and multi-dimensional polynomial parameter integrals. It is based on the sector decomposition algorithm described in Chap. 4, where dimensionally regulated singularities are extracted. Even though their coefficients are available in algebraic form, they are usually too complicated to be integrated analytically. Therefore the final computation of the coefficients to each order in the regulator  $\varepsilon$  is done by Monte Carlo integration. To deal with integrable singularities due to mass thresholds, the integration contour is deformed to the complex plane. Before the extension to arbitrary kinematics was achieved with SECDEC version 2, a first version of the program was publicly available [301]. Other public implementations of the sector decomposition algorithm working in the Euclidean space are introduced in Refs. [204, 284, 285, 293, 296]. Recently, a new version of the program FIESTA has become available [207], including interesting and valuable new features. The extension to arbitrary kinematics was also achieved there, though their approach is heavily based on the one employed in SECDEC, as mentioned in their publication.

The structure of this chapter is as follows: in Sec. 6.1, the functionality of the program SECDEC version 2 is reviewed. Its characteristic features are explained in Sec. 6.2, further capabilities are elaborated in Sec. 6.3. The operational sequence of the program is shown in Sec. 6.4, before studying two examples and discussing the computation times in Sec. 6.5. Prospective future developments are discussed in Sec. 6.6.

## 6.1 Functionality

In this section, the functionality of the program SECDEC is described. The program has two main branches, one where the computation of any loop integral or integral with a similar structure is possible. The user can start from a diagram knowing the propagators involved, or can even feed some of their own functions into the program. All other steps including the output of the final result are performed in a fully automated way. In the

other branch, more general parametric functions can be computed, including the special feature that additional finite functions can be left symbolic until shortly before numerical integration.

Up to the step of the final integration, the coefficients are computed in a fully analytical way, where all kinematic invariants are left symbolic by default. This feature allows for a fast evaluation of multiple kinematic points, as only the integration step is left to be done if any of the kinematic invariants change. If a user is interested in just the result for one particular diagram for one set of kinematics, it is also possible to insert kinematic values in the beginning.

Version 2 of SECDEC contains the following new features, which will be described in detail in the next sections.

### Loop integrals and integrals of similar structure

- Multi-scale loop integrals can be evaluated without restricting the kinematics to the Euclidean region. This has been achieved by performing a (numerical) contour integration in the complex plane. The program automatically tries to find an optimal deformation of the integration path. In addition, a kinematic threshold can be defined symbolically. Above this threshold, a complex contribution is expected and the deformation of the integration contour is automatically switched on.
- For scalar multi-loop integrals, the integrand can be constructed from the topological cuts of the diagram. The user only has to provide the vertices and the propagator masses, but does not have to provide the momentum flow.<sup>1</sup>
- Tensor integrals can be evaluated with (in principle) no limitation on the rank. This means that a numerical approach in certain cases can help to alleviate or even avoid the procedure of amplitude reduction to master integrals.<sup>1</sup>
- Another new feature is the option to apply the sector decomposition algorithm and subsequent contour deformation on user-defined functions which do not necessarily have the form of standard loop integrals, but have a similar structure.
- The files for the numerical integration of functions amenable to contour deformation (multi-scale multi-loop integrals, user-defined functions) are written in C++ rather than Fortran. For integrations in Euclidean space, the user can choose between using Fortran or C++.
- A parallelization of the algebraic part for Mathematica versions 7 and higher is possible if multiple cores are available. This is of special interest when computing very complicated multi-scale multi-loop integrals, see e.g. Chap. 7.
- A rescaling of all kinematic invariants by the absolute value of the largest invariant can be chosen to achieve a faster convergence of the numerical result.

---

<sup>1</sup>This new feature has been implemented in collaboration with J. Carter.



- Looping over ranges of parameter values is automated, allowing scans over different kinematic configurations within one topology. <sup>1</sup>
- A stable and recent version of the CUBA LIBRARY [302,303], CUBA-3.2, allowing for a parallelized numerical integration is added to the program and used by default.

### General parametric integrals

- The user can define additional (finite) functions at a symbolic level. These can be specified later, after the integrand has been transformed into a set of finite parameter integrals, for each order in  $\epsilon$ . <sup>1</sup>
- Looping over ranges of parameter values is automated, allowing scans over parameter sets for more general polynomial functions. <sup>1</sup>

Below, these new features are described in more detail, but also see Appendix A.2 for a user manual. Comprehensive documentation can be found with the code itself, available at <http://secdec.hepforge.org>.

## 6.2 Characteristic features

### 6.2.1 Loop integrals

The program is capable of integrating general loop and multi-loop diagrams, including kinematic thresholds, using Feynman parameters. In accordance with Sec. 3.3, such a loop integral is composed of five parts, the two Symanzik polynomials  $\mathcal{U}$  and  $\mathcal{F}$ , the numerator, the  $\delta$ -distribution and the powers of factorizing Feynman parameters. While the numerator in a scalar integral is equal to unity, it can contain contractions of loop momenta with each other or with external momenta when the integral is of higher rank. While any kinematic invariant or scalar factor is treated as a constant in the numerator, loop momenta appearing as contractions in the numerator influence the singularity structure of the integrand, compare Eq. (3.9).

Tensor integrals up to in principle arbitrary rank can be computed with SECDEC by evaluating the coefficient functions of the Lorentz decomposed tensors. Take for example, the Lorentz decomposition of a one-loop two-point (bubble) integral  $B_\mu$  of rank  $R = 1$  with one external momentum  $p$

$$B_\mu = p_\mu B_1, \quad (6.1)$$

where the coefficient function  $B_1$  reads

$$p^2 B_1 = P \int d^D q \frac{q_\mu p^\mu}{(q^2 - m_1^2)((q + p_1)^2 - m_2^2)} \quad (6.2)$$

with  $P = \left( \frac{(2\pi\mu_r)^{(4-D)}}{i\pi^2} \right)$ . In the case of  $B_\mu$ , the coefficient function  $B_1$  can be computed with SECDEC, thereby delivering a result for the whole tensor integral.

The algorithms in SECDEC are not restricted by any loop order, tensor rank or the number of scales. Provided with the information on the diagram to be computed SECDEC calculates the Laurent series up to the desired order in the regulator  $\varepsilon$  in a fully automated way. For the iterated sector decomposition two heuristic strategies, described in Sec. 4.2.2, are available. A diagram is specified by its propagators, loop momenta and irreducible numerators, and by the number of external legs and their on-shell conditions. The on-shell conditions become of special importance when external legs are light-like. This is the minimal information needed. Yet, SECDEC has several options allowing for a more efficient evaluation tailored to specific integrals and/or a customization of the output of the results. One of the features of SECDEC is that all kinematic invariants are left symbolic up to the numerical integration. This allows for a fast evaluation of integrals of the same topology for different sets of kinematic values. If only one kinematic point is of interest, it can be beneficial to set the values for the invariants already in the beginning to allow for an additional simplification of the integrands prior to numerical integration. This feature is included in SECDEC as well, by abuse of the on-shell conditions, see App. A.2.4. Furthermore, SECDEC allows for the choice of the desired prefactor and the maximal order in the regulator  $\varepsilon$  to be computed. Among further options regarding the numerical integration, see Sec. 6.3.8, SECDEC arranges for a user-adjustment of the contour-deformation parameters for calculations in the physical region, see Sec. 6.2.3. A removal of spurious divergences can be achieved using integration by parts, see Sec. 6.3.4.

### 6.2.2 Parametric integrals

The program SECDEC can also factorise singularities from parameter integrals which are more general than those in multi-loop integrals. The only restrictions are firstly that the integration domain should be a unit hypercube, and secondly singularities should reside only at the upper and/or lower integration boundary, i.e. at zero or one. Contour deformation is not available for more general parametric functions, because it requires the sign of the imaginary part to be known a priori in order not to give a wrong result. Currently the singularities are assumed to be regulated by non-integer powers of the integration parameters, e.g. the  $\varepsilon$  of dimensional regularization, or some other regulator. The general form of such integrals is

$$I = \int_0^1 dx_1 \dots \int_0^1 dx_N \prod_{i=1}^m P_i(\vec{x}, \{\alpha\})^{\nu_i}, \quad (6.3)$$

where  $P_i(\vec{x}, \{\alpha\})$  are polynomial functions of the parameters  $x_j$ , which can also contain a set of symbolic constants  $\{\alpha\}$ . The user can leave the parameters  $\{\alpha\}$  symbolic during the decomposition, assigning values only for the numerical integration step. This way the decomposition and subtraction steps do not have to be redone if the values for the constants are changed. In Eq. (6.3), the indices  $\nu_i$  are of the form  $\nu_i = a_i + b_i \varepsilon$ , with  $a_i$  such that the integral is convergent. Note that half integer powers are also possible.

### 6.2.3 Implementation of Contour deformation

As explained in Sec. 5.3.1, singularities on the real axis can be avoided by a deformation of the integration contour to the complex plane. The scale of the deformation is controlled by the parameter  $\lambda$  defined in Eq. (5.7). The convergence of the numerical integration can be improved significantly by choosing an “optimal” value for  $\lambda$ . As analyzed in Sec. 5.3.2, values of  $\lambda$  which are too small lead to contours which are too close to the poles on the real axis and therefore lead to bad convergence. Values of  $\lambda$  which are too large can modify the real part of the function to an unacceptable extent, and could even change the sign of the imaginary part if the terms of order  $\lambda^3$  become larger than those terms linear in  $\lambda$ . This would lead to a wrong result. Therefore a four-step procedure is implemented in SECDEC to optimize the value of  $\lambda$ . These are

- Ratio check: To make sure that terms of order  $\lambda^3$  in Eq. (5.8) do not spoil the sign of the imaginary part, the ratio of the terms linear and cubic in  $\lambda$  are evaluated for a quasi-randomly chosen set of samples to determine  $\lambda_{\max}$ . The size of the set can be chosen by the user.
- Modulus check: The imaginary part is vital at the points where the real part of  $\mathcal{F}$  is vanishing. In these regions, the deformation should be large enough to avoid large numerical fluctuations due to a highly peaked integrand. Therefore the modulus of each sub-sector function  $\mathcal{F}_i$  is checked at a number of sample points. At the points where the modulus is close to vanishing, the fraction of the value  $\lambda_{\max}$  is picked which maximizes the modulus of  $\mathcal{F}_i$ . Hereby, the value of  $\lambda$  which keeps  $\mathcal{F}_i$  furthest from zero is chosen.
- Individual  $\lambda(i, j)$  adjustments: If the discrepancy of the values of  $\frac{\partial \mathcal{F}_i}{\partial x_j}$  for different  $x_j$  is very large among one sub-sector  $i$ , it can be convenient to have an individual parameter  $\lambda(i, j)$  for each sub-sector function  $\mathcal{F}_i$  and each Feynman parameter  $x_j$ . As was shown in Sec. 5.3.2, it is beneficial to have small overall deformations of the integration contour. Therefore each individual parameter  $\lambda(i, j)$  is divided by the largest value of  $\frac{\partial \mathcal{F}_i}{\partial x_j}$  for all  $x_j$  in one sub-sector  $i$ , decreasing the overall size of the deformation. If the largest deformations is smaller or equal to one, the  $\lambda(i, j)$  are left unchanged.
- Further optional  $\lambda(i, j)$  adjustments:
  - 1) If the integrand is expected to be oscillatory and hence sensitive to small changes in the deformation parameter  $\lambda$ , SECDEC can minimize the argument of each sub-sector function  $\mathcal{F}_i$  by varying  $\lambda(i, j)$ . The effect is shown in Sec. 5.3.2.
  - 2) If the integrand is expected to have (integrable) singularities close to the endpoints of the integration ( $x_j = 0, 1$ ), the deformation should be as large as possible in order to move the contour away from the problematic region. To this end, each individual parameter  $\lambda(i, j)$  is multiplied by the largest value of  $\frac{\partial \mathcal{F}_i}{\partial x_j}$  for all  $x_j$  in one sub-sector  $i$ .

- Sign check: After the above adjustments to  $\lambda$  have been made, the sign of  $\text{Im}(\mathcal{F})$  is again checked for a number of sample points. If the sign is ever positive, this value of  $\lambda$  is disallowed.

The contour deformation can be switched on or off, see App. A.2.3. The calculation takes longer if a deformation of the integration contour is performed, so if the integrand is known to be positive definite, the contour deformation option should be switched off. It must also be emphasized that for integrands with a complicated singularity structure, the success of the numerical integration can critically depend on the parameters which tune the deformation and on the settings for the Monte Carlo integration.

## 6.3 Additional capabilities

### 6.3.1 Evaluation of user-defined functions with arbitrary kinematics

To calculate a “standard” loop integral, it is sufficient to specify the numerator, the loop momenta and the propagators. The program will construct the integrand in terms of Feynman parameters automatically. It can also be desirable to take a mixed approach of computing an integral numerically after having manipulated it analytically. An example approach is given in Chap. 7, where the numerical efficiency is shown to be improved by a clever analytical preparation of the integrand for the subsequent Monte Carlo integration. In this example, the preparation includes the analytical integration of one sub-loop. This implies that the constraint  $\delta(1 - \sum_i x_i)$  has been already used to achieve a convenient parametrization, and therefore no primary sector decomposition is needed anymore to eliminate the  $\delta$ -constraint. In such a case, the user can skip this step in SECDEC and insert the functions to be factorized directly into the Mathematica template file, using the favored parametrization. More generally, this option offers more flexibility regarding the functions to be integrated, such as expressions for loop integrals which are not in the “standard form”. For example, analytic manipulations which have already been performed on the integral can be dealt with as well. This includes the possibility to perform a deformation of the integration contour to the complex plane.

To better understand the types of function a user could insert, the reader is invited to look back to Eq. (3.9). A general loop integral in Feynman parametrization thus contains a numerator function  $\mathcal{N}$  non-divergent by construction, two Symanzik polynomials  $\mathcal{U}$  and  $\mathcal{F}$ , whose exponent can have either sign and therefore singular points. Furthermore, it contains a fully analytical, but arbitrary prefactor  $\mathcal{P}$  allowed to contain singularities in the regulator  $\varepsilon$ , factorizing powers of Feynman parameters, and a  $\delta$ -distribution constraint. A user-defined function, may contain any of the previously mentioned components or none, with the only exception that the  $\delta$ -constraint needs to either not exist or have been integrated out already. In a more general form, such a user-defined integral  $G_{\text{user}}$  may have any of the following components

$$G_{\text{user}} = \mathcal{P}(\varepsilon) \prod_{j=1}^N \left\{ \int_0^1 dx_j x_j^{a_j(\varepsilon)} \right\} \mathcal{N}(\varepsilon) \mathcal{U}^{\text{ex}\mathcal{U}}(\vec{x}, \{m\}, \{p\}) \mathcal{F}^{\text{ex}\mathcal{F}}(\vec{x}, \{m\}, \{p\}) . \quad (6.4)$$

The functions  $\mathcal{N}$ ,  $\mathcal{U}$  and  $\mathcal{F}$  can be polynomials or products of polynomials with the only condition that they share a common exponent,  $\text{ex}\mathcal{U}$  and  $\text{ex}\mathcal{F}$ . The factorizing Feynman parameters can appear with exponents  $a_j$  dependent or independent of  $\varepsilon$ . Any of the exponents may in principle also contain fractional numbers. Details about the usage of this option are given in the user manual, see App. A.2.6.

### 6.3.2 Topology-based construction of the integrand

As already mentioned in Sec. 3.3, the functions  $\mathcal{U}$  and  $\mathcal{F}$  can be constructed from the topology of the corresponding Feynman graph, without the need to assign the momenta for each propagator explicitly. The implementation in SECDEC is such that the user only has to label the external momenta, the vertices and the masses of a graph. An example is given in Sec. 6.5 and more examples can be found in SECDEC. This feature of constructing the graph topologically is only implemented for scalar integrals so far. The syntax is explained in App. A.2.5.

### 6.3.3 Looping over ranges of parameters

In phenomenological applications usually not just one kinematical point is of interest, but looping over ranges of parameters becomes necessary. To this end, it is beneficial to decrease the computation time where possible. The algebraic part of SECDEC can deal with symbolic expressions for the kinematic invariants, or other parameters contained in the integrand. Consequently, the decomposition and subtraction need only be done once, producing functions which contain general kinematics. The generality of these functions allows for the computation of many sets of different values for the invariants. SECDEC allows for an automated calculation of many numerical points, minimizing the effort for the user. Scripts are provided for “standard” loop, user-defined and more general parametric integrals, see App. A.2.7.

### 6.3.4 Integration-by-parts relations

After the iterated sector decomposition has been performed, poles of the type

$$G_l(A_j, B_j, \vec{t}, \varepsilon) \propto I(A_j, B_j, \vec{t}, \varepsilon) = \int_0^1 dt_j t_j^{A_j+B_j\varepsilon} R(\vec{t}, \varepsilon) \quad (6.5)$$

can arise in an integral  $G_l$  of the sub-sector  $l$ , where  $I$  is a sub-sector integrand. An exponent  $A_j = -2$  is associated with a spurious linear pole, powers  $A_j < -2$  correspond to spurious poles of higher order. These terms must be artificial because a renormalizable gauge theory must be integrable. The function  $R(\vec{t}, \varepsilon)$  denotes the residue integrand after subtraction, compare Eq. (4.20). Choosing  $A_j = -2$ , it would read

$$R(\vec{t}, \varepsilon) = \mathcal{I}(t_{\alpha_j}, \{t_{\alpha_i \neq \alpha_j}\}, \varepsilon) - \mathcal{I}(0, \{t_{i \neq j}\}, \varepsilon) - t_j \left[ \mathcal{I}^{(1)}(t_j, \{t_{i \neq j}\}, \varepsilon) \right]_{t_j=0}. \quad (6.6)$$

Even in the limit of a vanishing  $t_j$ , the integrand will remain integrable and finite assuming the decomposition into plus-distributions has already been performed. While

approaching  $t_j = 0$ , both the numerator and the denominator will become very small. This can introduce numerical instabilities resulting, e.g., from rounding errors. To mitigate this, the sub-sector integrand  $I$  can be integrated by parts

$$I(A_j, B_j, \vec{t}, \varepsilon) = \left[ \frac{t_j^{1+A_j+B_j\varepsilon}}{1+A_j+B_j\varepsilon} R(\vec{t}, \varepsilon) \right]_0^1 - \frac{1}{1+A_j+B_j\varepsilon} \int_0^1 dt_j t_j^{1+A_j+B_j\varepsilon} \frac{\partial}{\partial t_j} R(\vec{t}, \varepsilon) \quad (6.7)$$

$$= \frac{1}{1+A_j+B_j\varepsilon} \times \left[ R(1, \{t_{i \neq j}\}, \varepsilon) - \int_0^1 dt_j t_j^{1+A_j+B_j\varepsilon} \frac{\partial}{\partial t_j} R(\vec{t}, \varepsilon) \right], \quad (6.8)$$

thereby reducing the negative power in the Feynman parameter  $t_j$  by one and enhancing numerical stability, see Ref. [304] for a more detailed description of the implementation. This procedure is automated for arbitrary pole order.

### 6.3.5 Leaving functions implicit during the algebraic part

When evaluating general parametric functions, the user may wish to introduce a “dummy” function depending on (some of) the integration parameters, specifying the actual form of the function later at the numerical integration stage. There are a number of reasons why one might want to leave functions implicit during the algebraic stage: for example, squared matrix elements typically contain large but finite functions of the phase space variables in the numerator, so the algebraic part of the calculation will be quicker and produce much smaller intermediate files if these functions are left implicit. Also, one might like to use a number of measurement functions and be able to specify or change them without having to perform the decomposition more than once. Note that one may use more than one implicit function at a time, and that these functions can have any number of arguments. The syntax and usage are described in App. A.2.8.

### 6.3.6 Assessing the reliability of the numerical result

When dealing with numerical techniques, the knowledge of the reliability of the result is of major importance. Although the integrands of all sectors are stored analytically, it may, especially when dealing with complicated integrals, be time consuming to analyze these, either due to the abundance of Feynman parameters appearing in one function, or simply due to a large number of functions. And even then, the numerical integrator may still appear to be a black box. It is therefore appealing to get an estimate for the correctness of the stated uncertainty. The numerical integrators contained in the CUBA LIBRARY [302,303] return a probability for an estimated numerical uncertainty to be erroneous. A maximal probability of 1 therefore means that the stated uncertainty of a result cannot be trusted. The program collects the maximal probability for each computed order in the dimensional regulator  $\varepsilon$ . The probability can be reduced by

increasing the number of sampling points used in an evaluation. More options tuning the numerical integration parameters are given in the user manual, see App. A.2. To prevent a suffering from underestimation of the true error given by the numerical integrators, it is beneficial to check a result with different integrators when dealing with complicated integrands.

### 6.3.7 Automated remapping to one endpoint

The program is capable of remapping singularities in a Feynman parameter  $x_j$  appearing at the endpoint 1 of the integration region to zero. A remapping of the singularity to zero becomes necessary, if one of the sub-sectors of  $\mathcal{U}$  or  $\mathcal{F}$  in the case of loop integrals, or one of the  $P_i$  of Eq. (6.3) in the case of more general parametric functions, diverge in the limit of one or more  $t_j \rightarrow 1$ . It works as follows. The integration region is split into two parts at the point  $a$ , where  $a$  is chosen rather arbitrarily

$$\int_0^1 f(x)dx = \int_0^a f(x)dx + \int_a^1 f(x)dx \quad (6.9)$$

$$= \int_0^1 \frac{1}{a} f\left(\frac{\tilde{x}}{a}\right)d\tilde{x} + \int_0^1 \frac{1}{a} f\left(1 - \frac{x'}{a}\right)dx' . \quad (6.10)$$

From Eq. (6.9) to Eq. (6.10) the substitutions  $x \rightarrow \frac{\tilde{x}}{a}$  and  $x \rightarrow (1 - \frac{x'}{a})$  are applied to the first and the second integral of the right-hand side, respectively. Hereby, a remapping of the integration boundaries to the unit hypercube is achieved. The resulting functions  $f$  either vanish for  $\lim_{\tilde{x} \rightarrow 0}$  or do not vanish at all.

In SECDEC, the integration region of those integrals over Feynman parameters  $t_{j_i}$  leading to a divergence at the upper integration boundary, is split at 1/2 and the resulting two integrals are remapped to the unit interval.

This splitting of the integration region is performed before the iterated sector decomposition. It increases the number of primary sectors by  $2n$ , where  $n$  is the number of split integration variables, in favor of improved numerical convergence. After all singularities at the endpoint are remapped to the lower integration boundary, an iterated sector decomposition can be applied. The occurrence of singularities at both endpoints is typically encountered in massless diagrams. In Sec. 7.1.1, the integration of one sub-loop prior to the treatment of the full integral serves as an example.

### 6.3.8 A word on the numerical integration

The numerical integration forms a crucial part in the calculation of any type of integrand function resulting from a Laurent series expansion in  $\varepsilon$ . SECDEC contains interfaces to six different numerical integrators, BASES [305], Vegas, Suave, Divonne and Cuhre contained in the CUBA LIBRARY [302,303], and NINTEGRATE contained in Mathematica [306]. The user is offered to choose one of these in the input files, see App. A.2.3. It is crucial to have the parameters for the numerical integrator under control. SECDEC incorporates several options, allowing for a good adjustment of these parameters. Two of them are the desired relative and absolute accuracy, where the desired absolute accuracy is necessary

for integrals close to zero. If the real or imaginary part of the integral tends to zero, the relative accuracy can never be reached. The numerical integrators therefore attempt to find an estimate  $\hat{I}$  of the integral  $I$  that fulfills

$$\hat{I} - I \leq \max(\varepsilon_{\text{abs}}, \varepsilon_{\text{rel}}I), \quad (6.11)$$

see e.g. Ref. [302]. For vanishing values of the integral, the integration time then heavily depends on the value chosen for the desired absolute accuracy. When looping over ranges of kinematic invariants, points below threshold have a zero imaginary part. This can artificially increase the computation times, if the absolute accuracy goal was set to a reasonable, but small value. This artifact can be circumvented by setting the lowest threshold symbolically when specifying the integrand. This new feature is incorporated in SECDEC, switching off the contour deformation below the user-defined threshold. Hence, unnecessarily long calculations are avoided in kinematic regions where the imaginary part is known to be zero.

The other selectable parameters are described in the manuals of the different numerical integrators, BASES [305] and the CUBA LIBRARY [302, 303], and in the user manual in App. A.2. Regarding the advantages of these integrators, BASES is a Fortran compatible Monte Carlo integrator that allows for a sequential evaluation only. In the sequential mode it is fast, producing reliable results. The four integrators included in the CUBA LIBRARY can run in parallel mode and are usable with Fortran and C/C++. While Vegas gives very stable results and tends to overestimate the numerical integration uncertainty, Divonne is extremely adaptive but occasionally underestimates integration uncertainties. The latter is very useful for very complicated integrands and is especially good in regions close to a threshold. Suave is heuristically found to converge slowly, but gives very stable results. While Vegas, Suave and Divonne are mainly Monte Carlo integrators which can sample pseudo and quasi-random numbers, Cuhre is a fully deterministic integrator, able to reach high accuracy if the integrand is comparatively simple.

In the integration phase, SECDEC allows for different choices regarding the number of integrands to be summed before integration. Setting *togetherflag=0* and *grouping=0* at the same time leads to the separate integration of each sector in all different pole structures  $P_{iljkh}$  and orders *ord* in the regulator  $\varepsilon^{ord}$ . Here *i* denotes the number of logarithmic poles, *j* the number of linear poles and *k* the number of higher poles in  $\varepsilon$ . The summation of some integrand files before integration is enabled by entering the allowed summed size of the grouped files in bytes, e.g. *grouping=2000000* corresponds to a grouping of integrands with a maximal total file size of around 2 MB. Switching on *togetherflag=1*, all integrands leading to the full coefficient of a certain order in the regulator are first summed up and then integrated numerically.

The uncertainty resulting from the Monte Carlo integration is expected to be bigger when each sector is integrated individually before summing up all sectors. Yet, the difference turns out not to be large, as the numerical integrator can tackle single functions much better and yield more accurate results. Grouping files before integration can also lead to a faster convergence if the integrand contains highly oscillating terms which cancel



each other out, but will in general slow down the numerical calculation if the polynomial structure is rather smooth.

## 6.4 Operational sequence

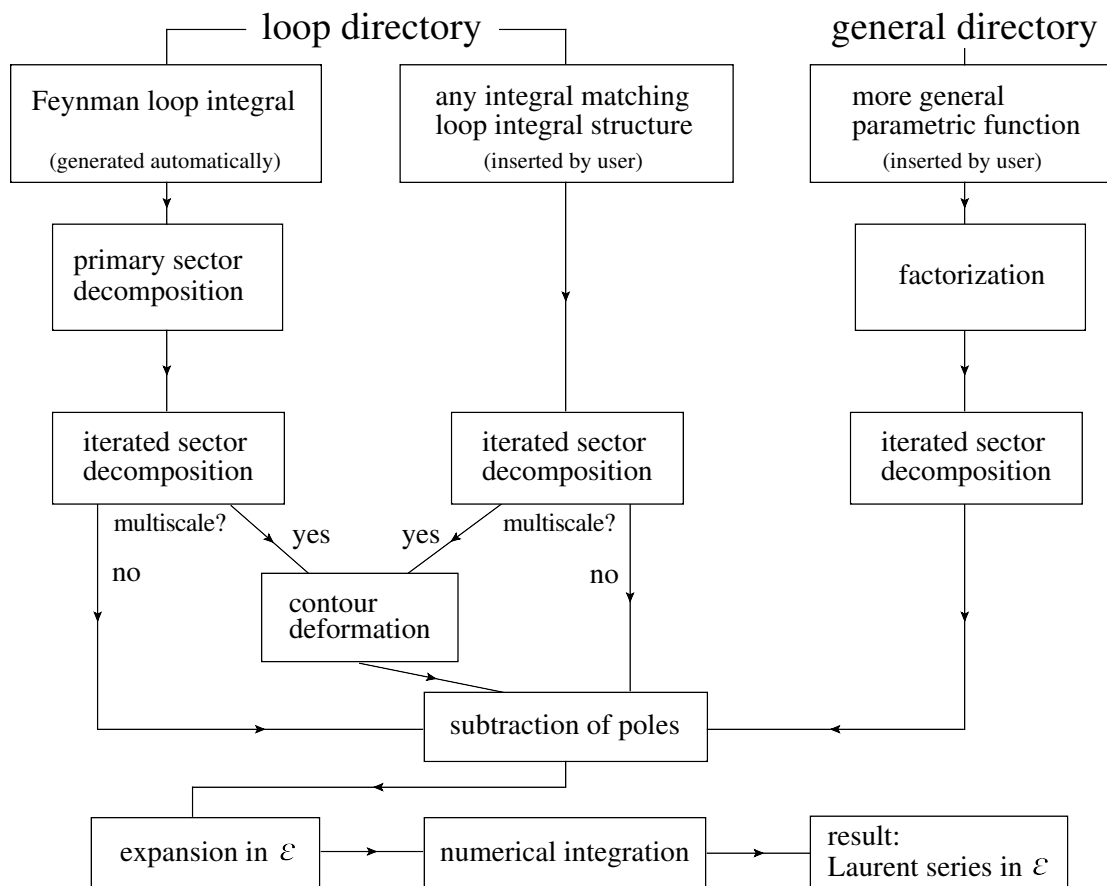


Figure 6.1: The operational sequence of SECDEC. This flowchart shows the main steps the program performs to produce the result as a Laurent series in the regulator  $\varepsilon$ .

The program is divided into two main directories, **loop** and **general**, respectively. They have the same global structure, only individual files are specific to either loop integrals and integrals of loop structure or to more general parametric functions. The directories contain a number of Perl scripts steering Mathematica [306] modules (located in the subdirectory **src**), writing the files necessary for numerical integration and executing them. The scripts use further Perl modules contained in the subdirectory **perlsrc**.

To calculate a loop integral within the standard or user-defined setup, the user needs to enter the `loop` directory in SECDEC, while for the computation of parameter integrals the user is referred to the `general` directory. When operating SECDEC in either of the two directories, the program works through algebraic and numerical parts. The algebraic part uses Mathematica code and performs the sector decomposition, the subtraction of the singularities, the expansion in  $\varepsilon$  and the generation of the files necessary for the numerical integration. In the numerical part, Fortran or C++ functions forming the coefficient of each Laurent series term in  $\varepsilon$  are integrated using the Monte Carlo integrators contained in the CUBA LIBRARY [302,303], BASES [305] or NINTEGRATE [306].

The flowchart of SECDEC shows the basic building blocks to calculate multi-loop or more general parametric integrals, see Fig. 6.1. The Mathematica source files are located in the subdirectories `src/deco` (files used for the decomposition), `src/subexp` (files used for the pole subtraction and expansion in  $\varepsilon$ ) and `src/util` (miscellaneous useful functions). The Robodoc [307] documentation is located in the subdirectory `doc`. It contains an index to look up a documentation of the source code in html format by loading `masterindex.html` into a browser. The program comes with example input and template files in the subdirectories `loop/demos` and `general/demos`, respectively. Further details on the installation and operation are found in App. A.2.1 and App. A.2.2.

## 6.5 Selection of checks and examples

In the following, two loop topologies are looked at in more detail. The first example is a two-loop three-point function which serves as the default graph when running SECDEC without an alteration of the `myparamfile.input`, `mytemplatefile.m` in the `loop` directory. The second example is the two-point two-loop function with five massive propagators. Different cases of numerators and numbers of mass scales are discussed. Further highly non-trivial two-loop examples are discussed in Chap. 7. For a detailed description of examples in the `general` directory, see the directory `SecDec/general/demos` and Refs. [1, 301, 304].

### 6.5.1 A two-loop three-point function

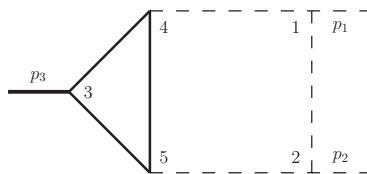


Figure 6.2: Two-loop vertex graph  $P_{126}$ , containing a massive triangle loop. Solid lines are massive, dashed lines are massless. The vertices are labeled to match the construction of the integrand from the topology as explained in the text.

In this example, three of the new features of SECDEC version 2 are demonstrated: the construction of the two Symanzik polynomials  $\mathcal{U}$  and  $\mathcal{F}$  from the topology of the graph and the evaluation of the graph in the physical region. Finally, it is shown how results for a whole set of different numerical values for the kinematic invariants can be produced and plotted in an automated way. The diagram under discussion is a two-loop three-point function, see Fig. 6.2. It has been studied extensively adopting either an analytical [308], or a numerical [309, 310] approach. The name for the diagram,  $P_{126}$ , was introduced in Ref. [308].

The template file `templateP126.m` in the `loop/demos` subdirectory contains the following lines

```
proplist = {{ms[1],{3,4}},{ms[1],{4,5}},{ms[1],{5,3}},{0,{1,2}},{0,{1,4}},{0,{2,5}}};
```

```
onshell = {ssp[1] → 0,ssp[2] → 0,ssp[3] → sp[1,2]};
```

where each entry in `proplist` corresponds to a propagator of the diagram; the first entry is the mass of the propagator and the second entry contains the labels of the two vertices which the propagator connects. The labels for the vertices are as shown in Fig. 6.2. For vertices containing only internal propagators the labeling is arbitrary. The `onshell` conditions in the above example state that  $p_1^2 = p_2^2 = 0$ ,  $p_3^2 = s_{12} = s$ . Results for the finite  $\varepsilon^0$  part of graph  $P_{126}$  agree very accurately with the analytic prediction, compare Fig. 6.3. The calculation time for the numerical integration of the finite part is

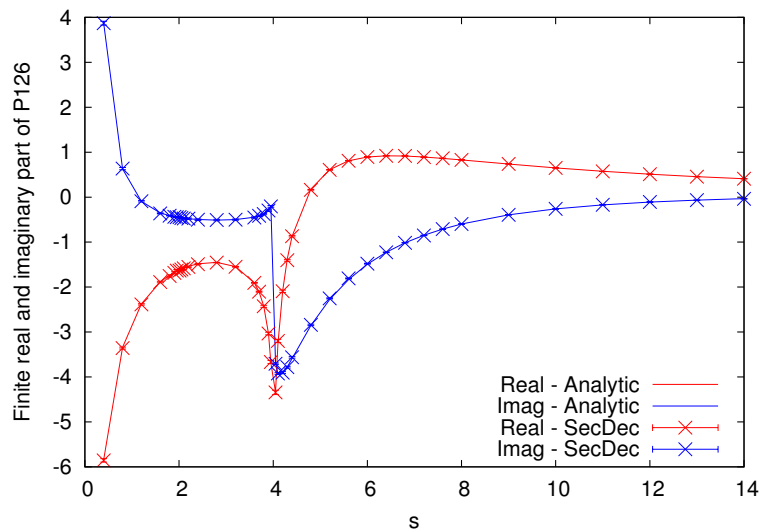


Figure 6.3: Comparison of analytic and numerical results for the diagram  $P_{126}$  using  $m^2 = 1$  and varying  $s$ . Due to the high accuracy of the numerical integration, error bars are barely seen.

around 5 secs, for a relative accuracy of about 1% and an absolute accuracy of  $10^{-5}$  using the integrator Divonne of the CUBA LIBRARY. This is for a typical point far from the  $s = 4m^2$  threshold on an Intel® Core™ i7-2600 CPU at 3.40GHz using two cores. For

a point close to threshold ( $s/m^2 = 3.9$ ), the timings are similar. To run this example, from the `loop` directory, issue the command `./launch -d demos -p paramP126.input -t templateP126.m`. The diagram  $P_{126}$  can also be computed using the user-defined setup, see App. A.2.6 for a detailed explanation.

### Producing data files for sets of numerical values

To loop over a set of numerical values for the invariants  $s$  and  $m^2$  once the C++ files are created, issue the command

```
'perl multinumericsloop.pl -d demos -p multiparamP126.input'
```

This will run the numerical integrations for the values of  $s$  and  $m^2$  specified in the file `demos/multiparamP126.input`. The files containing the results will be found in `demos/2loop/P126`, and the files `p-2.gpdat`, `p-1.gpdat` and `p0.gpdat` will contain the data files for each point, corresponding to the coefficients of  $\varepsilon^{-2}$ ,  $\varepsilon^{-1}$  and  $\varepsilon^0$ , respectively. These files can be used to plot the numerical results using gnuplot, see Fig. 6.3 for an exemplary result.

The same steps can be performed using the user-defined option, where the command reads `'perl multinumericsuserdefined.pl -p multiparamuserdefined.input'` and where the values for  $s$  and  $m^2$  are given in the `multiparamuserdefined.input` file.

### 6.5.2 Massive tensor two-loop two-point functions

In this subsection the option to evaluate integrals with a non-trivial numerator is demonstrated by calculating two-loop two-point functions involving different mass scales. This implies that a reduction to only scalar (master) integrals is not necessarily needed. The

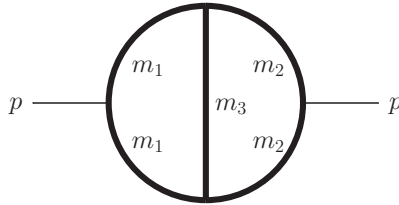


Figure 6.4: Two-loop bubble diagram with different masses

exemplary diagram considered here contains up to four different scales, see Fig. 6.4. As an example, a non-trivial numerator a coefficient function resulting from a rank three integral Lorentz decomposition is chosen

$$\mathcal{G}_B = \left( \frac{1}{i\pi^{\frac{D}{2}}} \right)^2 \int d^D k_1 d^D k_2 \frac{(k_1 \cdot k_2)(k_1 \cdot p_1)}{D_1 \dots D_5}, \quad (6.12)$$

$$D_1 = k_1^2 - m_1^2, \quad D_2 = (k_1 + p_1)^2 - m_1^2, \quad D_3 = (k_1 - k_2)^2 - m_3^2, \quad (6.13)$$

$$D_4 = (k_2 + p_1)^2 - m_2^2, \quad D_5 = k_2^2 - m_2^2, \quad (6.14)$$

where the causal  $i\delta$  prescription is omitted. The fact that this tensor integral is reducible does not play a role here, as the purpose is to demonstrate that a reduction may become obsolete, when considering the short integration times for the tensors.

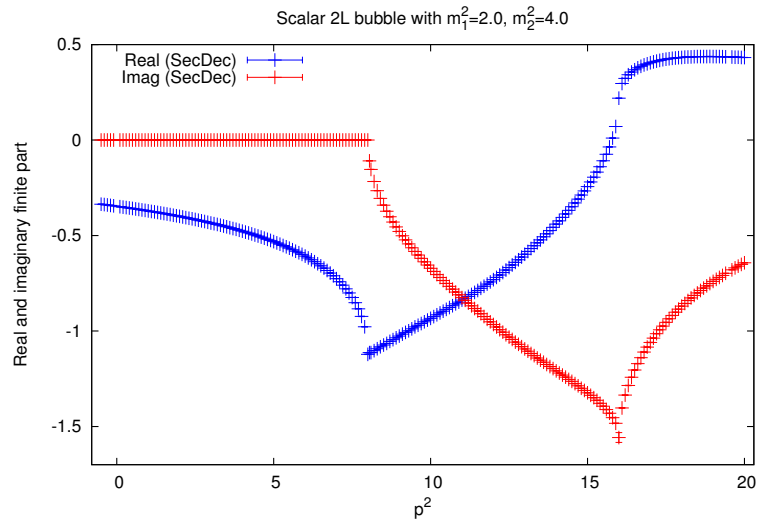
Results for the scalar and tensor integrals with  $m_3 = 0$  are shown in Fig. 6.5, while results for  $m_3^2 = 3$  are shown in Fig. 6.6.

The timings are expected to be higher for the rank three coefficient function because its leading pole is of order  $\mathcal{O}(\varepsilon^{-2})$ , while the scalar integral is finite. In the case of finite integrals, less functions need to be integrated, leading to a faster result. A comparison of the timings of the scalar massive two-point integrals with the rank three two-loop two-point coefficient function shows, that for values of  $p^2$  above the mass threshold at  $p^2 = 4m_2^2$ , the timings for the rank three integral coefficient function do not differ much from the ones for the scalar integrals, compare Fig. 6.7(a) for the  $m_3^2 = 0$  case and Fig. 6.7(b) for  $m_3^2 = 3$ . A relative accuracy of 0.1% and an absolute accuracy of  $10^{-5}$  was required for the Monte Carlo integration in scalar and rank 3 integrals alike. With the new feature of symbolically defining a threshold below which the contour deformation is switched off, unnecessarily long calculations are avoided in kinematic regions where the imaginary part is known to be zero. In the case of the rank three two-loop bubble with two masses, no threshold appears in the  $\mathcal{O}(\varepsilon^{-2})$  coefficient, a threshold at  $p^2 = 4m_2^2$  appears in the sub-leading pole and the lowest threshold of the finite part is located at  $p^2 = 4m_1^2$ . As only the lowest threshold is incorporated in the user-definition, the computing times of this integral are largest, where the imaginary part in the pole coefficients is zero, compare Fig. 6.7(a) and Sec. 6.3.8. The minimal numerical integration time for a kinematic point below threshold is 0.6ms for the scalar two-loop bubble with  $m_3^2 = 0$ . Above threshold, the scalar two-loop bubble integrals minimally take 0.1secs for  $m_3^2 \neq 0$  and 0.03secs for  $m_3^2 = 0$ . In Fig. 6.7(b), a small peak in the timings can be observed for  $p^2 = 12$ . When solving the Landau equations for the two-loop two-point function with two masses, a sub-threshold can be detected at exactly  $p^2 = 12$ . Given this observation, it may sometimes be of interest to have a closer look at the timings and possibly learn something about the singularity structure of the integrand.

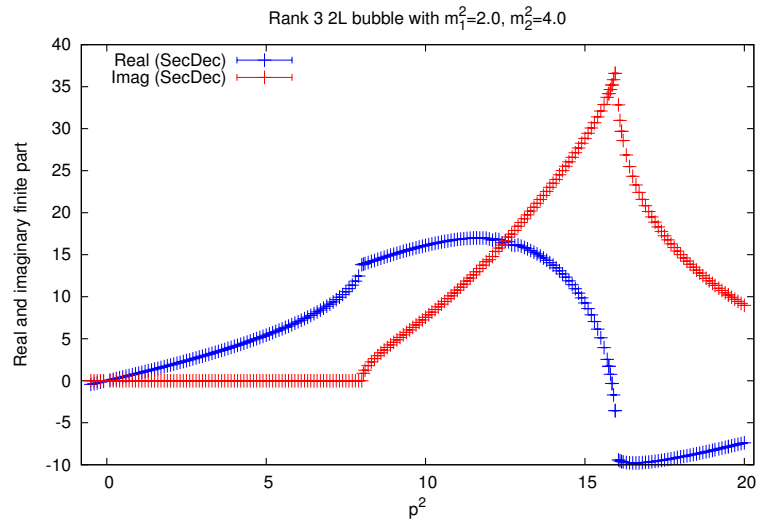
## 6.6 Future developments

The upgraded version 2 of the program SECDEC was presented. The main new feature, an implementation of an automated deformation of the integration contour to analytically continue the integrand, was described along with other new capabilities. It allows for the computation of multi-loop integrals with in principle no limitation on the number of scales involved. Examples to show its full power are discussed in Chap. 7, where numerical results for diverse two-loop four-point topologies are shown.

Although comparatively fast, the numerical evaluation of multi-loop diagrams can, in general, still not compete with the evaluation time of analytical results. Including



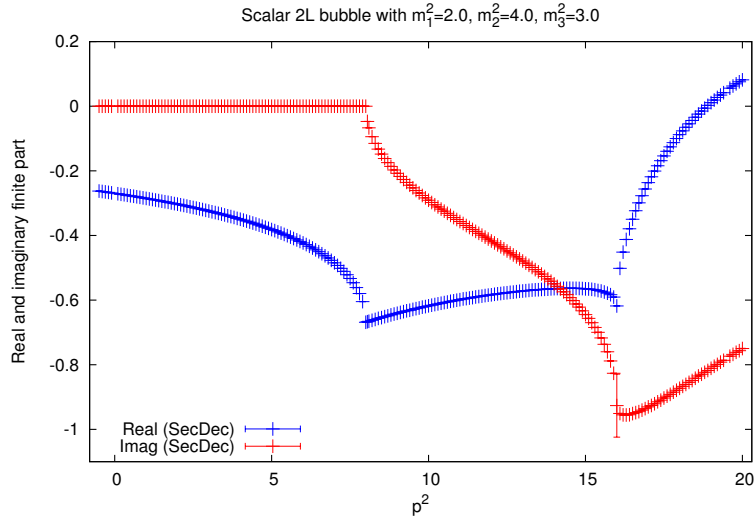
(a) scalar integral



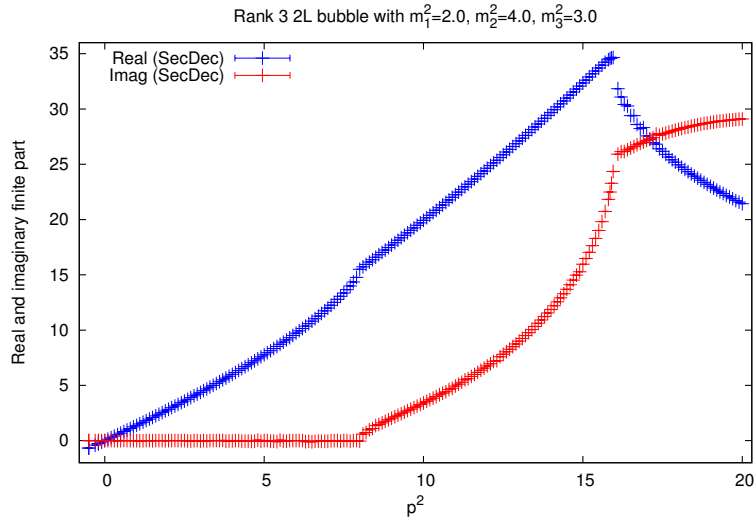
(b) rank 3 tensor integral

Figure 6.5: Results for the real (blue) and imaginary (red) parts of the two-loop two-point topology of Fig. 6.4 are shown in the scalar case (a) and for the the rank three coefficient function  $\mathcal{G}_B$  (b) with numerator  $(k_1 \cdot k_2)(k_1 \cdot p_1)$ . The masses are  $m_1^2 = 2, m_2^2 = 4, m_3 = 0$ .

more analytical calculations would therefore be very beneficial. A future version of the program could therefore integrate functions analytically where possible. Especially for the pole parts, the integration of several Feynman parameters prior to numerical



(a) scalar integral



(b) rank 3 tensor integral

Figure 6.6: Results for the real (blue) and imaginary (red) parts of the two-loop two-point topology of Fig. 6.4 are shown for three non-vanishing masses in the scalar case (a) and for the the rank three coefficient function  $\mathcal{G}_B$  (b) with numerator  $(k_1 \cdot k_2)(k_1 \cdot p_1)$ . The masses are  $m_1^2 = 2$ ,  $m_2^2 = 4$ ,  $m_3^2 = 3$ .

integration is feasible. This can lead to a significant decrease in the numerical integration times, as became apparent in the discussion of the timings in Sec. 6.5.2.

Furthermore, a decrease in the numerical integration times can be achieved using the

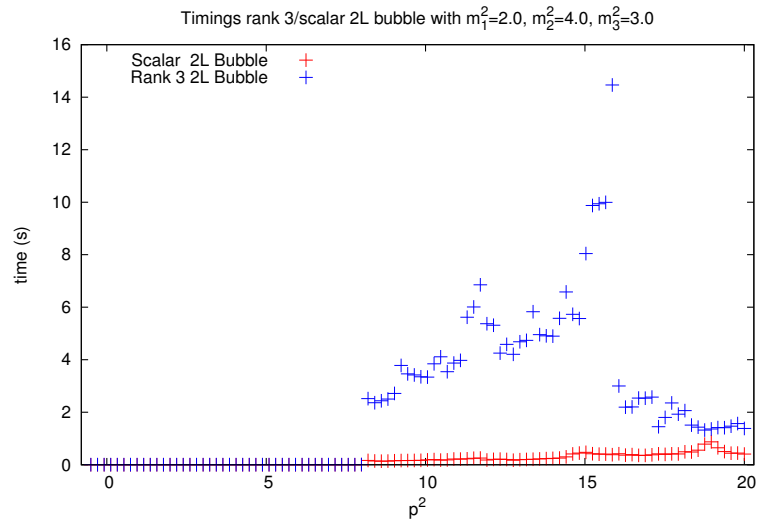
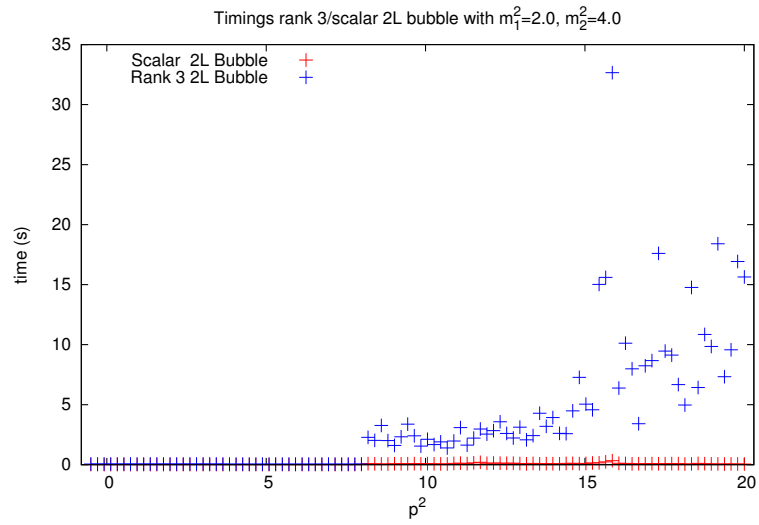


Figure 6.7: Comparison of evaluation times between scalar and rank three tensor integrals corresponding to a two-loop two-point function with (a) two, and (b) three masses. The red points are the evaluation times in seconds for the scalar integral at a given kinematic point, the timings for the rank three tensor integral are marked in blue. The timings were obtained on computers with Intel i7 processors and 4 cores.



fastest Monte Carlo integrator available for one-dimensional parameter representations, QUADPACK which is included in the GNU scientific library. Currently, the integrators Vegas or Suave are used in such cases, although they only rise to their full power when multiple integration parameters are involved.

Another missing piece, as mentioned in Sec. 4.2.3, is the implementation of an algorithm which is guaranteed to stop. It should set in automatically (if not already chosen in the beginning) when the heuristic algorithm runs into an infinite recursion.

Although some of the mentioned new features are already implemented in a private version of the code, they will be made publicly available as a whole in version 3 of SECDEC.

Besides new features accelerating SECDEC, further technological developments are needed, e.g., for kinematic configurations very close to pinch singularities. An extensive treatment of line singularities within the integration region or singularities appearing close to the endpoints of the integration region is still to be found.

Beyond improvements on the computation of the multi-loop integrals, interfaces to other programs are highly desirable. For example, the construction of interfaces to existing amplitude reduction programs would mean another cornerstone towards the long-term goal of assembling a highly automated program for the computation of processes beyond one loop.



# 7 | Non-planar two-loop four-point integrals with external or internal masses

In this chapter, the program SECDEC is used to make predictions for two-loop four-point integrals, with massive external legs and/or massive internal propagators, see Fig. 7.1. The diagrams considered are non-planar with a single planar case. The focus lies on the non-planar diagrams as they are usually more complicated. In this way the power of the program SECDEC can be explored and its limits extended. Contrary to analytical calculations, where several mass scales lead to unaccessible elliptic integrals, the limits for numerical integration are rather reached when spurious higher than logarithmic divergences occur. Such spurious divergences lead to more complicated subtraction terms which in turn may lead to numerical instabilities if the divergence canceling terms are not fully resolved by the numerical integrator.

Such spurious divergences appear, for example, in the case of the non-planar seven-propagator two-loop topology with a massive bracket/square bend and all other lines massless, see Fig. 7.1(a). To achieve a convenient representation for this integral (termed  $ggtt_2$ ), analytical transformations are performed prior to starting the sector decomposition algorithm; this way reducing the number of produced sub-sectors, leading to improved numerical behavior.

The  $ggtt_2$  diagram is the most complicated master topology occurring in the computation of the light fermionic two-loop corrections of  $t\bar{t}$  production in the  $gg$  channel. Analytic results are available, see Ref. [69,81]. Conversely, the master topology containing a massive sub-loop (termed  $ggtt_1$ , see Fig. 7.1(b)) is not available in analytic form. It enters the heavy fermionic corrections to top-quark pair production in the gluon fusion channel. While the leading pole of  $ggtt_2$  is of the order  $\mathcal{O}(1/\varepsilon^4)$ , and intermediate expressions during sector decomposition show (spurious) pole structures with a higher-than-logarithmic degree of divergence, the integral  $ggtt_1$  has only finite contributions. The same is true for the all-massive two-loop diagrams  $M_7^{\text{P}}$  and  $M_7^{\text{NP}}$ , where "P" refers to planar and "NP" to non-planar, see Figs. 7.1(c) and 7.1(d). To show the predictive power of the program, the  $M_7^{\text{P}}$  diagram is shown in a toy mass configuration with thirteen mass scales, a configuration which is not even close to being accessible in an analytic calculation. To compare with other numerical predictions, the two all-massive

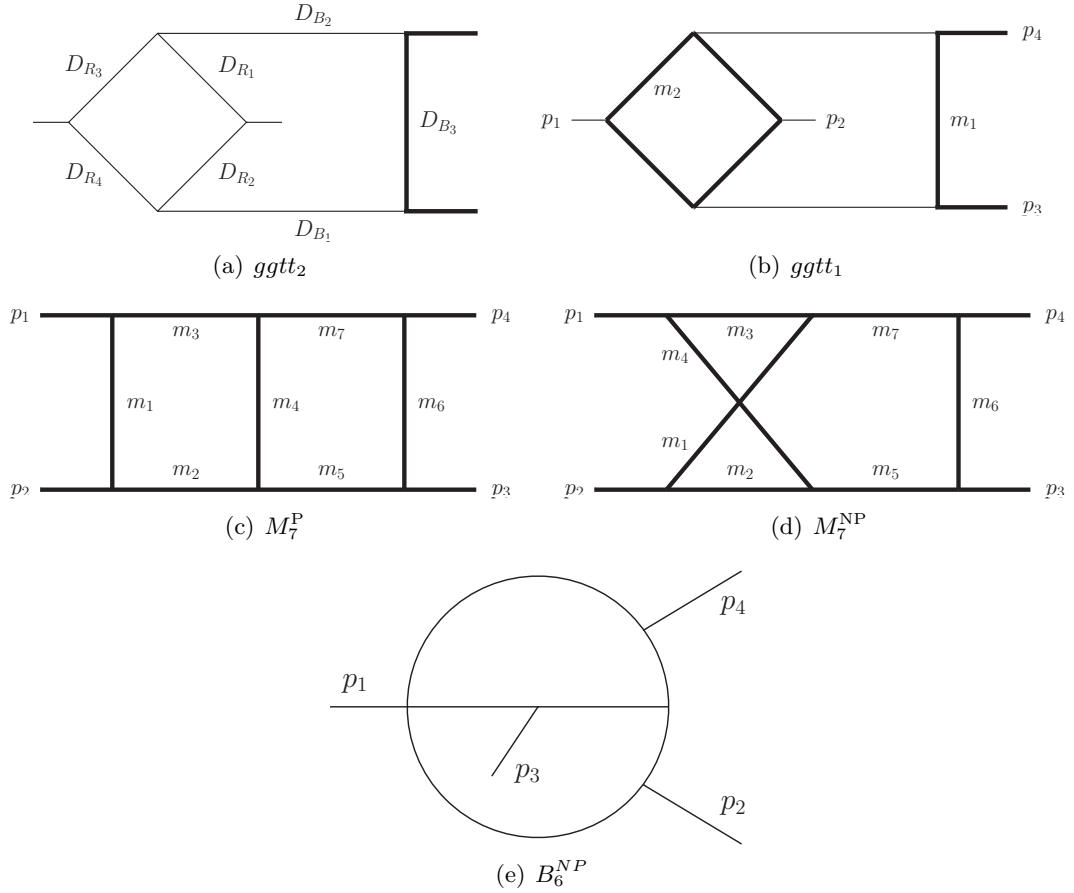


Figure 7.1: All diagrams considered in this chapter: the massive non-planar two-loop box diagrams entering the light (a) and heavy (b) fermionic correction to the  $gg$  channel, the all-massive planar  $M_7^P$  (c) and non-planar  $M_7^{NP}$  (d) seven-propagator diagram and the non-planar six-propagator diagram  $B_6^{NP}$  (e). The thick lines denote massive particles.

diagrams are also shown with three different scales involved. Lastly, a prediction for the non-planar six-propagator diagram of Fig. 7.1(e) is made, studied in the massless case by Tausk, see Ref. [201].

The diagrams  $B_6^{NP}$ ,  $gg_{tt_1}$ ,  $M_7^P$  and  $M_7^{NP}$  are evaluated with SECDEC 2.1 in a fully automated way. Apart from scalar master integrals, results for an irreducible tensor integral of rank two for the  $gg_{tt_1}$  diagram are given. In the case of the  $gg_{tt_2}$  diagram it is advantageous to make some analytical manipulations beforehand. The results, presented in Ref. [2] were useful as checks in the analytic result presented in Ref. [81].

The structure of this chapter is as follows: in Sec. 7.1, an expression serving as a starting point for evaluating the  $gg_{tt_2}$  diagram is derived, and a novel type of transfor-

mation is described which can be used to reduce the number of sector decompositions and improve numerical stability. To check consistency, the expected thresholds are derived from the Landau equations, see Sec. 7.2. In Sec. 7.3, numerical results are given for all four-point diagrams previously described, where the dependence of the evaluation on the number of mass scales, the singularity structure and integrals of higher rank are explored.

## 7.1 Analytical preparation of the non-planar seven propagator integral $ggtt_2$

This section explores the possibilities arising from a mixed approach, where reformulating the integral before sector decomposition algorithm can lead to a large gain in numerical efficiency. The  $ggtt_2$  diagram has four poles in the regulator  $\varepsilon$  and two spurious linear divergences in the Feynman parameters of the type  $t_i^{-2-\varepsilon}$ . The available numerical integrators can deal with logarithmic divergences efficiently, while the convergence of higher-than-logarithmic singularities depends heavily on the kinematics and the number of Feynman parameters involved.

After integrating out the  $\delta$ -constraint, the sub-sector functions of the  $ggtt_2$  diagram contain six Feynman parameters and subtraction terms from two spurious linear divergences. The numerical integrator fails convergence in this case. Decreasing the number of Feynman parameters or the degree of divergence would therefore be beneficial. Methods for the latter are already implemented by means of integration by parts, where the exponent of a factorized pole is increased. Though a solution for many integrand topologies, the tradeoff in the case of  $ggtt_2$  are long decomposition times (approximately one week on a multi-core, 16 GB computer), resulting in an order of  $\mathcal{O}(6000)$  functions to be integrated. Integrating so many expressions leads to computational problems: either large cancellations when terms are integrated in isolation, or memory/convergence issues when terms are grouped by summation prior to integration.

Below, a different approach is presented, reducing the number of Feynman parameters, the degree of divergence and the total number of functions to be integrated numerically. It is based on Ref. [2]. Firstly, a representation where one integration parameter of the  $ggtt_2$  diagram factorizes naturally is derived, such that it can be integrated out analytically. A subsequent remapping and the application of the recently introduced backwards transformation [2] to single sectors allows for an automated evaluation in arbitrary kinematics. The new feature allowing for a treatment of user-defined functions in the program SECDEC was developed for this particular computation and is explained in Sec. 6.3.1. It was tested, that an important byproduct of the backwards transformation is the reduction in the total number of functions by two thirds to be integrated numerically, compared to the initial sector decomposition approach and without usage of integration by parts relations.

### 7.1.1 Integration in a sub-loop

The expression for the scalar integral  $ggtt_2$  in momentum space is given by

$$\mathcal{G}_{ggtt_2} = \left( \frac{1}{i\pi^{\frac{D}{2}}} \right)^2 \int \frac{d^D k_1 d^D k_2}{D_{R_1} D_{R_2} D_{R_3} D_{R_4} D_{B_1} D_{B_2} D_{B_3}} \quad (7.1)$$

where  $D = 4 - 2\varepsilon$ . The Feynman propagators  $D_{R_i}$  corresponding to the ‘‘rhombus’’ sub-loop in Fig. 7.1(a) are given by

$$D_{R_1} = (k_1 - k_2)^2 + i\delta, \quad D_{R_2} = (k_1 - k_2 + p_2)^2 + i\delta, \quad (7.2a)$$

$$D_{R_3} = (k_2 + p_4)^2 + i\delta, \quad D_{R_4} = (k_2 + p_1 + p_4)^2 + i\delta, \quad (7.2b)$$

where the  $p_i$  are the external momenta with  $p_3^2 = p_4^2 = m^2$  and  $p_1^2 = p_2^2 = 0$ , and  $k_1, k_2$  are the loop momenta. All external momenta are assumed to be ingoing. Integrating out the loop momentum  $k_2$  first, we are left with an expression containing only  $k_1$  and external momenta, to be combined with the propagators

$$D_{B_1} = (k_1 - p_3)^2 + i\delta, \quad D_{B_2} = (k_1 + p_4)^2 + i\delta, \quad D_{B_3} = k_1^2 - m^2 + i\delta. \quad (7.3)$$

This procedure is not limited to our particular example, but requires an analytical step of introducing a convenient parametrization which can not be found when the sub-loop contains massive propagators. For the rest of this chapter, the causal  $i\delta$  will be omitted and the renormalization scale is set to  $\mu_R = 1$  for simplicity.

The introduction of Feynman parameters for the one-loop subgraph  $\mathcal{I}_R$  constructed from all propagators containing the loop momentum  $k_2$  leads to

$$\begin{aligned} \mathcal{I}_R &= \frac{1}{i\pi^{D/2}} \int \frac{d^D k_2}{D_{R_1} D_{R_2} D_{R_3} D_{R_4}} \\ &= \Gamma(2 + \varepsilon) \int \prod_{i=1}^4 dx_i \delta\left(1 - \sum_{j=1}^4 x_j\right) \mathcal{F}(\vec{x}, k_1)^{-2-\varepsilon}, \end{aligned} \quad (7.4)$$

with the second Symanzik polynomial reading

$$-\mathcal{F}(\vec{x}, k_1) = D_{B_1} x_1 x_2 + (k_1 + p_1 + p_4)^2 x_1 x_3 + (k_1 + p_2 + p_4)^2 x_2 x_4 + D_{B_2} x_3 x_4. \quad (7.5)$$

During integration of the  $\delta$ -distribution in Eq. (7.4), the first Symanzik polynomial reduces to unity. The substitutions

$$x_1 = t_2(1 - t_3), \quad x_2 = t_1 t_3, \quad x_3 = (1 - t_1)t_3, \quad (7.6)$$

facilitate a factorization of the parameter  $t_3$  which is integrated out analytically. This yields

$$\mathcal{I}_R = -\frac{2}{\varepsilon} \frac{\Gamma(2 + \varepsilon)\Gamma^2(1 - \varepsilon)}{\Gamma(1 - 2\varepsilon)} \int_0^1 dt_1 \int_0^1 dt_2 \tilde{\mathcal{F}}(\vec{t}, k_1)^{-2-\varepsilon} \quad (7.7)$$

with

$$-\tilde{\mathcal{F}}(\vec{t}, k_1) = D_{B_1} t_1 t_2 + (k_1 + p_1 + p_4)^2 t_1 \bar{t}_2 + (k_1 + p_2 + p_4)^2 \bar{t}_1 t_2 + D_{B_2} \bar{t}_1 \bar{t}_2, \quad (7.8)$$

where the shorthand notation  $\bar{t}_i = 1 - t_i$  is introduced. The expression for the 1-loop rhombus  $\mathcal{I}_R$  is combined with the remaining  $k_1$ -dependent propagators, treating the expression of Eq. (7.8) as a fourth propagator with power  $2 + \varepsilon$ , to obtain,

$$\mathcal{G}_{NP} = \frac{2}{\varepsilon} \frac{\Gamma(3 + 2\varepsilon)\Gamma^2(1 - \varepsilon)}{\Gamma(1 - 2\varepsilon)} \int_0^1 dt_1 \int_0^1 dt_2 \times \prod_{i=1}^4 \int_0^1 dz_i z_i^{1+\varepsilon} \delta(1 - \sum_{j=1}^4 z_j) \mathcal{F}_{NP}(\vec{z}, t_1, t_2)^{-3-2\varepsilon} \mathcal{U}_{NP}(\vec{z})^{1+3\varepsilon} \quad (7.9)$$

after integration of  $k_1$  and where

$$\mathcal{U}_{NP}(\vec{z}) = \sum_{j=1}^4 z_j \quad \text{and} \quad (7.10)$$

$$\mathcal{F}_{NP}(\vec{z}, t_i) = -s_{12}z_2z_3 - Tz_1z_4 - S_1z_2z_4 - S_2z_3z_4 + m^2z_1(z_1 + z_4Q), \quad (7.11)$$

with

$$T = s_{13}\bar{t}_1t_2 + s_{23}t_1\bar{t}_2, \quad S_1 = s_{12}t_1t_2, \quad S_2 = s_{12}\bar{t}_1\bar{t}_2 \\ Q = t_1\bar{t}_2 + \bar{t}_1t_2, \quad s_{ij} = (p_i + p_j)^2. \quad (7.12)$$

The full integral  $\mathcal{G}_{NP}$  is in total one Feynman parameter short. A primary sector decomposition in the newly introduced Feynman parameters  $z_1, \dots, z_4$  is performed to obtain

$$\mathcal{G}_{NP} = \frac{2}{\varepsilon} \frac{\Gamma(3 + 2\varepsilon)\Gamma^2(1 - \varepsilon)}{\Gamma(1 - 2\varepsilon)} \int_0^1 dt_1 \int_0^1 dt_2 \sum_{i=1}^4 G_{NP}^i, \quad (7.13)$$

with

$$G_{NP}^1 = \int_0^1 dz_2 dz_3 dz_4 z_4^{1+\varepsilon} (1 + z_2 + z_3 + z_4)^{1+3\varepsilon} \mathcal{F}^1(\vec{z}, t_i)^{-3-2\varepsilon}, \quad (7.14a)$$

$$\mathcal{F}^1(\vec{z}, t_i) = -s_{12}z_2z_3 - Tz_4 - S_1z_2z_4 - S_2z_3z_4 + m^2(1 + z_4Q), \quad (7.14b)$$

$$G_{NP}^2 = \int_0^1 dz_1 dz_3 dz_4 z_4^{1+\varepsilon} (1 + z_1 + z_3 + z_4)^{1+3\varepsilon} \mathcal{F}^2(\vec{z}, t_i)^{-3-2\varepsilon}, \quad (7.14c)$$

$$\mathcal{F}^2(\vec{z}, t_i) = -s_{12}z_3 - Tz_1z_4 - S_1z_4 - S_2z_3z_4 + m^2z_1(z_1 + z_4Q), \quad (7.14d)$$

$$G_{NP}^3 = \int_0^1 dz_1 dz_2 dz_4 z_4^{1+\varepsilon} (1 + z_1 + z_2 + z_4)^{1+3\varepsilon} \mathcal{F}^3(\vec{z}, t_i)^{-3-2\varepsilon}, \quad (7.14e)$$

$$\mathcal{F}^3(\vec{z}, t_i) = -s_{12}z_2 - Tz_1z_4 - S_1z_2z_4 - S_2z_4 + m^2z_1(z_1 + z_4Q), \quad (7.14f)$$

$$G_{NP}^4 = \int_0^1 dz_1 dz_2 dz_3 (1 + z_1 + z_2 + z_3)^{1+3\varepsilon} \mathcal{F}^4(\vec{z}, t_i)^{-3-2\varepsilon}, \quad (7.14g)$$

$$\mathcal{F}^4(\vec{z}, t_i) = -s_{12}z_2z_3 - Tz_1 - S_1z_2 - S_2z_3 + m^2z_1(z_1 + Q), \quad (7.14h)$$

where the  $\delta$ -distribution is naturally integrated out.

Observing the primary sectors, the first sector  $\mathcal{F}^1(\vec{z}, t_i)$  is of the form  $m^2 + \text{func}(z_i, t_i)$ , and does not need iterations of the decomposition into further sectors. Primary sector three can be remapped to primary sector two by exchanging  $z_2 \leftrightarrow z_3$  and  $S_1 \leftrightarrow S_2$ . The sectors two and four are therefore the only ones needing further treatment. This is a benefit from the prior integration of one sub-loop of the full integral. This treatment has a small drawback though: with the introduction of the substitutions in Eq. (7.6), singularities at the second endpoint are introduced. The integrals  $G_{NP}^{2,3,4}$  can diverge both at zero and one in  $t_1$  and  $t_2$ . With the sector decomposition algorithm, only singularities at zero are factorized automatically. Consequently, the singularities located at the upper integration limit are remapped to the origin of parameter space by splitting the integration region at  $\frac{1}{2}$  and transforming the integration variables to remap the integration domain to the unit hypercube, see Sec. 6.3.7.

This procedure results in 12 integrals, some of which are already finite, such that no subsequent sector decomposition is required. Other integrals lead to linear divergences of the type  $\int_0^1 dx x^{-2-\varepsilon}$  in two Feynman parameters after sector decomposition. These singularities are spurious and can be subtracted by expanding the Taylor series in the subtraction procedure up to the second term, see Sec. 4.1.3. This procedure is prone to introducing large cancellations between subtraction terms and a large number of sectors and therefore challenges numerical stability. Avoiding this type of singularity from scratch is therefore a highly desirable goal.

The next subsection describes a strategy which can help to reduce the number of higher than logarithmic divergences and functions to be integrated numerically.

### 7.1.2 Backwards transformation

The aim of the procedure described in this section is to achieve a transformation of potential linear divergences into logarithmic divergences as far as possible. A different procedure towards this goal based on integration-by-parts identities, has been described in Ref. [301] and Sec. 6.3.4. The latter method however can increase the number of functions to be integrated substantially, while the method described below in general reduces the number of further iterations and therefore the number of produced functions. Yet another method to reduce the number of functions produced during factorization has been suggested in Ref. [311], where a non-linear transformation in the Feynman parameters aims at a reduction of the exponent of the second Symanzik polynomial. Although an attractive idea, it was not beneficial in the case of the  $ggtt_2$  as further singularities at the upper integration limit are introduced with the transformation. A subsequent remapping of the divergences at the endpoint one to zero restores, or even deteriorates the original singularity structure with spurious linear divergences in two Feynman parameters.

Due to the fact that the iterated decomposition of the integral into sub-sectors introduces higher powers in the Feynman parameters, the desire to undo some of those decomposition steps before the final integration is rather natural. Yet, in most cases this is not possible without the introduction of unacceptable new divergences which have to



be subtracted before integration. Although it does not seem beneficial to “undo” single sector decomposition steps, there may still be a transformation that does a similar trick. Such a transformation was introduced and utilized by the author and collaborators in Ref. [2]. It relies on the possibility of blowing down an affine  $N$ -dimensional space as opposed to the blowing up used in the sector decomposition approach. After performing the blowing down, the splitting of the integration region as performed in the sector decomposition approach can be applied backwards. The original function is thereby split into two again. It may at first seem counter-intuitive to achieve a reduction in the number of sectors to be integrated, when a splitting of one primary sector using the backwards transformation doubles the number of functions. However, in spite of these arguments, it turns out that when applied in the right way, a reverse splitting of the integration region can rearrange the Feynman parameters, such that the double linear divergences of primary sectors two and three are transformed into logarithmic ones. This leads to an overall reduction in the number of functions describing  $G_{NP}$  by two thirds.

Below, the necessary preconditions for the application of such a backwards transformation and the transformation itself are analyzed in more detail.

### Preconditions

To explain the backwards transformation in more detail, it is convenient to recall the sector decomposition and highlighting the important aspects necessary for the transformation.

In the sector decomposition algorithm, the integration region is split into at least as many parts as there are integration variables. This splitting is done such that a clear and definite hierarchy can be observed among the integration parameters. As recollection, the example splitting of Sec. 4.1 reads

$$\begin{aligned} & \int_0^1 \int_0^1 dx_1 dx_2 \frac{1}{(x_1 + x_2)^{2+\varepsilon}} \\ &= \int_0^1 \int_0^1 dx_1 dx_2 \frac{1}{(x_1 + x_2)^{2+\varepsilon}} (\Theta(x_1 - x_2) + \Theta(x_2 - x_1)) , \end{aligned} \quad (7.15)$$

where it is evident that  $x_1$  in the first summand on the righthand side must always be bigger than  $x_2$ , otherwise the integral is zero. In the second summand of Eq. (7.15) the hierarchy between  $x_1$  and  $x_2$  is reversed. Both integrals in the second line of Eq. (7.15) are of definite hierarchy. In the sector decomposition example of Eqs. (4.1), a blowing up is applied to these two functions, leading to a factorization of the previously overlapping singularities. The hierarchy among the Feynman parameters is implicitly kept. Assuming one of the resulting functions with non-overlapping singularities to be the starting point of the backwards transformation, the sector decomposition of Eqs. (4.1) can be

reversed. It reads

$$\int_0^1 dx_1 \int_0^1 d\tilde{x}_2 \frac{1}{x_1^{1+\varepsilon}(1+\tilde{x}_2)^{2+\varepsilon}} \quad (7.16a)$$

$$= \int_0^1 dx_1 \int_0^{x_1} dx_2 \frac{1}{(x_1+x_2)^{2+\varepsilon}} \quad (7.16b)$$

$$= \int_0^1 dx_1 \int_0^1 dx_2 \frac{1}{(x_1+x_2)^{2+\varepsilon}} (\Theta(x_1-x_2) + \Theta(x_2-x_1)) \\ - \int_0^1 dx_2 \int_0^{x_2} dx_1 \frac{1}{(x_1+x_2)^{2+\varepsilon}} \quad (7.16c)$$

$$= \int_0^1 dx_1 \int_0^1 dx_2 \frac{1}{(x_1+x_2)^{2+\varepsilon}} - \int_0^1 dx_2 \int_0^1 d\tilde{x}_1 \frac{1}{x_2^{1+\varepsilon}(\tilde{x}_1+1)^{2+\varepsilon}} . \quad (7.16d)$$

Although the equations are just rearranged, the implications are different. While the factorization of singularities works due to the application of blowup sequences, here the prerequisite is the possibility of applying a blowing down. Looking at the transition from Eq. (7.16a) to Eq. (7.16b) more thoroughly, one finds

$$\int_0^1 \int_0^1 dx_1 d\tilde{x}_2 \frac{1}{x_1^{1+\varepsilon}(1+\tilde{x}_2)^{2+\varepsilon}} \quad (7.17a)$$

$$= \int_0^1 \int_0^1 dx_1 d\tilde{x}_2 \frac{1}{x_1^{1+\varepsilon}(1+\tilde{x}_2)^{2+\varepsilon}} \Theta(x_1 - x_1\tilde{x}_2) \quad (7.17b)$$

$$= \int_0^1 \int_0^1 dx_1 \frac{dx_2}{x_1} \frac{1}{x_1^{1+\varepsilon}(1+\frac{x_2}{x_1})^{2+\varepsilon}} \Theta(x_1 - x_2) \quad (7.17c)$$

$$= \int_0^1 dx_1 \int_0^{x_1} dx_2 \frac{1}{(x_1+x_2)^{2+\varepsilon}} . \quad (7.17d)$$

From Eq. (7.17b) to Eq. (7.17c) the integration parameters  $x_1$  and  $\tilde{x}_2$  are transformed as

$$x_1 \rightarrow x_1 , \quad (7.18a)$$

$$x_1\tilde{x}_2 \rightarrow x_2 . \quad (7.18b)$$

Having examined a symmetric and simple example, it should be noted that it is not trivial to a priori know that an equality of the type between Eqs. (7.17a) and (7.17b) indeed holds. In general polynomial integrals, the implicit hierarchies among the Feynman parameters must be made explicit through the introduction of Heaviside  $\Theta$  functions.

In the following, a realistic example is presented, uncovering the advantages of such a backwards transformation.

### Application to the $ggtt_2$

Returning to the non-planar double box integral  $G_{NP}$ , the following structure can be identified for the function of Eq. (7.14d) in sector two (and three) after remapping

$$I = \prod_{i=1}^N \left\{ \int_0^1 dt_i \right\} \left[ t_j \left( P(\vec{t}_{jk}) + t_k Q(\vec{t}_{jk}) \right) + R(\vec{t}_{jk}) \right]^{-\alpha}, \quad (7.19)$$

where  $N = 5$ ,  $t_j = z_4$  and  $t_k = z_1$  and  $\alpha > 0$ .  $P$ ,  $Q$  and  $R$  are polynomials of arbitrary degree in the Feynman parameters  $\vec{t}_{jk} = (t_1, \dots, \hat{t}_j, \dots, \hat{t}_k, \dots, t_N)$  and kinematic invariants. The carets denote those Feynman parameters which are *not* part of the vector of Feynman parameters. This definition of a vector of Feynman parameters with double index  $\vec{t}_{jk}$  will be used throughout this subsection.

In Eq. (7.19), all terms multiplied by the Feynman parameter  $t_k$  are also multiplied by the Feynman parameter  $t_j$ . An explicit hierarchy exists, allowing for a transformation of the type  $t_j t_k \rightarrow t_{\bar{k}}$ . The splitting of the integration region can be performed backwards as

$$I = \int_0^1 d\vec{t}_{\bar{k}} dt_{\bar{k}} \frac{1}{t_{\bar{k}}} \left[ t_j P(\vec{t}_{\bar{k}}) + t_{\bar{k}} Q(\vec{t}_{\bar{k}}) + R(\vec{t}_{\bar{k}}) \right]^{-\alpha} \quad (7.20a)$$

$$- \int_0^1 d\vec{t}_{\bar{j}\bar{k}} dt_{\bar{j}} dt_{\bar{k}} \frac{1}{t_{\bar{j}}} \left[ t_{\bar{k}} \left( t_{\bar{j}} P(\vec{t}_{\bar{j}\bar{k}}) + Q(\vec{t}_{\bar{j}\bar{k}}) \right) + R(\vec{t}_{\bar{j}\bar{k}}) \right]^{-\alpha}. \quad (7.20b)$$

To explain this in more detail, a rearrangement of the terms leads to the well-known sector decomposition

$$\int_0^1 d\vec{t}_{\bar{k}} dt_{\bar{k}} \frac{1}{t_{\bar{k}}} \left[ t_j P(\vec{t}_{\bar{k}}) + t_{\bar{k}} Q(\vec{t}_{\bar{k}}) + R(\vec{t}_{\bar{k}}) \right]^{-\alpha} \underbrace{[\Theta(t_j - t_{\bar{k}})]}_{(1)} + \underbrace{[\Theta(t_{\bar{k}} - t_j)]}_{(2)} \quad (7.21a)$$

$$= \int_0^1 d\vec{t} \left[ t_j \left( P(\vec{t}_{jk}) + t_k Q(\vec{t}_{jk}) \right) + R(\vec{t}_{jk}) \right]^{-\alpha} \quad (7.21b)$$

$$+ \int_0^1 d\vec{t}_{\bar{j}\bar{k}} dt_{\bar{j}} dt_{\bar{k}} \frac{1}{t_{\bar{j}}} \left[ t_{\bar{k}} \left( t_{\bar{j}} P(\vec{t}_{\bar{j}\bar{k}}) + Q(\vec{t}_{\bar{j}\bar{k}}) \right) + R(\vec{t}_{\bar{j}\bar{k}}) \right]^{-\alpha}, \quad (7.21c)$$

where  $t_{\bar{k}} \rightarrow t_j t_k$  was substituted in sector (1) and  $t_j \rightarrow t_{\bar{k}} t_{\bar{j}}$  in sector (2).

The effect of the backwards transformation is twofold: The degree of the polynomial in  $t_j t_k$  is reduced in Eq. (7.20a), and in Eq. (7.20b) the degree of divergence in  $t_j$  is reduced if  $\alpha > 1$ . It can be beneficial in the reduction of the number of functions as compared to the custom sector decomposition procedure, and can be particularly advantageous if the factor  $Q$  is much simpler than  $P$ .

After all transformations of this type, the result is a total of 15 functions partly needing an iterated sector decomposition. Together with the introduction of the new feature of *user-defined functions* in SECDEC 2.1 described in Sec. 6.3.1, the computation of the  $ggtt_2$  diagram is now possible in a reasonable amount of time. The timings are discussed in Sec. 7.3.1.

## 7.2 Expected thresholds from the Landau equations

Before turning to the numerical evaluation of the  $ggtt_2$  diagram and diverse other non-planar double box integrals, it should be analyzed roughly where the thresholds of the  $ggtt_2$  diagram are expected, to have a measure for the trustworthiness of the result. To this end, it is useful to analyze the Landau equations as described in Sec. 5.2, although the resulting singularities do not necessarily lead to a divergence in the integral. The first set of equations resulting from applying Eq. (5.3a) to  $ggtt_2$  reads

$$x_1 (k_1 - k_2)^2 = 0 , \quad (7.22a)$$

$$x_2 (k_1 - k_2 + p_2)^2 = 0 , \quad (7.22b)$$

$$x_3 (k_2 + p_4)^2 = 0 , \quad (7.22c)$$

$$x_4 (k_2 + p_1 + p_4)^2 = 0 , \quad (7.22d)$$

$$x_5 (k_1 + p_1 + p_2 + p_4)^2 = 0 , \quad (7.22e)$$

$$x_6 (k_1 + p_4)^2 = 0 , \quad (7.22f)$$

$$x_7 (k_1^2 - m^2) = 0 , \quad (7.22g)$$

where the  $k_i$  are again the loop momenta,  $p_i$  are the external momenta and  $m$  is the mass appearing in the propagators of the  $ggtt_2$  diagram. The second set of equations resulting from Eq. (5.3b) is

$$I : \quad x_1(k_1 - k_2)_\mu + x_2(k_1 - k_2 + p_2)_\mu + x_5(k_1 + p_1 + p_2 + p_4)_\mu + \\ x_6(k_1 + p_4)_\mu + x_7 k_{1\mu} = 0 , \quad (7.23a)$$

$$II : \quad -x_1(k_1 - k_2)_\mu - x_2(k_1 - k_2 + p_2)_\mu + x_3(k_2 + p_4)_\mu + \\ x_4(k_2 + p_1 + p_4)_\mu = 0 . \quad (7.23b)$$

Now, Eqs. (7.22a)-(7.22g) are either true when the  $x_i$  are vanishing or when the scalar products composed of the loop momenta  $k_i$  and external momenta  $p_i$  are either equal to a mass, see Eq. (7.22g) or vanish altogether. Now, if one Feynman parameter  $x_i$  is zero, the graph to be considered is a subgraph of the original one because the propagator connecting two vertices was removed. To analyze the singularities of the original graph it is therefore sufficient to assume  $x_i \neq 0 \forall i$ . This means, Eqs. (7.22a)-(7.22g) all serve as constraints on the scalar products to appear in Eq. (7.23a) and Eq. (7.23b) when contracting them with the loop  $k_i^\mu$  and respectively external momentum vectors  $p_i^\mu$ . Some of these are used to express the missing scalar products in terms of other scalar products. The resulting equations containing the Landau singularities for those sets of kinematic invariants and Feynman parameters for which the equations hold, then read

$$0 = s_{12} (x_1 x_5 - x_2 x_6) + x_7 \left[ x_1 (m^2 - s_{23}) + x_2 (m^2 - s_{12} - s_{23}) \right] , \quad (7.24a)$$

$$0 = s_{12} (x_2 x_5 - x_1 x_6) + x_7 \left[ x_2 (m^2 - s_{13}) + x_2 (m^2 - s_{12} - s_{13}) \right] , \quad (7.24b)$$

$$0 = s_{12} x_2 (x_1 - x_4) , \quad (7.24c)$$

$$0 = s_{12} x_1 x_2 , \quad (7.24d)$$

$$0 = s_{12} (x_1 x_3 - x_2 x_4) , \quad (7.24e)$$

$$0 = (s_{13} - m^2) x_2 x_3 + (s_{23} - m^2) x_1 x_4 + \\ (s_{13} + s_{23} - 2m^2) [x_5 (x_1 + x_3 + x_4) + x_2 (x_4 + x_5)] + \\ (-2m^2) x_7 (x_1 + x_2 + x_3 + x_4) , \quad (7.24f)$$

$$0 = s_{12} x_1 x_2 (x_1 + x_2) + (s_{12} + s_{13} - m^2) x_1 x_2 x_3 + (s_{13} - m^2) x_2^2 x_3 + \\ (s_{23} - m^2) x_4 x_1 (x_1 + x_2) + \\ (s_{13} + s_{23} - 2m^2) x_2 [x_2 x_4 + x_5 (x_1 + x_2 + x_3 + x_4)] - \\ x_7 (x_1 + x_2) [x_2 (3m^2 - s_{13}) + 2m^2(x_1 + x_3) + x_4 (s_{23} + m^2)] , \quad (7.24g)$$

$$0 = (m^2 - s_{13}) x_2 x_3 (x_1 + x_2) - s_{12} x_1 x_2 (x_1 + x_2 + x_3) + \\ x_4 [(m^2 - s_{23}) x_1 (x_1 + x_2) + (2m^2 - s_{13} - s_{23}) x_2^2] + \\ 2m^2 x_7 (x_1 + x_2) (x_1 + x_2 + x_3 + x_4) \quad (7.24h)$$

Still assuming all Feynman parameters  $x_i \neq 0$ , a leading Landau singularity cannot be detected in the above equations. The graph is regulated by its mass parameter. Yet, there are many sub-leading Landau singularities. These are given when one or more of the above displayed kinematic conditions are fulfilled. One such Landau singularity appears at  $s_{13} = m^2$ , when the Feynman parameters  $x_i$  with  $i = 1, 4, 5, 6, 7$  vanish simultaneously. Another one appears at  $s_{12} = 0$  when  $x_j \rightarrow 0$  for  $j = 3, 4, 5, 7$ .

## 7.3 Numerical evaluation

In this section, numerical results for several two-loop four-point functions are presented, in the same order as is shown in Fig. 7.1. The results for the analytically prepared  $ggtt_2$  diagram are shown first. All other results are obtained using the custom SECDEC setup.

### 7.3.1 The $ggtt_2$ diagram

Analytic results for the pole coefficients of the  $1/\varepsilon^4$  and  $1/\varepsilon^3$  part of the diagram  $ggtt_2$  shown in Fig. 7.1(a) have been provided in Ref. [312]. Using the mixed analytic and numerical approach presented in the work summarized in this thesis, the results of the purely analytical pole predictions can be numerically confirmed, see Fig. 7.2. The numerical results for the remaining pole coefficients and the finite part of  $ggtt_2$  are shown in Figs. 7.3 and 7.4. For Figs. 7.2 - 7.4, an overall factor of  $-16 \Gamma(1 + \varepsilon)^2$  is extracted.

Two Landau singularities can be observed, one is at  $s_{12} = 0$  and the other at  $s_{13} = m^2$ . All other Landau singularities do not appear in the plot, as the values for  $s_{23}$  and  $m^2$  are kept fixed.

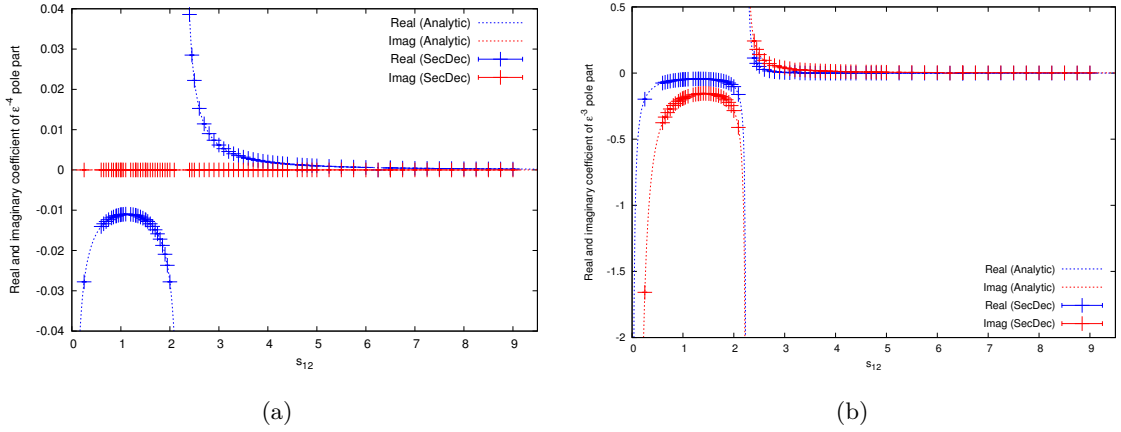


Figure 7.2: Comparison of (a) the leading and (b) the next-to-leading pole coefficients between the analytic result from [312] and the SECDEC result. The real part is shown in blue, the imaginary part in red. As numerical values  $p_3^2 = p_4^2 = m^2 = 1$ ,  $s_{23} = -1.25$  is chosen, assuming four-momentum conservation  $s_{13} = 2m^2 - s_{12} - s_{23}$ .

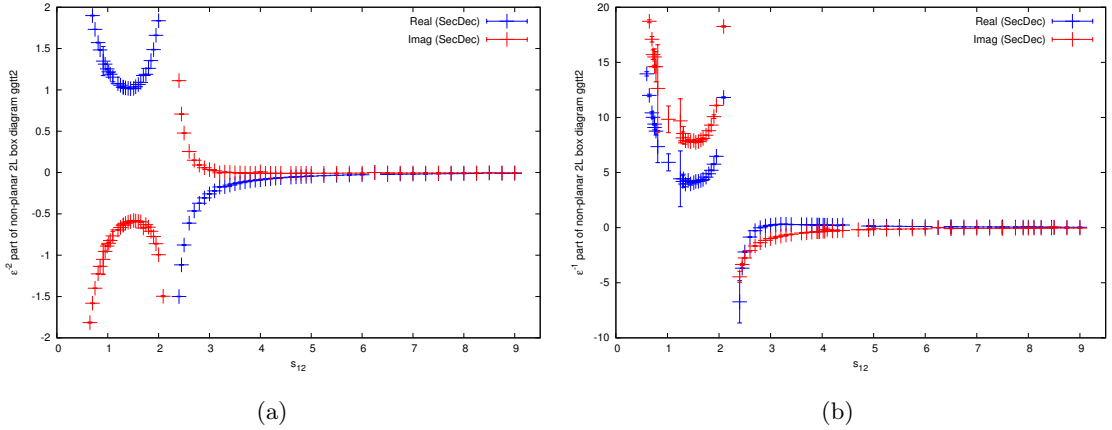
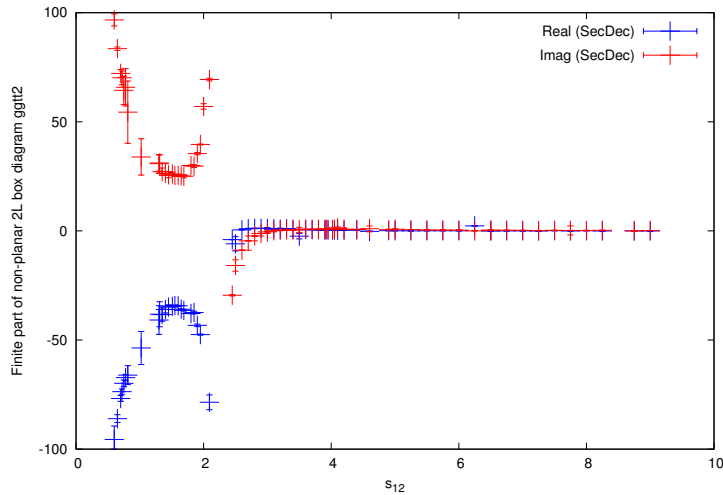


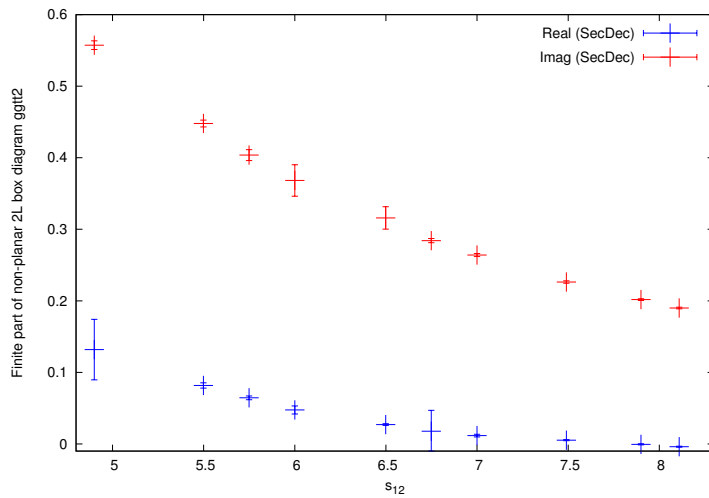
Figure 7.3: Results for (a) the  $1/\varepsilon^2$  and (b) the  $1/\varepsilon$  coefficients of the integral  $ggtt_2$ . The kinematics are the same as in Fig. 7.2.

The numerical result presented here was compared to the fully analytical result in two selected phase space points [313] for all Laurent coefficients up to the finite part, finding agreement within the numerical precision. The full prediction obtained from the numerical result of Figs. 7.2 - 7.4 were useful as a cross-check in Ref. [81]. The timings for the leading and next-to-leading pole coefficients of the diagram  $ggtt_2$  range between fractions of a second and around 20 seconds. The coefficients of the  $1/\varepsilon^2$  pole take 13 - 300 seconds, while the coefficients of the  $1/\varepsilon$  pole take between 75 seconds and 50

minutes, depending on their distance to thresholds. For the finite part, the integration times range from 250 seconds to 67 minutes. For all Laurent coefficients, a relative accuracy of  $5 \times 10^{-3}$  has been stipulated, which was not always reached for the  $1/\varepsilon$  and  $\varepsilon^0$  coefficients. It should also be noted that the timings for points close to threshold are rather sensitive to the Monte Carlo integration parameters.



(a)



(b)

Figure 7.4: Results for the finite part of the scalar integral  $ggtt_2$ , for a larger kinematic range (a), and a region further away from threshold (b). The kinematics are the same as in Fig. 7.2. The vertical bars display the uncertainty of the numerical result.

### 7.3.2 The $gg\bar{t}t_1$ diagram

Numerical results for the diagram  $gg\bar{t}t_1$  with two massive external legs are shown for the scalar integral and an irreducible rank two tensor integral, compare Fig. 7.1(b) for the corresponding diagram and Fig. 7.5 for the numerical results.

The integral representation of the diagram  $gg\bar{t}t_1$  is given by

$$\mathcal{G}_{gg\bar{t}t_1} = \left( \frac{1}{i\pi^{\frac{D}{2}}} \right)^2 \int \frac{d^D k_1 d^D k_2}{D_1 \dots D_7}, \quad (7.25a)$$

$$(7.25b)$$

with the corresponding Feynman propagators

$$D_1 = k_1^2 - m_2^2, \quad D_2 = (k_1 + p_1)^2 - m_2^2, \quad D_3 = k_2^2 - m_2^2, \quad (7.25c)$$

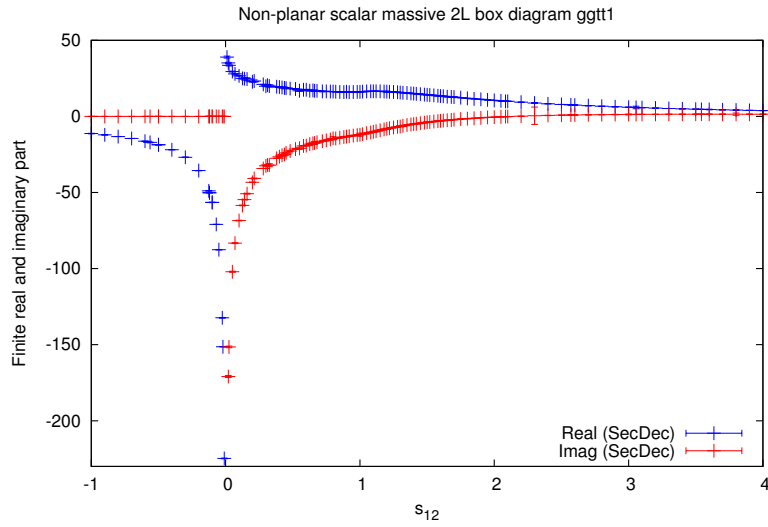
$$D_4 = (k_2 + p_2)^2 - m_2^2, \quad D_5 = (k_1 - k_2 + p_1)^2, \quad (7.25d)$$

$$D_6 = (k_1 - k_2 - p_2)^2, \quad D_7 = (k_1 - k_2 + p_1 + p_3)^2 - m_1^2, \quad (7.25e)$$

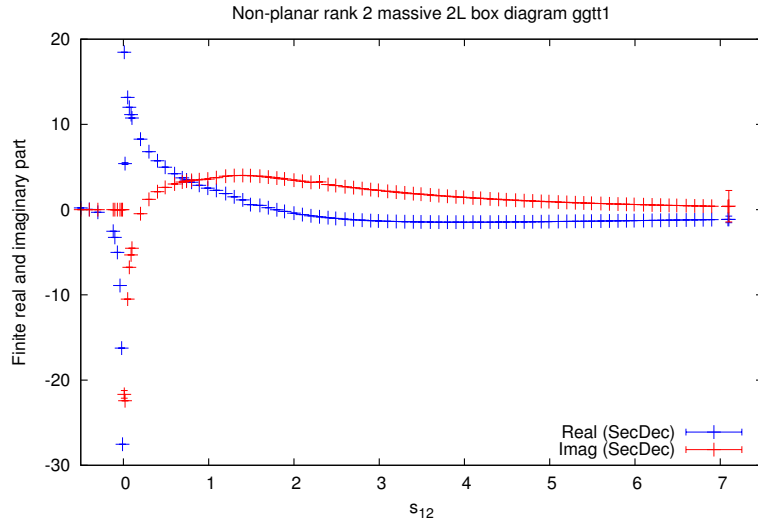
where the infinitesimal  $i\delta$  is omitted for brevity, and where the convention of all external momenta being ingoing was used. The dimension is denoted by  $D$ . Two external legs  $p_3$  and  $p_4$  are massive and equal,  $p_3^2 = p_4^2 = m_1^2$ . For the results shown in Fig. 7.5, the numerical values  $m_1^2 = m_2^2 = m^2 = 1$ ,  $s_{23} = -1.25$ ,  $s_{13} = 2m^2 - s_{12} - s_{23}$  were used. In Fig. 7.5, the two masses are set to  $m_1^2 = m_2^2$ , as this is the topology appearing in the process  $gg \rightarrow t\bar{t}$  at NNLO if the  $b$ -quarks are assumed to be massless. While numerical results for the scalar integral are shown in Fig. 7.5(a), (b) corresponds to a rank two tensor integral with the same propagators as (a), with a scalar product of loop momenta  $k_1 \cdot k_2$ , in the numerator.

The timings for one kinematic point for the scalar integral in Fig. 7.5(a) range from 11-60 secs for points far from threshold to 27 minutes that are very close. In the vicinity of the threshold, the average is around 500 secs. A relative accuracy of  $10^{-3}$  has been specified for terminating the numerical integration, while the absolute accuracy has been set to  $10^{-5}$ . For the tensor integral, the timings are better than for the scalar case, as the numerator present in this case smoothes out the integrand. A phase-space point far from threshold takes around 5-10 secs, while points very close to threshold do not exceed 1 hour for the rank 2 tensor integral. The results were obtained on a single 8 core Intel i7 machine.





(a)



(b)

Figure 7.5: (a) Results for the scalar integral  $gg_{tt_1}$  shown in Fig. 7.1(b), and (b) the corresponding rank two tensor integral  $gg_{tt_1}$  with the factor  $k_1 \cdot k_2$  in the numerator. The invariant  $s_{12}$  is varied, the invariants  $s_{23} = -1.25$ ,  $m_2 = m_1$ ,  $p_3^2 = p_4^2 = m_1^2 = 1$  are fixed. The uncertainties from numerical integration are shown as horizontal markers on the vertical lines. The absence of such markers means that the numerical uncertainty is not visible at this scale.

Numerical results with  $m_1 \neq m_2$  are shown in Fig. 7.6 to demonstrate that adding another mass scale is extremely straightforward with our approach, whereas analytical calculations would suffer from enormous additional complications.

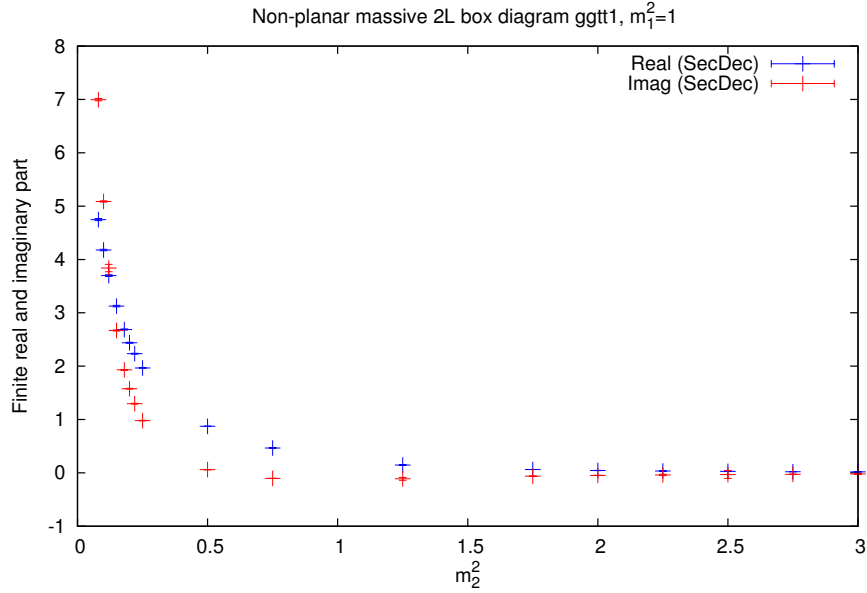


Figure 7.6: Results for the scalar integral  $ggtt_1$  shown in Fig. 7.1(b), with two different masses. The second mass  $m_2$  is varied, the other kinematic invariants are fixed with the values  $s_{12} = 5$ ,  $s_{23} = -1.25$  and  $p_3^2 = p_4^2 = m_1^2 = 1$ .

### 7.3.3 Planar seven-propagator all massive graph $M_7^P$

To demonstrate the possibility to compute diagrams with arbitrarily many scales, a planar seven-propagator toy graph involving the maximal amount of 13 independent scales is computed, compare Fig. 7.1(c). The diagram has no poles in the regulator  $\varepsilon$ . All propagators are assumed to have different masses, all external legs are chosen to be massive as well. While keeping  $s_{23} = -0.25$  fixed, numerical values of the finite part of the  $M_7^P$  diagram are shown, see Fig. 7.7, where  $s_{12}$  and  $s_{13}$  are varied using the physical constraint  $s_{12} + s_{23} + s_{13} = p_1^2 + p_2^2 + p_3^2 + p_4^2$ .

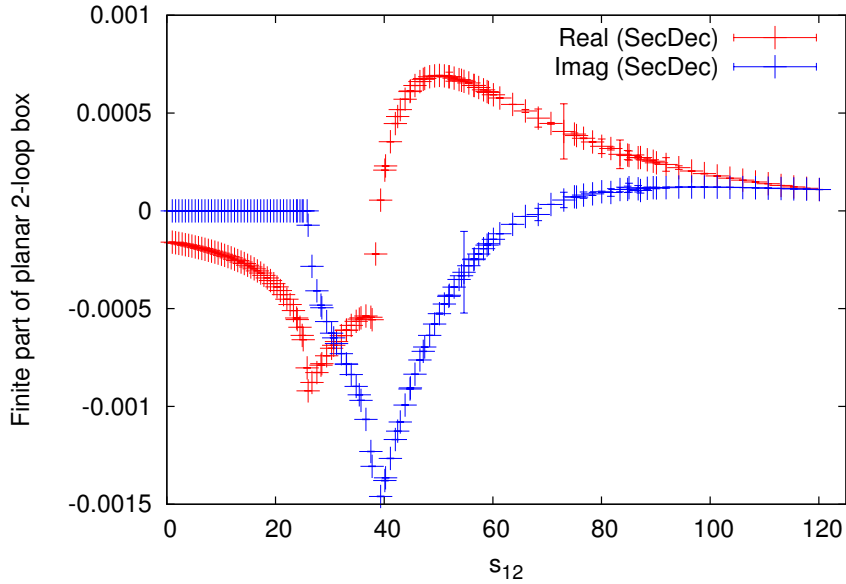


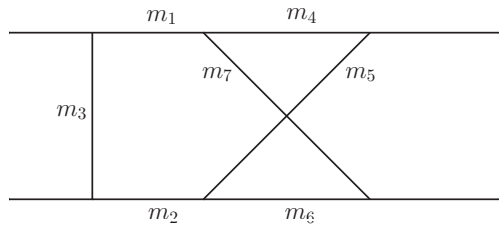
Figure 7.7: Results for the all massive planar seven-propagator graph  $M_7^P$  with all propagators and external legs massive, using  $m_1^2 = 2$ ,  $m_2^2 = 6$ ,  $m_3^2 = 7$ ,  $m_4^2 = 8$ ,  $m_5^2 = 9$ ,  $m_6^2 = 10$ ,  $m_7^2 = 12$ ,  $p_1^2 = 1$ ,  $p_2^2 = 3$ ,  $p_3^2 = 4$ ,  $p_4^2 = 5$  and  $s_{23} = -0.25$ .

The timings for the numerical integration range between 10 and 180 secs with a relative accuracy of  $10^{-3}$  or an absolute accuracy of  $10^{-8}$  if the imaginary part is zero, see Sec. 6.3.8 for a discussion on the relative vs absolute accuracy.

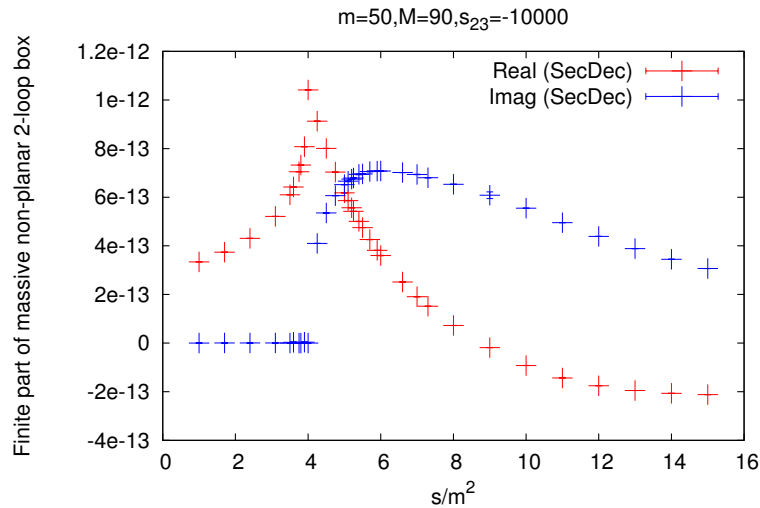
These results show that there is in principle no constraint on the number of scales involved.

### 7.3.4 Non-planar seven-propagator all massive graph $M_7^{NP}$

In this example, a seven-propagator non-planar two-loop box integral is considered, where all propagators are massive, using  $m_2 = m_4 = m_5 = m_7 = m$ ,  $m_1 = m_3 = m_6 = M$ ,  $p_1^2 = p_2^2 = p_3^2 = p_4^2 = m^2$ . The labeling is as shown in Fig. 7.8. Numerical results for this integral were obtained by Fujimoto et al. [314], where solutions are found


 Figure 7.8: Labeling of the masses for the non-planar graph  $M_7^{\text{NP}}$ .

by extrapolation in the  $i\delta$  parameter. For comparison, results produced with SECDEC are shown for the same mass configuration using  $m = 50, M = 90, s_{23} = -10^4$ , see Fig. 7.9. They are in agreement with Ref. [314]. The computation time for the longest sub-function (for both real and imaginary parts) for a relative accuracy of one per mil vary between about 20 secs for a point far from and about 500 secs close to the threshold.


 Figure 7.9: Results for the non-planar 7-propagator graph  $M_7^{\text{NP}}$  with all propagators massive, using  $m = 50, M = 90$  and  $s_{23} = -10^4$ .

### 7.3.5 Non-planar six-propagator diagram

First, the non-planar six-propagator two-loop four-point diagram is considered, compare Fig. 7.1(e). For light-like legs and massless propagators, the analytic result has been calculated, see Ref. [201]. The name of the graph  $B_6^{\text{NP}}$ , is adopted from this reference.

In the following, two different mass configurations of the graph  $B_6^{\text{NP}}$  are studied

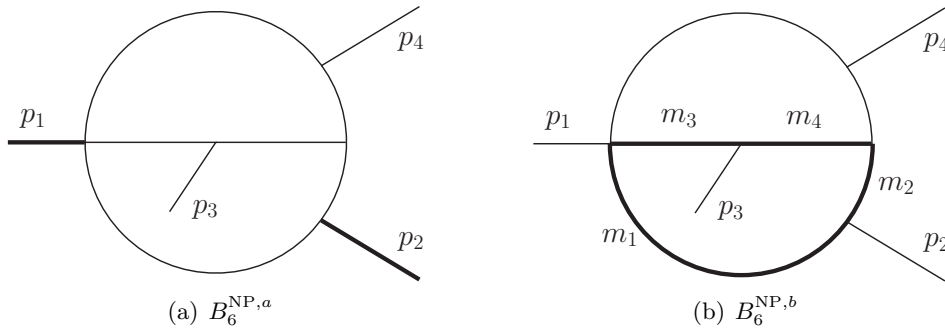


Figure 7.10: The two non-planar 6-propagator topologies studied here: (a)  $B_6^{\text{NP},a}$  and (b)  $B_6^{\text{NP},b}$ . The thick lines denote massive external legs and propagators, respectively.

$B_6^{\text{NP},a}$ : Two external legs,  $p_1^2$  and  $p_2^2$ , are massive, all propagators are massless. The leading pole of this topology is of order  $\mathcal{O}(1/\varepsilon^4)$ .

$B_6^{\text{NP},b}$ : All external legs are light-like, four propagators are massive with  $m_1 = m_2 = m_3 = m_4 \neq 0$ , the other two are massless. This topology contains poles starting from order  $\mathcal{O}(1/\varepsilon)$ .

For the topology with light-like legs as considered in Ref. [201], the leading pole is of the order  $\mathcal{O}(1/\varepsilon^2)$ . The difference in the pole structure is due to cancellations related to the high symmetry of the graph. See Figs. 7.11 and 7.12 for numerical results of the finite parts of  $B_6^{\text{NP},a}$  and  $B_6^{\text{NP},b}$  and Fig. 7.10 for the corresponding diagrams.

In accordance with Ref. [201], an overall prefactor of  $\Gamma(1+2\varepsilon)\Gamma(1-\varepsilon)^3/\Gamma(1-3\varepsilon)/(1+4\varepsilon)$  has been extracted in all numerical results. Also, for all the values given,  $s_{13}$  is determined by the physical constraint  $s_{12} + s_{23} + s_{13} = p_1^2 + p_2^2$ .

For Fig. 7.11, the numerical value  $s_{12} = 3$  was adopted while scanning over  $s_{23}$ . The massive external legs are set to  $p_1^2 = p_2^2 = 1$ . In Fig. 7.12, numerical values for the finite part of the  $B_6^{\text{NP},b}$  diagram are shown, where the mass scale is set to  $m = 0.5$ . The kinematic invariant  $s_{12}$  is varied, choosing  $s_{23} = -0.4$ .

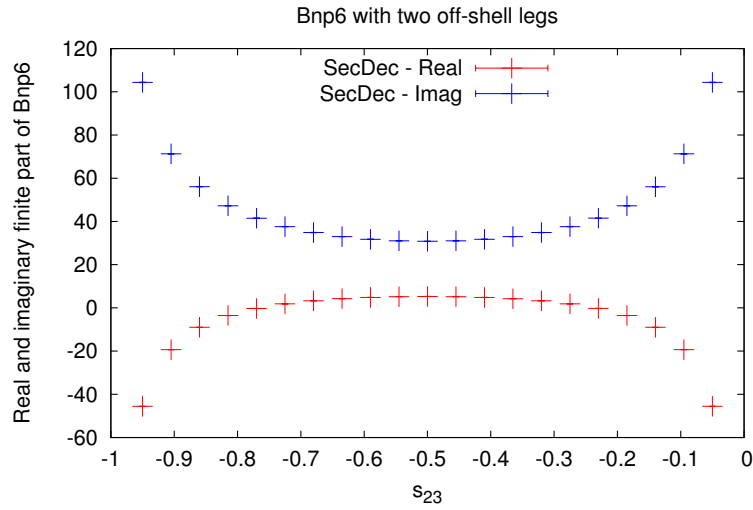


Figure 7.11: Results for the finite part of the graph  $B_6^{\text{NP},a}$  with massive legs  $p_1^2 = p_2^2 = 1$ . The error bars are barely seen in the figures as the numerical accuracy is about one per mil.

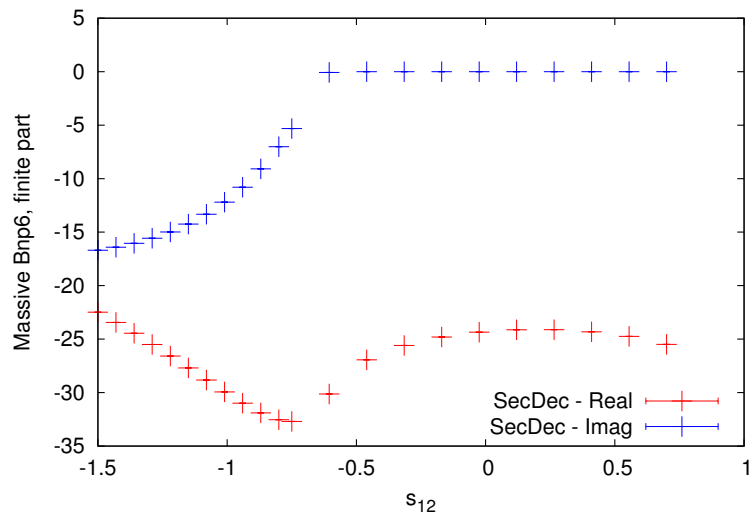


Figure 7.12: The non-planar 6-propagator graph  $B_6^{\text{NP},b}$  as a function of  $s_{12}$  in a region containing a threshold, where  $m_1^2 = m_2^2 = m_5^2 = m_6^2 = 0.25$  and  $s_{23} = -0.4$ . The error bars are barely seen in the figures as the numerical accuracy is about one per mil.

## 7.4 Summary

In this chapter the evaluation of diverse non-trivial two-loop diagrams, including planar and non-planar topologies with six or seven propagators, was shown. It was found that their evaluation with the upgraded version of the program SECDEC is not restricted by the number of involved scales. Complicated diagrams hardly or not accessible with analytical techniques can easily be computed, proving the program SECDEC a powerful tool for checks, comparisons and predictions. Yet, an evaluation can become difficult if the singularity structure is very complicated such that spurious linear divergences occur. In the example of the massive non-planar two-loop box  $gg_{tt_2}$  which exhibits such an extremely complicated singularity structure, it has proven beneficial to do an analytical preparation of the integral prior to numerical integration. A simplification of the functions to be integrated numerically can be achieved by a reduction in the number of Feynman parameters to integrate over numerically or in the removal of spurious divergences. The former was achieved by integration of one Feynman parameter in a sub-loop. Towards the latter a new type of transformation, introduced by the author and collaborators and summarized in this thesis, facilitated a trading of linear divergences for logarithmic ones, thereby achieving a reduction by two thirds in the total number of functions to be integrated. As was shown, the analytical preparation leads to an overall improved numerical convergence. Exploiting the newly developed feature of including user-defined functions into the SECDEC setup, an automated evaluation of the  $gg_{tt_2}$  diagram was possible. The examples demonstrated in this chapter may serve as a guideline for the evaluation of very complicated integrals, to become of importance in future phenomenological applications.





## 8 | Neutral MSSM Higgs-boson spectrum at the two-loop level

The momentum-dependent two-loop contributions to the neutral  $\mathcal{CP}$ -even MSSM Higgs-boson masses are computed at order  $\mathcal{O}(\alpha_s\alpha_t)$ . This requires the calculation of two-loop self-energies with a proper renormalization at the two-loop level. The calculation is performed using the Feynman-diagrammatic approach. An effective potential approach, though leading to compact expressions, does not allow for the incorporation of momentum dependence.

All relevant two-loop self-energy diagrams and those one- and two-loop diagrams contributing to the renormalization are generated using FEYNARTS [183, 184, 315]. From a diagrammatic point of view, the diagrams involved in the calculation including the momentum-dependence remain the same with respect to the calculation at zero momentum transfer. This is due to the fact that the diagrams are selected by coupling factors. The sole difference is in the dependence of the self-energy diagrams on the external momentum. Yet, this difference is non-trivial because analytical expressions involve the evaluation of elliptic integrals which can presently not be performed yielding fully analytical results. As numerical evaluations are generally more time-consuming, the number of diagrams involved needs to be reduced considerably, to a minimal set of master integrals.

A reduction of tensor integrals and the evaluation of traces is performed with the packages TWOCALC [316] and FORMCALC [186, 317, 318]. While the package TWOCALC condenses the two-loop amplitudes to only scalar master topologies, FORMCALC reduces all one-loop counter-terms and counter-term insertions to a basis of scalar integrals and a small number of tensor coefficients. In the reduction, the method of partial fractioning is used where applicable. Also the cancelation of denominators after taking the derivative with respect to a kinematic invariant is exploited, in addition to the application of symmetry relations. An important feature of TWOCALC is benefitting from the extension of the idea of a tensor decomposition introduced by Passarino and Veltman [319] as a reduction technique at one-loop. In TWOCALC, the latter is applied to a sub-loop of an integral before the remains of the integral can be further decomposed and simplified with the before mentioned techniques.

After studying the one- and two-loop counter-terms renormalizing the masses as well as the fields, and assuring a consistent cancellation of all divergences, the resulting

finite terms are evaluated. Where possible, analytic results are used, all other integral topologies are computed numerically using the program SECDEC. The resulting self-energy corrections are added to the inverse propagator matrix, as discussed in Sec. 2.3, and the resulting mass shifts to the neutral  $\mathcal{CP}$ -even Higgs-boson masses are computed. The two-loop calculation is performed in the  $\phi_1$ - $\phi_2$  basis. The rotation into the physical  $h^0$ - $H^0$  basis according to Eq. (2.5) is performed afterwards.

## 8.1 Dominant momentum-dependent two-loop QCD corrections

To compute the dominant momentum-dependent two-loop contributions to the neutral MSSM Higgs-boson spectrum, only those self-energy diagrams with couplings strictly of the order  $\mathcal{O}(\alpha_s\alpha_t)$  are taken into account. While electro-weak gauge contributions are incorporated up to the one-loop level, they are assumed negligible at the two-loop level. The corrections involving squares in the top Yukawa coupling, Eq. (2.40), dominate the electro-weak higher-order contributions, as  $m_t^2 \gg m_{Z,W}^2$ . Contributions involving couplings to gauge bosons are therefore expected to be relatively small.

Although the top Yukawa coupling is much larger than the bottom Yukawa coupling,  $y_t \gg y_b$ , it might be argued that the scalar bottom (sbottom) quark mass could be significantly larger than the bottom mass, when supersymmetry is broken. This region of parameter space could then lead to corrections of similar size with respect to the couplings proportional to  $y_t^2$ . However, the couplings of the squarks to the Higgs-bosons are all proportional to Yukawa couplings, see Sec. 2.2. They are composed of the fully supersymmetric F-term and the non-supersymmetric soft-breaking contributions, where fully supersymmetric refers to the relation  $y_{\tilde{t},\tilde{b}} = y_{t,b}$ . The relevant soft-breaking terms are proportional to the trilinear couplings  $A_{t,b}$  and the Standard Model Yukawa couplings. Assuming no inverse hierarchy among the trilinear couplings, the up-type Yukawa terms dominate over the down-type ones. Therefore, all bottom and sbottom contributions can be assumed to be negligible.

## 8.2 Self-energy diagrams

Twelve different two-loop topologies contribute to the MSSM Higgs-boson self-energy corrections at the order  $\mathcal{O}(\alpha_s\alpha_t)$ , see Fig. 8.1. They match Eq. (2.62) choosing the scalar fields  $\phi_1^0$  and  $\phi_2^0$  for  $x_a$ . Every vertex of Yukawa type involving a Higgs-boson and quarks or squarks contains a square root factor of  $\alpha_t$ . All quark or squark interactions with a gluon or gluino and the 4-squark vertices contribute with a factor of  $\sqrt{\alpha_s}$ . Products of these coupling factors lead to an overall order of  $\alpha_s\alpha_t$  for each diagram. The squared one-particle irreducible diagrams and reducible two-loop diagrams  $(\Sigma_{\phi_i\phi_j}^{(1)})^2$  do not contribute to the corrections because their amplitudes are not of the order  $\alpha_s\alpha_t$ .

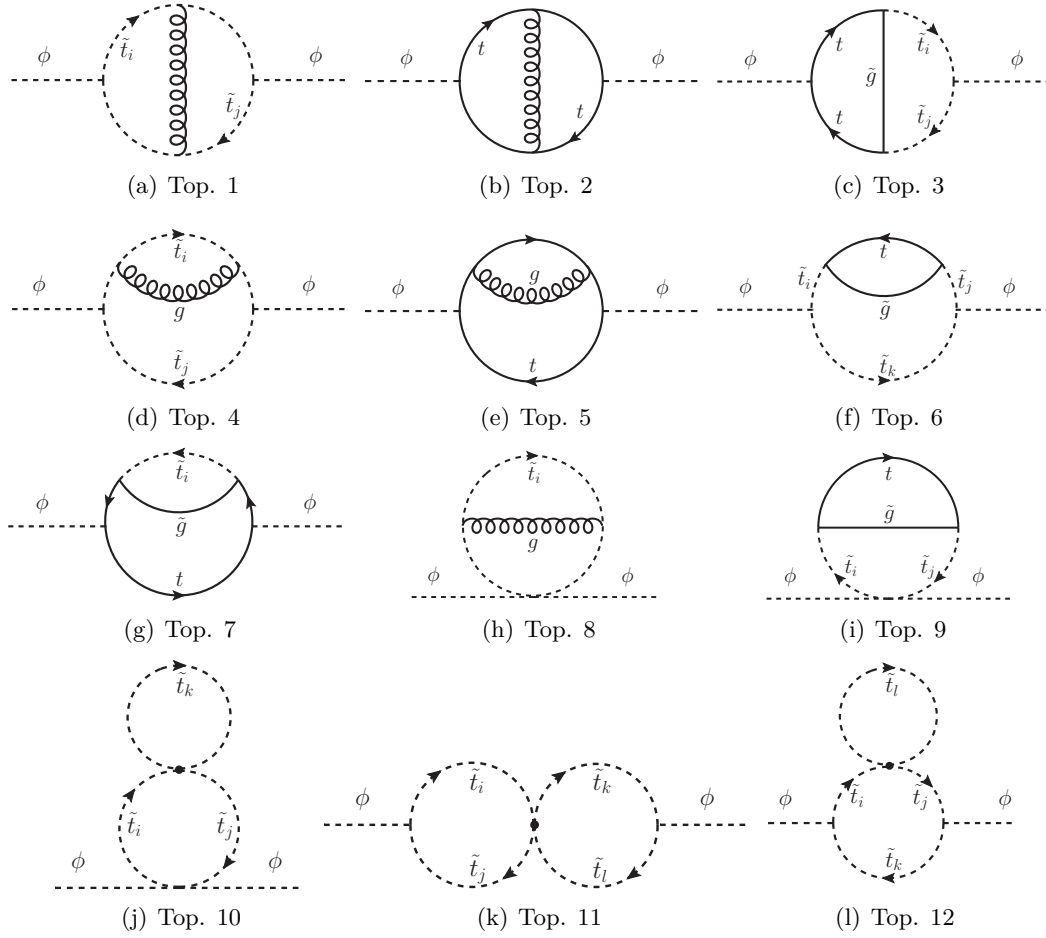


Figure 8.1: Generic two-loop self-energy diagrams contributing at the order  $\mathcal{O}(\alpha_s \alpha_t)$ , with  $\phi = \phi_1, \phi_2, A^0$  and  $i, j, k = 1, 2$ . The  $A^0$  boson self-energies enter the two-loop counter terms during renormalization. Stop particles  $t$  carry indices 1 and 2, in accordance with the Feynman rules.

After performing a tensor reduction with `TWOCALC`, the resulting amplitudes are given in terms of a few scalar master integrals. Those involve factorizing one-loop tadpole  $A(m^2)$ , one-loop bubble  $B(p^2, m_1^2, m_2^2)$  and two-loop bubble  $T(p^2, \{m_i^2\})$  topologies, compare Fig. 8.2. While the resulting one-loop integrals can only become UV divergent, the two-loop integrals can be ultraviolet and infrared divergent. As the gluons are the only massless particles in this calculation and appear singly, no infrared singularities arise in any of the two-loop diagrams. This remains valid throughout the whole calculation, even though some sub-topologies contain more than one massless internal line. In these cases, the integrand structure is such that an IR singularity does not occur. Though IR divergences are absent, additional sub-ultraviolet divergences can arise depending on

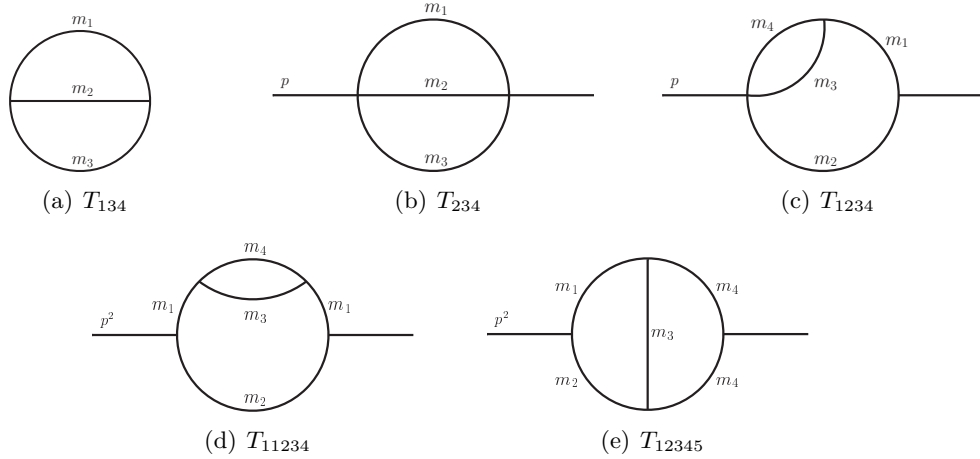


Figure 8.2: Two-loop master topologies resulting after tensor reduction. Some of the internal lines may also be massless.

the structure of the integrand. This is true for the diagrams  $T_{1234}$ ,  $T_{11234}$  and  $T_{234}$ . The integral  $T_{12345}$  is finite in all mass configurations appearing in this calculation. To summarize, the previously shown two-loop self-energies may contain single and double UV poles. The newly included momentum-dependence gives rise to additional divergent terms. It is desired to find the correct counter-terms for their renormalization.

It is beneficial to analyze which diagrams carry momentum dependence, and which contribute with additional divergent parts. First of all, the topologies 8, 9 and 10 of Figs. 8.1(h)-(j) do not contribute with an additional momentum dependence at the two-loop level. Taking a diagrammatic point of view, these diagrams appear as tadpoles with two external legs pinched to one vertex, and all tadpoles are independent of the external momentum. All other diagrams carry momentum dependence in the loop and contain momentum-dependent single UV divergent pole contributions. The diagram in Fig. 8.1(l) is the only one to contain a single UV pole, all other diagrams have the double amount. Only three diagrams contain momentum-dependent double UV divergent terms, namely 8.1(b), (e) and (g).

With the additional contributions stemming from momentum dependence being exposed, the divergent terms can be eliminated, before the momentum-dependent contributions in the finite self-energies can be analyzed.

### 8.3 Renormalization

As mentioned in the previous section, up to two UV poles appear in the unrenormalized self-energies. These can contain local divergences in a sub-loop. To renormalize these, one-loop self-energies with counter-term insertions have to cancel those divergences arising in a sub-loop of the two-loop diagrams. In addition, two-loop counter terms need to

cancel the rest of the divergences. In this calculation, a mixed on-shell and  $\overline{DR}$  scheme is used. Within the  $\overline{DR}$  renormalization scheme, conventional dimensional reduction, see Sec. 3.2, is imposed. The bar in  $\overline{DR}$  denotes that an additional factor of  $\gamma_E$  and  $\log(4\pi)$  stemming from prefactors to loop integrals is absorbed into the renormalization scale  $\mu_r$ .

In a renormalized theory, all ultraviolet poles have to be canceled and physical quantities need to be finite. The proof of the existence of a set of counter-term vertices rendering any theory of superficial divergence finite is summarized in the BPHZ theorem, see Refs. [143–145]. While the renormalization of a sub-loop of two-loop self-energies is constructed from vertex corrections, their two-loop counter terms are determined from the Lagrangian. The latter can be derived by looking at corrections to the fields and masses. To this end, each scalar doublet gets a multiplicative field renormalization,

$$\mathcal{H}_a \rightarrow \mathcal{H}_a \sqrt{Z_{\mathcal{H}_a}} , \quad (8.1)$$

where

$$Z_{\mathcal{H}_a} = 1 + \delta Z_{\mathcal{H}_a}^{(1)} + \delta Z_{\mathcal{H}_a}^{(2)} + \dots . \quad (8.2)$$

Similarly, the masses get renormalization constants. This is implemented by adding counter-terms to the tree-level mass matrices

$$M_x^2 \rightarrow M_x^2 + \delta M_x^{2(1)} + \delta M_x^{2(2)} + \dots , \quad (8.3)$$

with  $x = \phi^0, \chi^0, \phi^\pm$ . Recapitulating Sec. 2.1, the Higgs-boson masses are determined from both, the bilinear part of the Lagrangian, compare Eq. (2.20), and the linear part, see Eqs. (2.16)-(2.18). They contain parametric dependences on  $m_{A^0}$ ,  $m_Z$ ,  $m_W$ , the charge  $e$ , the electroweak mixing angle  $\theta_W$ , the angle relating the vacuum expectation values  $\beta$  and the tadpole coefficients  $T_1$  and  $T_2$ , compare Eqs. (2.16), (2.23) and (2.25b). Reformulating the kinetic part of the Lagrangian including field renormalization constants yields

$$\mathcal{L}_{\text{Hfree}} = \sum_{a=1}^2 \partial_\mu \left( \mathcal{H}_a \sqrt{Z_{\mathcal{H}_a}} \right)^\dagger \partial^\mu \mathcal{H}_a \sqrt{Z_{\mathcal{H}_a}} \quad (8.4a)$$

$$= \frac{1}{2} (|\partial_\mu \phi_1^0 \sqrt{Z_{H_1}}|^2 + |\partial_\mu \chi_1^0 \sqrt{Z_{H_1}}|^2) + |\partial_\mu \phi_1^- \sqrt{Z_{H_1}}|^2 \\ + \frac{1}{2} (|\partial_\mu \phi_2^0 \sqrt{Z_{H_2}}|^2 + |\partial_\mu \chi_2^0 \sqrt{Z_{H_2}}|^2) + |\partial_\mu \phi_2^+ \sqrt{Z_{H_2}}|^2 . \quad (8.4b)$$

Examining those parts of the potential part of the Lagrangian contributing to the Higgs-boson masses, the following substitutions appear in the formulation of UV finite quantities,

$$\mathcal{L}_{\text{Hmass}} = -\frac{1}{2} \begin{pmatrix} x_1 \sqrt{Z_{\mathcal{H}_1}} & x_2 \sqrt{Z_{\mathcal{H}_2}} \end{pmatrix} (M_x^2 + \delta M_x^{2(1)} + \delta M_x^{2(2)} + \dots) \begin{pmatrix} x_1 \sqrt{Z_{\mathcal{H}_1}} \\ x_2 \sqrt{Z_{\mathcal{H}_2}} \end{pmatrix} , \quad (8.5)$$

where the tree-level terms and the one, two and higher loop counter-terms can be identified. An expansion of the square root becomes necessary when the fields  $x_1$  and  $x_2$  mix,

$$\begin{aligned} x_1 \sqrt{Z_{\mathcal{H}_1}} x_2 \sqrt{Z_{\mathcal{H}_2}} &= x_1 \left( 1 + \frac{1}{2}(\delta Z_{\mathcal{H}_1}^{(1)} + \delta Z_{\mathcal{H}_1}^{(2)}) - \frac{1}{8}(\delta Z_{\mathcal{H}_1}^{(1)})^2 + \dots \right) \\ &\quad \times x_2 \left( 1 + \frac{1}{2}(\delta Z_{\mathcal{H}_2}^{(1)} + \delta Z_{\mathcal{H}_2}^{(2)}) - \frac{1}{8}(\delta Z_{\mathcal{H}_2}^{(1)})^2 + \dots \right) \end{aligned} \quad (8.6a)$$

$$\begin{aligned} &= x_1 x_2 \left( 1 + \frac{1}{2}(\delta Z_{\mathcal{H}_1}^{(1)} + \delta Z_{\mathcal{H}_2}^{(1)}) + \frac{1}{2}(\delta Z_{\mathcal{H}_1}^{(2)} + \delta Z_{\mathcal{H}_2}^{(2)}) \right. \\ &\quad \left. - \frac{1}{8}(\delta Z_{\mathcal{H}_1}^{(1)} - \delta Z_{\mathcal{H}_2}^{(1)})^2 + \dots \right) \end{aligned} \quad (8.6b)$$

where a record of the expansion is only kept until second order. As mentioned before, the terms linear in the field need to vanish at all orders. Looking at these after the application of the equations of motion Eq. (2.56), the dependence on the fields drops out, meaning that there is no field renormalization involved here. This is in agreement with the fact that tadpoles do not carry momentum dependence. Therefore, the only counter-term correction needed in Eq. (2.57) arises from the corrections to the tadpoles themselves

$$T_a \rightarrow T_a + \delta T_a^{(1)} + \delta T_a^{(2)} + \dots \quad (8.7)$$

The solution to the equations of motion including counter-terms therefore reads

$$T_a + T_a^{(1)} + T_a^{(2)} + \delta T_a^{(1)} + \delta T_a^{(2)} + \dots \stackrel{!}{=} 0 \quad (8.8)$$

### 8.3.1 Two-loop counter terms for the renormalization at $\mathcal{O}(\alpha_s \alpha_t)$

Applying field and parameter renormalization yields the renormalized self-energies in terms of the scalar fields  $\phi_1^0$  and  $\phi_2^0$

$$\hat{\Sigma}_{\phi_1^0 \phi_1^0}^{(2)}(p^2) = \Sigma_{\phi_1^0 \phi_1^0}^{(2)}(p^2) + \delta \Phi_1^{(2)} - \delta V_{\phi_1^0 \phi_1^0}^{(2)} \quad (8.9a)$$

$$\hat{\Sigma}_{\phi_2^0 \phi_2^0}^{(2)}(p^2) = \Sigma_{\phi_2^0 \phi_2^0}^{(2)}(p^2) + \delta \Phi_2^{(2)} - \delta V_{\phi_2^0 \phi_2^0}^{(2)} \quad (8.9b)$$

$$\hat{\Sigma}_{\phi_1^0 \phi_2^0}^{(2)}(p^2) = \Sigma_{\phi_1^0 \phi_2^0}^{(2)}(p^2) - \delta V_{\phi_1^0 \phi_2^0}^{(2)} \quad (8.9c)$$

The counter-terms  $\delta \Phi_a$  arise from the kinetic Lagrangian, see Eq. (8.4b), and  $\delta V_{x_a x_b}$  from the potential part of the Lagrangian, see Eq. (8.5).

The counter-terms originating from perturbative expansions to the free fields  $\phi_1^0$  and  $\phi_2^0$  read

$$\delta \Phi_a^{(2)} = p^2 \left( \delta Z_{\mathcal{H}_a}^{(2)} - \frac{1}{4}(\delta Z_{\mathcal{H}_a}^{(1)})^2 \right), \quad (8.10)$$

as deducible from Eqs. (8.2) and (8.4b). In the calculation of the self-energies of the two orders  $\alpha_s$  and  $\alpha_t$ , the squared one-loop field renormalization constants do not contribute.

They would be needed, e.g., in an order  $\mathcal{O}(\alpha_t^2)$  calculation. This reduces the field renormalization counter-terms to

$$\delta\Phi_1^{(2)} = p^2 \delta Z_{\mathcal{H}_1^0}^{(2)} \quad (8.11)$$

$$\delta\Phi_2^{(2)} = p^2 \delta Z_{\mathcal{H}_2^0}^{(2)}. \quad (8.12)$$

Based on the derivation from the beginning of Sec. 8.3, the counter-terms arising from the renormalization of the potential part of the Lagrangian are given by

$$\delta V_{\phi_1^0 \phi_1^0}^{(2)} = M_{\phi_1^0 \phi_1^0}^2 \delta Z_{\mathcal{H}_1^0}^{(2)} + \delta M_{\phi_1^0 \phi_1^0}^{2(2)} \quad (8.13)$$

$$\delta V_{\phi_2^0 \phi_2^0}^{(2)} = M_{\phi_2^0 \phi_2^0}^2 \delta Z_{\mathcal{H}_2^0}^{(2)} + \delta M_{\phi_2^0 \phi_2^0}^{2(2)} \quad (8.14)$$

$$\delta V_{\phi_1^0 \phi_2^0}^{(2)} = \frac{1}{2} M_{\phi_1^0 \phi_2^0}^2 (\delta Z_{\mathcal{H}_1^0}^{(2)} + \delta Z_{\mathcal{H}_2^0}^{(2)}) + \delta M_{\phi_1^0 \phi_2^0}^{2(2)}, \quad (8.15)$$

where  $\delta M_{\phi^0}^{2(2)}$  is computed from the Taylor series expansion of the mass matrix  $M_{\phi^0}^2$  in its parameters up to second order. Recalling the mass matrix  $M_{\phi^0}^2$  of Eq. (2.25b), the vanishing of the tree-level tadpole parameters due to the minimization of the MSSM Higgs-boson potential, Eq. (2.15), was already incorporated. Tadpole contributions must be taken into account at higher orders, as their coefficients do not necessarily vanish, see Eq. (2.57) and Eq. (8.8). Yet, they only enter in the renormalization of the momentum independent part. The mass matrix is then parametrized by  $m_{A^0}$ ,  $m_Z$ ,  $m_W$ , the charge  $e$ , the electroweak mixing angle  $\theta_W$ , the angle relating the vacuum expectation values  $\beta$  and the tadpole coefficients  $T_1$  and  $T_2$ . The computation of the Taylor series expansion of the mass matrix up to second order corresponds to a perturbative expansion in these parameters,

$$\begin{aligned} m_{A^0}^2 &\rightarrow m_{A^0}^2 + \delta m_{A^0}^{2(1)} + \delta m_{A^0}^{2(2)}, & T_1 &\rightarrow T_1 + \delta T_1^{(1)} + \delta T_1^{(2)}, \\ m_Z^2 &\rightarrow m_Z^2 + \delta m_Z^{2(1)} + \delta m_Z^{2(2)}, & T_2 &\rightarrow T_2 + \delta T_2^{(1)} + \delta T_2^{(2)}, \\ \tan \beta &\rightarrow \tan \beta \left( 1 + \delta \tan \beta^{(1)} + \delta \tan \beta^{(2)} \right). \end{aligned} \quad (8.16)$$

With the computation performed in the “gaugeless” limit, all counter-terms including electroweak gauge particles and their contributions are discarded. Furthermore, squares of one-loop renormalization constants appearing in  $\delta M_{\phi^0}^{2(2)}$  do not contribute, as they are proportional to electroweak coupling factors but they are not of the order  $\mathcal{O}(\alpha_s \alpha_t)$ . For a full explicit presentation of  $\delta M_{\phi^0}^{2(2)}$ , see e.g. Ref. [86]. The final counter-terms for

the potential in the quadratic  $\phi_a^0$  terms are

$$\begin{aligned}
 \delta V_{\phi_1^0 \phi_1^0}^{(2)} &= \delta m_{A^0}^{2(2)} \sin^2 \beta \\
 &\quad - \delta T_1^{(2)} \frac{e}{2 M_W \sin \theta_W} \cos \beta (1 + \sin^2 \beta) \\
 &\quad + \delta T_2^{(2)} \frac{e}{2 M_W \sin \theta_W} \sin \beta \cos^2 \beta \\
 &\quad + 2 \delta \tan \beta^{(2)} \cos^2 \beta \sin^2 \beta m_{A^0}^2 \\
 &\quad + \delta Z_{\mathcal{H}_1^0}^{(2)} m_{A^0}^2 \sin^2 \beta ,
 \end{aligned} \tag{8.17a}$$

$$\begin{aligned}
 \delta V_{\phi_2^0 \phi_2^0}^{(2)} &= \delta m_{A^0}^{2(2)} \cos^2 \beta \\
 &\quad + \delta T_1^{(2)} \frac{e}{2 M_W \sin \theta_W} \cos \beta \sin^2 \beta \\
 &\quad - \delta T_2^{(2)} \frac{e}{2 M_W \sin \theta_W} \sin \beta (1 + \cos^2 \beta) \\
 &\quad - 2 \delta \tan \beta^{(2)} \cos^2 \beta \sin^2 \beta m_{A^0}^2 \\
 &\quad + \delta Z_{\mathcal{H}_2^0}^{(2)} m_{A^0}^2 \cos^2 \beta ,
 \end{aligned} \tag{8.17b}$$

$$\begin{aligned}
 \delta V_{\phi_1^0 \phi_2^0}^{(2)} &= -\delta m_{A^0}^{2(2)} \sin \beta \cos \beta \\
 &\quad - \delta T_1^{(2)} \frac{e}{2 M_W \sin \theta_W} \sin^3 \beta \\
 &\quad - \delta T_2^{(2)} \frac{e}{2 M_W \sin \theta_W} \cos^3 \beta \\
 &\quad - \delta \tan \beta^{(2)} \cos \beta \sin \beta \cos(2\beta) m_{A^0}^2 \\
 &\quad - \frac{1}{2} (\delta Z_{\mathcal{H}_1^0}^{(2)} + \delta Z_{\mathcal{H}_2^0}^{(2)}) \sin \beta \cos \beta m_{A^0}^2 .
 \end{aligned} \tag{8.17c}$$

With the derived counter-terms at hand, the renormalization constants entering them need to be defined. As mentioned previously, these are renormalization scheme dependent. To be consistent with previous calculations incorporated in the public program FEYNHIGGS, all masses and the tadpole parameters are renormalized using the on-shell scheme, and all field contributions using the  $\overline{DR}$  scheme [140, 320–323]. In the latter, a dependence on the renormalization scale  $\mu_r$  is exhibited. The two-loop renormalization constants entering the mass renormalization counter-terms are known for vanishing external momentum, see Refs. [109, 117–119]. Taking the momentum dependence into account, only the tadpole contributions remain unchanged. The tadpole renormalization constants can be deduced from Eq. (8.8). To meet the condition that the sum of all tadpole contributions must vanish, it must follow

$$\delta T_a^{(2)} = -T_a^{(2)} , \tag{8.18}$$

adopting an on-shell renormalization. To obtain the renormalization constants  $\delta T_a^{(2)}$ , thus two-loop tadpole diagrams have to be computed, matching the right order in the couplings, compare the diagrams in Fig. 8.3.



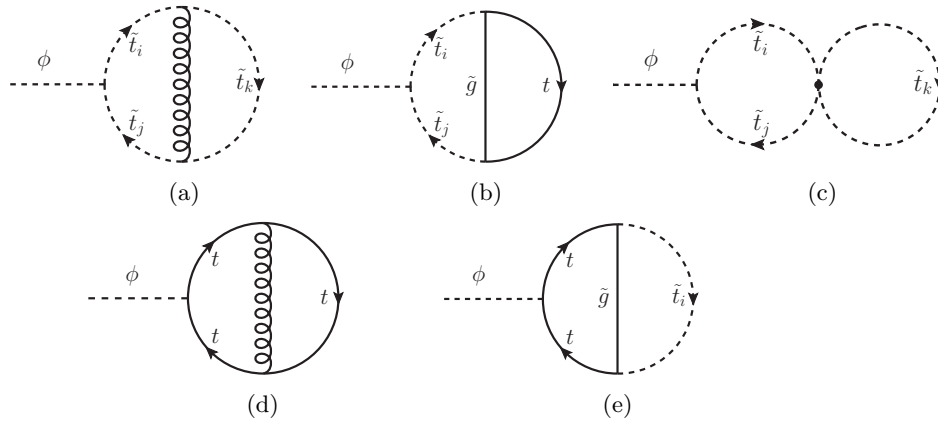


Figure 8.3: Two-loop tadpole diagrams contributing in the two-loop counter terms to the  $\mathcal{O}(\alpha_s \alpha_t)$  self-energies,  $\phi = \phi_1, \phi_2$  and  $i, j, k = 1, 2$ .

For the renormalization constants  $\delta Z_{\mathcal{H}_1}$ ,  $\delta Z_{\mathcal{H}_2}$  and  $\delta \tan \beta$  several choices are possible, see the discussion in [140, 324]. As shown there, the most convenient choice is a  $\overline{\text{DR}}$  renormalization of  $\delta \tan \beta$ ,  $\delta Z_{\mathcal{H}_1}$  and  $\delta Z_{\mathcal{H}_2}$ . The field renormalization constants can be extracted by taking the derivative of the renormalized self-energies, Eqs. (8.9), with respect to the external momentum squared, yielding in  $\overline{\text{DR}}$  renormalization

$$\delta Z_{\mathcal{H}_a}^{(2)} = \text{Re} \left[ \frac{\partial}{\partial p^2} \hat{\Sigma}_{\phi_a^0 \phi_a^0}(p^2) - \frac{\partial}{\partial p^2} \Sigma_{\phi_a^0 \phi_a^0}(p^2) \right]_{p^2=0} \quad (8.19)$$

$$= - \text{Re} \left[ \frac{\partial}{\partial p^2} \Sigma_{\phi_a^0 \phi_a^0} \right]_{p^2=0}^{\text{div}}. \quad (8.20)$$

The formulation of the field renormalization constants in the  $\overline{\text{DR}}$  scheme has the advantage that all ultraviolet divergences of the momentum-dependent integrals contained in the  $\Sigma_{\phi_a^0 \phi_a^0}$  self-energies are known analytically. The derivative with respect to  $p^2$  can therefore be performed in a fully analytical way. Adopting an on-shell field renormalization, the derivatives of some integrals in the finite part for which closed analytical expressions are not available, are expected to be less straightforward. It could be argued that the calculation can be simplified even further adopting a full  $\overline{\text{DR}}$  scheme, compare Refs. [136–138]. Yet, the dependence on the renormalization scale is decreased adopting a hybrid renormalization scheme, physical effects of higher order in the  $\overline{\text{DR}}$  scheme already appear at the current order in the on-shell scheme, and predictions are given with pole masses as input parameters.

Due to the fact that  $\tan \beta$  is defined in terms of the two vacuum expectation values  $v_1$  and  $v_2$ , Eq. (2.24), minimizing the MSSM Higgs-boson potential according to Eq. (2.15), the field renormalization also enters here. The renormalization of  $\tan \beta$  follows from

$$v_a \rightarrow \sqrt{Z_a} (v_a + \delta v_1^{(1)} + \delta v_1^{(2)}), \quad (8.21)$$

yielding in  $\overline{DR}$

$$\delta \tan \beta^{(2)} = \frac{1}{2} \tan \beta (\delta Z_{\mathcal{H}_2}^{(2)} - \delta Z_{\mathcal{H}_1}^{(2)}) . \quad (8.22)$$

The term in Eq. (8.22) is in general not the proper expression beyond one-loop order even in the  $\overline{DR}$  scheme. In the approximation with only the top Yukawa coupling at the two-loop level, it is the correct  $\overline{DR}$  form, see Refs. [325, 326].

Finally, the two-loop renormalization constant of the  $A^0$ -boson mass is determined in the on-shell scheme as

$$\delta m_{A^0}^{2(2)} = \text{Re} \left[ \Sigma_{A^0 A^0}^{(2)}(p^2 = m_{A^0}^2) \right] , \quad (8.23)$$

in terms of the unrenormalized two-loop  $A^0$ -boson self-energy  $\Sigma_{A^0 A^0}^{(2)}$  evaluated at the pole mass; see Fig. 8.1 for the generic  $A^0$ -boson self-energy diagrams at the two-loop level. The appearance of a non-zero momentum in the self-energy goes beyond the  $\mathcal{O}(\alpha_t \alpha_s)$  corrections evaluated in Refs. [109, 117–119]. Fixing the external momentum of the self-energy to the  $A^0$ -boson mass is necessary to cancel additional divergent terms arising from the two-loop counter-terms involving  $\tan \beta$ , compare Eqs. (8.17a)-(8.17c). The latter contain a dependence on  $m_{A^0}^2$ , giving rise to divergences which do not cancel any divergence arising in the neutral  $\mathcal{CP}$ -even Higgs-bosons. The latter are independent of the  $A^0$ -boson mass. These additional divergences must therefore be cancelled by  $\delta m_{A^0}^{2(2)}$ .

### 8.3.2 Renormalization at the sub-loop level

With the two-loop counter terms at hand, there is only one missing piece left in the renormalization procedure. Filling this gap, those one-loop diagrams with counter-term insertions are computed, which renormalize a sub-loop of the two-loop self-energies and of the two-loop tadpole diagrams. The latter are needed for the two-loop counter-terms, compare Eq. (8.18). The one-loop amplitudes with counter-term insertions are generated with the program FEYNARTS [183, 184, 315], using the model file including counter-terms from Ref. [327].

One-loop corrections  $x^{(1)}$  to the field  $x$  with one-loop counter-term insertions  $\delta P^{(1)}$  of a given parameter  $P$  were already shown in Eqs. (8.4b) and (8.5). The contributions there, however, are of the order  $\mathcal{O}(\alpha_t^2)$  and lack a dependence of  $\alpha_s$ . To find the proper sub-loop renormalization terms, the particle interactions proportional to  $\alpha_s$ , listed in Sec. 2.2, need to be taken into account. They amount to five different counter-term structures, see Fig. 8.4, required for the insertions in the one-loop amplitudes of order  $\mathcal{O}(\alpha_t)$  in Fig. 8.5. The latter involve the one-loop neutral  $\mathcal{CP}$ -even and  $\mathcal{CP}$ -odd Higgs-boson amplitudes. The  $\mathcal{CP}$ -odd amplitude is needed for the sub-loop renormalization of the  $A^0$ -boson self-energy entering the two-loop counter-terms. Furthermore, the tadpole diagrams entering the two-loop counter-terms need a proper sub-loop renormalization. Their one-loop amplitudes must be computed as well, see the diagrams in Fig. 8.6. The one-loop diagrams are either of order  $\mathcal{O}(\alpha_t)$  or  $\mathcal{O}(\sqrt{\alpha_t})$ , see Figs. 8.5 and 8.6, respectively.

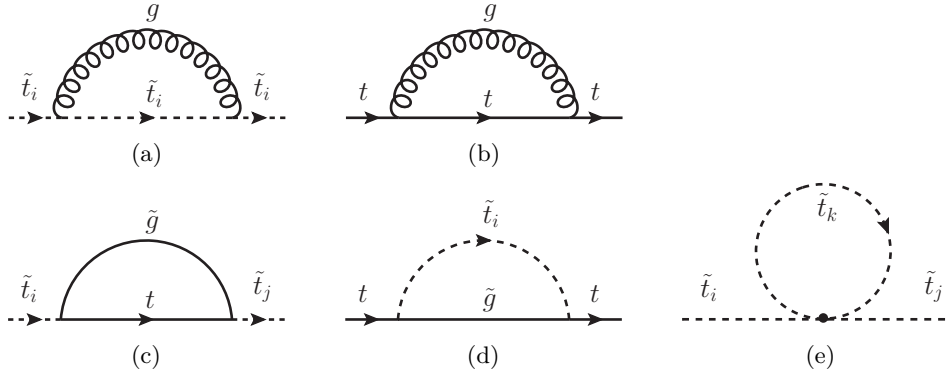


Figure 8.4: One-loop diagrams for the quark and squark counter-term insertions with  $i, j, k = 1, 2$ .

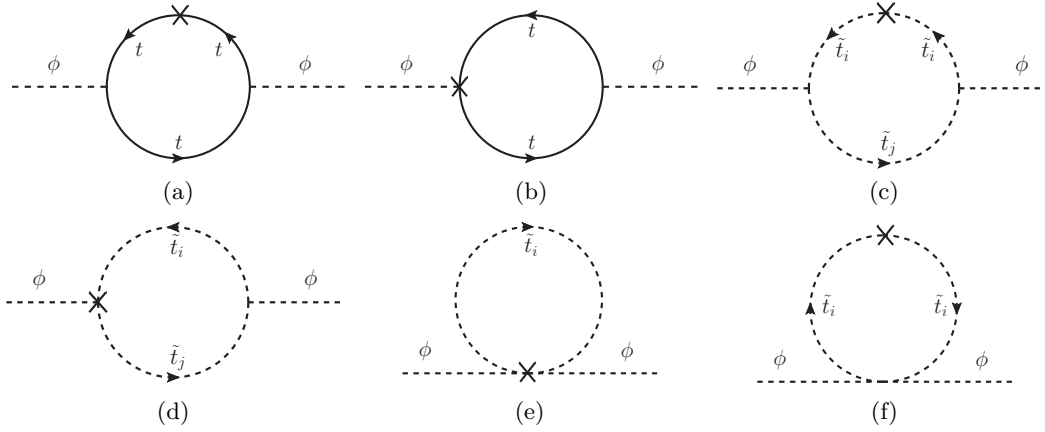


Figure 8.5: One-loop counter-term contributions to the sub-loop renormalization of the  $\mathcal{O}(\alpha_s \alpha_t)$  self-energies, with  $\phi = \phi_1, \phi_2, A$  and  $i, j = 1, 2$ .

An additional factor  $\sqrt{\alpha_t}$  comes in with the prefactor to the tadpole renormalization constants, compare Eqs. (8.17a)-(8.17c). The program FORMCALC [186] is used to perform the reduction of the one-loop diagrams to one-, two-, and three-point master integrals  $A$ ,  $B$  and  $C$ , respectively. In addition, tensor coefficients to the two- and three-point integrals can arise.

The counter-term insertions contain quark and squark field-renormalization components as well as terms resulting from the renormalization of the tree-level top-quark and squark mass matrices. The renormalization of the top and stop sector at the one-loop level as discussed below, has been analyzed in detail in Refs. [86, 119, 135, 320–323].

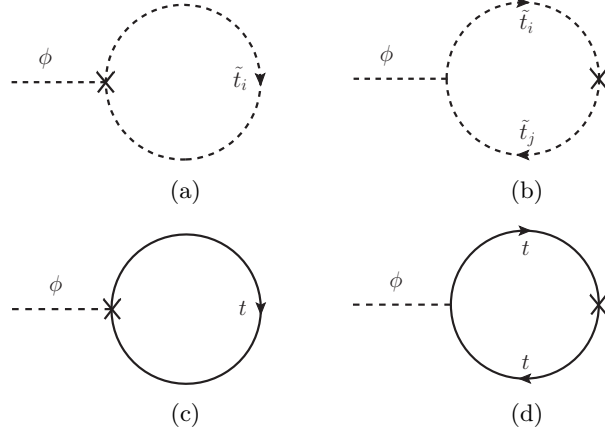


Figure 8.6: One-loop counter-term diagrams with insertions, needed in the sub-loop renormalization of the two-loop tadpoles,  $\phi = \phi_1, \phi_2$  and  $i, j = 1, 2$ .

One-loop counter-terms to the stop mass matrix  $M_{t_{12}}^2$  and the fields  $\tilde{t}_L$  and  $\tilde{t}_R$  read

$$m_{\tilde{t}_i}^2 \rightarrow m_{\tilde{t}_i}^2 + \delta m_{\tilde{t}_i}^{2(1)}, \quad (8.24a)$$

$$\theta_{\tilde{t}} \rightarrow \theta_{\tilde{t}} + \delta \theta_{\tilde{t}}^{(1)}, \quad (8.24b)$$

$$\tilde{t}_{L,R} \rightarrow \tilde{t}_{L,R} \sqrt{Z_{\tilde{t}_{L,R}}} \approx \tilde{t}_{L,R} \left(1 + \frac{1}{2} \delta Z_{\tilde{t}_{L,R}}^{(1)}\right). \quad (8.24c)$$

The stop fields are transformed into the physical components  $\tilde{t}_1$  and  $\tilde{t}_2$  via

$$\begin{pmatrix} \tilde{t}_1 \\ \tilde{t}_2 \end{pmatrix} = U_{\tilde{t}} \begin{pmatrix} \tilde{t}_L \\ \tilde{t}_R \end{pmatrix}, \quad (8.25)$$

where  $U_{\tilde{t}}$  is the stop mixing matrix defined in Eq. (2.54). The free-field kinetic terms of the stops are bilinear in the fields  $\tilde{t}_i$  and when computing the field renormalization counter-terms  $\propto |\partial_\mu \tilde{t}_i|^2$ ; these receive contributions from both the left-hand and right-hand components. To disentangle them, it is beneficial to introduce the field renormalization in the mass eigenstate basis

$$\begin{pmatrix} \tilde{t}_1 \\ \tilde{t}_2 \end{pmatrix} \rightarrow \mathcal{Z}_{\tilde{t}_{12}} \begin{pmatrix} \tilde{t}_1 \\ \tilde{t}_2 \end{pmatrix} = \begin{pmatrix} 1 + \frac{1}{2} \delta Z_{\tilde{t}_1}^{(1)} & \frac{1}{2} \delta Z_{\tilde{t}_{12}}^{(1)} \\ \frac{1}{2} \delta Z_{\tilde{t}_{21}}^{(1)} & 1 + \frac{1}{2} \delta Z_{\tilde{t}_2}^{(1)} \end{pmatrix} \begin{pmatrix} \tilde{t}_1 \\ \tilde{t}_2 \end{pmatrix}. \quad (8.26)$$

Now, a transformation of coordinates of the left- and right-handed field renormalization

matrix can be performed

$$U_{\tilde{t}} \begin{pmatrix} 1 + \frac{1}{2} \delta Z_{\tilde{t}_L}^{(1)} & 0 \\ 0 & 1 + \frac{1}{2} \delta Z_{\tilde{t}_R}^{(1)} \end{pmatrix} U_{\tilde{t}}^T \quad (8.27a)$$

$$= \begin{pmatrix} 1 + \frac{1}{2} (\cos^2 \theta_{\tilde{t}} \delta Z_{\tilde{t}_L}^{(1)} + \sin^2 \theta_{\tilde{t}} \delta Z_{\tilde{t}_R}^{(1)}) & \frac{1}{2} \sin \theta_{\tilde{t}} \cos \theta_{\tilde{t}} (\delta Z_{\tilde{t}_R}^{(1)} - \delta Z_{\tilde{t}_L}^{(1)}) \\ \frac{1}{2} \sin \theta_{\tilde{t}} \cos \theta_{\tilde{t}} (\delta Z_{\tilde{t}_R}^{(1)} - \delta Z_{\tilde{t}_L}^{(1)}) & 1 + \frac{1}{2} (\sin^2 \theta_{\tilde{t}} \delta Z_{\tilde{t}_L}^{(1)} + \cos^2 \theta_{\tilde{t}} \delta Z_{\tilde{t}_R}^{(1)}) \end{pmatrix}, \quad (8.27b)$$

where a comparison of the coefficients with Eq. (8.26) yields

$$\delta Z_{\tilde{t}_1}^{(1)} = \cos^2 \theta_{\tilde{t}} \delta Z_{\tilde{t}_L}^{(1)} + \sin^2 \theta_{\tilde{t}} \delta Z_{\tilde{t}_R}^{(1)}, \quad (8.28a)$$

$$\delta Z_{\tilde{t}_2}^{(1)} = \sin^2 \theta_{\tilde{t}} \delta Z_{\tilde{t}_L}^{(1)} + \cos^2 \theta_{\tilde{t}} \delta Z_{\tilde{t}_R}^{(1)}, \quad (8.28b)$$

$$\delta Z_{\tilde{t}_{12}}^{(1)} = \delta Z_{\tilde{t}_{21}}^{(1)} \quad (8.28c)$$

$$= \sin \theta_{\tilde{t}} \cos \theta_{\tilde{t}} (\delta Z_{\tilde{t}_R}^{(1)} - \delta Z_{\tilde{t}_L}^{(1)}) \quad (8.28d)$$

$$= \frac{\sin \theta_{\tilde{t}} \cos \theta_{\tilde{t}}}{\cos^2 \theta_{\tilde{t}} - \sin^2 \theta_{\tilde{t}}} (\delta Z_{\tilde{t}_2}^{(1)} - \delta Z_{\tilde{t}_1}^{(1)}). \quad (8.28e)$$

Now, the one-loop free field renormalization terms in the physical basis read

$$\delta \tilde{\mathbf{t}}_1^{(1)} = p^2 \delta Z_{\tilde{t}_1}^{(1)}, \quad (8.29a)$$

$$\delta \tilde{\mathbf{t}}_2^{(1)} = p^2 \delta Z_{\tilde{t}_2}^{(1)}, \quad (8.29b)$$

$$\delta \tilde{\mathbf{t}}_{12}^{(1)} = p^2 \delta Z_{\tilde{t}_{12}}^{(1)}. \quad (8.29c)$$

In analogy to the previous sections, the counter-terms arising from the squark potential get a field and a mass renormalization contribution. The one-loop squark potential counter-terms result from

$$\mathcal{L}_{\tilde{t}, \text{mass}}^{\text{ren}} \supset - \begin{pmatrix} \tilde{t}_1^\dagger & \tilde{t}_2^\dagger \end{pmatrix} \mathcal{Z}_{\tilde{t}_{12}}^T M_{\tilde{t}_{12}}^2 \mathcal{Z}_{\tilde{t}_{12}} \begin{pmatrix} \tilde{t}_1 \\ \tilde{t}_2 \end{pmatrix}, \quad (8.30)$$

where  $M_{\tilde{t}_{12}}^2$  is defined in Eq. (2.53) and  $\mathcal{Z}_{\tilde{t}_{12}}$  in Eq. (8.26). Expanding them up to the first order they read

$$\delta \mathbf{V}_{\tilde{t}_1 \tilde{t}_1} = m_{\tilde{t}_1}^2 \delta Z_{\tilde{t}_1}^{(1)} + \delta M_{\tilde{t}_1 \tilde{t}_1}^{2(1)}, \quad (8.31a)$$

$$\delta \mathbf{V}_{\tilde{t}_2 \tilde{t}_2} = m_{\tilde{t}_2}^2 \delta Z_{\tilde{t}_2}^{(1)} + \delta M_{\tilde{t}_2 \tilde{t}_2}^{2(1)}, \quad (8.31b)$$

$$\delta \mathbf{V}_{\tilde{t}_1 \tilde{t}_2} = \frac{1}{2} (m_{\tilde{t}_1}^2 + m_{\tilde{t}_2}^2) \delta Z_{\tilde{t}_{12}}^{(1)} + \delta M_{\tilde{t}_1 \tilde{t}_2}^{2(1)}. \quad (8.31c)$$

As the field renormalization matrices  $\mathcal{Z}_{\tilde{t}_{12}}$  are not diagonal, contributions from tree-level masses enter in the off-diagonal squark potential counter-terms, even though the mass matrix  $M_{\tilde{t}_{12}}^2$  is in diagonal form. The mass renormalization counter-terms read

$$\delta M_{\tilde{t}_{12}}^{2(1)} = U_{\tilde{t}} \delta M_{\tilde{t}_L \tilde{t}_R}^{2(1)} U_{\tilde{t}}^T \quad (8.32)$$

where the total differential of the matrix  $M_{\tilde{t}_{LR}}^2$  defines the one-loop counter-terms. Written out in explicit form, each contribution reads as follows,

$$\delta M_{\tilde{t}_1\tilde{t}_1}^{2(1)} = \delta m_{\tilde{t}_1}^{2(1)}, \quad \delta M_{\tilde{t}_2\tilde{t}_2}^{2(1)} = \delta m_{\tilde{t}_2}^{2(1)}, \quad \delta M_{\tilde{t}_1\tilde{t}_2}^{2(1)} = (m_{\tilde{t}_1}^2 - m_{\tilde{t}_2}^2) \delta\theta_{\tilde{t}}^{(1)}. \quad (8.33)$$

Collecting all counter-terms, the renormalized one-loop squark self-energies are given by

$$\hat{\Sigma}_{\tilde{t}_1\tilde{t}_1}^{(1)}(p^2) = \Sigma_{\tilde{t}_1\tilde{t}_1}^{(1)}(p^2) + \delta\tilde{\mathbf{t}}_1^{(1)} - \delta\mathbf{V}_{\tilde{t}_1\tilde{t}_1}^{(1)}, \quad (8.34a)$$

$$\hat{\Sigma}_{\tilde{t}_2\tilde{t}_2}^{(1)}(p^2) = \Sigma_{\tilde{t}_2\tilde{t}_2}^{(1)}(p^2) + \delta\tilde{\mathbf{t}}_2^{(1)} - \delta\mathbf{V}_{\tilde{t}_2\tilde{t}_2}^{(1)}, \quad (8.34b)$$

$$\hat{\Sigma}_{\tilde{t}_1\tilde{t}_2}^{(1)}(p^2) = \Sigma_{\tilde{t}_1\tilde{t}_2}^{(1)}(p^2) + \delta\tilde{\mathbf{t}}_{12}^{(1)} - \delta\mathbf{V}_{\tilde{t}_1\tilde{t}_2}^{(1)}. \quad (8.34c)$$

While the sum of all field renormalization contributions concerning inner fields vanishes, the massive contributions do not. All self-energies are renormalized on-shell where the following renormalization conditions were used, following Refs. [119, 320–323]

$$\text{Re}[\hat{\Sigma}_{\tilde{t}_1\tilde{t}_1}^{(1)}(m_{\tilde{t}_1}^2)] = 0, \quad (8.35a)$$

$$\text{Re}[\hat{\Sigma}_{\tilde{t}_2\tilde{t}_2}^{(1)}(m_{\tilde{t}_2}^2)] = 0, \quad (8.35b)$$

$$\text{Re}[\hat{\Sigma}_{\tilde{t}_1\tilde{t}_2}^{(1)}(m_{\tilde{t}_2}^2)] + \text{Re}[\hat{\Sigma}_{\tilde{t}_2\tilde{t}_1}^{(1)}(m_{\tilde{t}_1}^2)] = 0, \quad (8.35c)$$

$$\text{Re}\left[\frac{\partial}{\partial p^2} \hat{\Sigma}_{\tilde{t}_1\tilde{t}_1}^{(1)}(m_{\tilde{t}_1}^2)\right] = 0, \quad (8.35d)$$

$$\text{Re}\left[\frac{\partial}{\partial p^2} \hat{\Sigma}_{\tilde{t}_2\tilde{t}_2}^{(1)}(m_{\tilde{t}_2}^2)\right] = 0. \quad (8.35e)$$

These lead to the following determinations for the renormalization constants entering the mass counter-terms,

$$\delta m_{\tilde{t}_i}^{2(1)} = \text{Re}[\Sigma_{\tilde{t}_i\tilde{t}_i}^{(1)}(m_{\tilde{t}_i}^2)] \quad \text{with} \quad i = 1, 2, \quad (8.36)$$

$$\delta\theta_{\tilde{t}}^{(1)} = \frac{\text{Re}[\Sigma_{\tilde{t}_1\tilde{t}_2}^{(1)}(m_{\tilde{t}_1}^2)] + \text{Re}[\Sigma_{\tilde{t}_1\tilde{t}_2}^{(1)}(m_{\tilde{t}_2}^2)]}{2(m_{\tilde{t}_1}^2 - m_{\tilde{t}_2}^2)}, \quad (8.37)$$

and the field counter terms

$$\delta Z_{\tilde{t}_1}^{(1)} = -\text{Re}\left[\frac{\partial}{\partial p^2} \hat{\Sigma}_{\tilde{t}_1\tilde{t}_1}^{(1)}(m_{\tilde{t}_1}^2)\right], \quad (8.38)$$

$$\delta Z_{\tilde{t}_2}^{(1)} = -\text{Re}\left[\frac{\partial}{\partial p^2} \hat{\Sigma}_{\tilde{t}_2\tilde{t}_2}^{(1)}(m_{\tilde{t}_2}^2)\right]. \quad (8.39)$$

$\delta Z_{\tilde{t}_{12}}^{(1)}$  was already defined in Eq. (8.28e). In addition to the squarks, also the quark sector has to be renormalized. The top-quark mass is defined on-shell, yielding the one-loop counter-term

$$\delta m_t = \frac{m_t}{2} (\text{Re}[\Sigma_t^L(m_t^2)] + \text{Re}[\Sigma_t^R(m_t^2)] + 2 \text{Re}[\Sigma_t^S(m_t^2)]), \quad (8.40)$$

where  $\Sigma_t^{L,R}$  are the left- and right-handed components of the quark self-energy, respectively. The latter can be decomposed according to its Lorentz structure,

$$\Sigma_t(k) = \not{p}\Sigma_t^V(p^2) + \not{p}\gamma_5\Sigma_t^A(p^2) + m_t\Sigma_t^S(p^2), \quad (8.41)$$

where it is split into the scalar part of the quark self energy  $\Sigma_t^S$ , the vectorial  $\Sigma_t^V$  and the axial vectorial part  $\Sigma_t^A$ .

The renormalization of the stop-mixing soft breaking term  $X_{\tilde{t}}$ , defined in Eq. (2.55), reads

$$\delta X_{\tilde{t}}^{(1)} = X_{\tilde{t}} \left( \frac{1 - 2 \sin^2 \theta_{\tilde{t}}}{\sin \theta_{\tilde{t}} \cos \theta_{\tilde{t}}} \delta \theta_{\tilde{t}}^{(1)} + \frac{\delta m_{\tilde{t}_1}^{2(1)} - \delta m_{\tilde{t}_2}^{2(1)}}{m_{\tilde{t}_1}^2 - m_{\tilde{t}_2}^2} - \frac{\delta m_t^{2(1)}}{m_t} \right), \quad (8.42)$$

where the fact that neither  $\delta\mu^{(1)}$  nor  $\delta \tan \beta^{(1)}$  have couplings of the order  $\mathcal{O}(\alpha_s)$  was already taken into account. The renormalization constant  $\delta X_{\tilde{t}}^{(1)}$  enters in counter-term vertex insertions, e.g. in Fig. 8.5(d). All renormalization **constants** are independent of an external momentum, while the one-loop diagrams containing the counter-term insertions carry momentum dependence.

## 8.4 Treatment of the integrals

In Sec. 8.2, some relevant two-loop topologies have already been introduced diagrammatically, compare Fig. 8.2 in Sec. 8.2. Below, the following notation

$$T_{i_1 i_2 \dots i_n}(p^2, m_{i_1}^2, m_{i_2}^2, \dots, m_{i_n}^2) = (2\pi\mu_r)^{2(4-D)} \times \iint \frac{d^D q_1}{i\pi^2} \frac{d^D q_2}{i\pi^2} \frac{1}{(k_{i_1}^2 - m_{i_1}^2 + i\delta)(k_{i_2}^2 - m_{i_2}^2 + i\delta) \dots (k_{i_n}^2 - m_{i_n}^2 + i\delta)}, \quad (8.43)$$

for the scalar two-loop integrals is adopted, where  $p$  is the external momentum, the  $q_i$  are the loop momenta,  $\mu_r$  is the renormalization scale and the  $m_i$  denote the masses of the propagators. To comply with  $\overline{DR}$  renormalization, an additional factor of  $\gamma_E$  and  $\log(4\pi)$  is absorbed into the renormalization scale  $\mu_r$  as

$$\log(\mu_r) \rightarrow \log(\mu_r') = \log(\mu_r) + \log(4\pi) - \gamma_E. \quad (8.44)$$

The momenta are continued to  $D$  dimensions. The number  $n$  of indices of the two-loop integral  $T_{i_1 i_2 \dots i_n}$  corresponds to the number of propagators involved. The indices' numbers  $i_1, \dots, i_n = 1, \dots, 5$  label which propagator type appears in the integral. There are five different propagator types  $k_1, \dots, k_5$ , where the  $k_i$  read

$$k_1 = q_1, \quad k_2 = q_1 + p, \quad k_3 = q_2 - q_1, \quad k_4 = q_2, \quad k_5 = q_2 + p. \quad (8.45)$$

In accordance with Ref. [328], the letters  $A$ ,  $B$  and  $C$  are used to describe one-loop integrals with one, two and three external legs, respectively. Hence, a one-loop tadpole integral  $A$  can have one momentum-independent propagator of type  $k_1$  or  $k_4$ . A one-loop

bubble integral  $B$  is composed of two propagators of type  $k_1$  and  $k_2$  or  $k_4$  and  $k_5$ . The three-point vertex integrals  $C$  can carry dependence of two different external momenta  $p_1$  and  $p_2$  and have three propagators. In this calculation, however, being part of a self-energy computation, they depend on one external momentum  $p$  only and are therefore always reducible to two-point one-loop functions  $B$ .

### 8.4.1 Analytically known integrals

A series representation in the regulator  $\varepsilon$  of all one-loop integrals entering the sub-loop renormalization is known in analytical form and a variety of different representations is available. In this calculation, the approaches of Refs. [328–333] are used. At two loops, the resulting integrals from the reduction are mostly factorizing one-loop diagrams. Also all  $\varepsilon$ -divergent parts and a few finite parts of the two-loop integrals appearing in the calculation are known from Refs. [330–332, 334, 335]. Knowing the analytical representations of the divergent parts is vital in finding exact cancellation of all divergences. The full analytical cancellation of all divergences is achieved with the above mentioned integral representations, taking into consideration all counter-terms of Secs. 8.3.1 and 8.3.2, with their proper renormalization constants. The integral representations have all been cross-checked intensively with SECDEC and the GOLEM95 integral library [188, 336]. Especially for the imaginary parts these two tools were very useful.

Due to the occurrence of factorizing one-loop integrals, these must be known to first order in  $\varepsilon$  as they can contribute to the finite part through terms of the type

$$\left(\frac{a_1}{\varepsilon} + b_1 + c_1\varepsilon\right)\left(\frac{a_2}{\varepsilon} + b_2 + c_2\varepsilon\right) = \frac{a_1a_2}{\varepsilon^2} + \frac{a_1b_2 + a_2b_1}{\varepsilon} + b_1b_2 + a_1c_2 + a_2c_1 + \dots \quad (8.46)$$

All necessary parts for the one-loop integrals are known analytically [329–332]. As mentioned in the previous section, three-point integrals  $C$  result from the tensor reduction in the sub-loop renormalization part. The  $A$  and  $B$  integrals are UV divergent, the  $C$  integrals appear as finite integrals only because possible IR singularities are regulated by the massive propagators. Additionally, the third external leg occurs in the context of counter term insertions and therefore always has a vanishing external momentum, compare Figs. 8.4(a) and 8.4(c). It is due to this fact, that all three-point functions can be reduced to derivatives of two-point functions. A general three-point function reads

$$C_0(p_1^2, p_2^2, m_1^2, m_2^2, m_3^2) = \int d^D q \frac{1}{(q^2 - m_1^2)((q + p_1)^2 - m_2^2)((q + p_1 + p_2)^2 - m_3^2)} \quad (8.47)$$

Here, the notation of Ref. [328] is adopted. One example of a  $C$  integral occurring in



the calculation, to be reduced to the derivative of a two-point function, reads

$$C_0(p^2, 0, m_1^2, m_2^2, m_2^2) = \int d^D q \frac{1}{(q^2 - m_1^2)((q + p_1)^2 - m_2^2)((q + p_1)^2 - m_2^2)} \quad (8.48a)$$

$$= \frac{\partial}{\partial m_2^2} \int d^D q \frac{1}{(q^2 - m_1^2)((q + p_1)^2 - m_2^2)} \quad (8.48b)$$

$$= \frac{\partial}{\partial m_2^2} B_0(p^2, m_1, m_2) . \quad (8.48c)$$

From the derivative in the last line, the finiteness of the  $C$  integral becomes apparent; the divergent part of the two-point function does not depend on the masses.

The reduction to purely  $A$  and  $B$  integrals is especially useful as derivatives of all integrals occurring in the self-energies are required in the calculation of the field renormalization constants. Products of  $C$  integrals with  $A$  and  $B$  integrals, entering through the counter-term insertions, lead to finite three-point function contributions to the derivatives. Now, the derivatives of  $C$  integrals can be easily computed for simpler cases, but for the very general case of arbitrary masses in the loop and external momentum, analytical results are much more involved. For cross checks, the derivatives of the  $C$  integrals for the simpler cases could be computed using the algebraic output from SECDEC and integrating the expressions analytically.

Furthermore, the method of partial fractioning can be exploited, see Ref. [337]. It is used for the reduction of  $B$  integrals to one-point integrals. The method works at arbitrary loop order. At two loops, e.g., the vacuum integral  $T_{1134}$  function can be reduced as follows

$$\begin{aligned} T_{1134}(0, m_1^2, m_2^2, m_3^2, m_4^2) \\ = \frac{1}{m_1^2 - m_2^2} (T_{134}(0, m_1^2, m_3^2, m_4^2) - T_{134}(0, m_2^2, m_3^2, m_4^2)) , \end{aligned} \quad (8.49)$$

where the first entry in the integrals denotes a zero external momentum, in accordance with the notation set up in Eq. (8.43).

The additional relation

$$T_{1234}^{\text{div}}(p^2, m^2, m^2, m_3^2, m_4^2) = B_0^{\text{fin}}(p^2, m^2, m^2) + \frac{1}{2} , \quad (8.50)$$

is of use, where  $T_{1234}^{\text{div}}$  denotes the coefficient to the singly divergent  $\frac{1}{\varepsilon}$  term in the Laurent expansion of the  $T_{1234}$  integral in the regulator  $\varepsilon$ , and  $B_0^{\text{fin}}$  the finite part of the  $B_0$  integral. Relation Eq. (8.50) can be found as a direct consequence of the formulas in the appendix of Ref. [330]. Furthermore, the relation

$$C_0(0, p^2, m^2, m^2, m^2) = \int d^D q \frac{1}{(q^2 - m^2)^2((q + p)^2 - m^2)} \quad (8.51a)$$

$$= \frac{1}{2} \frac{\partial}{\partial m^2} B_0(p^2, m^2, m^2) , \quad (8.51b)$$

deduced from

$$\frac{\partial}{\partial m^2} B_0(p^2, m^2, m^2) \quad (8.52a)$$

$$= \int d^D q \frac{1}{(q^2 - m^2)((q+p)^2 - m^2)^2} + \int d^D q \frac{1}{(q^2 - m^2)^2((q+p)^2 - m^2)} \quad (8.52b)$$

$$= 2 \int d^D q \frac{1}{(q^2 - m^2)^2((q+p)^2 - m^2)}, \quad (8.52c)$$

helps achieving a stable cancellation of the UV poles. A momentum shift was performed in the first integral of Eq. (8.52b).

The tensor coefficients  $C_2$  and  $B_1$  can be treated by expanding their numerators. To give an example, the  $C_2$  tensor coefficients appearing in this calculation are of the type

$$C_2(0, p^2, m^2, m^2, m^2) \quad (8.53a)$$

$$= \frac{1}{p^2} \int d^D q \frac{q \cdot p}{(q^2 - m^2)^2((q+p)^2 - m^2)} \quad (8.53b)$$

$$= \frac{1}{2p^2} \int d^D q \frac{(q+p)^2 - q^2 - p^2 + m^2 - m^2}{(q^2 - m^2)^2((q+p)^2 - m^2)} \quad (8.53c)$$

$$= \frac{1}{2p^2} \left( B_0(0, m^2, m^2) - B_0(p^2, m^2, m^2) - p^2 C_0(0, p^2, m^2, m^2, m^2) \right). \quad (8.53d)$$

Similarly, the  $B_1$  coefficient can be reduced to  $B_0$  and  $A_0$  integrals.

After the cancellation of all divergent parts, the finite parts must be treated. These maximally include finite terms of two-loop integrals and terms up to the order  $\mathcal{O}(\varepsilon)$  in the one-loop case. As is visible from Eq. (8.50), the finite part of the one-loop bubble is part of a sub-divergence of the two-loop integral  $T_{1234}$ . This fact suggests that one-loop terms of order  $\mathcal{O}(\varepsilon)$  may contribute to the finite parts of some of the two-loop integrals. As a matter of fact,  $\mathcal{O}(\varepsilon)$  parts of the integral

$$\frac{\partial}{\partial m_1^2} B_0(p^2, m_1^2, m_2^2) = \int \frac{d^D q_1}{i\pi^2 (2\pi\mu)^{D-4}} \frac{1}{(k_1^2 - m_1^2)^2 (k_2^2 - m_2^2)}, \quad (8.54)$$

appear in sums and subtractions with the finite part of the integral

$$T_{11234}(p^2, m_1^2, m_1^2, m_2^2, m_3^2, m_4^2) = \frac{\partial}{\partial m_1^2} T_{1234}(p^2, m_1^2, m_2^2, m_3^2, m_4^2). \quad (8.55)$$

An analytic result of the finite part of the latter is not available. As the unknown integrals are computed numerically with version 2 of SECDEC, analytic and numeric results enter the self-energies and their counter-terms. A stable evaluation of the analytically available and the numerically computed functions is required. The analytically available integrals appearing in the final result are the one-point functions  $A_0$ , the scalar two-point integral  $B_0$ , the derivative of  $B_0$  by one mass, Eq. (8.54), the two-loop vacuum diagram

with arbitrary masses  $T_{134}$ , and the two-loop bubble diagram  $T_{234}$  with two massive propagators of the same mass and one massless propagator. Explicit expressions for the integrals are given in App. A.1. For the evaluation of the analytical integrals beyond threshold, the proper analytical continuation into the complex plane is essential. Square roots, as well as logarithms, get an imaginary part as soon as their arguments are negative. The correct prescription for the analytical continuation is given by the causal  $i\delta$  appearing in the Feynman propagators. For the kinematic invariants, they separately read

$$m^2 \rightarrow m^2 - i\delta , \quad (8.56a)$$

$$p^2 \rightarrow p^2 + i\delta , \quad (8.56b)$$

$$s_{ij} \rightarrow s_{ij} + i\delta . \quad (8.56c)$$

In practice, the infinitesimal quantity  $\delta$  must be assigned a tiny, but not infinitesimally small value. This can lead to numerical instabilities in the evaluation of an analytical result. These can be evaded by explicitly choosing a Riemann sheet of the square root

$$\sqrt{a^2 \pm i\delta} = \begin{cases} \sqrt{a^2} & , a^2 > 0 \\ \pm i\sqrt{-a^2} & , a^2 < 0 , \end{cases} \quad (8.57)$$

and the logarithm

$$\log(a^2 \pm i\delta) = \begin{cases} \log(a^2) & , a^2 > 0 \\ \log(-a^2) \pm i\pi & , a^2 < 0 , \end{cases} \quad (8.58)$$

as shown, e.g., in Ref. [332]. At the one-loop level, thresholds can be parametrized by square roots of the fully symmetric Källén function

$$\lambda(x, y, z) = x^2 + y^2 + z^2 - 2xy - 2xz - 2yz , \quad (8.59)$$

which frequently appears in the analytic expressions. Its sign in different parameter regions is

$$\lambda(x, y, z) \begin{cases} < 0 , & (y + z) - 2\sqrt{yz} < x < (y + z) + 2\sqrt{yz} \\ = 0 , & x = (y + z) \pm 2\sqrt{yz} \\ > 0 , & \text{else} \end{cases} . \quad (8.60)$$

With this knowledge at hand, all thresholds entering from the on-shell renormalization of the sub-loop can be explained as the square root of the Källén function becomes complex for a negative  $\lambda(x, y, z)$ .

### 8.4.2 Analytically unknown integrals

The evaluation of some of the integrals entering the calculation are not known. This concerns different topologies of the integrals  $T_{234}$ ,  $T_{1234}$ ,  $T_{11234}$  and  $T_{12345}$ , depicted in

Fig. 8.2. While the evaluation is straightforward in the massless cases, the all-massive cases are very hard to compute in a full analytical way. This is due to the fact that neither the  $T_{234}$  nor the  $T_{12345}$  can be expressed in terms of polylogarithms, see Refs. [338, 339] and references therein. An analytical description of the diagram  $T_{234}$  in terms of generalized Lauricella functions was found in Ref. [338]. The Appell functions appearing in their result are extremely hard to evaluate in a full analytical way, compare, e.g. Ref. [340]. Up to date, only one-dimensional integral representations are available for the evaluation of the  $T_{234}$  integral with arbitrary masses. Special cases (large momentum expansion, equation of masses) of the  $T_{234}$  integral are available, see Refs. [330, 331, 341, 342]. The general result for different masses in the three propagators is still discussed today, among physicists [343–345] and mathematicians [346] alike. A description of the finite  $T_{12345}$  function in terms of a double integral representation [347], and in terms of a single integral representation [335], is also available. Furthermore, special cases and asymptotic limits are known, see Refs. [330, 348–350]. The numerical evaluation of integrals not accessible with purely analytical methods can be achieved, benefitting from the automated setup of the program SECDEC.

### Numerical computation of two-point two-loop integrals

The aforementioned four integral topologies  $T_{234}$ ,  $T_{1234}$ ,  $T_{11234}$  and  $T_{12345}$  appear in 34 different mass configurations. These involve up to four different masses, in addition to the mass scale given by the external momentum  $p^2$ . They are all computed with SECDEC. For the whole evaluation, the integrator Divonne contained in the CUBA LIBRARY [302, 303] is used. The integrator uses a deterministic algorithm and can reach very accurate results in integrations of few, but more than one, Feynman parameters. An additional acceleration was achieved by introducing user-defined thresholds to the program SECDEC, see Secs. 6.3.8 and A.2. This allows the user to define a lowest threshold condition. Once it is met, SECDEC switches to a deformation of the integration contour into the complex plane. The kinematic values can differ by up to 14 orders of magnitude. The evaluation of a single phase space point for the most complicated topology, to reach a relative accuracy of at least  $10^{-5}$ , ranges between 0.01 and 100 seconds on an Intel i7 processor, where the larger timings are for points very close to a kinematic threshold. The huge differences in the kinematic invariants enter, for instance, when choosing a small value for the squared external momentum, while testing large squared masses. These configurations were of special interest in the performance of checks against the results obtained for vanishing external momenta. For two representative results, see Fig. 8.7. The configuration in Fig. 8.7(a) has three different mass scales where the first two masses can be associated with the top mass  $m_1 = m_2 = 173.2$  GeV, the third mass with one possible value for a stop mass  $m_3 = 826.8$  GeV and the fourth mass to a value for the gluino  $m_4 = 1.5$  TeV. In Fig. 8.7(b), the numerical values  $m_1 = 1173.2$  GeV,  $m_2 = 826.8$  GeV,  $m_3 = 1.5$  TeV and  $m_4 = 173.2$  GeV are chosen. The relative accuracy of the plots is beyond  $10^{-5}$ . When evaluating a specific scenario, some integrals needed to be evaluated up to a numerical relative accuracy of at least  $10^{-5}$  to make up for cancellations appearing between analytically evaluated integrals and numerical ones. For

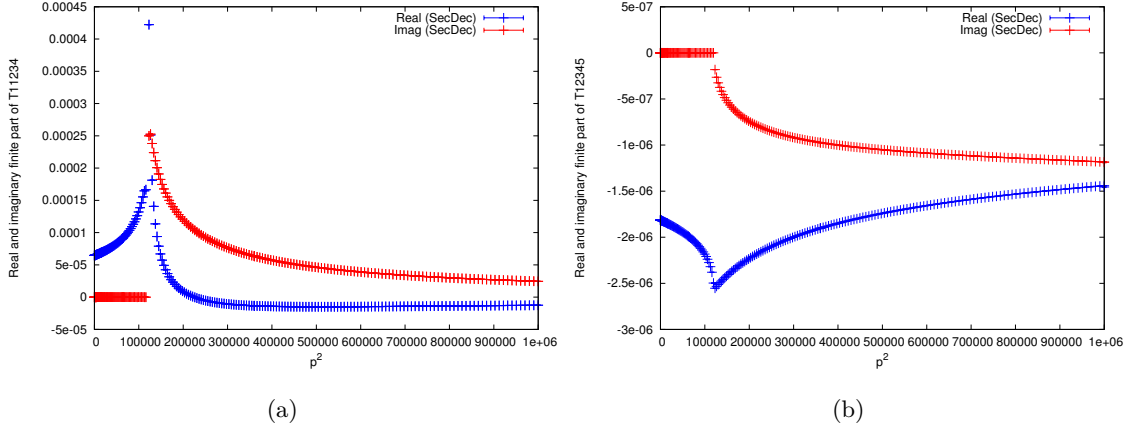


Figure 8.7: Two representative numerical SECDEC results for the integrals of type 8.2(d) in (a), and of type 8.2(e) in (b), with three and four different masses, respectively. In (a), the values  $m_1 = m_2 = 173.2$ ,  $m_3 = 826.8$  and  $m_4 = 1.5$  are used. In (b), the numerical values  $m_1 = 1173.2$ ,  $m_2 = 826.8$ ,  $m_3 = 1.5$  and  $m_4 = 173.2$  are chosen. Due to the high accuracy of the numerical integration, error bars are barely seen.

the evaluation of an arbitrary scenario with arbitrary rMSSM parameters, this accuracy was therefore demanded for every SECDEC integral.

## 8.5 Evaluation of the additional shifts to the Higgs-boson masses

The calculation is performed in the  $\phi_1$ - $\phi_2$  basis. To be consistent with all other higher-order contributions to the Higgs-boson masses incorporated in the public program FEYN-HIGGS, the renormalized self-energies in the  $\phi_1$ - $\phi_2$  basis can be rotated into the physical  $h^0$ - $H^0$  basis, where the tree-level propagator matrix is diagonal, via

$$\hat{\Sigma}_{H^0 H^0}^{(2)} = \cos^2 \alpha \hat{\Sigma}_{\phi_1^0 \phi_1^0}^{(2)} + \sin^2 \alpha \hat{\Sigma}_{\phi_2^0 \phi_2^0}^{(2)} + \sin(2\alpha) \hat{\Sigma}_{\phi_1^0 \phi_2^0}^{(2)}, \quad (8.61a)$$

$$\hat{\Sigma}_{h^0 h^0}^{(2)} = \sin^2 \alpha \hat{\Sigma}_{\phi_1^0 \phi_1^0}^{(2)} + \cos^2 \alpha \hat{\Sigma}_{\phi_2^0 \phi_2^0}^{(2)} - \sin(2\alpha) \hat{\Sigma}_{\phi_1^0 \phi_2^0}^{(2)}, \quad (8.61b)$$

$$\hat{\Sigma}_{h^0 H^0}^{(2)} = \sin \alpha \cos \alpha (\hat{\Sigma}_{\phi_2^0 \phi_2^0}^{(2)} - \hat{\Sigma}_{\phi_1^0 \phi_1^0}^{(2)}) + \cos(2\alpha) \hat{\Sigma}_{\phi_1^0 \phi_2^0}^{(2)}, \quad (8.61c)$$

where  $\alpha$  is the tree-level mixing angle and using Eq. (2.5). The former is expressible in terms of the parameters  $\tan \beta$ ,  $m_{A^0}$  and  $m_Z$ , see Eq. (2.30). The resulting new contributions to the neutral  $\mathcal{CP}$ -even Higgs-boson self-energies, containing all momentum-dependent and additional constant terms, are assigned to the differences

$$\Delta \hat{\Sigma}_{ab}^{(2)}(p^2) = \hat{\Sigma}_{ab}^{(2)}(p^2) - \hat{\Sigma}_{ab}^{(2)}(0), \quad ab = \{H^0 H^0, h^0 H^0, h^0 h^0\}. \quad (8.62)$$

Note the tilde (not hat) on  $\tilde{\Sigma}^{(2)}(0)$ , which signifies that not only the self-energies are evaluated at zero external momentum but also the corresponding counter-terms, following Refs. [117–119]. A finite shift  $\Delta\hat{\Sigma}^{(2)}(0)$  therefore remains in the limit  $p^2 \rightarrow 0$  due to  $\delta m_{A^0}^{2(2)} = \text{Re} \Sigma_{A^0 A^0}^{(2)}(m_{A^0}^2)$  being computed at  $p^2 = m_{A^0}^2$  in  $\hat{\Sigma}^{(2)}$ , but at  $p^2 = 0$  in  $\tilde{\Sigma}^{(2)}$ , as discussed in Sec. 8.3.1.

Subtracting the finite shift of  $\delta m_{A^0}^{2(2)}$ , the  $\Delta\hat{\Sigma}_{ab}^{(2)}(p^2)$  in Eq. (8.62) must vanish. This limit was tested numerically, see Sec. 8.4.2. Moreover, the zero momentum limit was checked analytically, deriving expressions for the vacuum diagrams  $T_{1134}$ ,  $T_{11134}$  and  $T_{11344}$  and using an available expression for  $T_{134}$ . The relations were computed from  $T_{134}$  using derivatives of the integral by the masses and partial fractioning as mentioned in Ref. [337]. Expressions for the vacuum diagram  $T_{134}$  with different mass configurations can be found in Refs. [349, 351]. All deduced integrals were checked with SECDEC, including the three-propagator vacuum bubble  $T_{134}$ . For further comparison, the expression for the  $T_{1134}$  integral of Ref. [352] could be used.

The higher-order corrected  $\mathcal{CP}$ -even Higgs-boson masses in the MSSM are obtained from the corresponding propagators dressed by their self-energies. Inserting the fields  $h^0$  and  $H^0$  in Eq. (2.64), the inverse propagator matrix in the  $h^0$ - $H^0$  basis is given by

$$(\Delta_{\text{Higgs}})^{-1} = -i \begin{pmatrix} p^2 - m_{H^0}^2 + \hat{\Sigma}_{H^0 H^0}(p^2) & \hat{\Sigma}_{h^0 H^0}(p^2) \\ \hat{\Sigma}_{h^0 H^0}(p^2) & p^2 - m_{h^0}^2 + \hat{\Sigma}_{h^0 h^0}(p^2) \end{pmatrix}. \quad (8.63)$$

The  $\mathcal{CP}$ -even Higgs boson masses are determined by the poles of the  $h^0$ - $H^0$ -propagator matrix. This is equivalent to solving the equation

$$\left[ p^2 - m_{h^0}^2 + \hat{\Sigma}_{h^0 h^0}(p^2) \right] \left[ p^2 - m_{H^0}^2 + \hat{\Sigma}_{H^0 H^0}(p^2) \right] - \left[ \hat{\Sigma}_{h^0 H^0}(p^2) \right]^2 = 0, \quad (8.64)$$

yielding the loop-corrected pole masses,  $M_h$  and  $M_H$ .

### 8.5.1 Phenomenological motivation for two different scenarios

Suitable scenarios to analyze the influence of the new self-energies on the Higgs-boson mass shifts should cover a range of experimentally allowed parameter space, in addition to maximizing the resulting additional shifts. It should be noted, that a complete parameter scan over the in principle more than one hundred free parameters of the MSSM is not feasible and the experimental sensitivity to collectively constrain many parameters is not sufficient with present experiments. In practice, parameter scans are therefore done for a smaller set of parameters with the highest phenomenological impact on the rMSSM Higgs sector, see e.g. Ref. [353]. These reflections result in an  $m_h^{\text{max}}$  and a light stop scenario, motivated in and following analyses from Refs. [353, 354].

The MSSM input parameters entering the calculation are

$$m_{\tilde{g}}, m_{\tilde{t}_1}, m_{\tilde{t}_2}, \theta_{\tilde{t}}, m_t, \mu, m_{A^0}, \tan \beta.$$

The benchmark scenarios of Ref. [354] are given in terms of the following set of MSSM input parameters

$$m_{\tilde{g}}, X_t, M_{\text{SUSY}}, m_t, \mu, m_{A^0}, \tan\beta .$$

In the conversion to the latter parameters, the left- and right-handed soft SUSY breaking stop mass parameters are equated and set to the soft SUSY breaking scale

$$M_{\text{SUSY}} := M_{\tilde{t}_L} = M_{\tilde{t}_R} . \quad (8.65)$$

The two stop masses  $m_{\tilde{t}_1}, m_{\tilde{t}_2}$  and the angle  $\theta_{\tilde{t}}$  are expressed in terms of  $M_{\text{SUSY}}$ , the soft SUSY breaking mixing parameter  $X_{\tilde{t}}$ , the top-quark mass  $m_t$  and  $m_Z$  using Eq. (2.50) with  $\tilde{u} = \tilde{t}$ . The value for the top mass  $m_t = 173.2$  GeV is used in both scenarios and taken from the latest combination of all top-mass measurements undertaken by the D0 and CDF collaborations [355], in agreement with the top mass resulting from the combination of the latest ATLAS, CMS results, see Ref. [356,357]. For the computation of the Higgs-boson mass shifts, a value of  $m_Z = 91.1875$  GeV [358] is used.<sup>1</sup>

Keeping the top and  $Z$  boson mass fixed, the stop masses can be plotted with respect to the ratio  $X_{\tilde{t}}/M_{\text{SUSY}}$ . For the limit  $X_{\tilde{t}} \rightarrow 0$ , the squark mass eigenstates are equal. Following the analyses in Ref. [353], degenerate stop masses are excluded, if the observed new particle at the LHC is associated with the light Higgs-boson at around  $m_h^{\text{obs}} \approx 125.7$  GeV. Therefore, a maximal mixing of  $X_{\tilde{t}} = 2 M_{\text{SUSY}}$  is assumed in all scenarios, varying only the SUSY breaking scale  $M_{\text{SUSY}}$  between 500 GeV and 1 TeV.

The gluino mass parameter  $m_{\tilde{g}}$  enters the MSSM Higgs-boson mass predictions from two-loop order on. It is therefore of special interest to analyze its impact on the MSSM Higgs-boson masses. The gluino mass can be indirectly constrained from the hitherto non-observation of a second neutral Higgs-boson.

The higgsino parameter  $\mu$  enters the self-energies through the trilinear coupling. In all scenarios considered, it is chosen  $\mu = 200$  GeV, in accordance with Ref. [353,354].

The  $\mathcal{CP}$ -odd  $A^0$  boson mass and  $\tan\beta$  are left as free parameters and can be varied between  $90 \text{ GeV} \leq m_{A^0} \leq 1 \text{ TeV}$  and  $1 \leq \tan\beta \leq 60$  respectively, compare Ref. [353]. When choosing  $m_{A^0}$  to be rather light, the observed particle  $m_h^{\text{obs}}$  GeV can be associated with the heavy Higgs-boson leaving room for an additional lighter state.

The corresponding renormalization scale,  $\mu_r$ , is set to  $\mu_r = m_t$  in all numerical evaluations. The scale uncertainties are expected to be much smaller than the parametric uncertainties due to variations of parameters like  $\tan\beta, m_{A^0}, m_{\tilde{g}}, m_{\tilde{t}}$ .

<sup>1</sup>For simplicity, the  $Z$  boson mass contribution is not taken into account in the Figs. 8.8, 8.9, 8.10 and 8.11.

### 8.5.2 Renormalized $\mathcal{O}(\alpha_s\alpha_t)$ self-energies

#### Scenario 1: $m_h^{\max}$ scenario

Scenario 1 is oriented at the  $m_h^{\max}$  scenario described in Ref. [354]. The following values are assigned to the MSSM parameters,

$$\begin{aligned} m_t &= 173.2 \text{ GeV}, \quad M_{\text{SUSY}} = 1 \text{ TeV}, \quad X_t = 2 M_{\text{SUSY}}, \\ m_{\tilde{g}} &= 1500 \text{ GeV}, \quad \mu = 200 \text{ GeV}, \end{aligned} \quad (8.66)$$

leading to stop mass values of

$$m_{\tilde{t}_1} = 826.8 \text{ GeV}, \quad m_{\tilde{t}_2} = 1173.2 \text{ GeV}.$$

With the introduction of the momentum dependence, thresholds occur in the self-energy diagrams when the external momentum  $p = \sqrt{p^2}$ , in the time-like region, is such that a cut of the diagram would correspond to the on-shell production of the massive particles of the cut propagators, compare the discussion of Sec. 5.1. The resulting imaginary parts will enter in the search for the complex poles of the inverse propagator matrix of the Higgs-bosons. Therefore it is interesting to study the behavior of the real and imaginary parts of the self-energies. The momentum-dependent parts of the renormalized two-loop self-energies are shown in the physical basis, Eq. (8.62), for two different values of  $\tan\beta$ ,  $\tan\beta = 5$  and  $\tan\beta = 20$ , at a fixed  $A^0$ -boson mass  $m_{A^0} = 250$  GeV, see Fig. 8.8. The data points are not connected by a line in order to show that each numerical point is obtained from a calculation of the 34 analytically unknown integrals with the program SECDEC. The insets in Fig. 8.8 magnify the region  $p^2 \leq (125 \text{ GeV})^2$ , where it can be observed that for  $p^2 \rightarrow 0$ , the subtracted self-energies are not exactly zero. As mentioned at the beginning of this section, this is due to the fact that the on-shell renormalization condition for the  $A^0$ -boson self-energy is defined differently with regard to the calculation without momentum dependence. The resulting constant contributions are additionally suppressed by factors  $\sin^2\beta$ ,  $\sin\beta \cos\beta$  and  $\cos^2\beta$  appearing in the counter-terms  $\delta V_{\phi_1^0\phi_1^0}^{(2)}$ ,  $\delta V_{\phi_2^0\phi_2^0}^{(2)}$  and  $\delta V_{\phi_1^0\phi_2^0}^{(2)}$ , respectively, see Eqs. (8.17).

The imaginary part is independent of the  $A^0$ -boson mass, as this mass parameter solely appears in the counter-terms of  $\overline{\text{DR}}$  renormalized quantities and the  $\delta m_{A^0}^{2(2)}$  counter-term, where only the real part contributes. Therefore, the imaginary parts do not contain additional constant terms, compare Fig. 8.8. As to be expected, the imaginary parts are zero below the  $t\bar{t}$  production threshold at  $p = 2m_t$ , which results from the fact that the top mass is the smallest mass appearing in the loop diagrams. Beyond this threshold, the imaginary parts are nonzero but of the same order of magnitude as the real parts. From these observations, the mass shifts in the region below the first threshold at  $p = 2m_t$  are expected not to be large.



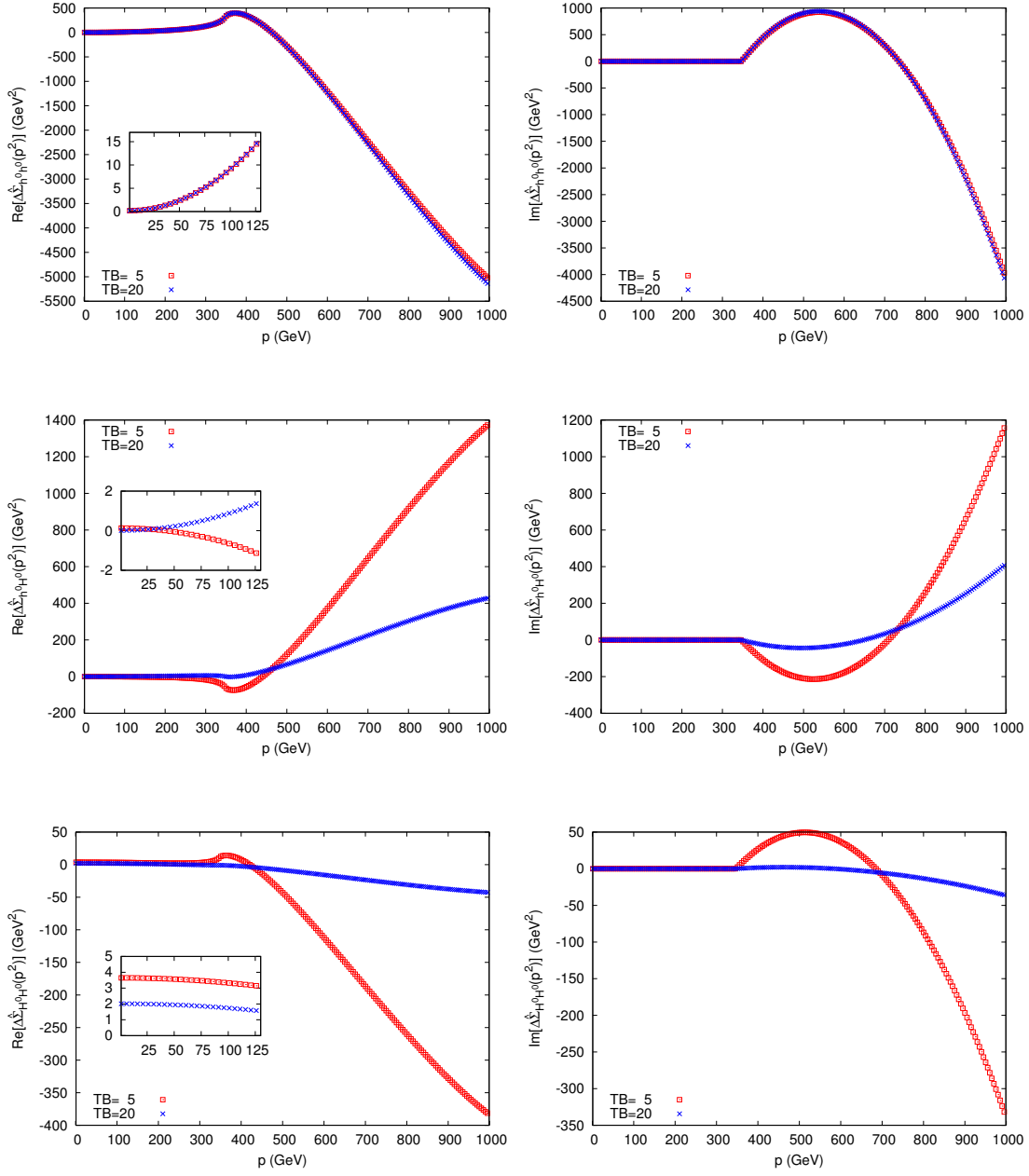


Figure 8.8: Momentum dependence of the real (left column) and imaginary (right column) parts of the two-loop selfenergies  $\Delta_{h^0 h^0}^{\hat{\Sigma}}, \Delta_{h^0 H^0}^{\hat{\Sigma}}, \Delta_{H^0 H^0}^{\hat{\Sigma}}$ , within scenario 1, for  $\tan \beta = 5$  (red squares) and  $\tan \beta = 20$  (blue crosses) and  $m_{A^0} = 250$  GeV. One can see that the selfenergies change substantially beyond the threshold at  $p^2 = (2m_t)^2$ .

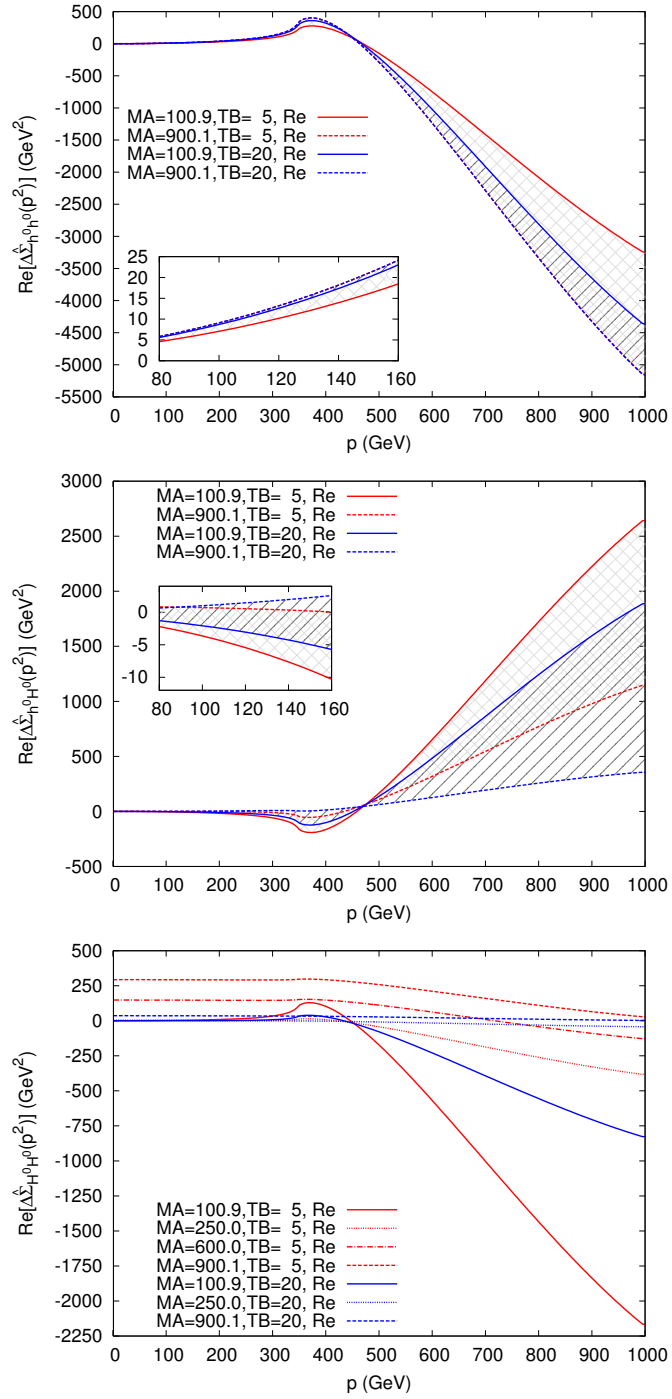


Figure 8.9: Momentum dependence of the real part of the two-loop self-energies  $\Delta\hat{\Sigma}_{h^0 h^0}$ ,  $\Delta\hat{\Sigma}_{h^0 H^0}$ ,  $\Delta\hat{\Sigma}_{H^0 H^0}$ , within scenario 1, for two different values of  $\tan\beta$  and a range of  $m_{A^0}$  values.

Similar results, now including a variation of  $m_{A^0}$  are shown in Fig. 8.9. In the upper plot for  $\Delta\hat{\Sigma}_{h^0h^0}$  and in the middle plot for  $\Delta\hat{\Sigma}_{h^0H^0}$  the solid lines depict  $m_{A^0} \sim 100$  GeV, while the dashed lines are for  $m_{A^0} \sim 900$  GeV. In these plots the light shading covers the range for  $\tan\beta = 5$ , while the dark shading for  $\tan\beta = 20$ . In the lower plot for  $\Delta\hat{\Sigma}_{H^0H^0}$  results for  $m_{A^0} \sim 100, 250, 600, 900$  GeV are shown as solid, dotted, dot-dashed, dashed lines, respectively (and shading has been omitted). For  $\Delta\hat{\Sigma}_{h^0h^0}$  at low values of the momentum  $p$  only a small variation with  $m_{A^0}$  can be observed. For  $p$  and  $m_{A^0}$  large, the contributions to the self-energy are bigger. In  $\Delta\hat{\Sigma}_{h^0H^0}$  larger effects are observed at smaller  $m_{A^0}$  for both, small and large  $p$  values. For  $\Delta\hat{\Sigma}_{H^0H^0}$ , on the other hand, at low  $p$  values, large effects can be observed for large  $m_{A^0}$  due to the aforementioned counter-term contribution  $\sim \delta m_{A^0}^{2(2)} = \text{Re} \Sigma_{A^0A^0}^{(2)}(m_{A^0}^2)$ . At large  $p$ , as before, small  $m_{A^0}$  values give a more sizable contribution.

### Scenario 2: Light stop scenario

Scenario 2 is oriented at the “light-stop scenario” of Ref. [354]<sup>2</sup>. The following values are assigned to the MSSM parameters

$$\begin{aligned} m_t &= 173.2 \text{ GeV}, \quad M_{\text{SUSY}} = 0.5 \text{ TeV}, \quad X_t = 2 M_{\text{SUSY}}, \\ m_{\tilde{g}} &= 1600 \text{ GeV}, \quad \mu = 200 \text{ GeV}, \end{aligned} \quad (8.67)$$

leading to stop mass values of

$$m_{\tilde{t}_1} = 326.8 \text{ GeV}, \quad m_{\tilde{t}_2} = 673.2 \text{ GeV}.$$

Scenario 2 is analyzed with the same set of plots shown for scenario 1. The effects of the new momentum-dependent two-loop contributions on the renormalized Higgs-boson self-energies,  $\Delta\hat{\Sigma}_{ab}(p^2)$ , are shown in Fig. 8.10. As before, separate results are shown for the real and imaginary parts of the self-energies. An additional threshold beyond the top-mass threshold appears at  $p = 2m_{\tilde{t}_1}$ . Analogously to scenario 1, the largest contributions in the region below 200 GeV arise in the real part of  $\Delta\hat{\Sigma}_{h^0h^0}$  amounting to about  $15 \text{ GeV}^2$  at  $p = 125 \text{ GeV}$ , where the dependence on the value of  $\tan\beta$  is rather weak. The imaginary part equals the one of scenario 1 up to the  $p = 2m_{\tilde{t}_1}$  threshold. The discontinuity at the latter enters through the integral involving the derivative of the  $B_0$  function with respect to  $m_{\tilde{t}_1}^2$ ,  $\frac{\partial}{\partial m_{\tilde{t}_1}^2} B_0(p^2, m_{\tilde{t}_1}^2, m_{\tilde{t}_1}^2)$ , see Sec. 8.4.1 and Eq. (8.51b) therein.

The dependence of  $\Delta\hat{\Sigma}_{ab}(p^2)$  on  $m_{A^0}$  is shown in Fig. 8.11, using the same line styles as in Fig. 8.9. The curves show the same qualitative behavior as in Fig. 8.10, exhibiting again the new threshold at  $p = 2m_{\tilde{t}_1}$ . In general, outside the threshold region the effects in scenario 2 are slightly smaller than in scenario 1.

<sup>2</sup>While the original scenario in Ref. [354] is challenged by recent scalar-top searches at ATLAS and CMS, a small modification in the gaugino-mass parameters (which play no or only a very minor role here) to  $M_1 = 340 \text{ GeV}$ ,  $M_2 = \mu = 400 \text{ GeV}$  leads to a SUSY spectrum that is very difficult to test at the LHC.

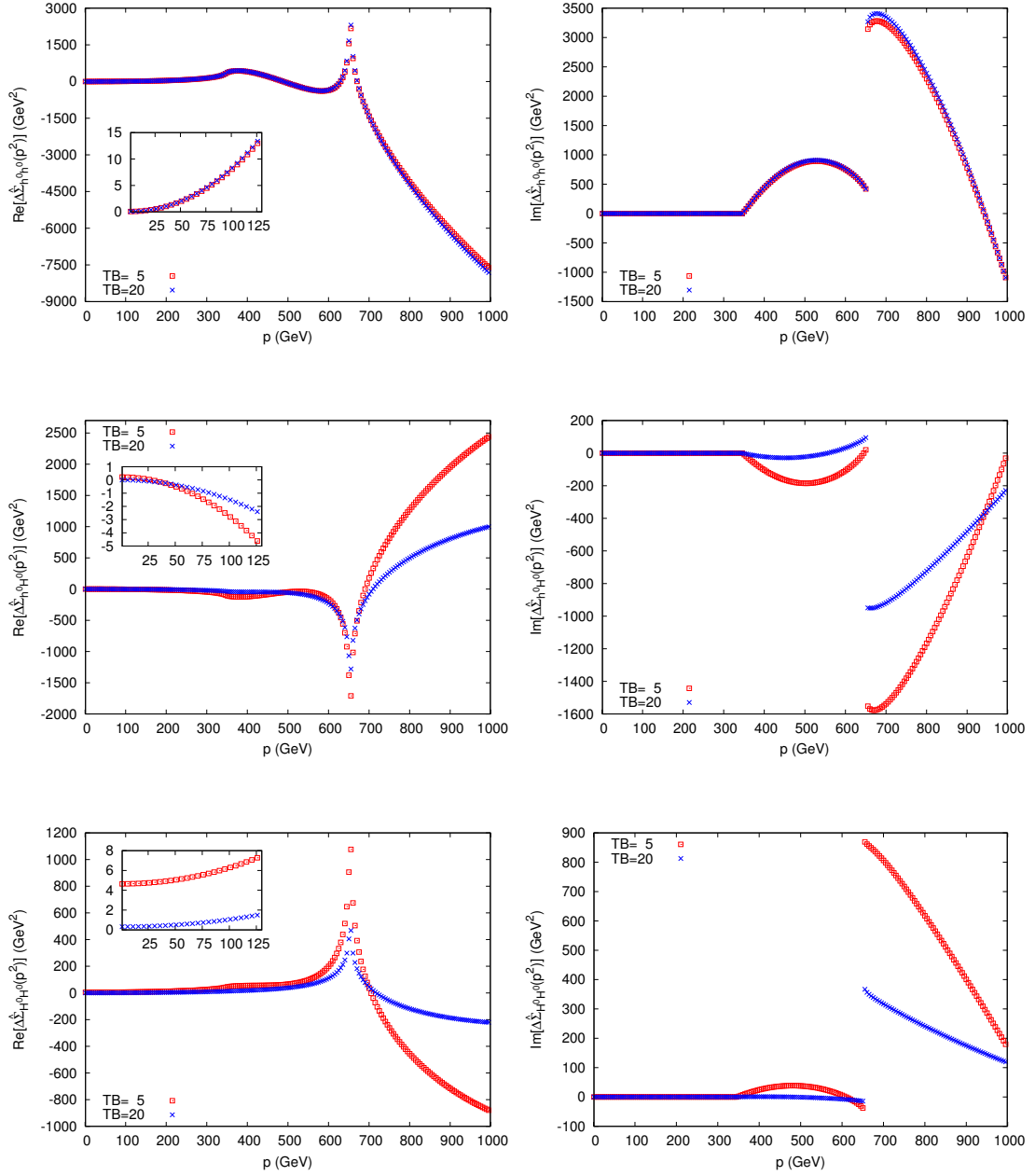


Figure 8.10: Momentum dependence of the real and imaginary parts of the two-loop self-energies  $\Delta\hat{\Sigma}_{h^0 h^0}$ ,  $\Delta\hat{\Sigma}_{h^0 H^0}$ ,  $\Delta\hat{\Sigma}_{H^0 H^0}$  within scenario 2, with  $\tan\beta = 5, 20$  and  $m_{A^0} = 250$  GeV with the same color coding as in Fig. 8.8.

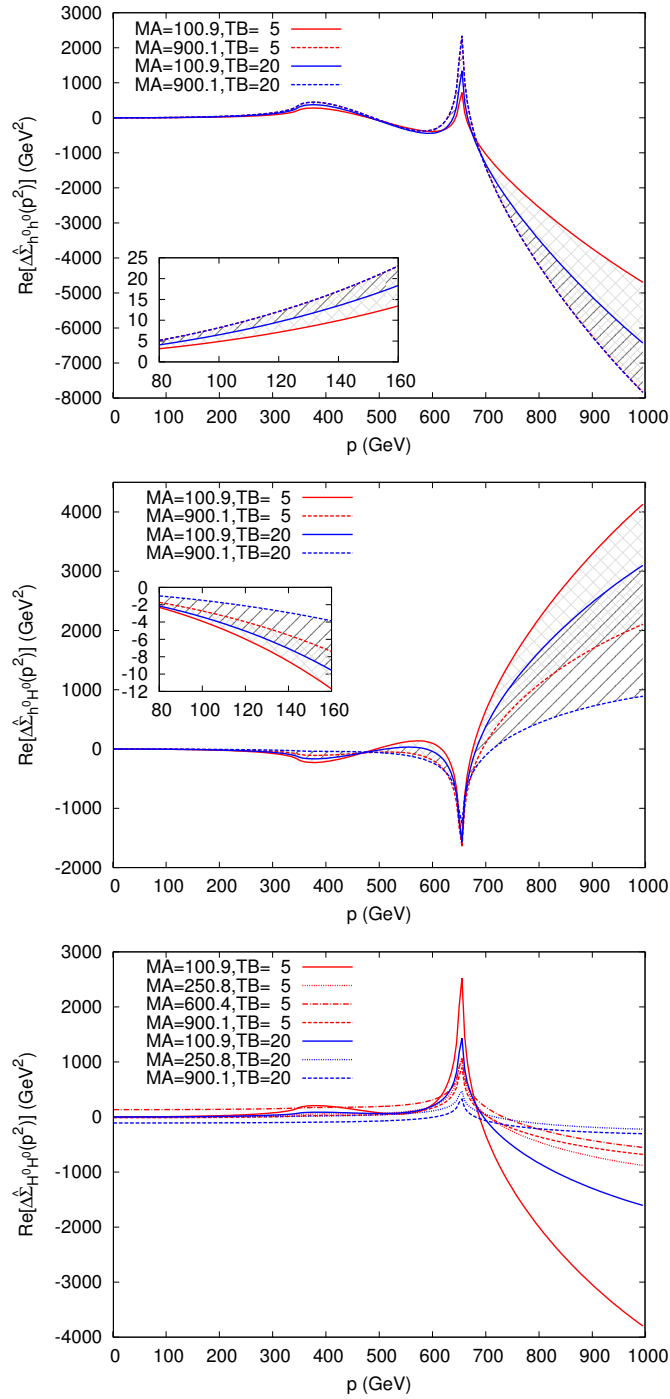


Figure 8.11: Momentum dependence of the real parts of the two-loop self-energies  $\Delta_{h^0 h^0}^{\hat{\Sigma}}$ ,  $\Delta_{h^0 H^0}^{\hat{\Sigma}}$ ,  $\Delta_{H^0 H^0}^{\hat{\Sigma}}$  in scenario 2 for two different values of  $\tan \beta$  and various values of  $m_{A^0}$  (see text).

### 8.5.3 Neutral $\mathcal{CP}$ -even Higgs-boson mass corrections

The numerical evaluation to derive the physical masses for  $h^0, H^0$  as the poles (real parts) of the dressed propagators proceeds on the basis of Eq. (8.64) in an iterative way.

- In a first step, the squared masses  $M_{h,0}^2, M_{H,0}^2$  are determined by solving Eq. (8.64) excluding the new terms  $\Delta\hat{\Sigma}_{ab}^{(2)}(p^2)$  from the self-energies. The masses  $M_{h,0}, M_{H,0}$  are computed based on the higher-order contributions of Refs. [119, 128, 132, 135, 139, 141].
- In a second step, the shifts  $\Delta\hat{\Sigma}_{ab}^{(2)}(M_{h,0}^2) \equiv c_{ab}^h$  and  $\Delta\hat{\Sigma}_{ab}^{(2)}(M_{H,0}^2) \equiv c_{ab}^H$  are calculated and added as constants to the self-energies in Eq. (8.64),  $\hat{\Sigma}_{ab}(p^2) \rightarrow \hat{\Sigma}_{ab}(p^2) + c_{ab}^{h(H)}$ .
- In the third step, Eq. (8.64) is solved again, now including the constant shifts  $c_{ab}^{h(H)}$  in the self-energies, to deliver the refined masses  $M_h$  (with  $c_{ab}^h$ ) and  $M_H$  (with  $c_{ab}^H$ ).

This procedure can be repeated for improving the accuracy; numerically it turns out that going beyond the first iteration yields only marginal changes. Below, results are shown for the mass shifts

$$\Delta M_h = M_h - M_{h,0}, \quad \Delta M_H = M_H - M_{H,0}. \quad (8.68)$$

The mass shifts, in particular  $\Delta M_h$  for the light  $\mathcal{CP}$ -even Higgs-boson, can directly be compared with the current experimental uncertainty as well as with the anticipated future ILC accuracy [359] of

$$\delta M_h^{\text{exp,ILC}} \lesssim 0.05 \text{ GeV}. \quad (8.69)$$

The results are obtained for two different scenarios, varying parameters like  $\tan\beta, m_{A^0}, m_{\tilde{g}}$ , and illustrate the impact of these parameters via the new two-loop corrections on the neutral  $\mathcal{CP}$ -even Higgs-boson masses,  $M_h$  and  $M_H$ .

#### Implementation in the program FEYNHIGGS

The corrections of Eq. (8.62) are incorporated in FEYNHIGGS<sup>3</sup> by the following recipe, which is more general and in principle applicable also to the case of the complex MSSM with  $\mathcal{CP}$ -violation.

1. Determine the Higgs-boson masses  $M_{h_i,0}$  without the momentum-dependent terms of Eq. (8.62); the index  $i = 1, \dots, 4$  enumerates the masses of  $h, H, A, H^\pm$  in the real MSSM. This is done by invoking the FEYNHIGGS mass-finder.
2. Compute the shifts  $c_{ab}^{h_k} = \Delta\hat{\Sigma}_{ab}^{(2)}(M_{h_k,0}^2)$  with  $a, b, h_k = h, H$ .

<sup>3</sup>The embedding of these corrections into the FEYNHIGGS code was performed with substantial support by Thomas Hahn.

3. Run FEYNHIGGS' mass-finder again including the  $c_{ab}^{h_k}$  as constant shifts in the self-energies to determine the refined Higgs masses  $M_h$  and  $M_H$ .

This procedure could conceivably be iterated until full self-consistency is reached; yet the resulting mass improvements turn out to be too small to justify extra CPU time.

On the technical side, an interface for an external program to FEYNHIGGS was added, which exports relevant model parameters to the external program's environment, currently

FHscalefactor	ren. scale multiplier,	FHTB	$\tan \beta$ ,
FHAlfasMT	$\alpha_s(m_t)$ ,	FHGF	$G_F$ ,
FMHiggs2i	$M_{h_i,0}^2$ , $i = 1 \dots 4$ ,	FHMSti	$m_{\tilde{t}_i}$ , $i = 1, 2$ ,
FH{Re,Im}USt1i	$U_{\tilde{t}_i,1i}$ , $i = 1, 2$ ,	FHMGl	$m_{\tilde{g}}$ ,
FH{Re,Im}MUE	$\mu$ ,	FHMAO	$M_A$ ,

where the  $U_{\tilde{t}_i,1i}$  denote the elements of the stop mixing matrix,  $\alpha_s(m_t)$  the running strong coupling at the scale  $m_t$ , and  $G_F$  the Fermi constant. The renormalization scale is defined within FEYNHIGGS as  $\mu_r = m_t \cdot \text{FHscalefactor}$ . Invocation of the external program is switched on by providing its path in the environment variable FHEXTSE. The program is executed from inside a temporary directory which is afterwards removed.

The output (stdout) is scanned for lines of the form '*se@m c<sub>r</sub> c<sub>i</sub>*' which specify the correction  $c_r + ic_i$  [with  $c_r = \text{Re}(c_{ab}^{h_k})$ ,  $c_i = \text{Im}(c_{ab}^{h_k})$ ] to self-energy  $se$  in the computation of mass  $m$ , where  $m$  is one of Mh0, MHH, MA0, MHP, and  $se$  is one of h0h0, HHHH, AOA0, HmHp, h0HH, h0A0, HHA0, GOG0, h0G0, HHG0, AOGO, GmGp, HmGp, F1F1, F2F2, F1F2. The latter three, if given, substitute

$$\text{HHHH} = \cos^2 \alpha \text{F1F1} + \sin^2 \alpha \text{F2F2} + \sin 2\alpha \text{F1F2}, \quad (8.70a)$$

$$\text{h0h0} = \sin^2 \alpha \text{F1F1} + \cos^2 \alpha \text{F2F2} - \sin 2\alpha \text{F1F2}, \quad (8.70b)$$

$$\text{h0HH} = \cos 2\alpha \text{F1F2} + \frac{1}{2} \sin 2\alpha (\text{F2F2} - \text{F1F1}), \quad (8.70c)$$

in accordance with Eq. (8.61). Self-energies not given are assumed zero.

The zero-momentum contributions  $\tilde{\Sigma}_{ab}^{(2)}(0)$  with  $ab = \{H^0 H^0, h^0 H^0, h^0 h^0\}$ , defined in Eq. (8.62) are subtracted if the output of the external program contains one or more of 'sub asat', 'sub atat', 'sub asab', 'sub atab' for the  $\alpha_s \alpha_t$ ,  $\alpha_t^2$ ,  $\alpha_s \alpha_b$ , and  $\alpha_t \alpha_b$  contributions, respectively. All other lines in the output are ignored.

### Scenario 1: $m_h^{\max}$ scenario

The effects of the newly computed momentum-dependent two-loop corrections on the Higgs-boson masses  $M_{h,H}$  via the mass shifts  $\Delta M_h$  and  $\Delta M_H$  are now studied. In Fig. 8.12,  $\Delta M_h$  (upper plot) and  $\Delta M_H$  (lower plot) are shown as a function of  $m_{A^0}$  for  $\tan \beta = 5$  (blue) and  $\tan \beta = 20$  (red). For  $m_{A^0} \gtrsim 200$  GeV, the additional shifts from momentum-dependence of up to  $\Delta M_h \sim -60$  MeV are of the size of the expected future experimental precision, see Eq. (8.69). The contribution to the heavy  $\mathcal{CP}$ -even

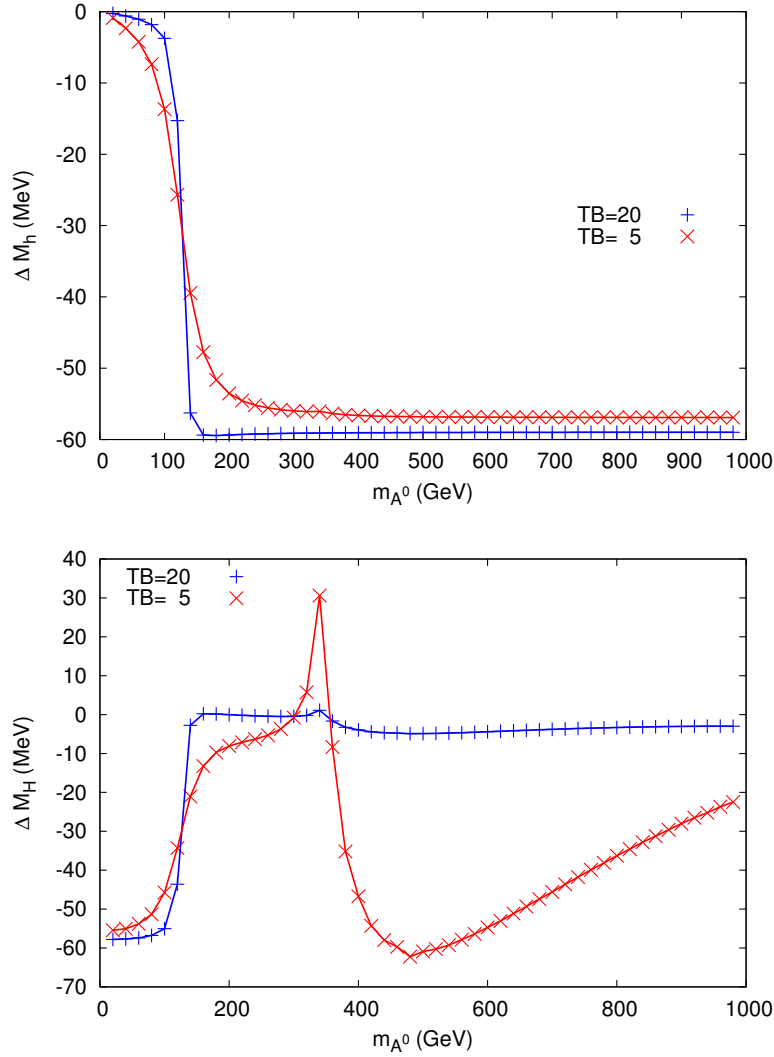


Figure 8.12: Variation of the mass shifts  $\Delta M_h, \Delta M_H$  with the  $A^0$ -boson mass  $m_{A^0}$  within scenario 1, for  $\tan \beta = 5$  (blue) and  $\tan \beta = 20$  (red). The small peak in  $\Delta M_H$  originates from a threshold at  $2m_t$ .

Higgs-boson mass is of similar order of magnitude. Around the threshold at  $m_{A^0} = 2m_t$ , the heavy Higgs-boson mass is shifted upwards.

Finally, the dependence of  $M_h$  and  $M_H$  on the gluino mass  $m_{\tilde{g}}$  is examined. The results are shown in Fig. 8.13 for  $\Delta M_h$  (upper plot) and  $\Delta M_H$  (lower plot) for  $m_{A^0} = 250$  GeV, with the same color coding as in Fig. 8.12. In the upper plot one can observe that the effects are particularly small for the default value of  $m_{\tilde{g}}$  in scenario 1. More sizeable shifts occur for larger gluino masses, by more than  $-400$  MeV for  $m_{\tilde{g}} \gtrsim 4$  TeV, reaching thus



the level of the current experimental accuracy in the Higgs-boson mass determination. The corrections to  $M_H$ , for the given value of  $m_{A^0} = 250$  GeV do not exceed  $-50$  MeV in the considered  $m_{\tilde{g}}$  range.

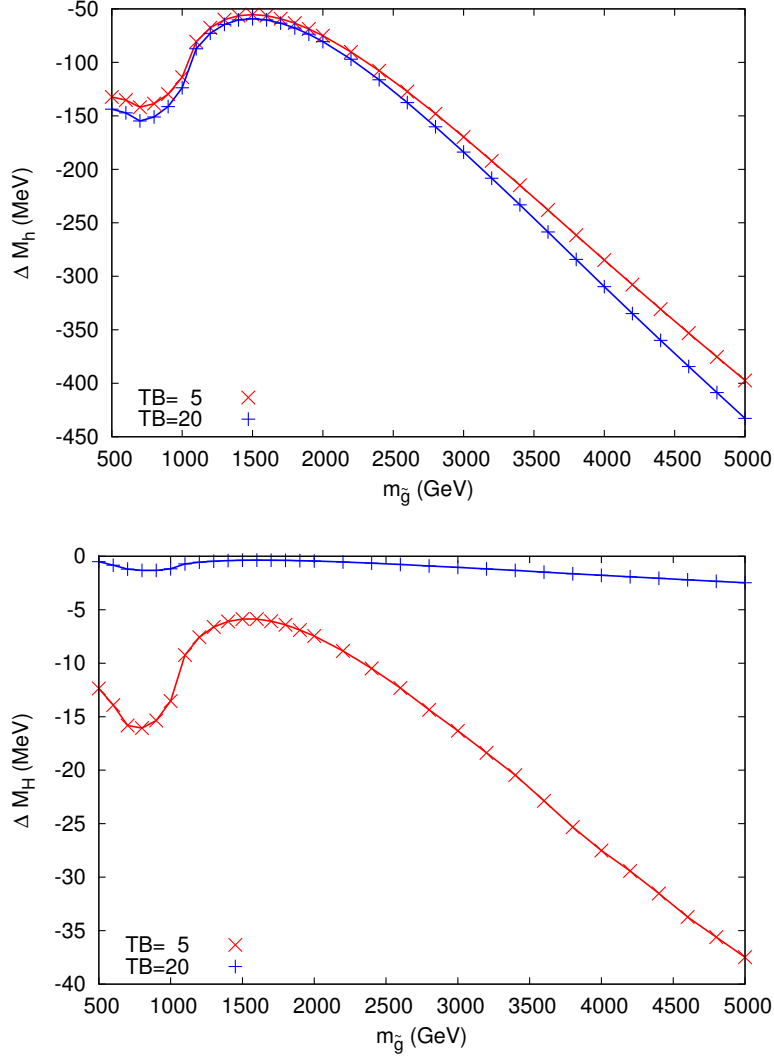


Figure 8.13: Variation of the mass shifts  $\Delta M_h, \Delta M_H$  with the gluino mass, within scenario 1, for two different values of  $\tan\beta = 5, 20$  and  $m_{A^0} = 250$  GeV.

### Scenario 2: Light stop scenario

The effects on the physical neutral  $\mathcal{CP}$ -even Higgs-boson masses are now analyzed within scenario 2. The results are shown for  $\Delta M_h$  (upper plot) and  $\Delta M_H$  (lower plot) as a function of  $m_{A^0}$  (with the same line styles as in Fig. 8.12), see Fig. 8.14. As can be

expected from the previous figures, below the  $p = 2m_t$  threshold, the effects on  $M_h$  and  $M_H$  are in general slightly smaller in scenario 2 than in scenario 1, where  $\Delta m_h$  still reaches the anticipated ILC accuracy, see Eq. (8.69). Above the  $p = 2m_t$  threshold, the variation of  $\Delta M_H$  is larger than in scenario 1 for  $\tan\beta = 5$ . Around the threshold  $p = 2m_{\tilde{t}_1}$  a shift in the GeV range towards lower masses is found, reaching the level of about 0.2%. Beyond this threshold, the heavy Higgs-boson mass can be shifted towards higher masses. The latter shift is also roughly in the GeV range.

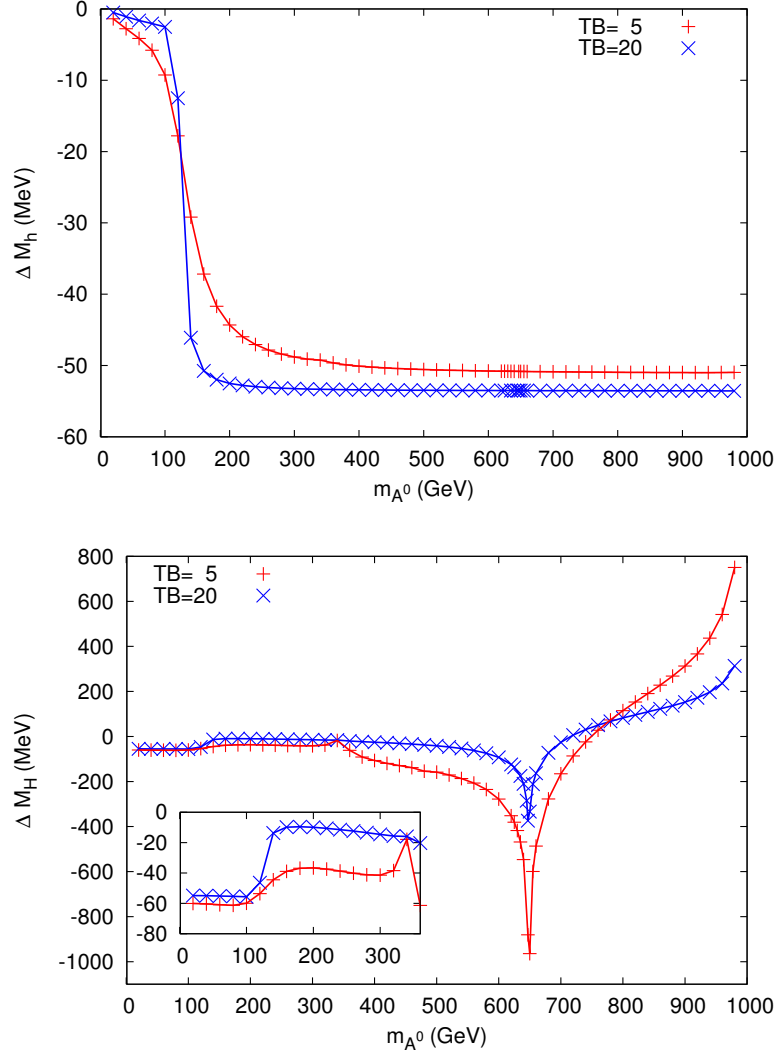


Figure 8.14: Variation of the mass shifts  $\Delta M_h, \Delta M_H$  with the  $A^0$ -boson mass  $m_{A^0}$  within scenario 2, for two different values of  $\tan\beta = 5, 20$ .

Finally the dependence on  $m_{\tilde{g}}$  is examined, see Fig. 8.15. In the upper plot  $\Delta M_h$  is

shown for  $\tan\beta = 5$  and  $\tan\beta = 20$ , where both values yield very similar results. As in scenario 1, “accidentally” small values of  $\Delta M_h$  are found around  $m_{\tilde{g}} \sim 1600$  GeV. For larger gluino mass values the shifts induced by the new momentum-dependent two-loop corrections exceed  $-500$  MeV and are thus larger than the current experimental uncertainty. The results for  $\Delta M_H$  are shown in the lower plot. While they are roughly twice as large as in scenario 1, they do not exceed  $-100$  MeV.

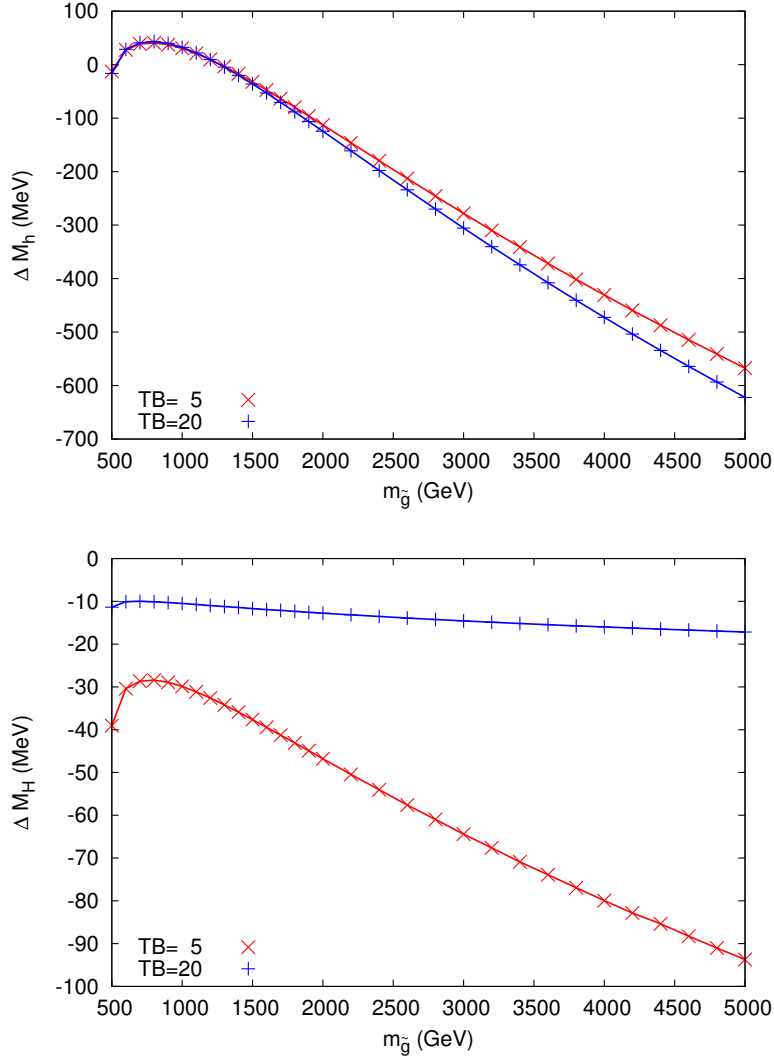


Figure 8.15: Variation of the mass shifts  $\Delta M_h, \Delta M_H$  with the gluino mass, within scenario 2, for two different values of  $\tan\beta = 5, 20$  and  $m_{A^0} = 250$  GeV.

## 8.6 Summary and Perspectives

The calculation and respective results for the leading momentum-dependent  $\mathcal{O}(\alpha_s\alpha_t)$  contributions to the masses of neutral  $\mathcal{CP}$ -even Higgs-bosons in the MSSM were presented. They are obtained by calculating the corresponding contributions to the dressed Higgs-boson propagators in the Feynman-diagrammatic approach.

The required two-loop self-energy diagrams and one-loop counter-terms with counter-term insertions are generated using FEYNARTS, and reduced to a set of basic integrals with the help of TWOCALC and FORMCALC.

The mass and field renormalization is performed adopting a mixed on-shell/ $\overline{\text{DR}}$  renormalization scheme. More precisely, the field renormalization part is renormalized in the  $\overline{\text{DR}}$  scheme, the on-shell scheme is used for the remaining mass renormalization. This scheme choice has been beneficial in other contexts [140, 320–323] and proved constructive in this calculation as well. Furthermore, the on-shell renormalization of the two-loop  $A^0$ -boson mass counter-term lead to an additional physical shift in the self-energies which has not been found in the calculation at zero momentum. The scheme choice is in contrast to Ref. [136, 137], where the same contribution was computed using a full  $\overline{\text{DR}}$  scheme.

The renormalized momentum-dependent two-loop Higgs-boson self-energies contain analytically inaccessible two-loop integrals. These are computed numerically using the program SECDEC. The new momentum-dependent contributions are incorporated in the public program FEYNHIGGS, including an interface to SECDEC. The analysis of the mass shifts is performed with the upgraded version of FEYNHIGGS.

The numerical analysis showed that the effects on the light  $\mathcal{CP}$ -even Higgs boson mass,  $M_h$ , depend strongly on the value of the gluino mass,  $m_{\tilde{g}}$ . For values of  $m_{\tilde{g}} \sim 1.5$  TeV corrections of about  $-50$  MeV are found, at the level of the anticipated future ILC accuracy. If the gluino mass is assumed very large,  $m_{\tilde{g}} \gtrsim 4$  TeV, the corrections are substantially larger and at the level of the current experimental accuracy [360]. The shifts in the heavy  $\mathcal{CP}$ -even Higgs-boson mass, resulting from the incorporation of the momentum dependence are mostly below current and future anticipated accuracies. Only close to thresholds, e.g. around  $p = 2m_{\tilde{t}_1}$ , the corrections are larger but do not exceed 0.2%.

The evaluation times for the computation of the  $\mathcal{CP}$ -even Higgs-boson masses including the new momentum-dependent two-loop contributions strongly depend on the performance of SECDEC. They range between one minute for a point far, and maximally one hour for a point very close to a threshold. Being able to compute multi-loop multi-scale integrals, the program SECDEC reaches far beyond the applicability to two-loop two-point functions which are required for the self-energy corrections of the MSSM Higgs-boson masses. Yet, it is due to its universal applicability that a program specifically tailored to the desired two-loop two-point functions may perform better in terms of evaluation times. One such alternative could be a package provided by Bauberger [332], which contains the desired loop integrals in terms of one-parameter integral representations.

With the computation of the renormalized  $\mathcal{CP}$ -odd Higgs-boson self-energy at hand, it could be interesting to extend the analysis of the mass shifts resulting from momentum dependence to the charged Higgs-bosons. Furthermore, it could be interesting to compute the effective couplings to gauge bosons.

As a further improvement on the precision of the prediction of the Higgs-boson masses, the contributions involving couplings to the electroweak gauge bosons can be included. Moreover, the computation of the leading QCD corrections at the three-loop order to be incorporated into FEYNHIGGS can be considered.



## 9 | Conclusions

The upgrade of the program SECDEC towards the automated computation of multi-loop multi-scale Feynman graphs in the physical region including thresholds was presented, thereby lifting the restriction to the Euclidean region.

The program allows for an automated algebraic factorization of dimensionally regulated singularities and a numerical evaluation of the resulting pole coefficients. These can be multi-loop Feynman integrals with up to several mass scales and with in principle no limitation on the tensor rank, or more general parametric functions with singularities only at the endpoints of the integration region. Additionally, the program was enhanced by allowing for the automated evaluation of user-defined functions in the physical region.

The extension to physical kinematics was achieved by the implementation of an automated analytical continuation of the integrand. An algorithm to find the optimal according deformation of the integration contour was further developed, allowing for a stable evaluation of integrals over large regions of values for the kinematic invariants.

Provided with the upgraded version of the program, a plethora of new applications are feasible. Two applications were shown in this thesis.

In the first application, massive planar and non-planar six- and seven-propagator integrals with four external legs were computed. It was shown that the method is in principle independent of the number of involved scales by providing numerical results for a planar four-point seven-propagator diagram with internal and external lines all massive.

Furthermore, and in contrast to analytical evaluation techniques, adding massive lines to a topology proved beneficial in terms of evaluation times. This was shown for two of the most complicated massive non-planar seven-propagator double box integrals, entering in the NNLO prediction for top-quark pair production. Differing in the massive sub-loop topology, the singularity structure of the diagram involved in the heavy fermionic corrections is significantly simpler than the diagram entering the light fermionic corrections. While the custom SECDEC setup can be used in the computation of the former, the latter diagram challenges the automated setup of the program. Therefore, an analytical preparation of this diagram prior to its treatment in SECDEC was explored, leading to an improved numerical behavior.

A systematic improvement of the numerical convergence can be achieved through a reduction in the number of integration parameters involved and the elimination of spurious divergences. The analytical preparation of the massive non-planar box diagram entering

the light fermionic corrections follows these aims, reducing the number of involved parameters by integration of one Feynman parameter in a sub-loop of the integral. Hereby, singularities are mapped to both ends of the integration region and spurious linear singularities appear in pairs. While a remapping cures the occurrence of singularities at both endpoints of the integration region, a newly introduced backwards transformation serves in distributing the linear divergences more evenly among the Feynman parameters, thereby achieving a total reduction by two thirds in the number of functions to be integrated numerically.

In its second application, the new features of the program are demonstrated in the computation of the the leading momentum-dependent two-loop QCD corrections to the masses of neutral  $\mathcal{CP}$ -even Higgs-bosons in the MSSM. These are obtained by calculating the corresponding contributions to the dressed Higgs-boson propagators using the Feynman-diagrammatic approach and adopting a mixed on-shell/ $\overline{\text{DR}}$  renormalization scheme.

A revised two-loop mass and field renormalization has to be carried out for the mass of the neutral Higgs-bosons to cancel the additional divergences arising from incorporating the momentum dependence. An additional shift with respect to previous calculations of the order  $\mathcal{O}(\alpha_s\alpha_t)$  at zero momentum transfer appears from evaluating the  $\mathcal{CP}$ -odd Higgs-boson mass counter-term at its pole mass,  $m_{A^0}^2$ .

The effect of the new momentum-dependent two-loop corrections on the predictions for the  $\mathcal{CP}$ -even Higgs boson masses were analyzed numerically. The program SECDEC is used in the evaluation of the finite parts of analytically inaccessible two-loop integrals with several mass scales.

The obtained mass shifts of the light  $\mathcal{CP}$ -even Higgs-boson mass exhibit an overall strong dependence on the mass of the gluino. For values of  $m_{\tilde{g}} \sim 1.5$  TeV corrections of about  $-50$  MeV are found, at the level of the anticipated future ILC accuracy. For very large gluino masses,  $m_{\tilde{g}} \gtrsim 4$  TeV, on the other hand, substantially larger corrections are found, at the level of the current experimental accuracy at the LHC. Additional shifts in the heavy  $\mathcal{CP}$ -even Higgs-boson mass, are mostly below current and future anticipated accuracies. Only close to thresholds, e.g. around  $p = 2m_{\tilde{t}_1}$ , the corrections are larger but do not exceed 0,2%. The new momentum-dependent two-loop contributions have been incorporated into the program FEYNHIGGS.

In conclusion, the leading momentum-dependent two-loop QCD corrections to the neutral  $\mathcal{CP}$ -even Higgs-boson masses should be taken into account in precision analyses interpreting the discovered scalar particle as a Higgs-boson in the MSSM.

Especially in this last application of the upgraded version of the program SECDEC within this thesis, it was shown that the program can be used in the computation of phenomenological quantities. Yet, for an application where Monte Carlo sampling of an amplitude at millions of phase-space points is required, the speed in the evaluation has to be improved.

Nonetheless, in its new version SECDEC has proven an invaluable tool in independent checks to analytical calculations of very complicated two-loop topologies involving masses and multiple scales.



---

Based on the observation that the numerical evaluation in SECDEC is rather limited in the cases of diagrams with very complicated singularity structures than limited by the number of mass scales involved, this numerical method forms a vital counter part to purely analytical approaches. Its extremely high potential needs to be exploited further in the future. Considering the fact that the method is very suitable for intense parallelization, the program has the potential to be further applicable in a multitude of higher-order corrections in quantum field theories.



# A | Appendix

## A.1 Analytical formulae

All following formulae are based on Refs. [328–332, 334, 335, 337] and were either recalculated analytically or checked numerically with SECDEC or Golem95 [188, 336].

The prefactor at loop order  $L$  reads

$$P^L = \left( \frac{(2\pi\mu_r)^{(4-D)}}{i\pi^2} \right)^L, \quad (\text{A.1})$$

where the dimension  $D = 4 - 2\varepsilon$  contains the dimensional regulator  $\varepsilon$ . The fully symmetric Källén function reads

$$\lambda(x, y, z) = x^2 + y^2 + z^2 - 2xy - 2xz - 2yz. \quad (\text{A.2})$$

The following definitions facilitate numerical stability of analytic results. They are based on work of, e.g., Refs. [280, 332].

$$\sqrt{\lambda(p^2, m_1^2, m_2^2)} = \begin{cases} \sqrt{(p^2 - m_{12}^+)(p^2 - m_{12}^-)}, & p^2 < m_{12}^+ \text{ and } p^2 \leq m_{12}^-, \\ i\sqrt{(p^2 - m_{12}^-)(m_{12}^+ - p^2)}, & p^2 < m_{12}^+ \text{ and } p^2 > m_{12}^-, \\ \sqrt{(p^2 - m_{12}^+)(p^2 - m_{12}^-)}, & p^2 \geq m_{12}^+. \end{cases} \quad (\text{A.3})$$

where

$$m_{12}^+ = (m_1 + m_2)^2, \quad (\text{A.4})$$

$$m_{12}^- = (m_1 - m_2)^2. \quad (\text{A.5})$$

Furthermore, the Riemann sheet of the logarithm can be chosen explicitly as

$$\log(x)^+ = \log(x + i\delta) = \begin{cases} \log(x), & x > 0, \\ \log(-x) + i\pi, & x < 0, \end{cases} \quad (\text{A.6})$$

or

$$\log(x)^- = \log(x - i\delta) = \begin{cases} \log(x), & x > 0, \\ \log(-x) - i\pi, & x < 0. \end{cases} \quad (\text{A.7})$$

Similarly, two choices for an analytical continuation of the dilogarithm read

$$\text{Li}_2(x)^+ = \text{Li}_2(x + i\delta) , \quad (\text{A.8})$$

$$\text{Li}_2(x)^- = \text{Li}_2(x - i\delta) . \quad (\text{A.9})$$

Furthermore, the following expressions can be abbreviated

$$L_m(m^2) = \gamma_E + \log \left( \frac{m^2}{4\pi\mu_r} \right)^- , \quad (\text{A.10})$$

$$L_p(p^2) = \gamma_E + \log \left( \frac{-p^2}{4\pi\mu_r} \right)^- . \quad (\text{A.11})$$

### A.1.1 One-loop representations

#### One-loop tadpole

The one-loop one-point function reads

$$A(m^2) = P \int d^D q \frac{1}{(q^2 - m^2)} \quad (\text{A.12})$$

$$= -m^2 \left( \frac{m^2}{4\pi\mu_r} \right)^{-\varepsilon} \Gamma(\varepsilon - 1) \quad (\text{A.13})$$

$$= \frac{m^2}{\varepsilon} + m^2(1 - L_m(m^2)) + \mathcal{O}(\varepsilon) . \quad (\text{A.14})$$

#### One-loop bubble

The one-loop two-point function is defined as follows

$$B(p^2, m_1^2, m_2^2) = P \int d^D q \frac{1}{(q^2 - m_1^2)((q + p_1)^2 - m_2^2)} \quad (\text{A.15})$$

$$= \frac{1}{\varepsilon} + B^{\text{fin}}(p^2, m_1^2, m_2^2) + \mathcal{O}(\varepsilon) . \quad (\text{A.16})$$

Special cases of the finite part read

$$B^{\text{fin}}(0, m^2, 0) = B^{\text{fin}}(0, 0, m^2) , \quad (\text{A.17})$$

$$B^{\text{fin}}(0, 0, m^2) = 1 - L_m(m^2) , \quad (\text{A.18})$$

$$B^{\text{fin}}(0, m^2, m^2) = -L_m(m^2) , \quad (\text{A.19})$$

$$B^{\text{fin}}(0, m_1^2, m_2^2) = \frac{A^{\text{fin}}(m_1^2) - A^{\text{fin}}(m_2^2)}{m_1^2 - m_2^2} , \quad (\text{A.20})$$

$$B^{\text{fin}}(p^2, 0, 0) = 2 - L_p(p^2) , \quad (\text{A.21})$$

$$B^{\text{fin}}(m^2, 0, m^2) = 2 - \gamma_E - \log \left( \frac{m^2}{4\pi\mu_r} \right)^+ , \quad (\text{A.22})$$

$$B^{\text{fin}}(p^2, 0, m^2) = B^{\text{fin}}(p^2, m^2, 0) , \quad (\text{A.23})$$

$$= 2 - \frac{m^2}{p^2} L_m(m^2) + \frac{m^2 - p^2}{p^2} L_m(m^2 - p^2) , \quad (\text{A.24})$$

For a general representation of the finite part  $B^{\text{fin}}(p^2, m_1^2, m_2^2)$ , see Ref. [330]. For the coefficient of order  $\mathcal{O}(\varepsilon)$ , see Refs. [329, 330, 332].

### Derivative of the one-loop bubble

The derivative of the one-loop two-point function with respect to the first mass reads

$$\frac{\partial}{\partial m_1^2} B(p^2, m_1^2, m_2^2) = \partial_{m_1^2} B(p^2, m_1^2, m_2^2) \quad (\text{A.25})$$

$$= P \int d^D q \frac{1}{(q^2 - m_1^2)^2 ((q + p_1)^2 - m_2^2)} \quad (\text{A.26})$$

$$= \partial_{m_1^2} B^{\text{fin}}(p^2, m_1^2, m_2^2) + \mathcal{O}(\varepsilon) . \quad (\text{A.27})$$

It is finite as the divergent terms are independent of the masses. Special cases read

$$\partial_{m_1^2} B^{\text{fin}}(0, m_1^2, 0) = -\frac{1}{m_1^2} , \quad (\text{A.28})$$

$$\partial_{m_1^2} B^{\text{fin}}(0, m^2, m^2) = -\frac{1}{2m_1^2} , \quad (\text{A.29})$$

$$\partial_{m_1^2} B^{\text{fin}}(0, m_1^2, m_2^2) = \frac{1}{m_2^2 - m_1^2} + \frac{m_2^2}{(m_1^2 - m_2^2)^2} \log \left( \frac{m_1}{m_2} \right) , \quad (\text{A.30})$$

$$\partial_{m_1^2} B^{\text{fin}}(p^2, m_1^2, 0) = \frac{1}{p^2} \log \left( \frac{m_1^2 - p^2}{m_1^2} \right)^- . \quad (\text{A.31})$$

For a representation of the general case with arbitrary masses, see Ref. [329, 332].

## A.1.2 Two-loop representations

### Two-loop vacuum diagram

The two-loop three-propagator vacuum integral corresponding to the diagram in Fig. 8.2(a) reads

$$T_{134}(m_1^2, m_2^2, m_3^2) = P^2 \iint \frac{d^D q_1 d^D q_2}{(k_1^2 - m_1^2 + i\delta)(k_3^2 - m_2^2 + i\delta)(k_4^2 - m_3^2 + i\delta)} \quad (\text{A.32})$$

$$= \frac{1}{\varepsilon^2} T_{134}^{\text{div}^2}(m_1^2, m_2^2, m_3^2) + \frac{1}{\varepsilon} T_{134}^{\text{div}}(m_1^2, m_2^2, m_3^2) + T_{134}^{\text{fin}}(m_1^2, m_2^2, m_3^2) + \mathcal{O}(\varepsilon) \quad (\text{A.33})$$

$$= \frac{1}{2\varepsilon^2} (m_1^2 + m_2^2 + m_3^2) + \frac{1}{\varepsilon} \left[ \frac{3}{2} (m_1^2 + m_2^2 + m_3^2) - m_1^2 L_m(m_1^2) - m_2^2 L_m(m_2^2) - m_3^2 L_m(m_3^2) \right] + T_{134}^{\text{fin}}(m_1^2, m_2^2, m_3^2) + \mathcal{O}(\varepsilon). \quad (\text{A.34})$$

A representation of the finite part  $T_{134}^{\text{fin}}(m_1^2, m_2^2, m_3^2)$  is included in Ref. [331].

### Two-loop two-point three-propagator (sunrise) diagram

The two-loop two-point three-propagator function corresponding to the diagram in Fig. 8.2(b) reads

$$T_{234}(p^2, m_1^2, m_2^2, m_3^2) = P^2 \iint \frac{d^D q_1 d^D q_2}{(k_2^2 - m_1^2 + i\delta)(k_3^2 - m_2^2 + i\delta)(k_4^2 - m_3^2 + i\delta)}. \quad (\text{A.35})$$

The special case of one massless propagator reads

$$T_{234}(p^2, m_1^2, m_2^2, 0) = \frac{1}{2\varepsilon^2} (m_1^2 + m_2^2) + \frac{1}{\varepsilon} (T_{134}^{\text{fin}}(m_1^2, m_2^2, 0) - \frac{1}{4} p^2) + \quad (\text{A.36})$$

$$T_{234}^{\text{fin}}(p^2, m_1^2, m_2^2, 0) + \mathcal{O}(\varepsilon). \quad (\text{A.37})$$

A representation of the finite part  $T_{234}^{\text{fin}}(p^2, m_1^2, m_2^2, 0)$  is included in Ref. [331].

### Two-loop two-point four-propagator diagram

The two-loop two-point four-propagator function corresponding to the diagram in Fig. 8.2(c) reads

$$T_{1234}(p^2, m_1^2, m_2^2, m_3^2, m_4^2) = P^2 \iint \frac{d^D q_1 d^D q_2}{(k_1^2 - m_1^2 + i\delta)(k_2^2 - m_2^2 + i\delta)(k_3^2 - m_3^2 + i\delta)(k_4^2 - m_4^2 + i\delta)}. \quad (\text{A.38})$$

The divergent part can be expressed as

$$T_{1234}(p^2, m_1^2, m_2^2, m_3^2, m_4^2) = \frac{1}{2\varepsilon^2} + \frac{1}{\varepsilon} \left( B^{\text{fin}}(p^2, m_1^2, m_2^2) + \frac{1}{2} \right) + T_{1234}^{\text{fin}}(p^2, m_1^2, m_2^2, m_3^2, m_4^2) + \mathcal{O}(\varepsilon). \quad (\text{A.39})$$

A result for the finite part is not available in analytical form.

### Two-loop two-point five-propagator diagram

The two-loop two-point five-propagator function corresponding to the diagram in Fig. 8.2(d) reads

$$T_{11234}(p^2, m_1^2, m_2^2, m_3^2, m_4^2) \quad (\text{A.40})$$

$$= \frac{\partial}{\partial m_1^2} T_{1234}(p^2, m_1^2, m_2^2, m_3^2, m_4^2) \quad (\text{A.41})$$

$$= P^2 \iint \frac{d^D q_1 d^D q_2}{(k_1^2 - m_1^2 + i\delta)^2 (k_2^2 - m_2^2 + i\delta) (k_3^2 - m_3^2 + i\delta) (k_4^2 - m_4^2 + i\delta)} . \quad (\text{A.42})$$

The divergent part can be expressed as

$$\begin{aligned} & T_{11234}(p^2, m_1^2, m_2^2, m_3^2, m_4^2) \\ &= \frac{1}{\varepsilon} \partial_{m_1^2} B^{\text{fin}}(p^2, m_1^2, m_2^2) + T_{11234}^{\text{fin}}(p^2, m_1^2, m_2^2, m_3^2, m_4^2) + \mathcal{O}(\varepsilon) . \end{aligned} \quad (\text{A.43})$$

A result for the finite part is not available in analytical form.

## A.2 SecDec User Manual

### A.2.1 Installation

The program can be downloaded from <http://secdec.hepforge.org>.

Unpacking the tar archive via ‘`tar xzvf SecDec-2.x.tar.gz`’ will create a directory called `SecDec-2.x` with the subdirectories as described in the previous section. Changing to the directory `SecDec-2.x`, the program is installed by running ‘`./install`’.

Prerequisites are Mathematica, version 6 or above, Perl (installed by default on most Unix/Linux systems), a Fortran compiler (e.g. `gfortran`, `ifort`) or a C++ compiler if the C++ option is used.

In order to use the program, the user only has to edit the two files `param*.input` and `template*.m`. SECDEC has three different setups, the user might be interested in. This is the setup to compute standard loop integrals, termed ‘Loop setup’ in the following, generalized parametric functions, termed ‘General setup’ in what follows, and and functions with a similar structure as loop integrals, referred to as ‘User-defined setup’.

#### Loop setup

- `paramloop.input`: (text file, Perl readable format)

In this file the user needs to specify paths, the type of integrand, the desired order in  $\varepsilon$ , the output format, the parameters and kinematic values for numerical integration, the parameters for contour deformation and further options.

- `templateloop.m`: (Mathematica syntax)  
Here enters the specification of the loop momenta and propagators, resp. of the topology; optionally a numerator different from 1, non-standard propagator powers, parameters to be split in the middle of the integration region and the space-time dimension.

### General setup

- `param.input`: (text file, Perl readable format)  
In this file the user needs to specify paths, the type of integrand, the symbols and dummy functions utilized in the template file, the desired order in  $\varepsilon$ , the output format, the parameters and values for numerical integration and further options.
- `Template.m`: (Mathematica syntax)  
Here enters the specification of the integration variables, the factors of the integrand, variables to be split in the middle of the integration region and the space-time dimension.

### User-defined setup

- `paramuserdefined.input`: (text file, Perl readable format)  
In this file the user needs to specify paths, the type of integrand, the desired order in  $\varepsilon$ , the output format, the parameters and kinematic values for numerical integration, the parameters for contour deformation and further options.
- `templateuserdefined.m`: (Mathematica syntax)  
Here enters the specification of the user-defined functions, the list of powers of the original propagators (optional), the rank of the integrand, the variables to be split in the middle of the integration region and the space-time dimension. As the file is read in by Mathematica, additional functions needed to evaluate the user-defined functions can be included without further specification in the parameter file.

## A.2.2 Operation

1. Change to the subdirectory `loop` for the calculation of a loop or a user-defined integral or to the subdirectory `general` to evaluate a more general parameter integral.
2. Copy the files `param*.input` and `template*.m` to create your own parameter and template files `myparamfile.input` and `mytemplatefile.m`, respectively. These two files serve to define the integrand and the parameters for the numerical integration.
3. Set the desired parameters in `myparamfile.input` and specify the integrand in `mytemplatefile.m`.



4. Issue the command `./launch -p myparamfile.input -t mytemplatefile.m` in the shell. If you run the command with an additional `-u` the user-defined setup is used. If you omit the option `-p myparamfile.input`, the file `param.input`, `paramloop.input` or `paramuserdefined.input` will be taken as default, depending on the current directory (either `general` or `loop`) and whether the user-defined setup was chosen by adding the `-u`. Likewise, if you omit the option `-t mytemplatefile.m`, the file `Template.m`, `templateloop.m` or `templateuserdefined.m` will be taken as default. If your files `myparamfile.input`, `mytemplatefile.m` are in a different directory, say, `myworkingdir`, use the option `-d myworkingdir`. The shell command then reads `./launch -d myworkingdir -p myparamfile.input -t mytemplatefile.m`, executed from the directory `SecDec/general` or `SecDec/loop`.
5. Collect the results. Depending on whether you have used a single machine or submitted the jobs to a cluster, the following actions will be performed:
  - If the calculations are done sequentially on a single machine, the results will be collected automatically (via `results.pl`, `resultsloop.pl` or `resultsuserdefined.pl` called by `launch`). The output file will be displayed with the text editor specified in the `myparamfile.input`.
  - If the jobs have been submitted to a cluster, execute the command `./results*.pl [-d myworkingdir -p myparamfile]` when all jobs have finished. This will write the final results to files in the `graph` subdirectory specified in the input file.
6. After the calculation and the collection of the results is completed, you can use the shell command `./launchclean[graph]` to remove obsolete files.

It should be mentioned that the code starts working on the most complicated pole structure, which also takes longest. When the jobs expected to take longest are submitted to a cluster first, the time the user has to wait for the results is minimized.

### A.2.3 Program input parameters

The user manual is for loop diagrams; the input files in the subdirectory `general` to compute more general parametric functions are very similar.

For the computation of an arbitrary loop integral the user should switch to the directory `loop`, copy the files `paramloop.input` and `templateloop.m` and rename them arbitrarily to arrive at `myparamloop.input` and `mytemplateloop.m`, respectively. In the file `myparamloop.input` which is written in Perl readable format, the user then needs to name the graph to be computed and specify its number of propagators, external legs and loops. Furthermore, the kinematic invariants  $s_{ij}$ ,  $p^2$  and  $m^2$  need to be given numeric values. Apart from these definitions only one further flag (`cutconstruct=0` or `1`) needs to be set which decides how the user chooses to define the propagators of the diagram at hand in the `mytemplateloop.m` file, compare Sec. 6.3.2 for further explanations. All other parameters do not need to be specified, default values will be chosen.

The following parameters can be specified:

**subdir** specifies the name of the subdirectory to which the graph should be written to. If it does not exist yet, it will be created. The specified *subdir* contains the directory specified in *outputdir*.

**outputdir** The name for the desired output directory can be given here by specifying the full path to the desired output directory. If *outputdir* is not specified, the default directory for the output will have the graph name (see below) appended to the directory *subdir*.

The output directory will contain all the files produced during the decomposition, subtraction, expansion and numerical integration, and the results. The output of the decomposition into sectors is found in the *outputdir* directly. The functions from subtraction and expansion and the respective files for numerical integration are found in subdirectories. The latter are named by the pole structure and contain subdirectories named after the order in  $\varepsilon$  to which the Laurent coefficients contained in these folders contribute.

**graph** The name of the diagram or parametric function to be computed is specified here. The graph name can contain underscores and numbers, but should not contain commas.

**propagators** Here, the number of propagators the diagram has is specified. This specification is mandatory in the computation of loop integrals using the automated setup. When utilizing the user-defined setup, the number of propagators only needs to be specified if the exponent of the two Symanzik polynomials should be computed in an automated way.

**legs** The number of external legs the diagram has is specified here (mandatory).

**loops** The number of loops the diagram has is specified here (mandatory).

**cutconstruct** If the graph to be computed corresponds to a scalar integral, the integrand ( $\mathcal{F}$  and  $\mathcal{U}$ ) can be constructed via topological cuts. In this case set *cutconstruct=1*, the default is =0. If *cutconstruct* is switched on, the input for the graph structure (\*.m file) is just a list of labels connecting vertices, as explained in Secs. 6.3.2 and A.2.4.

**epsord** The order to which the Laurent series in  $\varepsilon$  should be expanded, starting from  $\varepsilon^{-maxpole}$ , can be specified here. The default is *epsord=0* where the Laurent series is cut after finite part  $\varepsilon^0$ . If *epsord* is set to a negative value, only the pole coefficients up to this order are computed.

**prefactorflag** Possible values for the *prefactorflag* are 0 (default), 1 and 2.

- 0: The default prefactor  $(-1)^N \Gamma[N - Nloops * Dim/2]$  is factored out of the numerical result.

- 1: The default prefactor  $(-1)^N \Gamma[N - Nloops * Dim/2]$  is included in the numerical result.
- 2: Give the desired prefactor in *prefactor=* to be factored out in the final result.

**prefactor** If option 2 has been chosen in the *prefactorflag*, write down the desired *prefactor* in Mathematica syntax. In combination with options 0 or 1 in the *prefactorflag* this entry will be ignored. Use *Nn*, *Nloops* and *Dim* to denote the number of propagators, loops and dimension ( $Dim=4-2*eps$  by default).

**IBPflag** Set *IBPflag=0* if the integration by parts option should not be used and *=1* if it should be used. *IBPflag=2* is designed to use IBP relations when it is more efficient to do so.

Using the integrations by parts method takes more time in the subtraction and expansion step and generally results in more functions for numerical integration. However, it can be useful if (spurious) linear poles of the type  $x^{-2-b\epsilon}$  are found in the decomposition, as it reduces the power of  $x$  in the denominator.

**compiler** Choose a Fortran compiler (tested with gfortran, ifort, g77) if *language=Fortran*. Left blank, the default is gfortran.

**exeflag** The *exeflag* can be used to execute the program in steps within one calculation.

- 0: The iterated sector decomposition is done and the scripts to do the subtraction, the expansion in epsilon, the creation of the Fortran/C++ files and to launch the numerical integration are created (scripts *batch\** in the subdirectory *graph*) but not run. This can be useful if a cluster is available to run each pole structure on a different node.
- 1: In addition to the steps done in 0, the subtraction and epsilon expansion is performed and the resulting functions are written to Fortran/C++ files.
- 2: In addition to the steps done in 1, all the files needed for the numerical integration are created.
- 3: In addition to the steps done in 2, the compilation of the Fortran/C++ files is launched to make the executables.
- 4: In addition to the steps done in 3, the executables are run, either by batch submission or locally.

**clusterflag** The *clusterflag* determines how jobs are submitted. Setting *clusterflag=0* (default) the jobs will run on a single machine, setting it *=1* the jobs will run on a cluster (a batch system to submit jobs).

**batchsystem** If a cluster is used (*clusterflag=1*), this flag should be set to 0 to use the setup for the PBS (Portable batch system). If the flag is set to 1 a user-defined setup is activated. Currently this is the submission via *condor*, but it can be adapted to other batch systems by editing *perlsrc/makejob.pm*.

- maxjobs** When using a cluster, specify the maximum number of jobs allowed in the queue here.
- maxcput** Specify the estimated maximal CPU time (in hours). This option is only used to send a job to a particular queue on a batch system.
- pointname** The name of the point to calculate is specified here. It should be either blank or a string and is useful to label the result files in case of different runs for different numerical values of the Mandelstam variables, masses etc.
- sij** The values for Mandelstam invariants  $s_{ij} = (p_i + p_j)^2$  in numbers are specified here (mandatory). The  $s_{ij}$  should be  $\leq 0$  in the Euclidean region.
- pi2** Massive external legs  $p_1^2, p_2^2, \dots$  are specified here (mandatory).  $p_i^2$  should be  $\leq 0$  in the Euclidean region. Light-like external legs must be specified in the *onshell*= conditions in the `mytemplatefile.m`, see Sec. A.2.4.
- ms2** Specify the masses of propagators  $m_1^2, m_2^2, \dots$  using the notation `ms[i]` for  $m_i^2$  (mandatory). The masses should not be complex numbers.
- integrator** The program for numerical integration can be chosen here. BASES (*integrator=0*) can only be used in the Fortran version. Vegas (*integrator=1*), Suave (*integrator=2*), Divonne (*integrator=3*, default) and Cuhre (*integrator=4*) are part of the CUBA library and can be used in both the Fortran and the C++ version. In practice, Divonne usually gives the fastest results when using the C++ version. In the following we therefore concentrate on the adjustment of the parameters needed for numerical integration using Divonne. For more details about the CUBA parameters, the reader is referred to Ref. [302].
- cubapath** The path to the CUBA library can be specified here. The default directory is *[your path to SecDec]/Cuba-3.2*. CUBA-3.2 uses parallel processing during the numerical evaluation of the integral. The older version (CUBA-2.1) is still supported and can be used.
- maxeval** Separated by commas and starting with the lowest order coefficient in  $\varepsilon$ , specify the maximal number of evaluations to be used by the numerical integrator for each order in  $\varepsilon$ . If *maxeval* is not equal to *mineval*, the maximal number of evaluations does not have to be reached.
- mineval** Separated by commas and starting with the lowest order coefficient in  $\varepsilon$ , specify the number of evaluations which should at least be done before the numerical integrator returns a result. The default is 0.
- epsrel** Separated by commas and starting with the lowest order coefficient in  $\varepsilon$ , specify the desired relative accuracy for the numerical evaluation.
- epsabs** Separated by commas and starting with the lowest order coefficient in  $\varepsilon$ , specify the desired absolute accuracy for the numerical evaluation. These values are

particularly important when either the real or the imaginary part of an integral is close to zero. Note, *epsabs=* must be chosen smaller than the resulting values for the integral.

**cubaflags** Set the cuba verbosity flags. The default is 2 which means, the CUBA input parameters and other useful information, e.g. about numerical convergence, are echoed during the numerical integration.

**key1** Separated by commas and starting with the lowest order coefficient in  $\varepsilon$ , specify *key1* which determines the sampling to be used for the partitioning phase in Divonne. With a positive *key1*, a Korobov quasi-random sample of *key1* points is used. A *key1* of about 1000 (default) usually is a good choice.

**key2** Separated by commas and starting with the lowest order coefficient in  $\varepsilon$ , specify *key2* which determines the sampling to be used for the final integration phase in Divonne. With a positive *key2*, a Korobov quasi-random sample is used. The default is *key2=1* which means, the number of points needed to reach the prescribed accuracy is estimated by Divonne.

**key3** Separated by commas and starting with the lowest order coefficient in  $\varepsilon$ , specify the *key3* to be used for the refinement phase in Divonne. Setting *key3=1* (default), each subregion is split once more.

**maxpass** Separated by commas and starting with the lowest order coefficient in  $\varepsilon$ , specify how good the convergence has to be during the partitioning phase until the program passes on to the main integration phase. A *maxpass* of 3 (default) is usually sufficient to get a quick and good result.

**border** Separated by commas and starting with the lowest order coefficient in  $\varepsilon$ , specify the border for the numerical integration. The points in the interval  $[0, \textit{border}]$  and  $[1 - \textit{border}, 1]$  are not included in the integration but are extrapolated from a few points of the excluded range. This can be useful if the integrand is known to be peaked close to endpoints of the integration variables.

**maxchisq** Separated by commas and starting with the lowest order coefficient in  $\varepsilon$ , specify the maximally allowed  $\chi^2$  at the end of the numerical integration.

**mindeviation** Separated by commas and starting with the lowest order coefficient in  $\varepsilon$ , specify the deviation two sample averages in one region can show without being treated any further.

These parameters are advanced options:

**primarysectors** Specify a list of primary sectors to be treated here. If left blank, *primarysectors* defaults to all, i.e. *primarysectors=1,...,N* will be assumed, where *N* is the number of propagators. This option is useful if a diagram has symmetries such that some primary sectors yield the same result.

**multiplicities** Specify the *multiplicities* of the primary sectors listed above. List the *multiplicities* in same order as the corresponding sectors above. If left blank, a default multiplicity of 1 is set for each primary sector.

**infinitesectors** The alternative heuristic sector decomposition strategy, compare Sec. 4.2.2, is activated when specifying, separated by commas, those primary sectors which should get a pre-decomposition. Writing *infinitesectors=2,3* results in the application of the alternative sector decomposition strategy to primary sectors 2 and 3. *infinitesectors* must be left empty for the default strategy to be applied to all primary sectors.

**togetherflag** This flag defines whether to integrate subsets of functions for each pole order separately *togetherflag=0* (default) or to sum all functions for a certain pole order prior to integration *togetherflag=1*. The latter will allow cancellations between different functions and thus give a more realistic error, but should not be used for complicated diagrams where the individual functions are very large.

**grouping** Even though *togetherflag=0* is chosen, it can be beneficial to first sum a few functions before integrating them. Choosing a value for the grouping which is unequal to zero, defines how many bytes a summed function may have. The number of bytes is set by *grouping=#bytes*. Setting *grouping=0*, all functions *f\*.f* resp. *f\*.cc* are integrated separately. In practice, a *grouping=0* has proven to lead to faster convergence and more accurate results. When considering integrals where large cancellations among the different functions occur, the grouping value should be chosen  $\neq 0$ . The log files *\*results\*.log* in the results directory contain the results from the individual sub-sector integration. They can be viewed to spot cancellations between the individual functions.

**editor** Choose here which editor should be used to display the result. If *editor=none* is set, the full result will not be displayed in an editor window at the end of the calculation.

**language** The choice between Fortran and C<sup>++</sup> can be made in the *myparam.input* file by choosing either *language=Cpp* (default) or *language=Fortran*. For diagrams with purely Euclidean kinematics, both languages can be chosen. In combination with *contourdef=True*, *language=Cpp* must be used, as the inclusion of an imaginary part in the result is implemented in C<sup>++</sup> only.

**rescale** If all invariants are very small or very large it is beneficial to rescale them to reach faster convergence during numerical integration. The rescaling (scaling out the largest invariant in the numerical integration part) can be switched on with *rescale=1* and switched off when set to 0 (default). If switched on, it is not possible to set explicit values for any non-zero invariant in the *onshell=* conditions in the Mathematica template file *mytemplate.m*.

**contourdef** The contour deformation can be switched on or off, by choosing *contourdef=True/False* in the input file *myparamloop.input*. For multi-scale problems, respectively diagrams with non-Euclidean kinematics, set *contourdef=True* (default is *False*). In this case, a deformation of the integration contour in the form of Eq. (5.7) is done. In addition to the functions *f\*.cc* to be integrated, auxiliary files *g\*.cc* are produced which serve to optimize the deformation for each integrand function.

**lambda** The initial value for  $\lambda$  can be set for the deformation of Eq. (5.7) by assigning a value to *lambda=*. The program takes the  $\lambda$  value given by the user in the *myparam.input* file as a starting point. During the checks listed in Sec. 6.2.3, the appropriate value for  $\lambda$  is found automatically by the program. The user should pick an initial value which is rather too large than too small. A too large initial value for  $\lambda$  can easily be accommodated to have the right size during the computation, while a too small initial value can not be increased anymore. *lambda=3.0* usually serves as a good initial value. Without any knowledge about the characteristics of the integrand, *lambda=1.0* is a good choice. If the diagram contains mostly massless propagators and light-like legs, it can be useful to choose the initial  $\lambda$  larger (e.g. *lambda=5.0*), in order to compensate for cases where the remainders of the IR subtraction lead to large cancellations for  $x_i \rightarrow 0$ . For diagrams with mostly massive propagators the initial lambda can be chosen smaller, e.g. *lambda=0.1*.

**smalldefs** If the integrand is expected to be oscillatory and hence sensitive to small changes in the deformation parameter  $\lambda$ , *smalldefs* should be set to 1 (default is 0). If switched on, the argument of each sub-sector function  $\mathcal{F}$  is minimized.

**largedefs** If the integrand is expected to have (integrable) endpoint singularities at  $x_j = 0$  or 1, the deformation should be maximized. If *largedefs=1*, the program maximizes the deformation. The default is *largedefs=0*.

**optlamevals** The number of pre-samples to determine the optimal contour deformation parameter  $\lambda$  can be chosen by assigning a number to *optlamevals=* in the *myparam.input*. The default value is 4000.

#### A.2.4 Input for the definition of the integrand

The Mathematica input file should be called *\*.m*. The following parameters can be specified in Mathematica readable format

**momlist** If *cutconstruct=0* is set in the input file, specify the names of the loop momenta here.

**proplist** Specify the diagram topology here (mandatory). The syntax for *cutconstruct=1* is described in Section A.2.5. If *cutconstruct=0* has been chosen, the propagators have to be given explicitly. An example propagator list could be

$proplist=\{k^2-ms[1],(k+p1)^2-ms[1]\}$

with the loop momentum  $k$ , the propagator mass  $m_1^2$  and external momentum  $p_1$ .

**numerator** If present, specify the numerator of the integrand here. If not given, a  $numerator=\{1\}$  is assumed. Please note that the option  $cutconstruct=1$  is not available in combination with numerator functions.

**powerlist** The propagator powers must be specified. If all propagators are raised to the power one, an example syntax reads  $powerlist=Table[1,\{i,Length[proplist]\}];$  .

**onshell** Specify replacements for kinematic invariants here. The specification of light-like external legs is of specific importance in the generation of the correct integrand topology. These can be assigned by writing

$onshell=\{ssp[1] \rightarrow 0\}$ ,

where  $ssp[1]$  denotes the first external momentum squared,  $p_1^2$ . The kinematic invariants can be assigned other specific values, e.g.  $ssp[1] \rightarrow 0.25$ . Furthermore, relations among the invariants can be set (e.g.  $ssp[1] \rightarrow sp[1,3]$ ). This option can not be used in combination with  $rescale=1$ .

**Dim** Set the space-time dimension. The default is  $Dim=4-2*eps$ . The symbol for the regulator,  $eps$ , must be kept.

**threshold** This option works in combination with C++ and  $contourdef=True$ . Specify a kinematical threshold condition above which, an imaginary part is expected. For the calculation below this threshold, the imaginary part is set to zero and the contour deformation parameter  $\lambda$  is decreased to a very small value. Set  $threshold=none$ , remove or comment the line out if the threshold option should not be used (default). Usage of constants and kinematic invariants  $ms[i]$ ,  $ssp[i]$  and  $sp[i,j]$  is allowed. An example syntax reads  $threshold = sp[1,2] > 0;$ .

**splitlist** The integration region of those integrals over Feynman parameters  $t_{j_i}$ , specified in a  $splitlist=\{j_1, j_2, \dots, j_n\}$  in the `mytemplatefile.m` is split at 1/2 and the resulting two integrals are remapped to the unit interval. The procedure follows the explanations of Sec. 6.3.7.

## A.2.5 Topology based construction of an integrand

The implementation of the topology based construction of an integrand in the program SECDEC is such that the user only has to label the external momenta  $p_i$ , the vertices  $i$  and the masses  $ms[k]$  of a graph. It is selected by choosing  $cutconstruct=1$  in the input file. If an external momentum  $p_i$  is part of a vertex, this vertex needs to carry the label  $i$ . The labeling of vertices containing only internal lines is arbitrary. In the `mytemplate.m` file, the user has to specify the  $proplist$  as a list of entries of the form  $\{ms[k], \{i, j\}\}$ , where  $ms[k]$  is the mass squared of the propagator connecting vertex  $i$  and vertex  $j$ . The mass label  $k$  must correspond the the  $k$ th entry of the list of masses given in `paramloop.input`. While  $k$  needs to be the number labeling the masses,  $ms[k]$



(with  $k$  being an integer) can be left symbolic until numerical integration. If the mass is zero, the user has to put  $\{0, \{i, j\}\}$ , because this changes the singularity structure at the level of the decomposition into sectors. More examples can be found in the Mathematica template files `templateP126.m`, `templateBnp6*.m`, `templateJapNP.m`, `templateggtt*.m` in the subdirectory `loop/demos`. The original form of specifying the propagators by their momenta and including numerators different from one, as done in SECDEC 1.0 [301], is still operational. To use the latter option, the flag `cutconstruct=` must be set to zero.

### A.2.6 Utilization of the user-defined setup

When the functions  $\mathcal{U}$  and  $\mathcal{F}$  are already known and the  $\delta$ -distribution is integrated out, a user-defined setup can be considered. The integrand could then be defined in the `mytemplateuserdefined.m` file. First, the two known Symanzik polynomials, the numerator and the rank of the integral are written to the template file. Taking the diagram  $P_{126}$  as an example, compare Sec. 6.5.1, the input in the `mytemplateuserdefined.m` file reads

$$U[z\_ ] := z[1]*z[2] + z[2]*z[3] + z[1]*z[4] + z[2]*z[4] + z[3]*z[4] + z[1]*z[5] + z[2]*z[5] + z[3]*z[5] + z[1]*z[6] + z[2]*z[6] + z[3]*z[6]$$

$$F[z\_ ] := -(sp[1, 2]*z[1]*z[2]*z[3]) - sp[1, 2]*z[1]*z[3]*z[4] - sp[1, 2]*z[1]*z[3]*z[5] - sp[1, 2]*z[2]*z[3]*z[5] - sp[1, 2]*z[1]*z[2]*z[6] - sp[1, 2]*z[1]*z[3]*z[6] - sp[1, 2]*z[1]*z[5]*z[6] - sp[1, 2]*z[2]*z[5]*z[6] - sp[1, 2]*z[3]*z[5]*z[6] + (ms[1]*z[1] + ms[1]*z[2] + ms[1]*z[3])* (z[1]*z[2] + z[2]*z[3] + z[1]*z[4] + z[2]*z[4] + z[3]*z[4] + z[1]*z[5] + z[2]*z[5] + z[3]*z[5] + z[1]*z[6] + z[2]*z[6] + z[3]*z[6])$$

$$\begin{aligned} Num &= 1; \\ rank &= 0; \end{aligned}$$

The naming of these functions is arbitrary and only needed for a clearer presentation of the functions in the *functionlist*, to be explained now. The diagram  $P_{126}$  has six propagators and is therefore assumed to have six primary sectors after having integrated out the  $\delta$ -distribution. The primary sectors are counted in the first entry of each function. In a more general application, the first entry just lists those functions of equal exponents in the Symanzik polynomials which should be grouped together. The second entry of each function in the *functionlist* gives the exponents of each Feynman parameter, starting with the exponent of  $t_1$ . The total number of Feynman parameters occurring here (and to be integrated over afterwards) is 5 because the  $\delta$ -distribution was already integrated out. The third entry in the list is the function, corresponding to the first Symanzik polynomial in the first primary sector, followed by its exponent and a flag whether the function needs further sector decomposition or not. Here,  $B$  denotes that further decomposition is necessary while  $A$  means that the function is already fully decomposed into sectors.

```

functionlist = {
{1, {0,0,0,0,0}, {{(U[t]/.t[1]->1)/.t[6]->t[1], XU, B}, {(F[t]/.t[1]->1)/.t[6]->t[1], XF, B}, Num},
{2, {0,0,0,0,0}, {{(U[t]/.t[2]->1)/.t[6]->t[2], XU, B}, {(F[t]/.t[2]->1)/.t[6]->t[2], XF, B}, Num},
{3, {0,0,0,0,0}, {{(U[t]/.t[3]->1)/.t[6]->t[3], XU, B}, {(F[t]/.t[3]->1)/.t[6]->t[3], XF, B}, Num},
{4, {0,0,0,0,0}, {{(U[t]/.t[4]->1)/.t[6]->t[4], XU, B}, {(F[t]/.t[4]->1)/.t[6]->t[4], XF, B}, Num},
{5, {0,0,0,0,0}, {{(U[t]/.t[5]->1)/.t[6]->t[5], XU, B}, {(F[t]/.t[5]->1)/.t[6]->t[5], XF, B}, Num},
{6, {0,0,0,0,0}, {{U[t]/.t[6]->1, XU, B}, {F[t]/.t[6]->1, XF, B}, Num}};

```

Choosing  $XU$  and  $XF$ , the exponents of the functions  $\mathcal{U}$  and  $\mathcal{F}$ , respectively, are computed automatically by the program using the information about the number of loops, the number of propagators, their powers, the rank and the space-time dimension. To run this example, from the `loop` directory, issue the command `./launch -p paramuserdefined.input -t templateuserdefined.m -u`. The demo files `paramuserdefined.m` and `templateuserdefined.m` in the `loop` directory come with the code.

### A.2.7 Looping over ranges of parameters

A looping over ranges of parameters in SECDEC is put into practice using the perl script `multinumerics*`, where the `*` stands either for `loop.pl`, `userdefined.pl` or just `.pl`, depending on whether a standard loop, a user-defined integral or a more general parametric integral should be computed for ranges of parameters. The sets of parameters to be evaluated are specified in a text file `mymultiparam.input` in `myworkingdir`, to be read by the `multinumerics*-script`.

The following information must be contained in this textfile:

- *paramfile* = *myparam.input*: Specify the name of the parameter file containing the graph info.
- *pointname* = *my\_prefix* (optional): Specify a name which is used as prefix to each kinematical point. To distinguish different kinematical points, each gets a different name using the prefix and sequential number, e.g. *my\_prefix1* for the first point, *my\_prefix2* for the second and so on.
- *lines* = *a* (optional): Specify the number *a* of points you wish to calculate - if omitted all points (listed in separate lines) will be calculated.
- *xplot* = *b* (optional): If this option is set, a tab-separated data file is written with a variable of choice in the first column, the numeric result for the real part in the second column, the uncertainty in the third column, the numeric result for the imaginary part in the fourth column and its uncertainty in the fifth. The integer *b* defines the number of the column in the `multiparam.input` file containing the values which should be stored in the first column of the data file (default is 1). The resulting data files can directly be used for producing plots with, e.g., `gnuplot`.

The subsequent specifications are different for parametric integrals and loop (or similar) integrals.

multinumericsloop.pl and multinumericsuserdefined.pl:

When computing either a standard loop or a user-defined integral, the number of values given for  $s_{ij}$ ,  $p_i^2$  and  $m_i^2$  need to be specified by

```
numsj=  
numpi2=  
numms2= .
```

Numerical values of the parameters for each point to calculate need to ensue these definitions. Examples come with the code of the program, one is found in `loop/demos/multiparam.input`. The perl script `helpmulti.pl` can be used to generate `multiparam.input` files automatically, to avoid typing large sets of numerical values.

multinumerics.pl:

When computing a more general parametric function, depending, for instance, on the two symbols  $a$  and  $b$  (defined as such in the `param.input` file), values for these can either be specified explicitly in the `multiparam.input` file as

```
values1=0.1,0.2,0.4  
values2=0.1,0.3,0.6 ,
```

where `values1` is linked to the first symbol specified in the `param.input` file, `values2` to the second symbol and so on. Or, if the user desires to calculate the integrand for values of parameters at incremental steps, the following syntax applies

```
minvals=0.1,0.1  
maxvals=0.3,0.7  
stepvals=0.1,0.2 .
```

This input would calculate each combination of  $a = 0.1, 0.2, 0.3$  and  $b = 0.1, 0.3, 0.5, 0.7$ , where  $a$  and  $b$  are specified first and second in the list of symbols in the `param.input` file. Further examples can be found in `general/demos/multiparam.input`.

Before executing the script `multinumerics*`, the functions generated by Mathematica must already be in place. The simplest way to guarantee this is to run the `launch` script, choosing `exeflag=1` in the `myparamfile.input` and subsequently issue the command `./multinumerics* [-d myworkingdir -p multiparamfile]`.

In the single-machine mode (`clusterflag=0`) all integrations are performed sequentially, in the batch mode, they are run in parallel.

Running the script again with the additional argument "1" as

```
./multinumerics* [-d myworkingdir -p multiparamfile] 1 ,
```

all results are collated before writing the output as `*.out` files into the graph directory specified in the `myparamfile.input`. If specified in the `multiparam.input` file, an additional `*.gpd` file is written, containing the results of all computed points.

The script generates a parameter file for each numerical point calculated. To remove

such intermediate parameter files, issue the command  
`./multinumerics* [-d myworkingdir -p multiparamfile] 2`.  
This should only be done after the results have been collected.

### A.2.8 Leaving functions implicit during the algebraic part

To use this option, the Mathematica template file can contain a function which is left undefined, but needs to be listed with the option `dummys=` in the `myparam.input` file. If symbolic parameters are used in addition, these do not need to be listed as arguments of the implicit function.

Once the template and parameter files are set up, the functions need to be defined explicitly so that they can be used in the calculation. The simplest way to do this is to prepare a Mathematica syntax file for each implicit function, and place them in the output directory specified as `outputdir=` in the `myparam.input` file. For a function named `dum1` of two variables, defined as  $dum1(x_1, x_2) = 1 + x_1 + x_2$ , the following lines would need to be inserted in a file `dum1.m` named after the dummy function

```
intvars = {z1, z2};  
dum1 = 1 + z1 + z2;
```

where  $z_1, z_2$  can be replaced by any variable name you wish, as long as they are used consistently in `dum1.m`. Once these Mathematica files are in place, issue the command  
`createdummyfortran.pl [-d myworkingdir -p myparamfile]` .

This triggers the generation of the necessary Fortran files for the user-defined dummy functions. The files are stored in the same subdirectory as the originals.

It is equally possible to write these Fortran files oneself instead of having them generated by the program, although the automated procedure is recommended. An example of this can be found in the directory `general/demos`, comprised in the files `paramdummy.input`, `templatedummy.m` and in the directory `/testdummy`.

# Bibliography

- [1] S. Borowka, J. Carter, G. Heinrich, Numerical Evaluation of Multi-Loop Integrals for Arbitrary Kinematics with SecDec 2.0, *Comput.Phys.Commun.* 184 (2013) 396–408. arXiv:1204.4152, doi:10.1016/j.cpc.2012.09.020.
- [2] S. Borowka, G. Heinrich, Massive non-planar two-loop four-point integrals with SecDec 2.1, *Comput.Phys.Commun.* 184 (2013) 2552–2561. arXiv:1303.1157, doi:10.1016/j.cpc.2013.05.022.
- [3] S. Borowka, T. Hahn, S. Heinemeyer, G. Heinrich, W. Hollik, Momentum-dependent two-loop QCD corrections to the neutral Higgs-boson masses in the MSSM arXiv:1404.7074.
- [4] S. Borowka, J. Carter, G. Heinrich, SecDec: A tool for numerical multi-loop calculations, *J.Phys.Conf.Ser.* 368 (2012) 012051. arXiv:1206.4908, doi:10.1088/1742-6596/366/1/012051.
- [5] S. Borowka, G. Heinrich, Numerical evaluation of massive multi-loop integrals with SecDec, *PoS LL2012* (2012) 038. arXiv:1209.6345.
- [6] S. Borowka, G. Heinrich, Numerical multi-loop calculations with SecDec, *C 13-05-16*. arXiv:1309.3492.
- [7] S. Borowka, G. Heinrich, Two-loop applications of the program SecDec, *PoS RAD-COR2013* (2014) 009. arXiv:1311.6476.
- [8] S. Glashow, Partial Symmetries of Weak Interactions, *Nucl.Phys.* 22 (1961) 579–588. doi:10.1016/0029-5582(61)90469-2.
- [9] S. Weinberg, A Model of Leptons, *Phys.Rev.Lett.* 19 (1967) 1264–1266. doi:10.1103/PhysRevLett.19.1264.
- [10] A. Salam, Weak and Electromagnetic Interactions, *Conf.Proc.* C680519 (1968) 367–377.
- [11] H. Fritzsch, M. Gell-Mann, H. Leutwyler, Advantages of the Color Octet Gluon Picture, *Phys.Lett.* B47 (1973) 365–368. doi:10.1016/0370-2693(73)90625-4.

- [12] D. Gross, F. Wilczek, Asymptotically Free Gauge Theories. 1, *Phys.Rev. D8* (1973) 3633–3652. doi:10.1103/PhysRevD.8.3633.
- [13] D. J. Gross, F. Wilczek, Ultraviolet Behavior of Nonabelian Gauge Theories, *Phys.Rev.Lett.* 30 (1973) 1343–1346. doi:10.1103/PhysRevLett.30.1343.
- [14] H. D. Politzer, Reliable Perturbative Results for Strong Interactions?, *Phys.Rev.Lett.* 30 (1973) 1346–1349. doi:10.1103/PhysRevLett.30.1346.
- [15] G. Guralnik, C. Hagen, T. Kibble, Global Conservation Laws and Massless Particles, *Phys.Rev.Lett.* 13 (1964) 585–587. doi:10.1103/PhysRevLett.13.585.
- [16] F. Englert, R. Brout, Broken Symmetry and the Mass of Gauge Vector Mesons, *Phys.Rev.Lett.* 13 (1964) 321–323. doi:10.1103/PhysRevLett.13.321.
- [17] P. W. Higgs, Broken symmetries, massless particles and gauge fields, *Phys.Lett.* 12 (1964) 132–133. doi:10.1016/0031-9163(64)91136-9.
- [18] P. W. Higgs, Spontaneous Symmetry Breakdown without Massless Bosons, *Phys.Rev.* 145 (1966) 1156–1163. doi:10.1103/PhysRev.145.1156.
- [19] G. Aad, et al., Observation of a new particle in the search for the Standard Model Higgs boson with the ATLAS detector at the LHC, *Phys.Lett. B716* (2012) 1–29. arXiv:1207.7214, doi:10.1016/j.physletb.2012.08.020.
- [20] S. Chatrchyan, et al., Observation of a new boson at a mass of 125 GeV with the CMS experiment at the LHC, *Phys.Lett. B716* (2012) 30–61. arXiv:1207.7235, doi:10.1016/j.physletb.2012.08.021.
- [21] G. Aad, et al., Evidence for the spin-0 nature of the Higgs boson using ATLAS data, *Phys.Lett. B726* (2013) 120–144. arXiv:1307.1432, doi:10.1016/j.physletb.2013.08.026.
- [22] Updated coupling measurements of the Higgs boson with the ATLAS detector using up to 25 fb<sup>-1</sup> of proton-proton collision data, Tech. Rep. ATLAS-CONF-2014-009, CERN, Geneva (Mar 2014).
- [23] S. Chatrchyan, et al., Measurement of the properties of a Higgs boson in the four-lepton final state arXiv:1312.5353.
- [24] S. Chatrchyan, et al., Measurement of Higgs boson production and properties in the WW decay channel with leptonic final states, *JHEP* 1401 (2014) 096. arXiv:1312.1129, doi:10.1007/JHEP01(2014)096.
- [25] K. Begeman, A. Broeils, R. Sanders, Extended rotation curves of spiral galaxies: Dark haloes and modified dynamics, *Mon.Not.Roy.Astron.Soc.* 249 (1991) 523.
- [26] D. Clowe, M. Bradac, A. H. Gonzalez, M. Markevitch, S. W. Randall, et al., A direct empirical proof of the existence of dark matter, *Astrophys.J.* 648 (2006) L109–L113. arXiv:astro-ph/0608407, doi:10.1086/508162.

- 
- [27] P. Ade, et al., Planck 2013 results. XVI. Cosmological parameters arXiv:1303.5076.
- [28] N. Cabibbo, L. Maiani, G. Parisi, R. Petronzio, Bounds on the Fermions and Higgs Boson Masses in Grand Unified Theories, Nucl.Phys. B158 (1979) 295–305. doi:10.1016/0550-3213(79)90167-6.
- [29] P. Q. Hung, Vacuum Instability and New Constraints on Fermion Masses, Phys.Rev.Lett. 42 (1979) 873. doi:10.1103/PhysRevLett.42.873.
- [30] M. Lindner, Implications of Triviality for the Standard Model, Z.Phys. C31 (1986) 295. doi:10.1007/BF01479540.
- [31] G. Degrandi, S. Di Vita, J. Elias-Miro, J. R. Espinosa, G. F. Giudice, et al., Higgs mass and vacuum stability in the Standard Model at NNLO, JHEP 1208 (2012) 098. arXiv:1205.6497, doi:10.1007/JHEP08(2012)098.
- [32] S. Weinberg, Implications of Dynamical Symmetry Breaking: An Addendum, Phys.Rev. D19 (1979) 1277–1280. doi:10.1103/PhysRevD.19.1277.
- [33] E. Gildener, S. Weinberg, Symmetry Breaking and Scalar Bosons, Phys.Rev. D13 (1976) 3333. doi:10.1103/PhysRevD.13.3333.
- [34] J. Cao, Y. He, P. Wu, M. Zhang, J. Zhu, Higgs Phenomenology in the Minimal Dilaton Model after Run I of the LHC, JHEP 1401 (2014) 150. arXiv:1311.6661, doi:10.1007/JHEP01(2014)150.
- [35] D. B. Kaplan, H. Georgi,  $SU(2) \times U(1)$  Breaking by Vacuum Misalignment, Phys.Lett. B136 (1984) 183. doi:10.1016/0370-2693(84)91177-8.
- [36] G. Giudice, C. Grojean, A. Pomarol, R. Rattazzi, The Strongly-Interacting Light Higgs, JHEP 0706 (2007) 045. arXiv:hep-ph/0703164, doi:10.1088/1126-6708/2007/06/045.
- [37] H. P. Nilles, Supersymmetry, Supergravity and Particle Physics, Phys.Rept. 110 (1984) 1–162. doi:10.1016/0370-1573(84)90008-5.
- [38] H. E. Haber, G. L. Kane, The Search for Supersymmetry: Probing Physics Beyond the Standard Model, Phys.Rept. 117 (1985) 75–263. doi:10.1016/0370-1573(85)90051-1.
- [39] R. Barbieri, Looking Beyond the Standard Model: The Supersymmetric Option, Riv.Nuovo Cim. 11N4 (1988) 1–45. doi:10.1007/BF02725953.
- [40] P. Ramond, Dual Theory for Free Fermions, Phys.Rev. D3 (1971) 2415–2418. doi:10.1103/PhysRevD.3.2415.
- [41] A. Neveu, J. Schwarz, Factorizable dual model of pions, Nucl.Phys. B31 (1971) 86–112. doi:10.1016/0550-3213(71)90448-2.

- [42] J.-L. Gervais, B. Sakita, Field Theory Interpretation of Supergauges in Dual Models, Nucl.Phys. B34 (1971) 632–639. doi:10.1016/0550-3213(71)90351-8.
- [43] Y. Golfand, E. Likhtman, Extension of the Algebra of Poincare Group Generators and Violation of p Invariance, JETP Lett. 13 (1971) 323–326.
- [44] D. Volkov, V. Akulov, Is the Neutrino a Goldstone Particle?, Phys.Lett. B46 (1973) 109–110. doi:10.1016/0370-2693(73)90490-5.
- [45] J. Wess, B. Zumino, A Lagrangian Model Invariant Under Supergauge Transformations, Phys.Lett. B49 (1974) 52. doi:10.1016/0370-2693(74)90578-4.
- [46] J. Wess, B. Zumino, Supergauge Transformations in Four-Dimensions, Nucl.Phys. B70 (1974) 39–50. doi:10.1016/0550-3213(74)90355-1.
- [47] R. Haag, J. T. Lopuszanski, M. Sohnius, All Possible Generators of Supersymmetries of the s Matrix, Nucl.Phys. B88 (1975) 257. doi:10.1016/0550-3213(75)90279-5.
- [48] S. R. Coleman, J. Mandula, All Possible Symmetries of the S Matrix, Phys.Rev. 159 (1967) 1251–1256. doi:10.1103/PhysRev.159.1251.
- [49] P. Fayet, Supergauge Invariant Extension of the Higgs Mechanism and a Model for the electron and Its Neutrino, Nucl.Phys. B90 (1975) 104–124. doi:10.1016/0550-3213(75)90636-7.
- [50] E. Witten, Dynamical Breaking of Supersymmetry, Nucl.Phys. B188 (1981) 513. doi:10.1016/0550-3213(81)90006-7.
- [51] S. Dimopoulos, H. Georgi, Softly Broken Supersymmetry and SU(5), Nucl.Phys. B193 (1981) 150. doi:10.1016/0550-3213(81)90522-8.
- [52] N. Sakai, Naturalness in Supersymmetric Guts, Z.Phys. C11 (1981) 153. doi:10.1007/BF01573998.
- [53] K. Inoue, A. Kakuto, H. Komatsu, S. Takeshita, Low-Energy Parameters and Particle Masses in a Supersymmetric Grand Unified Model, Prog.Theor.Phys. 67 (1982) 1889. doi:10.1143/PTP.67.1889.
- [54] K. Inoue, A. Kakuto, H. Komatsu, S. Takeshita, Aspects of Grand Unified Models with Softly Broken Supersymmetry, Prog.Theor.Phys. 68 (1982) 927. doi:10.1143/PTP.68.927.
- [55] K. Inoue, A. Kakuto, H. Komatsu, S. Takeshita, Renormalization of Supersymmetry Breaking Parameters Revisited, Prog.Theor.Phys. 71 (1984) 413. doi:10.1143/PTP.71.413.
- [56] S. L. Glashow, S. Weinberg, Natural Conservation Laws for Neutral Currents, Phys.Rev. D15 (1977) 1958. doi:10.1103/PhysRevD.15.1958.



- 
- [57] J. Butterworth, G. Dissertori, S. Dittmaier, D. de Florian, N. Glover, et al., Les Houches 2013: Physics at TeV Colliders: Standard Model Working Group Report arXiv:1405.1067.
- [58] M. Czakon, P. Fiedler, A. Mitov, Total Top-Quark Pair-Production Cross Section at Hadron Colliders Through  $O(\alpha_s^4)$ , Phys.Rev.Lett. 110 (25) (2013) 252004. arXiv:1303.6254, doi:10.1103/PhysRevLett.110.252004.
- [59] J. Korner, Z. Merebashvili, M. Rogal, NNLO  $O(\alpha_s^4)$  results for heavy quark pair production in quark-antiquark collisions: The One-loop squared contributions, Phys.Rev. D77 (2008) 094011. arXiv:0802.0106, doi:10.1103/PhysRevD.77.094011, 10.1103/PhysRevD.85.119904.
- [60] R. Bonciani, A. Ferroglia, T. Gehrmann, D. Maitre, C. Studerus, Two-Loop Fermionic Corrections to Heavy-Quark Pair Production: The Quark-Antiquark Channel, JHEP 0807 (2008) 129. arXiv:0806.2301, doi:10.1088/1126-6708/2008/07/129.
- [61] R. Bonciani, A. Ferroglia, T. Gehrmann, C. Studerus, Two-Loop Planar Corrections to Heavy-Quark Pair Production in the Quark-Antiquark Channel, JHEP 0908 (2009) 067. arXiv:0906.3671, doi:10.1088/1126-6708/2009/08/067.
- [62] R. Bonciani, A. Ferroglia, T. Gehrmann, A. Manteuffel, C. Studerus, Two-Loop Leading Color Corrections to Heavy-Quark Pair Production in the Gluon Fusion Channel, JHEP 1101 (2011) 102. arXiv:1011.6661, doi:10.1007/JHEP01(2011)102.
- [63] M. Aliev, H. Lacker, U. Langenfeld, S. Moch, P. Uwer, et al., HATHOR: HAdronic Top and Heavy quarks crOss section calculatoR, Comput.Phys.Commun. 182 (2011) 1034–1046. arXiv:1007.1327, doi:10.1016/j.cpc.2010.12.040.
- [64] G. Abelof, A. Gehrmann-De Ridder, Double real radiation corrections to  $t\bar{t}$  production at the LHC: the all-fermion processes, JHEP 1204 (2012) 076. arXiv:1112.4736, doi:10.1007/JHEP04(2012)076.
- [65] M. Czakon, Double-real radiation in hadronic top quark pair production as a proof of a certain concept, Nucl.Phys. B849 (2011) 250–295. arXiv:1101.0642, doi:10.1016/j.nuclphysb.2011.03.020.
- [66] M. Czakon, A. Mitov, NNLO corrections to top pair production at hadron colliders: the quark-gluon reaction, JHEP 1301 (2013) 080. arXiv:1210.6832, doi:10.1007/JHEP01(2013)080.
- [67] M. Czakon, A. Mitov, NNLO corrections to top-pair production at hadron colliders: the all-fermionic scattering channels, JHEP 1212 (2012) 054. arXiv:1207.0236, doi:10.1007/JHEP12(2012)054.
- [68] P. Baernreuther, M. Czakon, A. Mitov, Percent Level Precision Physics at the Tevatron: First Genuine NNLO QCD Corrections to  $q\bar{q} \rightarrow t\bar{t} + X$ , Phys.Rev.Lett. 109 (2012) 132001. arXiv:1204.5201, doi:10.1103/PhysRevLett.109.132001.

- [69] A. von Manteuffel, C. Studerus, Top quark pairs at two loops and Reduze 2 To appear in the proceedings of the conference “Loops and Legs in Quantum Field Theory”, 2012. arXiv:1210.1436.
- [70] G. Abelof, A. Gehrmann-De Ridder, O. Dekkers, Antenna subtraction with massive fermions at NNLO: Double real initial-final configurations, JHEP 1212 (2012) 107. arXiv:1210.5059, doi:10.1007/JHEP12(2012)107.
- [71] G. Abelof, A. Gehrmann-De Ridder, Double real radiation corrections to  $t\bar{t}$  production at the LHC: the  $gg \rightarrow t\bar{t}q\bar{q}$  channel, JHEP 1211 (2012) 074. arXiv:1207.6546, doi:10.1007/JHEP11(2012)074.
- [72] M. Czakon, A. Mitov, Precision top pair production at hadron colliders, J.Phys.Conf.Ser. 452 (2013) 012026. arXiv:1303.0693, doi:10.1088/1742-6596/452/1/012026.
- [73] S. Moch, P. Uwer, A. Vogt, On top-pair hadro-production at next-to-next-to-leading order, Phys.Lett. B714 (2012) 48–54. arXiv:1203.6282, doi:10.1016/j.physletb.2012.06.048.
- [74] M. Cacciari, M. Czakon, M. Mangano, A. Mitov, P. Nason, Top-pair production at hadron colliders with next-to-next-to-leading logarithmic soft-gluon resummation, Phys.Lett. B710 (2012) 612–622. arXiv:1111.5869, doi:10.1016/j.physletb.2012.03.013.
- [75] M. Czakon, A. Mitov, Top++: A Program for the Calculation of the Top-Pair Cross-Section at Hadron Colliders arXiv:1112.5675.
- [76] M. Beneke, P. Falgari, S. Klein, C. Schwinn, Hadronic top-quark pair production with NNLL threshold resummation, Nucl.Phys. B855 (2012) 695–741. arXiv:1109.1536, doi:10.1016/j.nuclphysb.2011.10.021.
- [77] M. Beneke, P. Falgari, S. Klein, J. Piclum, C. Schwinn, et al., Inclusive Top-Pair Production Phenomenology with TOPIX, JHEP 1207 (2012) 194. arXiv:1206.2454, doi:10.1007/JHEP07(2012)194.
- [78] V. Ahrens, A. Ferroglia, M. Neubert, B. D. Pecjak, L. L. Yang, Precision predictions for the  $t+t(\text{bar})$  production cross section at hadron colliders, Phys.Lett. B703 (2011) 135–141. arXiv:1105.5824, doi:10.1016/j.physletb.2011.07.058.
- [79] N. Kidonakis, Next-to-next-to-leading soft-gluon corrections for the top quark cross section and transverse momentum distribution, Phys.Rev. D82 (2010) 114030. arXiv:1009.4935, doi:10.1103/PhysRevD.82.114030.
- [80] R. Bonciani, A. Ferroglia, T. Gehrmann, A. von Manteuffel, C. Studerus, Light-quark two-loop corrections to heavy-quark pair production in the gluon fusion channel, JHEP 1312 (2013) 038. arXiv:1309.4450, doi:10.1007/JHEP12(2013)038.

- 
- [81] A. von Manteuffel, C. Studerus, Massive planar and non-planar double box integrals for light  $N_f$  contributions to  $gg \rightarrow t\bar{t}$ , JHEP 1310 (2013) 037. arXiv:1306.3504, doi:10.1007/JHEP10(2013)037.
- [82] J. Gunion, H. E. Haber, Higgs Bosons in Supersymmetric Models. 1., Nucl.Phys. B272 (1986) 1. doi:10.1016/0550-3213(86)90340-8.
- [83] J. Gunion, H. E. Haber, Higgs Bosons in Supersymmetric Models. 2. Implications for Phenomenology, Nucl.Phys. B278 (1986) 449. doi:10.1016/0550-3213(86)90050-7.
- [84] P. Fayet, S. Ferrara, Supersymmetry, Phys.Rept. 32 (1977) 249–334. doi:10.1016/0370-1573(77)90066-7.
- [85] J. F. Gunion, H. E. Haber, G. L. Kane, S. Dawson, The Higgs Hunter’s Guide, Vol. 80, 2000.
- [86] H. A. Rzehak, Two-loop contributions to the supersymmetric Higgs sector, Ph.D. thesis (2005).
- [87] L. Faddeev, V. Popov, Feynman Diagrams for the Yang-Mills Field, Phys.Lett. B25 (1967) 29–30. doi:10.1016/0370-2693(67)90067-6.
- [88] L. Girardello, M. T. Grisaru, Soft Breaking of Supersymmetry, Nucl.Phys. B194 (1982) 65. doi:10.1016/0550-3213(82)90512-0.
- [89] M. S. Carena, H. E. Haber, H. E. Logan, S. Mrenna, Distinguishing a MSSM Higgs boson from the SM Higgs boson at a linear collider, Phys.Rev. D65 (2002) 055005. arXiv:hep-ph/0106116, doi:10.1103/PhysRevD.65.055005, 10.1103/PhysRevD.65.099902.
- [90] S. Ferrara, B. Zumino, Supergauge Invariant Yang-Mills Theories, Nucl.Phys. B79 (1974) 413. doi:10.1016/0550-3213(74)90559-8.
- [91] M. Drees, R. Godbole, P. Roy, Theory and phenomenology of sparticles: An account of four-dimensional N=1 supersymmetry in high energy physics , 2004.
- [92] R. Jackiw, Functional evaluation of the effective potential, Phys.Rev. D9 (1974) 1686. doi:10.1103/PhysRevD.9.1686.
- [93] M. E. Peskin, D. V. Schroeder, An Introduction to quantum field theory .
- [94] J. R. Ellis, G. Ridolfi, F. Zwirner, Radiative corrections to the masses of supersymmetric Higgs bosons, Phys.Lett. B257 (1991) 83–91. doi:10.1016/0370-2693(91)90863-L.
- [95] H. E. Haber, R. Hempfling, Can the mass of the lightest Higgs boson of the minimal supersymmetric model be larger than  $m(Z)$ ?, Phys.Rev.Lett. 66 (1991) 1815–1818. doi:10.1103/PhysRevLett.66.1815.

- [96] Y. Okada, M. Yamaguchi, T. Yanagida, Upper bound of the lightest Higgs boson mass in the minimal supersymmetric standard model, *Prog.Theor.Phys.* 85 (1991) 1–6. doi:10.1143/PTP.85.1.
- [97] A. Brignole, Radiative corrections to the supersymmetric neutral Higgs boson masses, *Phys.Lett.* B281 (1992) 284–294. doi:10.1016/0370-2693(92)91142-V.
- [98] P. H. Chankowski, S. Pokorski, J. Rosiek, One loop corrections to the supersymmetric Higgs boson couplings and LEP phenomenology, *Phys.Lett.* B286 (1992) 307–314. doi:10.1016/0370-2693(92)91780-D.
- [99] P. H. Chankowski, S. Pokorski, J. Rosiek, Complete on-shell renormalization scheme for the minimal supersymmetric Higgs sector, *Nucl.Phys.* B423 (1994) 437–496. arXiv:hep-ph/9303309, doi:10.1016/0550-3213(94)90141-4.
- [100] A. Dabelstein, The One loop renormalization of the MSSM Higgs sector and its application to the neutral scalar Higgs masses, *Z.Phys.* C67 (1995) 495–512. arXiv:hep-ph/9409375, doi:10.1007/BF01624592.
- [101] A. Dabelstein, Fermionic decays of neutral MSSM Higgs bosons at the one loop level, *Nucl.Phys.* B456 (1995) 25–56. arXiv:hep-ph/9503443, doi:10.1016/0550-3213(95)00523-2.
- [102] S. P. Martin, Two loop effective potential for the minimal supersymmetric standard model, *Phys.Rev.* D66 (2002) 096001. arXiv:hep-ph/0206136, doi:10.1103/PhysRevD.66.096001.
- [103] S. P. Martin, Complete two loop effective potential approximation to the lightest Higgs scalar boson mass in supersymmetry, *Phys.Rev.* D67 (2003) 095012. arXiv:hep-ph/0211366, doi:10.1103/PhysRevD.67.095012.
- [104] J. Kodaira, Y. Yasui, K. Sasaki, The Mass of the lightest supersymmetric Higgs boson beyond the leading logarithm approximation, *Phys.Rev.* D50 (1994) 7035–7041. arXiv:hep-ph/9311366, doi:10.1103/PhysRevD.50.7035.
- [105] A. Gladyshev, D. Kazakov, Renormalization group improved radiative corrections to the supersymmetric Higgs boson masses, *Mod.Phys.Lett.* A10 (1995) 3129–3138. arXiv:hep-ph/9411209, doi:10.1142/S0217732395003288.
- [106] M. S. Carena, J. Espinosa, M. Quiros, C. Wagner, Analytical expressions for radiatively corrected Higgs masses and couplings in the MSSM, *Phys.Lett.* B355 (1995) 209–221. arXiv:hep-ph/9504316, doi:10.1016/0370-2693(95)00694-G.
- [107] J. Casas, J. Espinosa, M. Quiros, A. Riotto, The Lightest Higgs boson mass in the minimal supersymmetric standard model, *Nucl.Phys.* B436 (1995) 3–29. arXiv:hep-ph/9407389, doi:10.1016/0550-3213(94)00508-C.

- 
- [108] M. S. Carena, M. Quiros, C. Wagner, Effective potential methods and the Higgs mass spectrum in the MSSM, *Nucl.Phys.* B461 (1996) 407–436. arXiv:hep-ph/9508343, doi:10.1016/0550-3213(95)00665-6.
- [109] R. Hempfling, A. H. Hoang, Two loop radiative corrections to the upper limit of the lightest Higgs boson mass in the minimal supersymmetric model, *Phys.Lett.* B331 (1994) 99–106. arXiv:hep-ph/9401219, doi:10.1016/0370-2693(94)90948-2.
- [110] R.-J. Zhang, Two loop effective potential calculation of the lightest CP even Higgs boson mass in the MSSM, *Phys.Lett.* B447 (1999) 89–97. arXiv:hep-ph/9808299, doi:10.1016/S0370-2693(98)01575-5.
- [111] J. R. Espinosa, R.-J. Zhang, MSSM lightest CP even Higgs boson mass to  $O(\alpha(s)\alpha(t))$ : The Effective potential approach, *JHEP* 0003 (2000) 026. arXiv:hep-ph/9912236, doi:10.1088/1126-6708/2000/03/026.
- [112] J. R. Espinosa, R.-J. Zhang, Complete two loop dominant corrections to the mass of the lightest CP even Higgs boson in the minimal supersymmetric standard model, *Nucl.Phys.* B586 (2000) 3–38. arXiv:hep-ph/0003246, doi:10.1016/S0550-3213(00)00421-1.
- [113] G. Degrassi, P. Slavich, F. Zwirner, On the neutral Higgs boson masses in the MSSM for arbitrary stop mixing, *Nucl.Phys.* B611 (2001) 403–422. arXiv:hep-ph/0105096, doi:10.1016/S0550-3213(01)00343-1.
- [114] A. Brignole, G. Degrassi, P. Slavich, F. Zwirner, On the  $O(\alpha(t)**2)$  two loop corrections to the neutral Higgs boson masses in the MSSM, *Nucl.Phys.* B631 (2002) 195–218. arXiv:hep-ph/0112177, doi:10.1016/S0550-3213(02)00184-0.
- [115] A. Brignole, G. Degrassi, P. Slavich, F. Zwirner, On the two loop sbottom corrections to the neutral Higgs boson masses in the MSSM, *Nucl.Phys.* B643 (2002) 79–92. arXiv:hep-ph/0206101, doi:10.1016/S0550-3213(02)00748-4.
- [116] A. Dedes, G. Degrassi, P. Slavich, On the two loop Yukawa corrections to the MSSM Higgs boson masses at large tan beta, *Nucl.Phys.* B672 (2003) 144–162. arXiv:hep-ph/0305127, doi:10.1016/j.nuclphysb.2003.08.033.
- [117] S. Heinemeyer, W. Hollik, G. Weiglein, QCD corrections to the masses of the neutral CP - even Higgs bosons in the MSSM, *Phys.Rev.* D58 (1998) 091701. arXiv:hep-ph/9803277, doi:10.1103/PhysRevD.58.091701.
- [118] S. Heinemeyer, W. Hollik, G. Weiglein, Precise prediction for the mass of the lightest Higgs boson in the MSSM, *Phys.Lett.* B440 (1998) 296–304. arXiv:hep-ph/9807423, doi:10.1016/S0370-2693(98)01116-2.
- [119] S. Heinemeyer, W. Hollik, G. Weiglein, The Masses of the neutral CP - even Higgs bosons in the MSSM: Accurate analysis at the two loop level, *Eur.Phys.J.* C9 (1999) 343–366. arXiv:hep-ph/9812472, doi:10.1007/s100529900006.

- [120] S. Heinemeyer, W. Hollik, G. Weiglein, The Mass of the lightest MSSM Higgs boson: A Compact analytical expression at the two loop level, *Phys.Lett.* B455 (1999) 179–191. arXiv:hep-ph/9903404, doi:10.1016/S0370-2693(99)00417-7.
- [121] J. Espinosa, M. Quiros, Two loop radiative corrections to the mass of the lightest Higgs boson in supersymmetric standard models, *Phys.Lett.* B266 (1991) 389–396. doi:10.1016/0370-2693(91)91056-2.
- [122] R. Hempfling, Yukawa coupling unification with supersymmetric threshold corrections, *Phys.Rev.* D49 (1994) 6168–6172. doi:10.1103/PhysRevD.49.6168.
- [123] L. J. Hall, R. Rattazzi, U. Sarid, The Top quark mass in supersymmetric SO(10) unification, *Phys.Rev.* D50 (1994) 7048–7065. arXiv:hep-ph/9306309, doi:10.1103/PhysRevD.50.7048.
- [124] M. S. Carena, M. Olechowski, S. Pokorski, C. Wagner, Electroweak symmetry breaking and bottom - top Yukawa unification, *Nucl.Phys.* B426 (1994) 269–300. arXiv:hep-ph/9402253, doi:10.1016/0550-3213(94)90313-1.
- [125] M. S. Carena, D. Garcia, U. Nierste, C. E. Wagner, Effective Lagrangian for the  $\bar{t}bH^+$  interaction in the MSSM and charged Higgs phenomenology, *Nucl.Phys.* B577 (2000) 88–120. arXiv:hep-ph/9912516, doi:10.1016/S0550-3213(00)00146-2.
- [126] J. Espinosa, I. Navarro, Radiative corrections to the Higgs boson mass for a hierarchical stop spectrum, *Nucl.Phys.* B615 (2001) 82–116. arXiv:hep-ph/0104047, doi:10.1016/S0550-3213(01)00429-1.
- [127] M. S. Carena, H. Haber, S. Heinemeyer, W. Hollik, C. Wagner, et al., Reconciling the two loop diagrammatic and effective field theory computations of the mass of the lightest CP - even Higgs boson in the MSSM, *Nucl.Phys.* B580 (2000) 29–57. arXiv:hep-ph/0001002, doi:10.1016/S0550-3213(00)00212-1.
- [128] G. Degrandi, S. Heinemeyer, W. Hollik, P. Slavich, G. Weiglein, Towards high precision predictions for the MSSM Higgs sector, *Eur.Phys.J.* C28 (2003) 133–143. arXiv:hep-ph/0212020, doi:10.1140/epjc/s2003-01152-2.
- [129] S. P. Martin, Three-loop corrections to the lightest Higgs scalar boson mass in supersymmetry, *Phys.Rev.* D75 (2007) 055005. arXiv:hep-ph/0701051, doi:10.1103/PhysRevD.75.055005.
- [130] R. Harlander, P. Kant, L. Mihaila, M. Steinhauser, Higgs boson mass in supersymmetry to three loops, *Phys.Rev.Lett.* 100 (2008) 191602. arXiv:0803.0672, doi:10.1103/PhysRevLett.101.039901, 10.1103/PhysRevLett.100.191602.
- [131] P. Kant, R. Harlander, L. Mihaila, M. Steinhauser, Light MSSM Higgs boson mass to three-loop accuracy, *JHEP* 1008 (2010) 104. arXiv:1005.5709, doi:10.1007/JHEP08(2010)104.

- 
- [132] T. Hahn, S. Heinemeyer, W. Hollik, H. Rzehak, G. Weiglein, High-precision predictions for the light CP-even Higgs Boson Mass of the MSSM arXiv:1312.4937.
- [133] P. Draper, G. Lee, C. E. M. Wagner, Precise Estimates of the Higgs Mass in Heavy SUSY, *Phys.Rev. D* 89 (2014) 055023. arXiv:1312.5743, doi:10.1103/PhysRevD.89.055023.
- [134] S. Heinemeyer, MSSM Higgs physics at higher orders, *Int.J.Mod.Phys. A* 21 (2006) 2659–2772. arXiv:hep-ph/0407244, doi:10.1142/S0217751X06031028.
- [135] M. Frank, T. Hahn, S. Heinemeyer, W. Hollik, H. Rzehak, et al., The Higgs Boson Masses and Mixings of the Complex MSSM in the Feynman-Diagrammatic Approach, *JHEP* 0702 (2007) 047. arXiv:hep-ph/0611326, doi:10.1088/1126-6708/2007/02/047.
- [136] S. P. Martin, Two loop scalar self energies in a general renormalizable theory at leading order in gauge couplings, *Phys.Rev. D* 70 (2004) 016005. arXiv:hep-ph/0312092, doi:10.1103/PhysRevD.70.016005.
- [137] S. P. Martin, Strong and Yukawa two-loop contributions to Higgs scalar boson self-energies and pole masses in supersymmetry, *Phys.Rev. D* 71 (2005) 016012. arXiv:hep-ph/0405022, doi:10.1103/PhysRevD.71.016012.
- [138] S. P. Martin, D. G. Robertson, TSIL: A Program for the calculation of two-loop self-energy integrals, *Comput.Phys.Commun.* 174 (2006) 133–151. arXiv:hep-ph/0501132, doi:10.1016/j.cpc.2005.08.005.
- [139] S. Heinemeyer, W. Hollik, G. Weiglein, FeynHiggs: A Program for the calculation of the masses of the neutral CP even Higgs bosons in the MSSM, *Comput.Phys.Commun.* 124 (2000) 76–89. arXiv:hep-ph/9812320, doi:10.1016/S0010-4655(99)00364-1.
- [140] M. Frank, S. Heinemeyer, W. Hollik, G. Weiglein, FeynHiggs1.2: Hybrid MS-bar / on-shell renormalization for the CP even Higgs boson sector in the MSSM arXiv:hep-ph/0202166.
- [141] T. Hahn, S. Heinemeyer, W. Hollik, H. Rzehak, G. Weiglein, FeynHiggs: A program for the calculation of MSSM Higgs-boson observables - Version 2.6.5, *Comput.Phys.Commun.* 180 (2009) 1426–1427. doi:10.1016/j.cpc.2009.02.014.
- [142] T. Hahn, S. Heinemeyer, W. Hollik, H. Rzehak, G. Weiglein, FeynHiggs 2.7, *Nucl.Phys.Proc.Suppl.* 205-206 (2010) 152–157. arXiv:1007.0956, doi:10.1016/j.nuclphysbps.2010.08.035.
- [143] N. Bogoliubov, O. a. Parasiuk, On the Multiplication of the causal function in the quantum theory of fields, *Acta Math.* 97 (1957) 227–266. doi:10.1007/BF02392399.
- [144] K. Hepp, Proof of the Bogolyubov-Parasiuk theorem on renormalization, *Commun. Math. Phys.* 2 (1966) 301–326.

- [145] W. Zimmermann, The power counting theorem for minkowski metric, *Commun.Math.Phys.* 11 (1968) 1–8. doi:10.1007/BF01654298.
- [146] S. Frixione, Z. Kunszt, A. Signer, Three jet cross-sections to next-to-leading order, *Nucl.Phys.* B467 (1996) 399–442. arXiv:hep-ph/9512328, doi:10.1016/0550-3213(96)00110-1.
- [147] S. Frixione, A General approach to jet cross-sections in QCD, *Nucl.Phys.* B507 (1997) 295–314. arXiv:hep-ph/9706545, doi:10.1016/S0550-3213(97)00574-9.
- [148] S. Catani, M. Seymour, A General algorithm for calculating jet cross-sections in NLO QCD, *Nucl.Phys.* B485 (1997) 291–419. arXiv:hep-ph/9605323, doi:10.1016/S0550-3213(96)00589-5.
- [149] S. Catani, M. Grazzini, Collinear factorization and splitting functions for next-to-next-to-leading order QCD calculations, *Phys.Lett.* B446 (1999) 143–152. arXiv:hep-ph/9810389, doi:10.1016/S0370-2693(98)01513-5.
- [150] S. Catani, M. Grazzini, Infrared factorization of tree level QCD amplitudes at the next-to-next-to-leading order and beyond, *Nucl.Phys.* B570 (2000) 287–325. arXiv:hep-ph/9908523, doi:10.1016/S0550-3213(99)00778-6.
- [151] T. Binoth, G. Heinrich, An automatized algorithm to compute infrared divergent multi-loop integrals, *Nucl. Phys.* B585 (2000) 741–759. arXiv:hep-ph/0004013.
- [152] G. Heinrich, Sector Decomposition, *Int. J. Mod. Phys.* A23 (2008) 1457–1486. arXiv:0803.4177, doi:10.1142/S0217751X08040263.
- [153] G. Heinrich, A numerical method for NNLO calculations, *Nucl.Phys.Proc.Suppl.* 116 (2003) 368–372. arXiv:hep-ph/0211144, doi:10.1016/S0920-5632(03)80201-3.
- [154] A. Gehrmann-De Ridder, T. Gehrmann, G. Heinrich, Four particle phase space integrals in massless QCD, *Nucl.Phys.* B682 (2004) 265–288. arXiv:hep-ph/0311276, doi:10.1016/j.nuclphysb.2004.01.023.
- [155] C. Anastasiou, K. Melnikov, F. Petriello, A new method for real radiation at NNLO, *Phys.Rev.* D69 (2004) 076010. arXiv:hep-ph/0311311, doi:10.1103/PhysRevD.69.076010.
- [156] T. Binoth, G. Heinrich, Numerical evaluation of phase space integrals by sector decomposition, *Nucl.Phys.* B693 (2004) 134–148. arXiv:hep-ph/0402265, doi:10.1016/j.nuclphysb.2004.06.005.
- [157] C. Anastasiou, K. Melnikov, F. Petriello, Real radiation at NNLO:  $e^+e^- \rightarrow 2$  jets through  $O(\alpha^2(s))$ , *Phys.Rev.Lett.* 93 (2004) 032002. arXiv:hep-ph/0402280, doi:10.1103/PhysRevLett.93.032002.



- 
- [158] M. Czakon, A novel subtraction scheme for double-real radiation at NNLO, *Phys.Lett.* B693 (2010) 259–268. arXiv:1005.0274, doi:10.1016/j.physletb.2010.08.036.
- [159] R. Boughezal, K. Melnikov, F. Petriello, A subtraction scheme for NNLO computations, *Phys.Rev.* D85 (2012) 034025. arXiv:1111.7041, doi:10.1103/PhysRevD.85.034025.
- [160] D. A. Kosower, Antenna factorization of gauge theory amplitudes, *Phys.Rev.* D57 (1998) 5410–5416. arXiv:hep-ph/9710213, doi:10.1103/PhysRevD.57.5410.
- [161] J. M. Campbell, M. Cullen, E. N. Glover, Four jet event shapes in electron - positron annihilation, *Eur.Phys.J.* C9 (1999) 245–265. arXiv:hep-ph/9809429, doi:10.1007/s100529900034.
- [162] D. A. Kosower, Antenna factorization in strongly ordered limits, *Phys.Rev.* D71 (2005) 045016. arXiv:hep-ph/0311272, doi:10.1103/PhysRevD.71.045016.
- [163] A. Gehrmann-De Ridder, T. Gehrmann, E. N. Glover, Infrared structure of  $e^+e^- \rightarrow 2$  jets at NNLO, *Nucl.Phys.* B691 (2004) 195–222. arXiv:hep-ph/0403057, doi:10.1016/j.nuclphysb.2004.05.017.
- [164] A. Gehrmann-De Ridder, T. Gehrmann, E. N. Glover, Antenna subtraction at NNLO, *JHEP* 0509 (2005) 056. arXiv:hep-ph/0505111, doi:10.1088/1126-6708/2005/09/056.
- [165] A. Gehrmann-De Ridder, T. Gehrmann, E. Glover, G. Heinrich, Second-order QCD corrections to the thrust distribution, *Phys.Rev.Lett.* 99 (2007) 132002. arXiv:0707.1285, doi:10.1103/PhysRevLett.99.132002.
- [166] J. Currie, E. Glover, S. Wells, Infrared Structure at NNLO Using Antenna Subtraction, *JHEP* 1304 (2013) 066. arXiv:1301.4693, doi:10.1007/JHEP04(2013)066.
- [167] G. Somogyi, Z. Trocsanyi, A New subtraction scheme for computing QCD jet cross sections at next-to-leading order accuracy arXiv:hep-ph/0609041.
- [168] G. Somogyi, Z. Trocsanyi, V. Del Duca, A Subtraction scheme for computing QCD jet cross sections at NNLO: Regularization of doubly-real emissions, *JHEP* 0701 (2007) 070. arXiv:hep-ph/0609042, doi:10.1088/1126-6708/2007/01/070.
- [169] J. Alwall, R. Frederix, S. Frixione, V. Hirschi, F. Maltoni, et al., The automated computation of tree-level and next-to-leading order differential cross sections, and their matching to parton shower simulations arXiv:1405.0301.
- [170] C. Berger, Z. Bern, L. Dixon, F. Febres Cordero, D. Forde, et al., An Automated Implementation of On-Shell Methods for One-Loop Amplitudes, *Phys.Rev.* D78 (2008) 036003. arXiv:0803.4180, doi:10.1103/PhysRevD.78.036003.

- [171] T. Hahn, Feynman Diagram Calculations with FeynArts, FormCalc, and LoopTools, PoS ACAT2010 (2010) 078. arXiv:1006.2231.
- [172] G. Cullen, H. van Deurzen, N. Greiner, G. Heinrich, G. Luisoni, et al., GoSam-2.0: a tool for automated one-loop calculations within the Standard Model and beyond arXiv:1404.7096.
- [173] G. Bevilacqua, M. Czakon, M. Garzelli, A. van Hameren, A. Kardos, et al., HELAC-NLO, Comput.Phys.Commun. 184 (2013) 986–997. arXiv:1110.1499, doi:10.1016/j.cpc.2012.10.033.
- [174] M. Bahr, S. Gieseke, M. Gigg, D. Grellscheid, K. Hamilton, et al., Herwig++ Physics and Manual, Eur.Phys.J. C58 (2008) 639–707. arXiv:0803.0883, doi:10.1140/epjc/s10052-008-0798-9.
- [175] S. Platzer, S. Gieseke, Dipole Showers and Automated NLO Matching in Herwig++, Eur.Phys.J. C72 (2012) 2187. arXiv:1109.6256, doi:10.1140/epjc/s10052-012-2187-7.
- [176] J. M. Campbell, R. K. Ellis, C. Williams, Vector boson pair production at the LHC, JHEP 1107 (2011) 018. arXiv:1105.0020, doi:10.1007/JHEP07(2011)018.
- [177] S. Badger, B. Biedermann, P. Uwer, V. Yundin, Numerical evaluation of virtual corrections to multi-jet production in massless QCD, Comput.Phys.Commun. 184 (2013) 1981–1998. arXiv:1209.0100, doi:10.1016/j.cpc.2013.03.018.
- [178] F. Cascioli, P. Maierhofer, S. Pozzorini, Scattering Amplitudes with Open Loops, Phys.Rev.Lett. 108 (2012) 111601. arXiv:1111.5206, doi:10.1103/PhysRevLett.108.111601.
- [179] S. Alioli, P. Nason, C. Oleari, E. Re, A general framework for implementing NLO calculations in shower Monte Carlo programs: the POWHEG BOX, JHEP 1006 (2010) 043. arXiv:1002.2581, doi:10.1007/JHEP06(2010)043.
- [180] S. Actis, A. Denner, L. Hofer, A. Scharf, S. Uccirati, Recursive generation of one-loop amplitudes in the Standard Model, JHEP 1304 (2013) 037. arXiv:1211.6316, doi:10.1007/JHEP04(2013)037.
- [181] T. Gleisberg, S. Hoeche, F. Krauss, M. Schonherr, S. Schumann, et al., Event generation with SHERPA 1.1, JHEP 0902 (2009) 007. arXiv:0811.4622, doi:10.1088/1126-6708/2009/02/007.
- [182] K. Arnold, J. Bellm, G. Bozzi, M. Brieg, F. Campanario, et al., VBFNLO: A Parton Level Monte Carlo for Processes with Electroweak Bosons – Manual for Version 2.5.0 arXiv:1107.4038.
- [183] J. Kublbeck, M. Bohm, A. Denner, Feyn Arts: Computer Algebraic Generation of Feynman Graphs and Amplitudes, Comput.Phys.Commun. 60 (1990) 165–180. doi:10.1016/0010-4655(90)90001-H.

- 
- [184] T. Hahn, Generating Feynman diagrams and amplitudes with FeynArts 3, *Comput.Phys.Commun.* 140 (2001) 418–431. arXiv:hep-ph/0012260, doi:10.1016/S0010-4655(01)00290-9.
- [185] P. Nogueira, Automatic Feynman graph generation, *J.Comput.Phys.* 105 (1993) 279–289. doi:10.1006/jcph.1993.1074.
- [186] T. Hahn, M. Perez-Victoria, Automatized one loop calculations in four-dimensions and D-dimensions, *Comput.Phys.Commun.* 118 (1999) 153–165. arXiv:hep-ph/9807565, doi:10.1016/S0010-4655(98)00173-8.
- [187] R. K. Ellis, G. Zanderighi, Scalar one-loop integrals for QCD, *JHEP* 0802 (2008) 002. arXiv:0712.1851, doi:10.1088/1126-6708/2008/02/002.
- [188] T. Binoth, J.-P. Guillet, G. Heinrich, E. Pilon, T. Reiter, Golem95: A Numerical program to calculate one-loop tensor integrals with up to six external legs, *Comput.Phys.Commun.* 180 (2009) 2317–2330. arXiv:0810.0992, doi:10.1016/j.cpc.2009.06.024.
- [189] A. van Hameren, OneLOop: For the evaluation of one-loop scalar functions, *Comput.Phys.Commun.* 182 (2011) 2427–2438. arXiv:1007.4716, doi:10.1016/j.cpc.2011.06.011.
- [190] G. 't Hooft, M. Veltman, Regularization and Renormalization of Gauge Fields, *Nucl.Phys.* B44 (1972) 189–213. doi:10.1016/0550-3213(72)90279-9.
- [191] F. Tkachov, A Theorem on Analytical Calculability of Four Loop Renormalization Group Functions, *Phys.Lett.* B100 (1981) 65–68. doi:10.1016/0370-2693(81)90288-4.
- [192] K. Chetyrkin, F. Tkachov, Integration by Parts: The Algorithm to Calculate beta Functions in 4 Loops, *Nucl.Phys.* B192 (1981) 159–204. doi:10.1016/0550-3213(81)90199-1.
- [193] T. Gehrmann, E. Remiddi, Differential equations for two loop four point functions, *Nucl.Phys.* B580 (2000) 485–518. arXiv:hep-ph/9912329, doi:10.1016/S0550-3213(00)00223-6.
- [194] D. Y. Bardin, G. Passarino, The standard model in the making: Precision study of the electroweak interactions .
- [195] W. Hollik, D. Stockinger, MSSM Higgs-boson mass predictions and two-loop non-supersymmetric counterterms, *Phys.Lett.* B634 (2006) 63–68. arXiv:hep-ph/0509298, doi:10.1016/j.physletb.2006.01.030.
- [196] W. Siegel, Supersymmetric Dimensional Regularization via Dimensional Reduction, *Phys.Lett.* B84 (1979) 193. doi:10.1016/0370-2693(79)90282-X.

- [197] D. Capper, D. Jones, P. van Nieuwenhuizen, Regularization by Dimensional Reduction of Supersymmetric and Nonsupersymmetric Gauge Theories, *Nucl.Phys. B167* (1980) 479. doi:10.1016/0550-3213(80)90244-8.
- [198] O. Tarasov, Connection between Feynman integrals having different values of the space-time dimension, *Phys.Rev. D54* (1996) 6479–6490. arXiv:hep-th/9606018, doi:10.1103/PhysRevD.54.6479.
- [199] V. A. Smirnov, *Feynman integral calculus*, Springer, 2006.
- [200] V. A. Smirnov, Analytical result for dimensionally regularized massless on shell double box, *Phys.Lett. B460* (1999) 397–404. arXiv:hep-ph/9905323, doi:10.1016/S0370-2693(99)00777-7.
- [201] J. Tausk, Nonplanar massless two loop Feynman diagrams with four on-shell legs, *Phys.Lett. B469* (1999) 225–234. arXiv:hep-ph/9909506, doi:10.1016/S0370-2693(99)01277-0.
- [202] M. Czakon, Automatized analytic continuation of Mellin-Barnes integrals, *Comput.Phys.Commun.* 175 (2006) 559–571. arXiv:hep-ph/0511200, doi:10.1016/j.cpc.2006.07.002.
- [203] A. Smirnov, V. Smirnov, On the Resolution of Singularities of Multiple Mellin-Barnes Integrals, *Eur.Phys.J. C62* (2009) 445–449. arXiv:0901.0386, doi:10.1140/epjc/s10052-009-1039-6.
- [204] J. Gluza, K. Kajda, T. Riemann, V. Yundin, Numerical Evaluation of Tensor Feynman Integrals in Euclidean Kinematics, *Eur.Phys.J. C71* (2011) 1516. arXiv:1010.1667, doi:10.1140/epjc/s10052-010-1516-y.
- [205] C. Anastasiou, A. Daleo, Numerical evaluation of loop integrals, *JHEP* 0610 (2006) 031. arXiv:hep-ph/0511176, doi:10.1088/1126-6708/2006/10/031.
- [206] A. Freitas, Y.-C. Huang, On the Numerical Evaluation of Loop Integrals With Mellin-Barnes Representations, *JHEP* 1004 (2010) 074. arXiv:1001.3243, doi:10.1007/JHEP04(2010)074.
- [207] A. V. Smirnov, FIESTA 3: cluster-parallelizable multiloop numerical calculations in physical regions arXiv:1312.3186.
- [208] V. Pilipp, Semi-numerical power expansion of Feynman integrals, *JHEP* 0809 (2008) 135. arXiv:0808.2555, doi:10.1088/1126-6708/2008/09/135.
- [209] A. Kotikov, Differential equations method: New technique for massive Feynman diagrams calculation, *Phys.Lett. B254* (1991) 158–164. doi:10.1016/0370-2693(91)90413-K.
- [210] E. Remiddi, Differential equations for Feynman graph amplitudes, *Nuovo Cim. A110* (1997) 1435–1452. arXiv:hep-th/9711188.

- 
- [211] M. Caffo, H. Czyz, S. Laporta, E. Remiddi, Master equations for master amplitudes, *Acta Phys.Polon. B29* (1998) 2627–2635. arXiv:hep-th/9807119.
- [212] E. Remiddi, J. Vermaseren, Harmonic polylogarithms, *Int.J.Mod.Phys. A15* (2000) 725–754. arXiv:hep-ph/9905237, doi:10.1142/S0217751X00000367.
- [213] A. B. Goncharov, Multiple polylogarithms, cyclotomy and modular complexes, *Math.Res.Lett.* 5 (1998) 497–516. arXiv:1105.2076, doi:10.4310/MRL.1998.v5.n4.a7.
- [214] R. Bonciani, A. Ferroglia, P. Mastrolia, E. Remiddi, J. van der Bij, Planar box diagram for the  $(N(F) = 1)$  two loop QED virtual corrections to Bhabha scattering, *Nucl.Phys. B681* (2004) 261–291. arXiv:hep-ph/0310333, doi:10.1016/j.nuclphysb.2004.08.003.
- [215] D. Zagier, Polylogarithms, Dedekind zeta functions, and the algebraic K-theory of fields., *Prog. Math.* 89 (1991) 391–430.
- [216] A. Goncharov, Geometry of configurations, polylogarithms, and motivic cohomology., *Adv. Math.* 114 (2) (1995) 197–318. doi:10.1006/aima.1995.1045.
- [217] A. B. Goncharov, A simple construction of Grassmannian polylogarithms, ArXiv e-prints arXiv:0908.2238.
- [218] A. B. Goncharov, M. Spradlin, C. Vergu, A. Volovich, Classical Polylogarithms for Amplitudes and Wilson Loops, *Phys.Rev.Lett.* 105 (2010) 151605. arXiv:1006.5703, doi:10.1103/PhysRevLett.105.151605.
- [219] L. F. Alday, Some analytic results for two-loop scattering amplitudes, *JHEP* 1107 (2011) 080. arXiv:1009.1110, doi:10.1007/JHEP07(2011)080.
- [220] D. Gaiotto, J. Maldacena, A. Sever, P. Vieira, Pulling the straps of polygons, *JHEP* 1112 (2011) 011. arXiv:1102.0062, doi:10.1007/JHEP12(2011)011.
- [221] V. Del Duca, C. Duhr, V. A. Smirnov, The massless hexagon integral in  $D = 6$  dimensions, *Phys.Lett. B703* (2011) 363–365. arXiv:1104.2781, doi:10.1016/j.physletb.2011.07.079.
- [222] L. J. Dixon, J. M. Drummond, J. M. Henn, The one-loop six-dimensional hexagon integral and its relation to MHV amplitudes in  $N=4$  SYM, *JHEP* 1106 (2011) 100. arXiv:1104.2787, doi:10.1007/JHEP06(2011)100.
- [223] V. Del Duca, C. Duhr, V. A. Smirnov, The One-Loop One-Mass Hexagon Integral in  $D=6$  Dimensions, *JHEP* 1107 (2011) 064. arXiv:1105.1333, doi:10.1007/JHEP07(2011)064.
- [224] V. Del Duca, L. J. Dixon, J. M. Drummond, C. Duhr, J. M. Henn, et al., The one-loop six-dimensional hexagon integral with three massive corners, *Phys.Rev. D84* (2011) 045017. arXiv:1105.2011, doi:10.1103/PhysRevD.84.045017.

- [225] S. Caron-Huot, Superconformal symmetry and two-loop amplitudes in planar N=4 super Yang-Mills, JHEP 1112 (2011) 066. arXiv:1105.5606, doi:10.1007/JHEP12(2011)066.
- [226] L. J. Dixon, J. M. Drummond, J. M. Henn, Bootstrapping the three-loop hexagon, JHEP 1111 (2011) 023. arXiv:1108.4461, doi:10.1007/JHEP11(2011)023.
- [227] P. Heslop, V. V. Khoze, Wilson Loops @ 3-Loops in Special Kinematics, JHEP 1111 (2011) 152. arXiv:1109.0058, doi:10.1007/JHEP11(2011)152.
- [228] A. Brandhuber, G. Travaglini, G. Yang, Analytic two-loop form factors in N=4 SYM, JHEP 1205 (2012) 082. arXiv:1201.4170, doi:10.1007/JHEP05(2012)082.
- [229] S. Buehler, C. Duhr, CHAPLIN - Complex Harmonic Polylogarithms in Fortran arXiv:1106.5739.
- [230] C. Duhr, H. Gangl, J. R. Rhodes, From polygons and symbols to polylogarithmic functions, JHEP 1210 (2012) 075. arXiv:1110.0458, doi:10.1007/JHEP10(2012)075.
- [231] C. Duhr, Hopf algebras, coproducts and symbols: an application to Higgs boson amplitudes, JHEP 1208 (2012) 043. arXiv:1203.0454, doi:10.1007/JHEP08(2012)043.
- [232] T. Gehrmann, L. Tancredi, E. Weihs, Two-loop QCD helicity amplitudes for  $gg \rightarrow Zg$  and  $gg \rightarrow Z\gamma$ , JHEP 1304 (2013) 101. arXiv:1302.2630, doi:10.1007/JHEP04(2013)101.
- [233] C. Anastasiou, C. Duhr, F. Dulat, B. Mistlberger, Soft triple-real radiation for Higgs production at N3LO, JHEP 1307 (2013) 003. arXiv:1302.4379, doi:10.1007/JHEP07(2013)003.
- [234] T. Gehrmann, L. Tancredi, E. Weihs, Two-loop master integrals for  $q\bar{q} \rightarrow VV$ : the planar topologies, JHEP 1308 (2013) 070. arXiv:1306.6344, doi:10.1007/JHEP08(2013)070.
- [235] S. Abreu, R. Britto, C. Duhr, E. Gardi, From multiple unitarity cuts to the coproduct of Feynman integrals arXiv:1401.3546.
- [236] T. Gehrmann, A. von Manteuffel, L. Tancredi, E. Weihs, The Two-Loop Master Integrals for  $q\bar{q} \rightarrow VV$  arXiv:1404.4853.
- [237] A. B. Goncharov, Galois symmetries of fundamental groupoids and noncommutative geometry, ArXiv Mathematics e-prints arXiv:math/0208144.
- [238] F. Brown, On the decomposition of motivic multiple zeta values, ArXiv e-prints arXiv:1102.1310.

- 
- [239] J. M. Henn, Multiloop integrals in dimensional regularization made simple, *Phys.Rev.Lett.* 110 (25) (2013) 251601. arXiv:1304.1806, doi:10.1103/PhysRevLett.110.251601.
- [240] J. M. Henn, A. V. Smirnov, V. A. Smirnov, Analytic results for planar three-loop four-point integrals from a Knizhnik-Zamolodchikov equation, *JHEP* 1307 (2013) 128. arXiv:1306.2799, doi:10.1007/JHEP07(2013)128.
- [241] J. M. Henn, V. A. Smirnov, Analytic results for two-loop master integrals for Bhabha scattering I, *JHEP* 1311 (2013) 041. arXiv:1307.4083, doi:10.1007/JHEP11(2013)041.
- [242] J. M. Henn, A. V. Smirnov, V. A. Smirnov, Evaluating single-scale and/or non-planar diagrams by differential equations, *JHEP* 1403 (2014) 088. arXiv:1312.2588, doi:10.1007/JHEP03(2014)088.
- [243] M. Argeri, S. Di Vita, P. Mastrolia, E. Mirabella, J. Schlenk, et al., Magnus and Dyson Series for Master Integrals, *JHEP* 1403 (2014) 082. arXiv:1401.2979, doi:10.1007/JHEP03(2014)082.
- [244] J. M. Henn, K. Melnikov, V. A. Smirnov, Two-loop planar master integrals for the production of off-shell vector bosons in hadron collisions arXiv:1402.7078.
- [245] S. Caron-Huot, J. M. Henn, Iterative structure of finite loop integrals arXiv:1404.2922.
- [246] Z. Bern, L. J. Dixon, D. A. Kosower, Dimensionally regulated pentagon integrals, *Nucl.Phys.* B412 (1994) 751–816. arXiv:hep-ph/9306240, doi:10.1016/0550-3213(94)90398-0.
- [247] O. Tarasov, A New approach to the momentum expansion of multiloop Feynman diagrams, *Nucl.Phys.* B480 (1996) 397–412. arXiv:hep-ph/9606238, doi:10.1016/S0550-3213(96)00466-X.
- [248] J. M. Campbell, E. N. Glover, D. Miller, One loop tensor integrals in dimensional regularization, *Nucl.Phys.* B498 (1997) 397–442. arXiv:hep-ph/9612413, doi:10.1016/S0550-3213(97)00268-X.
- [249] O. Tarasov, Reduction of Feynman graph amplitudes to a minimal set of basic integrals, *Acta Phys.Polon.* B29 (1998) 2655. arXiv:hep-ph/9812250.
- [250] J. Fleischer, F. Jegerlehner, O. Tarasov, Algebraic reduction of one loop Feynman graph amplitudes, *Nucl.Phys.* B566 (2000) 423–440. arXiv:hep-ph/9907327, doi:10.1016/S0550-3213(99)00678-1.
- [251] I. Halliday, R. Ricotta, Negative dimensional integrals. 1. Feynman graphs, *Phys.Lett.* B193 (1987) 241. doi:10.1016/0370-2693(87)91229-9.

- [252] G. V. Dunne, I. Halliday, Negative Dimensional Integration. 2. Path Integrals and Fermionic Equivalence, *Phys.Lett.* B193 (1987) 247. doi:10.1016/0370-2693(87)91230-5.
- [253] G. V. Dunne, I. Halliday, Negative dimensional oscillators, *Nucl.Phys.* B308 (1988) 589. doi:10.1016/0550-3213(88)90579-2.
- [254] R. M. Ricotta, Negative dimensions in quantum field theory .
- [255] D. J. Broadhurst, Two loop negative dimensional integration, *Phys.Lett.* B197 (1987) 179. doi:10.1016/0370-2693(87)90364-9.
- [256] C. Anastasiou, E. N. Glover, C. Oleari, Scalar one loop integrals using the negative dimension approach, *Nucl.Phys.* B572 (2000) 307–360. arXiv:hep-ph/9907494, doi:10.1016/S0550-3213(99)00637-9.
- [257] L. D. Landau, On analytic properties of vertex parts in quantum field theory, *Nucl. Phys.* 13 (1959) 181–192.
- [258] R. Cutkosky, Singularities and discontinuities of Feynman amplitudes, *J.Math.Phys.* 1 (1960) 429–433. doi:10.1063/1.1703676.
- [259] G. 't Hooft, M. Veltman, DIAGRAMMAR, *NATO Adv.Study Inst.Ser.B Phys.* 4 (1974) 177–322.
- [260] E. Remiddi, Dispersion Relations for Feynman Graphs, *Helv.Phys.Acta* 54 (1982) 364.
- [261] F. Brown, Single-valued multiple polylogarithms in one variable, *C. R. Acad. Sci. Paris Ser. I* 338.
- [262] F. C. Brown, On the periods of some Feynman integrals arXiv:0910.0114.
- [263] F. C. Brown, Multiple zeta values and periods of moduli spaces  $M_{0,n}(\mathbb{R})$ , *Annales Sci.Ecole Norm.Sup.* 42 (2009) 371. arXiv:math/0606419.
- [264] F. Brown, The Massless higher-loop two-point function, *Commun.Math.Phys.* 287 (2009) 925–958. arXiv:0804.1660, doi:10.1007/s00220-009-0740-5.
- [265] C. Bogner, M. Luders, Multiple polylogarithms and linearly reducible Feynman graphs arXiv:1302.6215.
- [266] E. Panzer, On the analytic computation of massless propagators in dimensional regularization arXiv:1305.2161, doi:10.1016/j.nuclphysb.2013.05.025.
- [267] E. Panzer, On hyperlogarithms and Feynman integrals with divergences and many scales, *JHEP* 1403 (2014) 071. arXiv:1401.4361, doi:10.1007/JHEP03(2014)071.
- [268] E. Panzer, Algorithms for the symbolic integration of hyperlogarithms with applications to Feynman integrals arXiv:1403.3385.



- 
- [269] G. Passarino, An Approach toward the numerical evaluation of multiloop Feynman diagrams, Nucl.Phys. B619 (2001) 257–312. arXiv:hep-ph/0108252, doi:10.1016/S0550-3213(01)00528-4.
- [270] G. Passarino, S. Uccirati, Algebraic numerical evaluation of Feynman diagrams: Two loop selfenergies, Nucl.Phys. B629 (2002) 97–187. arXiv:hep-ph/0112004, doi:10.1016/S0550-3213(02)00138-4.
- [271] G. Passarino, S. Uccirati, Two-loop vertices in quantum field theory: Infrared and collinear divergent configurations, Nucl.Phys. B747 (2006) 113–189. arXiv:hep-ph/0603121, doi:10.1016/j.nuclphysb.2006.04.014.
- [272] G. Passarino, C. Sturm, S. Uccirati, Complete Two-Loop Corrections to  $H \rightarrow \gamma\gamma$ , Phys.Lett. B655 (2007) 298–306. arXiv:0707.1401, doi:10.1016/j.physletb.2007.09.002.
- [273] S. Actis, G. Passarino, C. Sturm, S. Uccirati, NNLO Computational Techniques: The Cases  $H \rightarrow \gamma\gamma$  and  $H \rightarrow gg$ , Nucl.Phys. B811 (2009) 182–273. arXiv:0809.3667, doi:10.1016/j.nuclphysb.2008.11.024.
- [274] C. Anastasiou, S. Beerli, A. Daleo, Evaluating multi-loop Feynman diagrams with infrared and threshold singularities numerically, JHEP 0705 (2007) 071. arXiv:hep-ph/0703282, doi:10.1088/1126-6708/2007/05/071.
- [275] S. Beerli, A New method for evaluating two-loop Feynman integrals and its application to Higgs production, Ph.D. thesis (2008).
- [276] C. Anastasiou, S. Beerli, A. Daleo, The Two-loop QCD amplitude  $gg \rightarrow h, H$  in the Minimal Supersymmetric Standard Model, Phys.Rev.Lett. 100 (2008) 241806. arXiv:0803.3065, doi:10.1103/PhysRevLett.100.241806.
- [277] A. Freitas, Numerical evaluation of multi-loop integrals using subtraction terms, JHEP 1207 (2012) 132. arXiv:1205.3515, doi:10.1007/JHEP07(2012)132, 10.1007/JHEP09(2012)129.
- [278] R. Boughezal, F. Caola, K. Melnikov, F. Petriello, M. Schulze, Higgs boson production in association with a jet at next-to-next-to-leading order in perturbative QCD, JHEP 1306 (2013) 072. arXiv:1302.6216, doi:10.1007/JHEP06(2013)072.
- [279] D. E. Soper, Techniques for QCD calculations by numerical integration, Phys. Rev. D62 (2000) 014009. arXiv:hep-ph/9910292.
- [280] T. Binoth, J. P. Guillet, G. Heinrich, E. Pilon, C. Schubert, An algebraic / numerical formalism for one-loop multi-leg amplitudes, JHEP 10 (2005) 015. arXiv:hep-ph/0504267.
- [281] Z. Nagy, D. E. Soper, Numerical integration of one-loop Feynman diagrams for N-photon amplitudes, Phys. Rev. D74 (2006) 093006. arXiv:hep-ph/0610028.

- [282] M. Roth, A. Denner, High-energy approximation of one-loop Feynman integrals, Nucl. Phys. B479 (1996) 495–514. arXiv:hep-ph/9605420.
- [283] R. Hartshorne, Algebraic geometry., 1977.
- [284] C. Bogner, S. Weinzierl, Resolution of singularities for multi-loop integrals, Comput.Phys.Commun. 178 (2008) 596–610. arXiv:0709.4092, doi:10.1016/j.cpc.2007.11.012.
- [285] A. Smirnov, M. Tentyukov, Feynman Integral Evaluation by a Sector decomposition Approach (FIESTA), Comput.Phys.Commun. 180 (2009) 735–746. arXiv:0807.4129, doi:10.1016/j.cpc.2008.11.006.
- [286] H. Hironaka, Resolution of singularities of an algebraic variety over a field of characteristic zero: I, Annals of Mathematics 79 (1) (1964) pp. 109–203. URL <http://www.jstor.org/stable/1970486>
- [287] D. Zeillinger, A short solution to Hironaka’s polyhedra game. .
- [288] M. Spivakovsky, A solution to Hironaka’s polyhedra game.
- [289] S. Encinas, H. Hauser, Strong resolution of singularities in characteristic zero., Comment. Math. Helv. 77 (4) (2002) 821–845. doi:10.1007/PL00012443.
- [290] C. Bogner, S. Weinzierl, Blowing up Feynman integrals, Nucl.Phys.Proc.Suppl. 183 (2008) 256–261. arXiv:0806.4307, doi:10.1016/j.nuclphysbps.2008.09.113.
- [291] E. Speer, Ultraviolet and Infrared Singularity Structure of Generic Feynman Amplitudes, Annales Poincare Phys.Theor. 23 (1975) 1–21.
- [292] A. Smirnov, V. Smirnov, Hepp and Speer Sectors within Modern Strategies of Sector Decomposition, JHEP 0905 (2009) 004. arXiv:0812.4700, doi:10.1088/1126-6708/2009/05/004.
- [293] A. Smirnov, V. Smirnov, M. Tentyukov, FIESTA 2: Parallelizeable multiloop numerical calculations, Comput.Phys.Commun. 182 (2011) 790–803. arXiv:0912.0158, doi:10.1016/j.cpc.2010.11.025.
- [294] T. Kaneko, T. Ueda, A Geometric method of sector decomposition, Comput.Phys.Commun. 181 (2010) 1352–1361. arXiv:0908.2897, doi:10.1016/j.cpc.2010.04.001.
- [295] T. Kaneko, T. Ueda, Sector Decomposition Via Computational Geometry, PoS ACAT2010 (2010) 082. arXiv:1004.5490.
- [296] T. Ueda, J. Fujimoto, New implementation of the sector decomposition on FORM, PoS ACAT08 (2008) 120. arXiv:0902.2656.
- [297] C. B. Barber, D. P. Dobkin, H. Huhdanpaa, The quickhull algorithm for convex hulls, ACM Transactions on mathematical software 22 (4) (1996) 469–483.

- 
- [298] R. J. Eden, P. V. Landshoff, D. I. Olive, J. C. Polkinghorne, *The Analytic S-Matrix*, Cambridge University Press, 1966.
- [299] N. Nakanishi, *Graph Theory and Feynman Integrals*, Gordon and Breach, New York, 1971.
- [300] J. D. Bjorken, S. D. Drell, *Relativistic quantum fields* .
- [301] J. Carter, G. Heinrich, SecDec: A general program for sector decomposition, *Comput.Phys.Commun.* 182 (2011) 1566–1581. arXiv:1011.5493, doi:10.1016/j.cpc.2011.03.026.
- [302] T. Hahn, CUBA: A library for multidimensional numerical integration, *Comput. Phys. Commun.* 168 (2005) 78–95. arXiv:hep-ph/0404043, doi:10.1016/j.cpc.2005.01.010.
- [303] S. Agrawal, T. Hahn, E. Mirabella, FormCalc 7, *J.Phys.Conf.Ser.* 368 (2012) 012054. arXiv:1112.0124, doi:10.1088/1742-6596/368/1/012054.
- [304] J. P. Carter, *Higher Order Corrections in Perturbative Quantum Field Theory via Sector Decomposition*, Ph.D. thesis.
- [305] S. Kawabata, A New version of the multidimensional integration and event generation package BASES/SPRING, *Comp. Phys. Commun.* 88 (1995) 309–326. doi:10.1016/0010-4655(95)00028-E.
- [306] Mathematica, Copyright by Wolfram Research.
- [307] F. Slothouber, et al., ROBODoc 4.99.40, <http://www.xs4all.nl/rfsber/Robo/robodoc.html>.
- [308] A. I. Davydychev, M. Y. Kalmykov, Massive Feynman diagrams and inverse binomial sums, *Nucl.Phys.* B699 (2004) 3–64. arXiv:hep-th/0303162, doi:10.1016/j.nuclphysb.2004.08.020.
- [309] A. Ferroglia, M. Passera, G. Passarino, S. Uccirati, Two loop vertices in quantum field theory: Infrared convergent scalar configurations, *Nucl.Phys.* B680 (2004) 199–270. arXiv:hep-ph/0311186, doi:10.1016/j.nuclphysb.2003.12.016.
- [310] R. Bonciani, P. Mastrolia, E. Remiddi, Master integrals for the two loop QCD virtual corrections to the forward backward asymmetry, *Nucl.Phys.* B690 (2004) 138–176. arXiv:hep-ph/0311145, doi:10.1016/j.nuclphysb.2004.04.011.
- [311] C. Anastasiou, F. Herzog, A. Lazopoulos, On the factorization of overlapping singularities at NNLO, *JHEP* 1103 (2011) 038. arXiv:1011.4867, doi:10.1007/JHEP03(2011)038.
- [312] A. von Manteuffel, Talk given at the conference ACAT 2011, Uxbridge, London, September 2011 .

- [313] A. von Manteuffel, private communication.
- [314] F. Yuasa, E. de Doncker, N. Hamaguchi, T. Ishikawa, K. Kato, et al., Numerical Computation of Two-loop Box Diagrams with Masses arXiv:1112.0637.
- [315] T. Hahn, C. Schappacher, The Implementation of the minimal supersymmetric standard model in FeynArts and FormCalc, *Comput.Phys.Commun.* 143 (2002) 54–68. arXiv:hep-ph/0105349, doi:10.1016/S0010-4655(01)00436-2.
- [316] G. Weiglein, R. Scharf, M. Bohm, Reduction of general two loop selfenergies to standard scalar integrals, *Nucl.Phys. B*416 (1994) 606–644. arXiv:hep-ph/9310358, doi:10.1016/0550-3213(94)90325-5.
- [317] T. Hahn, A Mathematica interface for FormCalc-generated code, *Comput.Phys.Commun.* 178 (2008) 217–221. arXiv:hep-ph/0611273, doi:10.1016/j.cpc.2007.09.004.
- [318] S. Agrawal, T. Hahn, E. Mirabella, FormCalc 7, *J.Phys.Conf.Ser.* 368 (2012) 012054. arXiv:1112.0124, doi:10.1088/1742-6596/368/1/012054.
- [319] G. Passarino, M. Veltman, One Loop Corrections for  $e^+ e^-$  Annihilation Into  $\mu^+ \mu^-$  in the Weinberg Model, *Nucl.Phys. B*160 (1979) 151. doi:10.1016/0550-3213(79)90234-7.
- [320] S. Heinemeyer, W. Hollik, H. Rzehak, G. Weiglein, High-precision predictions for the MSSM Higgs sector at  $O(\alpha(b) \alpha(s))$ , *Eur.Phys.J. C*39 (2005) 465–481. arXiv:hep-ph/0411114, doi:10.1140/epjc/s2005-02112-6.
- [321] W. Hollik, H. Rzehak, The Sfermion mass spectrum of the MSSM at the one loop level, *Eur.Phys.J. C*32 (2003) 127–133. arXiv:hep-ph/0305328, doi:10.1140/epjc/s2003-01387-9.
- [322] S. Heinemeyer, H. Rzehak, C. Schappacher, Proposals for Bottom Quark/Squark Renormalization in the Complex MSSM, *Phys.Rev. D*82 (2010) 075010. arXiv:1007.0689, doi:10.1103/PhysRevD.82.075010.
- [323] T. Fritzsche, S. Heinemeyer, H. Rzehak, C. Schappacher, Heavy Scalar Top Quark Decays in the Complex MSSM: A Full One-Loop Analysis, *Phys.Rev. D*86 (2012) 035014. arXiv:1111.7289, doi:10.1103/PhysRevD.86.035014.
- [324] A. Freitas, D. Stoeckinger, Gauge dependence and renormalization of  $\tan \beta$  in the MSSM, *Phys.Rev. D*66 (2002) 095014. arXiv:hep-ph/0205281, doi:10.1103/PhysRevD.66.095014.
- [325] M. Sperling, D. Stoeckinger, A. Voigt, Renormalization of vacuum expectation values in spontaneously broken gauge theories, *JHEP* 1307 (2013) 132. arXiv:1305.1548, doi:10.1007/JHEP07(2013)132.

- 
- [326] M. Sperling, D. Stoeckinger, A. Voigt, Renormalization of vacuum expectation values in spontaneously broken gauge theories: Two-loop results, *JHEP* 1401 (2014) 068. arXiv:1310.7629, doi:10.1007/JHEP01(2014)068.
- [327] T. Fritzsche, T. Hahn, S. Heinemeyer, F. von der Pahlen, H. Rzehak, et al., The Implementation of the Renormalized Complex MSSM in FeynArts and FormCalc arXiv:1309.1692.
- [328] G. 't Hooft, M. Veltman, Scalar One Loop Integrals, *Nucl.Phys.* B153 (1979) 365–401. doi:10.1016/0550-3213(79)90605-9.
- [329] U. Nierste, D. Muller, M. Bohm, Two loop relevant parts of D-dimensional massive scalar one loop integrals, *Z.Phys.* C57 (1993) 605–614. doi:10.1007/BF01561479.
- [330] R. Scharf, J. Tausk, Scalar two loop integrals for gauge boson selfenergy diagrams with a massless fermion loop, *Nucl.Phys.* B412 (1994) 523–552. doi:10.1016/0550-3213(94)90391-3.
- [331] F. A. Berends, J. Tausk, On the numerical evaluation of scalar two loop selfenergy diagrams, *Nucl.Phys.* B421 (1994) 456–470. doi:10.1016/0550-3213(94)90336-0.
- [332] S. Bauberger, Massive scalar two-loop self-energy integrals, Master's thesis (1994).
- [333] A. Denner, Techniques for calculation of electroweak radiative corrections at the one loop level and results for W physics at LEP-200, *Fortsch.Phys.* 41 (1993) 307–420. arXiv:0709.1075, doi:10.1002/prop.2190410402.
- [334] S. Bauberger, F. A. Berends, M. Bohm, M. Buza, Analytical and numerical methods for massive two loop selfenergy diagrams, *Nucl.Phys.* B434 (1995) 383–407. arXiv:hep-ph/9409388, doi:10.1016/0550-3213(94)00475-T.
- [335] S. Bauberger, M. Bohm, Simple one-dimensional integral representations for two loop selfenergies: The Master diagram, *Nucl.Phys.* B445 (1995) 25–48. arXiv:hep-ph/9501201, doi:10.1016/0550-3213(95)00199-3.
- [336] J. P. Guillet, G. Heinrich, J. von Soden-Fraunhofen, Tools for NLO automation: extension of the golem95C integral library arXiv:1312.3887.
- [337] J. van der Bij, M. Veltman, Two Loop Large Higgs Mass Correction to the rho Parameter, *Nucl.Phys.* B231 (1984) 205. doi:10.1016/0550-3213(84)90284-0.
- [338] F. A. Berends, M. Buza, M. Bohm, R. Scharf, Closed expressions for specific massive multiloop selfenergy integrals, *Z.Phys.* C63 (1994) 227–234. doi:10.1007/BF01411014.
- [339] R. Scharf, University of Würzburg, Master's thesis (1991).
- [340] V. K. Tuan, R. G. Buschman, Integral representations of generalized Lauricella hypergeometric functions, *International Journal of Mathematics and Mathematical Sciences* 15 number 4 (1992) 653–657. doi:10.1155/S0161171292000863.

- [341] A. I. Davydychev, V. A. Smirnov, J. Tausk, Large momentum expansion of two loop selfenergy diagrams with arbitrary masses, Nucl.Phys. B410 (1993) 325–342. arXiv:hep-ph/9307371, doi:10.1016/0550-3213(93)90436-S.
- [342] S. Laporta, E. Remiddi, Analytic treatment of the two loop equal mass sunrise graph, Nucl.Phys. B704 (2005) 349–386. arXiv:hep-ph/0406160, doi:10.1016/j.nuclphysb.2004.10.044.
- [343] L. Adams, C. Bogner, S. Weinzierl, The two-loop sunrise graph with arbitrary masses in terms of elliptic dilogarithms arXiv:1405.5640.
- [344] L. Adams, C. Bogner, S. Weinzierl, The two-loop sunrise graph with arbitrary masses arXiv:1302.7004.
- [345] E. Remiddi, L. Tancredi, Schouten identities for Feynman graph amplitudes; The Master Integrals for the two-loop massive sunrise graph, Nucl.Phys. B880 (2014) 343–377. arXiv:1311.3342, doi:10.1016/j.nuclphysb.2014.01.009.
- [346] D. Greynat, J. Sesma, G. Vulvert, Epsilon expansion of Appell and Kampé de Fériet functions arXiv:1310.7700.
- [347] D. Kreimer, The Master two loop two point function: The General case, Phys.Lett. B273 (1991) 277–281. doi:10.1016/0370-2693(91)91684-N.
- [348] D. J. Broadhurst, The Master Two Loop Diagram With Masses, Z.Phys. C47 (1990) 115–124. doi:10.1007/BF01551921.
- [349] A. I. Davydychev, J. Tausk, Two loop selfenergy diagrams with different masses and the momentum expansion, Nucl.Phys. B397 (1993) 123–142. doi:10.1016/0550-3213(93)90338-P.
- [350] D. J. Broadhurst, J. Fleischer, O. Tarasov, Two loop two point functions with masses: Asymptotic expansions and Taylor series, in any dimension, Z.Phys. C60 (1993) 287–302. arXiv:hep-ph/9304303, doi:10.1007/BF01474625.
- [351] F. A. Berends, A. I. Davydychev, V. A. Smirnov, J. Tausk, Zero threshold expansion of two loop selfenergy diagrams, Nucl.Phys. B439 (1995) 536–560. arXiv:hep-ph/9410232, doi:10.1016/0550-3213(95)00018-N.
- [352] F. Hoogeveen, The Influence of a Heavy Fermion Doublet on Higgs Boson Production via the Gluon Fusion Mechanism, Nucl.Phys. B259 (1985) 19. doi:10.1016/0550-3213(85)90295-0.
- [353] P. Bechtle, S. Heinemeyer, O. Stal, T. Stefaniak, G. Weiglein, et al., MSSM Interpretations of the LHC Discovery: Light or Heavy Higgs?, Eur.Phys.J. C73 (2013) 2354. arXiv:1211.1955, doi:10.1140/epjc/s10052-013-2354-5.

- 
- [354] M. Carena, S. Heinemeyer, O. Stal, C. Wagner, G. Weiglein, MSSM Higgs Boson Searches at the LHC: Benchmark Scenarios after the Discovery of a Higgs-like Particle, *Eur. Phys. J. C* 73 (2013) 2552. arXiv:1302.7033, doi:10.1140/epjc/s10052-013-2552-1.
- [355] M. Muether, CDF, Combination of CDF and DO results on the mass of the top quark using up to  $8.7 \text{ fb}^{-1}$  at the Tevatron arXiv:1305.3929.
- [356] LHC Combination: Top mass, Tech. Rep. CMS-PAS-TOP-12-001, CERN, Geneva (2012).
- [357] First combination of Tevatron and LHC measurements of the top-quark mass arXiv:1403.4427.
- [358] M. Acciarri, et al., Determination of  $\gamma/Z$  interference in  $e^+e^-$  annihilation at LEP, *Phys.Lett. B* 489 (2000) 93–101. arXiv:hep-ex/0007006, doi:10.1016/S0370-2693(00)00889-3.
- [359] H. Baer, T. Barklow, K. Fujii, Y. Gao, A. Hoang, et al., The International Linear Collider Technical Design Report - Volume 2: Physics arXiv:1306.6352.
- [360] S. Gennai, S. Heinemeyer, A. Kalinowski, R. Kinnunen, S. Lehti, et al., Search for heavy neutral MSSM Higgs bosons with CMS: Reach and Higgs-mass precision, *Eur.Phys.J. C* 52 (2007) 383–395. arXiv:0704.0619, doi:10.1140/epjc/s10052-007-0398-0.





# List of Figures

3.1	Example diagrams for double virtual (a), real virtual (b) and double real radiation (c) contributions entering an NNLO calculation are shown. . . .	20
3.2	The one-loop box diagram with massless propagators. . . . .	24
3.3	Two-loop two-point massive bubble diagram, also termed the "sunrise" topology. . . . .	29
4.1	The basic idea of sector decomposition. . . . .	33
5.1	Two-loop two-point "sunrise" graph with three internal masses. . . . .	43
5.2	Schematic picture of the closed contour avoiding poles on the real axis. . .	45
5.3	Influence of the deformation on the real part for the one-loop bubble and $m = 1, s = 4.5$ . . . . .	48
5.4	Influence of the deformation on the imaginary part for the one-loop bubble and $m = 1, s = 4.5$ . . . . .	48
5.5	Implications for the best choice of $\lambda$ from the modulus of $\mathcal{F}(z(x))$ for the one-loop bubble and $m = 1, s = 4.5$ . . . . .	49
5.6	Implications for the best choice of $\lambda$ from the minimization of the complex argument of $\mathcal{F}(z(x))$ for the one-loop bubble and $m = 1, s = 4.5$ . . . . .	50
6.1	The operational sequence of SECDEC. This flowchart shows the main steps the program performs to produce the result as a Laurent series in the regulator $\varepsilon$ . . . . .	63
6.2	Two-loop vertex graph $P_{126}$ , containing a massive triangle loop. Solid lines are massive, dashed lines are massless. The vertices are labeled to match the construction of the integrand from the topology as explained in the text. . . . .	64
6.3	Comparison of analytic and numerical results for the diagram $P_{126}$ using $m^2 = 1$ and varying $s$ . Due to the high accuracy of the numerical integration, error bars are barely seen. . . . .	65
6.4	Two-loop bubble diagram with different masses . . . . .	66

6.5	Results for the real (blue) and imaginary (red) parts of the two-loop two-point topology of Fig. 6.4 are shown in the scalar case (a) and for the the rank three coefficient function $\mathcal{G}_B$ (b) with numerator $(k_1 \cdot k_2)(k_1 \cdot p_1)$ . The masses are $m_1^2 = 2, m_2^2 = 4, m_3 = 0$ . . . . .	68
6.6	Results for the real (blue) and imaginary (red) parts of the two-loop two-point topology of Fig. 6.4 are shown for three non-vanishing masses in the scalar case (a) and for the the rank three coefficient function $\mathcal{G}_B$ (b) with numerator $(k_1 \cdot k_2)(k_1 \cdot p_1)$ . The masses are $m_1^2 = 2, m_2^2 = 4, m_3^2 = 3$ . . . . .	69
6.7	Comparison of evaluation times between scalar and rank three tensor integrals corresponding to a two-loop two-point function with (a) two, and (b) three masses. The red points are the evaluation times in seconds for the scalar integral at a given kinematic point, the timings for the rank three tensor integral are marked in blue. The timings were obtained on computers with Intel i7 processors and 4 cores. . . . .	70
7.1	All diagrams considered in this chapter: the massive non-planar two-loop box diagrams entering the light (a) and heavy (b) fermionic correction to the $gg$ channel, the all-massive planar $M_7^P$ (c) and non-planar $M_7^{NP}$ (d) seven-propagator diagram and the non-planar six-propagator diagram $B_6^{NP}$ (e). The thick lines denote massive particles. . . . .	74
7.2	Comparison of (a) the leading and (b) the next-to-leading pole coefficients between the analytic result from [312] and the SECDEC result. The real part is shown in blue, the imaginary part in red. As numerical values $p_3^2 = p_4^2 = m^2 = 1, s_{23} = -1.25$ is chosen, assuming four-momentum conservation $s_{13} = 2m^2 - s_{12} - s_{23}$ . . . . .	84
7.3	Results for (a) the $1/\varepsilon^2$ and (b) the $1/\varepsilon$ coefficients of the integral $ggtt_2$ . The kinematics are the same as in Fig. 7.2. . . . .	84
7.4	Results for the finite part of the scalar integral $ggtt_2$ , for a larger kinematic range (a), and a region further away from threshold (b). The kinematics are the same as in Fig. 7.2. The vertical bars display the uncertainty of the numerical result. . . . .	85
7.5	(a) Results for the scalar integral $ggtt_1$ shown in Fig. 7.1(b), and (b) the corresponding rank two tensor integral $ggtt_1$ with the factor $k_1 \cdot k_2$ in the numerator. The invariant $s_{12}$ is varied, the invariants $s_{23} = -1.25, m_2 = m_1, p_3^2 = p_4^2 = m_1^2 = 1$ are fixed. The uncertainties from numerical integration are shown as horizontal markers on the vertical lines. The absence of such markers means that the numerical uncertainty is not visible at this scale. . . . .	87
7.6	Results for the scalar integral $ggtt_1$ shown in Fig. 7.1(b), with two different masses. The second mass $m_2$ is varied, the other kinematic invariants are fixed with the values $s_{12} = 5, s_{23} = -1.25$ and $p_3^2 = p_4^2 = m_1^2 = 1$ . . . . .	88

7.7	Results for the all massive planar seven-propagator graph $M_7^P$ with all propagators and external legs massive, using $m_1^2 = 2$ , $m_2^2 = 6$ , $m_3^2 = 7$ , $m_4^2 = 8$ , $m_5^2 = 9$ , $m_6^2 = 10$ , $m_7^2 = 12$ , $p_1^2 = 1$ , $p_2^2 = 3$ , $p_3^2 = 4$ , $p_4^2 = 5$ and $s_{23} = -0.25$ . . . . .	89
7.8	Labeling of the masses for the non-planar graph $M_7^{\text{NP}}$ . . . . .	90
7.9	Results for the non-planar 7-propagator graph $M_7^{\text{NP}}$ with all propagators massive, using $m = 50$ , $M = 90$ and $s_{23} = -10^4$ . . . . .	90
7.10	The two non-planar 6-propagator topologies studied here: (a) $B_6^{\text{NP},a}$ and (b) $B_6^{\text{NP},b}$ . The thick lines denote massive external legs and propagators, respectively. . . . .	91
7.11	Results for the finite part of the graph $B_6^{\text{NP},a}$ with massive legs $p_1^2 = p_2^2 = 1$ . The error bars are barely seen in the figures as the numerical accuracy is about one per mil. . . . .	92
7.12	The non-planar 6-propagator graph $B_6^{\text{NP},b}$ as a function of $s_{12}$ in a region containing a threshold, where $m_1^2 = m_2^2 = m_5^2 = m_6^2 = 0.25$ and $s_{23} = -0.4$ . The error bars are barely seen in the figures as the numerical accuracy is about one per mil. . . . .	92
8.1	Generic two-loop self-energy diagrams contributing at the order $\mathcal{O}(\alpha_s \alpha_t)$ , with $\phi = \phi_1, \phi_2, A^0$ and $i, j, k = 1, 2$ . The $A^0$ boson self-energies enter the two-loop counter terms during renormalization. Stop particles $\tilde{t}$ carry indices 1 and 2, in accordance with the Feynman rules. . . . .	97
8.2	Two-loop master topologies resulting after tensor reduction. Some of the internal lines may also be massless. . . . .	98
8.3	Two-loop tadpole diagrams contributing in the two-loop counter terms to the $\mathcal{O}(\alpha_s \alpha_t)$ self-energies, $\phi = \phi_1, \phi_2$ and $i, j, k = 1, 2$ . . . . .	103
8.4	One-loop diagrams for the quark and squark counter-term insertions with $i, j, k = 1, 2$ . . . . .	105
8.5	One-loop counter-term contributions to the sub-loop renormalization of the $\mathcal{O}(\alpha_s \alpha_t)$ self-energies, with $\phi = \phi_1, \phi_2, A$ and $i, j = 1, 2$ . . . . .	105
8.6	One-loop counter-term diagrams with insertions, needed in the sub-loop renormalization of the two-loop tadpoles, $\phi = \phi_1, \phi_2$ and $i, j = 1, 2$ . . . . .	106
8.7	Two representative numerical SECDEC results for the integrals of type 8.2(d) in (a), and of type 8.2(e) in (b), with three and four different masses, respectively. In (a), the values $m_1 = m_2 = 173.2$ , $m_3 = 826.8$ and $m_4 = 1.5$ are used. In (b), the numerical values $m_1 = 1173.2$ , $m_2 = 826.8$ , $m_3 = 1.5$ and $m_4 = 173.2$ are chosen. Due to the high accuracy of the numerical integration, error bars are barely seen. . . . .	115
8.8	Momentum dependence of the real (left column) and imaginary (right column) parts of the two-loop selfenergies $\Delta\hat{\Sigma}_{h^0 h^0}$ , $\Delta\hat{\Sigma}_{h^0 H^0}$ , $\Delta\hat{\Sigma}_{H^0 H^0}$ , within scenario 1, for $\tan\beta = 5$ (red squares) and $\tan\beta = 20$ (blue crosses) and $m_{A^0} = 250$ GeV. One can see that the selfenergies change substantially beyond the threshold at $p^2 = (2m_t)^2$ . . . . .	119

8.9	Momentum dependence of the real part of the two-loop self-energies $\Delta\hat{\Sigma}_{h^0h^0}$ , $\Delta\hat{\Sigma}_{h^0H^0}$ , $\Delta\hat{\Sigma}_{H^0H^0}$ , within scenario 1, for two different values of $\tan\beta$ and a range of $m_{A^0}$ values. . . . .	120
8.10	Momentum dependence of the real and imaginary parts of the two-loop self-energies $\Delta\hat{\Sigma}_{h^0h^0}$ , $\Delta\hat{\Sigma}_{h^0H^0}$ , $\Delta\hat{\Sigma}_{H^0H^0}$ within scenario 2, with $\tan\beta = 5, 20$ and $m_{A^0} = 250$ GeV with the same color coding as in Fig. 8.8. . . . .	122
8.11	Momentum dependence of the real parts of the two-loop self-energies $\Delta\hat{\Sigma}_{h^0h^0}$ , $\Delta\hat{\Sigma}_{h^0H^0}$ , $\Delta\hat{\Sigma}_{H^0H^0}$ in scenario 2 for two different values of $\tan\beta$ and various values of $m_{A^0}$ (see text). . . . .	123
8.12	Variation of the mass shifts $\Delta M_h, \Delta M_H$ with the $A^0$ -boson mass $m_{A^0}$ within scenario 1, for $\tan\beta = 5$ (blue) and $\tan\beta = 20$ (red). The small peak in $\Delta M_H$ originates from a threshold at $2m_t$ . . . . .	126
8.13	Variation of the mass shifts $\Delta M_h, \Delta M_H$ with the gluino mass, within scenario 1, for two different values of $\tan\beta = 5, 20$ and $m_{A^0} = 250$ GeV. . . . .	127
8.14	Variation of the mass shifts $\Delta M_h, \Delta M_H$ with the $A^0$ -boson mass $m_{A^0}$ within scenario 2, for two different values of $\tan\beta = 5, 20$ . . . . .	128
8.15	Variation of the mass shifts $\Delta M_h, \Delta M_H$ with the gluino mass, within scenario 2, for two different values of $\tan\beta = 5, 20$ and $m_{A^0} = 250$ GeV. . . . .	129

# Acknowledgement

First and foremost, I would like to express my deep gratitude to Dr. Gudrun Heinrich and Prof. Dr. Wolfgang Hollik, my research supervisors, for their patient guidance and enlightening discussions. In particular, I am grateful to Gudrun Heinrich for the continuous support, openness to discussions and detailed explanations, and Wolfgang Hollik for the opportunity to join the institute and for giving me the freedom and support to pursue the proposed project in my own way.

I gratefully acknowledge collaboration with Jonathon Carter, Thomas Hahn and Sven Heinemeyer.

I would also like to extend my thanks to Thomas Hahn and Peter Breitenlohner for the computer administration and their constructive comments and advice on good programming practices.

Furthermore, I wish to thank all current and former PhD students of the theory group, especially Andreas Deser, Stephan Steinfurt, Hansjörg Zeller, Migael Strydom, Sebastian Halter, Federico Bonetti, Sebastian Passehr and Jonas Lindert for interesting discussions. I want to thank my office mates Thi Nhung Dao, Davide Pagani, Tiziano Peraro and Johannes Schlenk for interesting discussions and a productive environment.

I am grateful to Scott Mandry and Raphaela Borowka for proofreading (parts of) this thesis.

Importantly, the easy access to literature, knowledgeable surrounding, the up-to-date equipment, very well working IT-support, travel opportunities and good overall management of the institute must be acknowledged, as it made working at the institute particularly fun. Moreover, I would like to thank all people working at the institute for contributing to such a friendly atmosphere, especially the secretaries of the theory department Rosita Jurgeleit and Monika Goldammer, Silke Zollinger from the PR department and Karim Kannouf at the reception desk.

I am furthermore very grateful to my whole family and friends for their enduring moral support. Particular thanks go to my mother, father and sister for their support, and to my grandfather for his invaluable advice.